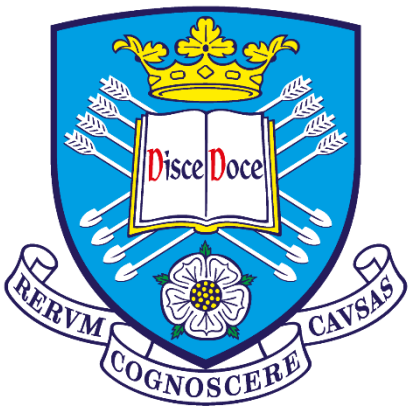

The University Of Sheffield.

Investigating the function and regulation of STX19

Amber Suzanne Marie Shun-Shion

A thesis submitted for the degree of Doctor of Philosophy

Department of Biomedical Sciences

September 2021

Acknowledgements

I would firstly like to express my gratitude to my supervisor, Andrew Peden. Andrew is an exceptional scientist, teacher, and mentor who has provided me with continued support and guidance. This allowed me to develop not only the technical skills needed but helped me to grow as a scientist and gave me the motivation to continue despite numerous setbacks - thank you for not shouting at me when I messed up the same experiment for the third time.

I am very grateful to my PhD advisors, Tanya Whitfield and Elizabeth Smythe. They have been extremely supportive, not only with my research, but with my personal and career development and shown me how women in science can excel.

I would also like to thank Jason King for all of his help and advice with my experiments and for allowing me to use his antibodies. I would like to thank Darren Robinson in the Light Microscopy Facility who has provided me with excellent training and helped me develop my microscopy skills.

I would like to thank all of my friends in the lab over the years including Asral Wirda Ahmad Asnawi, Jessica Willmott, Nabila Rahman, Ola Shehata, and Sam Lewin. They have always listened when I complained about the same experiment not working for weeks on end and always made me laugh and smile. I would also like to thank my friends outside of the lab, Gideon Hughes, Holly Stainton, Matthew Wind, and Anzar Asad. They have always been there for me and made my time in Sheffield truly unforgettable.

Last but not least, I would like to dedicate this thesis to my mum and dad, Karen and Jacques Shun-Shion. They have given me all the love and support in the world and words could not express how grateful I am. Love you loads.

Abstract

Soluble NSF attachment protein receptors (SNAREs) are the core machinery involved in membrane fusion. There are 39 SNAREs in humans that drive the fusion of different membranes and intracellular compartments, however, the machinery that regulates fusion between post-Golgi vesicles and the plasma membrane remains unclear. Syntaxin 19 (STX19) is a poorly characterised post-Golgi SNARE that localises to tubular recycling endosomes and the plasma membrane. There is limited literature describing the function of STX19 but previous studies have suggested a role in the secretion of soluble and membrane-anchored cargos. It remains unclear which pathways STX19 functions on and how STX19 function is regulated.

The main aim of this study was to gain insight into the function and regulation of STX19. To do so, we used mitochondrial re-routing assays to investigate potential STX19 interactors. We found that STX19 is likely regulated by Munc18-2 through interaction at a well-conserved peptide in the STX19 N-terminus. We also validated the STX19 interaction with kinetochore-localised protein, ZWINT, and spectraplakin protein, Dystonin (DST). Additionally, we used overexpression studies to analyse the effect of STX19 expression on its SNARE binding partners and different compartmental markers. STX19 expression alters the steady-state distribution of VAMP8 and lysosomal markers, CD63 and LAMP1. We also found STX19 expression results in a striking reduction in the levels of autophagosomal markers, LC3 and P62 suggesting STX19 may function in an autophagy-dependent pathway.

Finally, we have established a physiological model for studying STX19 function based on human keratinocytes. We found that STX19 is expressed upon calcium-induced differentiation and localises to distinct polarised regions of the plasma membrane in support of STX19 playing a role in the fusion of vesicles with the plasma membrane. Excitingly, we found that STX19 localises in close proximity to the activated serine/threonine kinase, AKT suggesting that STX19 could function in AKT-dependent pathways.

Abbreviations

aa	Refers to the amino acid number in a protein
ABD	Actin binding domain
AP complex	Adaptor protein complex
APC	Adenomatous polyposis coli
APS	Ammonium persulphate
ARF	ADP-ribosylation factor
ATG	Autophagy-related gene
ATP	Adenosine triphosphate
Bio-ID	Proximity dependent biotinylation assays
BoNT	Botulinum neurotoxin
BPAG1	Bullous Pemphigoid Antigen 1 (also known as Dystonin)
CACO-2	Human colorectal adenocarcinoma cell line
CD55	Complement decay-accelerating factor 55
CD59	Cluster of differentiation 59
CD63	Cluster of differentiation 63 (lysosomal marker)
CDC42	Cell division control protein 42
CDE	Clathrin-dependent endocytosis
CFTR	Cystic fibrosis transmembrane conductance regulator
CIE	Clathrin-independent endocytosis
COPI/II	Coat protein complex (COPI, COPII)
CSF1	Colony stimulating factor
DH5α	Cloning competent E. Coli cells
DMEM	Dulbecco's modified eagle medium
DMSO	Dimethyl sulfoxide
DNA	Deoxyribonucleic acid
DST	Dystonin (also known as BPAG1)
EDTA	Ethylenediaminetetraacetic acid
EEA1	Early endosome antigen 1 (early endosomal marker)
EGF	Epithelial growth factor
EGF-R	Epithelial growth factor receptor
EHD1/3	EH domain containing (EHD1, EHD3)
EM	Electron microscopy

ER	Endoplasmic reticulum
ERC	Endosomal recycling compartment
ERGIC	Endoplasmic reticulum Golgi intermediate compartment
ESCRT	Endosomal sorting complexes required for transport
FBS	Fetal bovine serum
FGF21	Fibroblast growth factor 21
FHL4/5	Familial hemophagocytic lymphohistiocytosis (FHL4, FHL5)
FKBP	FK506 binding protein
FLIM	Fluorescence lifetime imaging microscopy
FRB	FKBP-rapamycin binding domain
FRET	Fluorescence resonance energy transfer
GABA-R	Gamma-aminobutyric acid receptor
GABARAP	GABA Type A Receptor-Associated Protein
GAR	Gas2-related domain
GDP	Guanosine diphosphate
GEF	Guanine nucleotide exchange factor
GFP	Green fluorescence protein
GGA	Golgi localised gamma-adpatin ear containing protein
GLUT4	Glucose transporter type 4
GPI	Glycosylphosphatidylinositol (anchored-proteins)
GRAF1	GTPase regulator associated with focal adhesion kinase-1
GRASP	Golgi reassembly stacking protein
GST	Glutathione S-transferases
GTP	Guanosine triphosphate
HA tag	Hemagglutinin tag derived from the human influenza hemagglutinin protein
HEK293	Human embryonic kidney 293 cell line
HEKa	Adult human epiderminal keratinocytes
HeLa	Human cervical carcinoma cell line
HeLaM	Subclone of HeLa cell line
HEPES	4-(2-hydroxyethyl)-1-piperazineethanesulfonic acid
HGF	Hepatocyte growth factor
HKGS	Human keratinocyte growth supplement
HRP	Horseradish peroxidase
IF	Immunofluorescence

ILV	Intraluminal vesicles
LAMP1	Lysosomal associated membrane protein (lysosomal marker)
LC3	Microtubule-associated protein 1A/1B-light chain 3 (autophagosomal marker)
LIR	LC3 interacting region
MAO	Monoamine oxidase
MDCK	Madin-Darby Canine Kidney cells
MHC	Major histocompatibility complex class 1 proteins
MICAL3	Microtubule Associated Monooxygenase, Calponin And LIM Domain Containing 3
MICAL-L1	MICAL like 1
MT1-MMP	Membrane type 1 matrix metalloproteinase
MUNC18	Mammalian homologue of unc-18 (also known as STXBP)
MVID	Microvillus inclusions disease
MYO5B	Myosin VB
NAG	Neuroblastoma-amplified gene protein
NEM	N-ethylmaleimide
NHE3	Sodium hydrogen antiporter 3
NK	Natural killer cells
NMR	Nuclear magnetic resonance
NRZ	NAG ZW10 RINT1 protein complex
NSF	N-ethylmaleimide sensitive factor
NSP6	Non-structual protein 6
P62	Sequestosome 1 (also known as SQSTM1)
PBS	Phosphate buffered saline
PC12	Rat adrenal phaeochromocytoma cells
PCI	Protease cocktail inhibitor
PCR	Polymerase chain reaction
PEI	Polyethylenimine
PFA	Paraformaldehyde
PI3K	Phosphoinositide 3-kinase
PI3P	Phosphatidylinositol 3-phosphate
PKB	Protein kinase B (also known as Akt)
PM	Plasma memrbane
RAC1	Ras-related C3 botulinum toxin substrate 1
RASSF8	Ras association domain family 8

RINT1	Rad50 interactor 1
RNA	Ribonucleic acid
RPE1	Human retinal pigment ephitilial cells
SDS-PAGE	Sodium doceyl sulphate-polyacrylamide gel electrophoresis
SM	Sec/Munc (family of proteins)
SNAP	Synaptosomal-associated protein (Qbc-SNAREs)
SNARE	Soluble NSF attachment protein receptor
SR	Serine repeats
STX	Syntaxin (Qa-SNAREs)
STXBP	Syntaxin binding proteins (also known as Munc18 proteins)
TBE	Tris-borate-EDTA
TBK1	TANK binding kinase 1
TEMED	Tetramethylethylenediamine
TGFβ1	Transforming growth factor beta 1
TGN	Trans-Golgi network
TGS	Tris-Glycine-SDS
TIRF	Total internal reflection microscopy
TMD	Transmembrane domain
TNFα	Tumor necrosis factor alpha
TPD45	Tumour protein D45
TRAPII	Transport protein particle complex (TRAPPI, TRAPII)
TRE	Tubular recycling endosomes
TRIO	Triple functional domain protein
VAMP	Vesicle-associated membrane protein
VSV-G	Vesicular stomatitis virus G protein
WB	Western blot
Y2H	Yeast-two hybrid
ZW10	Zeste White 10
ZWINT	ZW10 interactor

Table of Contents

Table of Figures

Table of Tables

Chapter 1

Introduction

1.1 Overview of the secretory pathway

First described by Palade in 1975, the secretory pathway plays a vital role in all eukaryotic cells (Palade, 1975). This fundamental process is crucial for the survival and normal homeostasis of cells, as well as underpinning more specialised cellular functions. For example, all cells secrete extracellular matrix proteins that provide a physical scaffold to build tissues and organs whilst the B cells in our immune systems secrete antibodies to fight infection and pancreatic acini secrete enzymes to aid digestion (Kelly, 1985).

The pathway begins with protein synthesis on ribosomes and recognition of a signal peptide by receptors on endoplasmic reticulum (ER) membranes (Deshaies and Schekman, 1987). Proteins co-translationally enter the ER where protein folding, post-translation modifications, and quality control take place. Proteins are subsequently trafficked to ER-Golgi intermediate compartment (ERGIC) membranes via COPII coated vesicles (Barlowe *et al.*, 1994). From here, proteins advance through the Golgi and undergo post-transcriptional modifications such as glycoslation, sulfation, and phosphorylation. At the trans-Golgi network (TGN), proteins are sorted for their destination and packaged into vesicles (Harter and Reinhard, 2002). These vesicles are trafficked along microtubule networks to the plasma membrane where they are tethered and docked. Finally, SNARE-mediated fusion releases the proteins into the extracellular space or inserts the protein into the plasma membrane (Chen and Scheller, 2001).

1.1.1 Early research on the secretory pathway

Our understanding of the secretory pathway started over 100 years ago with the discovery of the Golgi complex by Camillo Golgi in 1898. Advances in electron microscopy (EM) and cell fractionation during the 40s and 50s led to further discoveries. Porter, Claude, and Fullham used EM to visualise cellular ultrastructure and described the lace-like reticulum of the ER in 1945 (Porter, Claude and Fullam, 1945). Building on their work, Siekevitz and Palade began to uncover the secretory pathway in 1958 when they injected guinea pigs with radioactive leucine and isolated cell fractions from secretory pancreatic acinar cells. Purification of radioactive digestive enzyme chymotrypsinogen at different time points following injection revealed that the enzyme first appeared in ER fractions and eventually became concentrated in specialised secretory granules (Siekevitz and Palade, 1958a). Combining this approach with EM in 1964, Caro and Palade also uncovered the intermediate stages of the secretory pathway showing that the radioactive enzyme is also transported through the Golgi (Caro and Palade, 1964). Using these methods, Jamieson and Palade published a series of papers in the late 60s/early 70s further defining the role of vesicles, the kinetics, and the metabolic requirements of secretory protein transport from the ER to secretory granules via the Golgi (Jamieson and Palade, 1967). Palade went on to fully describe the vesicular model of the secretory pathway in 1975 (Palade, 1975).

With the stages of the secretory pathway defined, the field set out to elucidate the molecular mechanisms that were involved in protein secretion in the 70s and 80s.

Fundamental yeast genetic analysis by Novick and Schekman in 1979 led to the discovery of proteins (sec proteins) required for different stages of secretion. Novick and Schekman first reported a temperature-sensitive secretion deficient strain of yeast that, when incubated at 37 °C, accumulates intracellular vesicles containing the secretory enzyme, acid phosphatase. Incubation at a non-restrictive temperature led to a reduction in the accumulated vesicles and the enzyme was secreted (Novick and Schekman, 1979). From there, Novick and Schekman determined that, whilst the mutant yeast has an accumulation of vesicles, the overall size did not change, meaning that secretory mutant strains were denser than wildtype strains. This allowed them to isolate secretory deficient cells from wildtype cells along a density gradient. This work ultimately led to the identification of 23 genes required for secretion at different stages of the secretory pathway (Novick, Field and Schekman, 1980).

Meanwhile, the Rothman lab set out to determine the molecular mechanisms of the secretory pathway using a cell-free *in vitro* reconstitution assay. They utilised mutant CHO cells that lacked Golgi enzyme, GlcNAc-transferase I, which resides in the medial Golgi compartment and is required for the addition of GlcNAc to form complex oligosaccharides. Mutant CHO cells were infected with vesicular stomatitis virus (VSV) in order to study the transport of VSV encoded G protein (VSV-G) which has GlcNAc added when it reaches the medial compartment of the Golgi. Golgi compartments from mutant infected CHO cells and wildtype cells were isolated by fractionation and mixed *in vitro*. This allowed VSV-G protein to be transported from mutant donor compartments to wildtype acceptor compartments that did contain the enzyme and thus were able to add GlcNAc to the G protein. Measuring the amount of GlcNAc incorporated G protein gave a measure of the rate of transport from the donor compartment to the acceptor compartment (Braell *et al.*, 1984). Combining this assay with the used of radioactive GlcNAc and EM, Balch and Rothman went on to determine the stages of transport and were able to reconstitute vesicle budding, attachment, and fusion *in vitro*, thus confirming vesicular transport of secretory proteins (Balch *et al.*, 1984; Balch, Glick and Rothman, 1984). With an understanding of the mechanisms of the secretory pathway forming, continued research further uncovered the molecular details of secretion including the identification of SNAREs (Thomas Söllner *et al.*, 1993).

1.1.2 Constitutive vs regulated secretion

Whilst secretory proteins follow the same general pathway to the cell surface, secretion can be separated into two types – constitutive and regulated. Constitutive secretion is the continuous release of proteins without any extracellular cue, the rate of which is regulated by only protein production. Also known as bulk flow, proteins that are constitutively secreted lack export signals and flow through the pathway

without dependency on receptors for cargo sorting (Burgess and Kelly, 1987). Prevention of misfolded constitutive secretory proteins from being released relies on recognition of misfolding and retention in the ER by ER-resident chaperones (Barlowe and Helenius, 2016). This type of secretion is important for general cell homeostasis as well as other specialised functions such as the release of cytokines by immune cells and albumin by hepatocytes.

Regulated secretion is secretion of proteins coupled to an extracellular stimulus. This leads to an increase in intracellular Ca^{2+} resulting in vesicle fusion. Proteins that undergo regulated secretion contain export signals that sort them into specific secretory vesicles at the TGN. Certain secretory cells, such as endocrine and exocrine cells, have specialised vesicles known as secretory granules. Secretory granules are typically larger than vesicles and can be distinguished by EM as having an electron dense core. Proteins can be concentrated into secretory granules with a 200-fold increase in concentration from the ER, as opposed to a 2-fold increase in constitutive secretory vesicles. Cells accumulate secretory granules in the cytoplasm under the plasma membrane. Concentrated protein in accumulated granules allows for rapid secretion of a large amount of protein in response to extracellular stimuli. A variety of extracellular stimuli can trigger regulated secretion. Electrical signals in neurons stimulate the release of neurotransmitters at the synapse, and detection of blood glucose levels by pancreatic β cells can lead to the release of insulin (Burgess and Kelly, 1987; Tooze, 1998).

1.1.3 Post-Golgi trafficking

The trans-Golgi network is the main cargo sorting station in which proteins are packed into different transport carriers and targeted to various destinations. Cargo can be sorted into vesicles or tubules that are constitutively formed. Adaptor proteins play a fundamental role in this process by recognising sorting motifs on cargo (Guo *et al*., 2014). 5 adaptors belonging to the adaptor protein (AP) family have been identified in eukaryotes. AP-1 and AP-2 bind and concentrate cargo into vesicles whilst recruiting the clathrin lattice responsible for vesicle budding. AP-1 facilitates a direct trafficking pathway from the TGN to the plasma membrane whereas AP-2 is involved in vesicle formation at the plasma membrane during endocytosis (Hirst and Robinson, 1998). AP-3 facilitates trafficking from the TGN to lysosomes, however whether AP-3 binds clathrin remains controversial (Peden *et al.*, 2002). AP-4 does not bind clathrin and is thought to be responsible for the trafficking of specific cargo proteins from the TGN to endosomes such as amyloid precursor protein (APP) (Robinson, 2004; Guo *et al*., 2014). AP-5 is the most recently discovered adaptor protein and thought to play a role in retrieval of the cation-independent mannose-6-phosphate receptor (CI-MPR) from the lysosome to the TGN (Hirst *et al.*, 2018). Other clathrin-associated adaptors include Golgi-localized, gamma-ear-containing, Arf binding proteins (GGAs) and epsin-related proteins that mediate transport from the TGN to endosomes (Guo *et al*., 2014).

Once cargo is sorted and packaged, vesicles traffic to the target membrane along microtubules. The fast growing plus end of the microtubule usually extends towards the cell periphery whilst the minus end is anchored by centrosomes at the cell cortex. Motors facilitate the movement of vesicles along microtubules with kinesin moving towards the plus end and dynein towards the minus end (reviewed in Barlan and Gelfand, 2017).

Vesicles are subsequently tethered to target membranes by tethering complexes. Tethering occurs through interaction of the complex with coat proteins and phospholipids (Liu *et al.*, 2007). Post-Golgi tethering complex, the exocyst, is recruited to the membrane by GTP-bound Rab8 and tethers vesicles arriving from the TGN to the plasma membrane (Guo *et al.*, 1999; Whyte and Munro, 2002).

Vesicle fusion immediately follows tethering. Different SNAREs reside in specific subcellular compartments. Syntaxin (STX) 1 and STX 2 mediate fusion at the plasma membrane whereas STX7 mediates fusion with the lysosome (Jahn and Scheller, 2006). The specificity that SNAREs confer to vesicle trafficking is still debated, however, polarised cells require different SNARE complexes for polarised trafficking. STX3 is localised and mediates fusion at the apical membrane whereas STX4 mediates fusion at the basolateral membrane (Low *et al.*, 1996). Similarly in neurons, STX3 mediates fusion at axonal membranes whilst STX4 does so at somadendritic membranes (Soo Hoo *et al.*, 2016).

1.1.4 Recycling pathways

After delivery to the cell surface, membrane proteins such as signalling receptors, as well as extracellular materials, and lipids can all be internalised within the cell via endocytosis. Internalisation of cargo is important for many physiological processes, such as signal transduction and nutrient uptake. There are a variety of endocytic mechanisms which can be broadly classified as clathrin-dependent endocytosis (CDE) or clathrin-independent endocytosis (CIE). Clathrin-dependent endocytosis relies of the formation of clathrin-coated pits facilitated by AP-2 which leads to membrane invagination and the formation of endocytic vesicles. Clathrin-independent endocytosis includes an array of mechanisms that do not rely on clathrin-coated pits, such as caveolae formation, phagocytosis, macropinocytosis, and non-clathrin coated pit formation (reviewed in Grant and Donaldson, 2009).

After endocytosis, proteins have three fates. They can be trafficked to lysosomes to be degraded, recycled back to the cell surface, or trafficked through a retrograde pathway to the Golgi. Proteins destined for degradation are endocytosed into early endosomes and labelled for degradation by ubiquitinylation. The ESCRT family of protein complexes functions to sort ubiquitinylated proteins into a degradative subdomain of the early endosome. This domain ultimately forms intraluminal vesicles (ILVs) as early endosomes mature into late endosomes. From here, late endosomes fuse with lysosomes to form

an endolysosomal compartment that provides the right acidic environment for protein degradation (reviewed in Cullen and Steinberg, 2018).

Alternatively, proteins can be recycled back to the cell surface. Recycling maintains proper protein and lipid composition at the cell surface and is essential for various processes including cell division, maintaining polarity, and migration. Recycling can also influence signalling outputs by mediating the intracellular residence time of signalling receptors or altering transport rates to increase or decrease cell surface expression (Maxfield and McGraw, 2004; Grant and Donaldson, 2009).

1.1.4.1 Fast recycling

Fast recycling traffics endocytosed proteins from the early endosome directly to the plasma membrane. Rab proteins make up the largest subfamily of small GTPases and, in concert with their effectors, are known to co-ordinate various stages of transport through different trafficking pathways (figure 1-1, Zerial and McBride, 2001). Rab4 was initially identified as having a role in transferrin receptor (Tfr) recycling and is considered a regulator of rapid recycling (van der Sluijs *et al.*, 1992; Sönnichsen *et al.*, 2000). Further studies supported this showing that dominant negative forms of Rab4 reduce Tfr and EGF recycling (McCaffrey *et al.*, 2001). Rab4 was also shown to mediate the rapid recycling of β2 adrenergic receptor (B2AR) within 1 minute of ligand-induced endocytosis (Yudowski *et al.*, 2009). There is, however, contradicting evidence for the role of Rab4. Studies on Rab4 and its effector rabaptin-5 showed that knockdown of Rab4 increased recycling of Tfr (Deneka *et al.*, 2003). This suggests there may be other ways in which Rab4 regulates recycling and its specific roles remain unclear.

Rab35 has also been identified as a regulator of rapid recycling. Pulse-chase experiments in HeLa cells demonstrated expression of a dominant negative mutant of Rab35 impairs rapid Tfr recycling with chase times of 5 minutes or less, but not the slow trafficking with chase times of 15 minutes or more (Kouranti *et al.*, 2006). Rab35 was also shown to mediate the recycling of yolk receptors in *C. elegans* as Rab35 mutants exhibited perturbed yolk receptor recycling. This phenotype was exaggerated with additional knockdown of Rab11 suggesting that Rab35 acts in a parallel pathway to Rab11 (Sato *et al.*, 2008). Since Rab11 is known to regulate slow receptor recycling, this evidence is consistent with the idea that Rab35 regulates fast recycling.

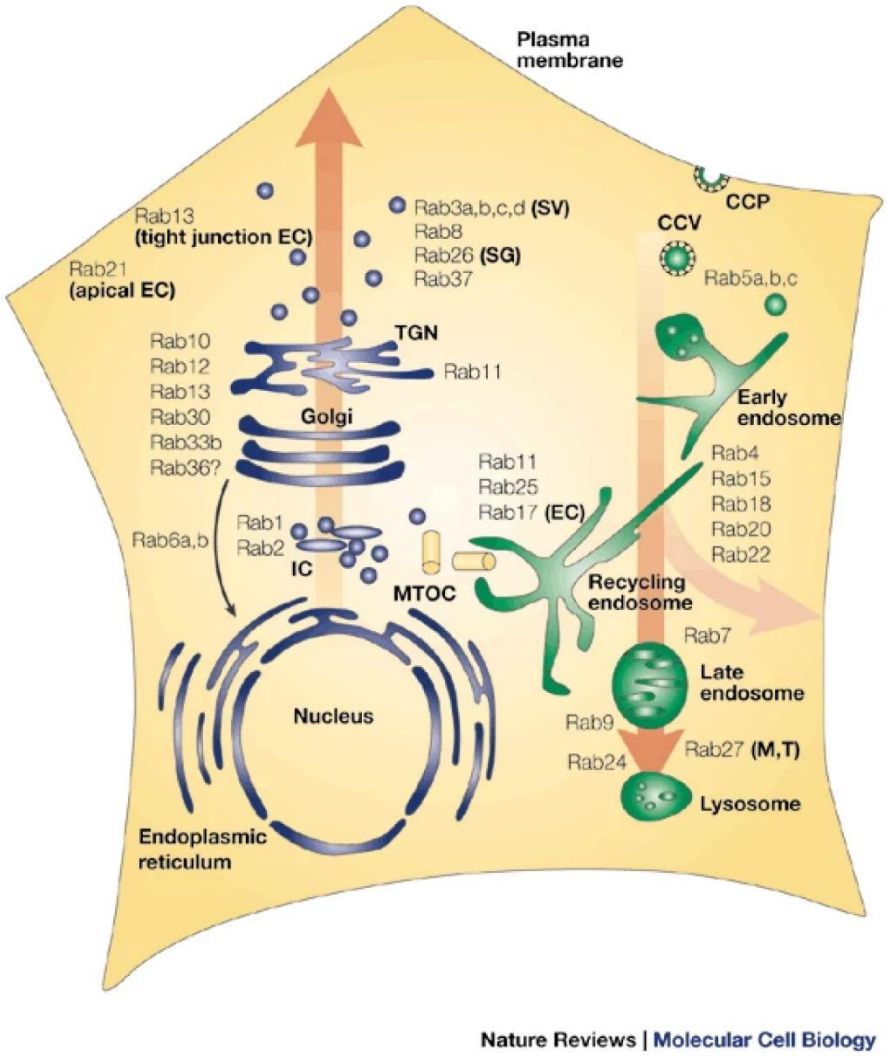

Figure 1-1: Map of intracellular Rab protein localisations. *Figure taken from Zerial and McBride, 2001. Nature Reviews Molecular Cell Biology.* Members of the small GTPase Rab protein family localise to different trafficking pathways to regulate transport through different compartments. Some rabs are cell type specific (e.g. Rab3a in neurons) and tissue-specific (e.g. Rab17 in epithelial tissues). Green compartments represent endocytic and recycling pathways. Blue compartments represent exocytotic pathways. CCV, clathrin-coated vesicle; CCP, clathrin-coated pit; EC, epithelial cells; IC, ER–Golgi intermediate compartment; M, melanosomes; MTOC, microtubule-organizing centre; SG, secretory granules; SV, synaptic vesicles; T, T-cell granules; TGN, trans-Golgi nextwork.

1.1.4.2 Slow recycling

Proteins on the slow recycling route are endocytosed into the early endosome and subsequently trafficked through an endosomal recycling compartment (ERC) before reaching the cell surface. The ERC has been described as group of tubular and vesicular structures that often condense around the microtubule organising centre (MTOC), however the exact morphology remains unclear. Super resolution microscopy has been used to show that the ERC may not be a singular membrane bound organelle but rather a complex arrangement of independent endosomal membranes which may be linked by membrane bridges (Xie *et al.*, 2016).

How proteins are sorted into a slow recycling pathway and the ERC remains poorly understood. Membrane-bound proteins may sort by a geometry-based mechanism. The tubulation of membranes at the early endosome results in a recycling subdomain in which there is a high membrane to vacuole ratio compared to the vesicular portion. Membrane-bound proteins are generally sorted with the bulk flow of membrane into the tubular domains whilst proteins with a ubiquitin sorting signal are sorted into the vesicular degradative domains. Evidence for this model came from visualising distinct membrane domains of the ERC marked by Rab GTPases that regulate different parts of the pathway (Sönnichsen *et al.*, 2000). Rab11, a known regulator and marker of the ERC, may also play a central role in sorting. Campa et al., describe a model in which the generation of PI3P by clathrin-binding phosphoinositide 3-kinase class 2 alpha (PI3K-C2α) leads to the activation of Rab11 on sorting endosomal membranes. Rab11 in turn recruits phosphatidylinositol 3-phosphatase myotubularin 1 (MTM1) which hydrolyses PI3P. The reduction in PI3P allows vesicle fission and the transport of cargo from the early sorting endosome to the Rab11-positive ERC (Campa *et al.*, 2018).

In addition to entry into the recycling pathway, Rab11 regulates recycling from the ERC to the cell surface. Early studies identified Rab11 to have a role in Tfr recycling (Ullrich *et al.*, 1996) and analysis of constitutively active and dominant negative mutants demonstrated that activation of Rab11 is required for recycling through the ERC (Ren *et al.*, 1998). Rab11 exerts its effects through the Rab11 family of interacting proteins (FIPs) which play roles in targeting Rab11-positive vesicles to the plasma membrane. Studies in baby hamster kidney (BHK) cells demonstrated that truncation of the C2 domain of FIPs impairs Tfr recycling and Rab11/FIPs complexes promote vesicle docking on membranes (Lindsay *et al.*, 2002; Lindsay and McCaffrey, 2004). Class I FIP, Rab coupling protein (RCP), has been shown to interact with Rab11 to mediate the sorting of Tfr. RCP knockdown leads to degradation of Tfr suggesting that RCP acts to sort Tfr into the recycling pathway and avoid a degradative fate (Peden *et al.*, 2004).

Recycling to the cell surface may depend on the mechanism by which proteins are endocytosed. Following either CDE or CIE cargo using high resolution microscopy, Xie et al., demonstrated that CIE cargo remains separate from Rab11-positive regions at the ERC and is recycled to the cell surface through tubular recycling endosomes (TREs) (Xie *et al.*, 2016).

1.1.5 Rab8

One Rab protein that regulates recycling through the clathrin-independent tubular recycling endosomal compartment is Rab8. There are two isoforms of Rab8, Rab8a and Rab8b, which share 83 % identity. The different roles the two isoforms play is not well defined and therefore, both isoforms shall be referred to as Rab8. Rab8 has a number of roles in various processes including recycling pathways, epithelial polarisation, cell migration, and ciliogenesis (Peränen, 2011). Subcellularly, Rab8 localises to tubular recycling endosomes (TREs) where it mediates the recycling of clathrin-independent endocytosed cargos such as integrins (β1-integrins) and GPI-anchored proteins (CD55 and CD59) (Hattula *et al.*, 2006; Koubek and Santy, 2018). Expression of a constitutively active form of Rab8 results in co-localisation of β1-integrin and Rab8 on TREs. Expression of dominant negative forms of Rab8 lead to accumulation of β1-integrin in vacuoles suggesting Rab8 mediates β1-integrin recycling through the TREs. Rab8 has also been shown to partially co-localise with the transferrin receptor (TrfR) on TREs. Inhibition of Rab8 results in the trapping of TrfR in the endosomal recycling compartment (ERC) (Hattula *et al.*, 2006).

Rab8 recruitment to TREs is mediated by MICAL-L1. Rab8 co-localises with MICAL-L1 on TREs and depletion of MICAL-L1 results in dissociation of Rab8 from this compartment (Sharma *et al.*, 2009a). Additionally, MICAL-L1 functionally links Rab8 and EHD1 to TREs to mediate receptor recycling (Rahajeng *et al.*, 2012). It has also been shown that Rab35 acts as a master regulator to promote MICAL-L1 recruitment and subsequently Rab8 recruitment to TREs (Kobayashi *et al.*, 2014).

As well as receptor recycling, Rab8 has been shown to have roles in membrane protrusion formation. Using live cell-imaging, Hattula et al., demonstrated that Rab8 localises macropinosomes at the ruffling surface of the plasma membrane. Subsequently, these structures form tubular recycling endosomes which mediate Rab8-positive membrane recycling back to the cell surface to promote lamellipodia formation (Hattula *et al.*, 2006). This pathway is also defined by Arf6. Arf6 also localises to TREs and is known to mediate recycling of clathin-independent endocytosed cargo (Eyster *et al.*, 2009). Arf6 and Rab8 have been shown to co-localise to the same TREs. Expressing a constitutively active form of Arf6 inhibits the formation of Rab8-positive TREs and inhibits cell surface extension formation promoted by a Rab8 constitutively active mutant. Expression of a dominant negative Arf6 mutant allows prominent Rab8-positive TRE formation (Hattula *et al.*, 2006). This suggests that Arf6 acts upstream of Rab8 to regulate its function in membrane recycling and membrane protrusion formation.

The role for Rab8 in membrane protrusion formation is important in cell migration. It has been shown that expression of Rab8 promotes cell invasiveness in 3D matrices as well as loss of contact inhibition (Bravo-Cordero *et al.*, 2007). Rab8 has been shown to mediate actin and focal adhesion re-organisation. High-content analysis of actin and focal adhesions showed that Rab8 induces activation of Rac1 and Tiam1-dependent actin polymerisation and focal adhesion disassembly (Bravo-Cordero *et al.*, 2016). This suggests a role for Rab8 in driving cell motility.

Rab8 is also a key player in epithelial polarisation. Rab8 has been shown to mediate recycling of apical proteins in epithelial cells *in vivo*. Knockout of Rab8 leads to an accumulation of apical proteins in vacuoles. Rab8 knockout mice demonstrate a microvillus inclusion phenotype consistent with the loss of apical trafficking (Sato *et al.*, 2007). Additionally, Rab8, in concert with Rab8-specific GEF Rabin8 and Rab11, have been shown to regulate apical trafficking and lumen formation. Analysis of lumen formation after combinatorial knockdown of Rab8 with or without Rab11 knockdown suggested Rab11 functions upstream of Rab8 to regulate lumen formation. Rab8 internalisation and turnover by GRAF1 has also been shown to be important in establishing the polarity axis. GRAF1 has been shown to remove active Rab8 from the cell surface into TREs. Depletion of GRAF1 results in Rab8 accumulation in the tips of membrane protrusions in HeLa cells and impairs luminal polarity in MDCK cells grown in 3D cultures. Taken together, this data suggests that Rab8 endocytosis by GRAF1 is important in establishing epithelial polarity (Vidal-Quadras *et al.*, 2017).

Rab8 also regulates polarised vesicle trafficking during ciliogenesis. Rab8 was originally identified to have a role in trafficking rhodopsin-containing vesicles to primary cilia in photoreceptors (Moritz *et al.*, 2001). It was later identified in screens to be located at primary cilia in serum starved cells (Nachury *et al.*, 2007; Yoshimura *et al.*, 2007; Westlake *et al.*, 2011). GFP-tagged Rab8 was shown to enter the primary cilium and promote extension of the ciliary membrane (Nachury *et al.*, 2007). Depletion of Rab8 inhibited cilia formation (Westlake *et al.*, 2011).

As well as receptor and membrane recycling, Rab8 has roles in exocytosis. MT1-matrix metalloproteinase (MT1-MMP) is secreted from invasive structures during cell migration. MT1-MMP was shown to be present in Rab8-positive vesicles in invasive structures of invasive MDA-MB-231 adenocarcinoma cells. Expression of constitutively active Rab8 mutants promotes invasion and cell migration, whilst Rab8 knockdown inhibited these processes. This suggested that Rab8 regulated the polarised exocytosis of MT1-MMP to regulate invasiveness in cancer cells (Bravo-Cordero *et al.*, 2007).

Rab8 has also been shown to be required for the docking and fusion of secretory vesicles with the plasma membrane. Grigoreiv et al., demonstrated using a flow-cytometry based assay to measure constitutive secretion that knockdown of Rab8 results in a secretion delay. Using live cell imaging and streptavidin

pulldowns, they showed that Rab8 is recruited to Rab6-positive vesicles through interactions with ELKS and MICAL3. Rab8 was suggested to dock vesicles and mediate fusion with the plasma membrane in complex with ELKS and MICAL3 (Grigoriev *et al.*, 2011).

Finally, Rab8 has been reported to be involved in an unconventional secretory pathway that utilises autophagic machinery. Transforming growth factor beta 1 (TGFβ1) was shown to be present in LC3-positive autophagosomal intermediates. Knockdown of ATG5 abolished the formation of early autophagosomal intermediates and the secretion of TGFβ1. Rab8 was also shown to be partially co-localised TGFβ1 and knockdown of Rab8 reduced levels of TGFβ1 in the culture supernatant. Taken together, this suggested that Rab8 regulates the secretion of TGFβ1 through an unconventional autophagy-dependent secretory pathway (Nüchel *et al.*, 2018). Similarly, Rab8 was shown to drive autophagy-dependent secretion of proinflammatory cytokine, interleukin-1β (IL-1β). Rab8 was shown to localise to LC3/IL-1β-positive structures and depletion of Rab8 abolished IL-1β secretion (Dupont *et al.*, 2011).

1.1.6 MICAL-L1

MICAL-L1 is also a marker of TREs. As discussed, MICAL-L1 is required for the recruitment of Rab8 to TREs where it can mediate recycling. MICAL-L1 belongs to the molecules interacting with CasL (MICAL) family of proteins. Members of this family function in a diverse array of cellular processes such as cell division, axonal growth, angiogenesis, cell migration, and endocytic recycling. There are 5 MICAL family members in humans, 3 of which are classic MICAL proteins (MICAL1, MICAL2, and MICAL3) and 2 are MICAL-like proteins (MICAL-L1 and MICAL-L2) (Giridharan and Caplan, 2014; Frémont *et al.*, 2017).

MICAL-L1 contains a CC domain that mediates association with membranes containing phosphotidic acid (PA) (Giridharan *et al.*, 2013), as well as Rab proteins including Rab8 (Fukuda *et al.*, 2008). MICAL-L1 itself associates with TREs through PA binding. PA is an essential component of TREs and recruits both MICAL-L1 and syndapin II (also known as PACSIN II) where they contribute to TRE biogenesis. MICAL-L1 recruitment to TREs is regulated by small GTPases, Rab35 and Arf6. Rab35 interacts with MICAL-L1 and overexpression results in a decrease in the levels of MICAL-L1 associated with TREs (Rahajeng *et al.*, 2012). Arf6 is a key regulator of CIE cargo recycling through TREs and regulates the localisation of MICAL-L1 and EHD1. Arf6 depletion leads to decreased levels of MICAL-L1 on TREs (Rahajeng *et al.*, 2012). Since Rab35 effectors inactivate Arf6 (Kanno *et al.*, 2010), Rab35 and Arf6 are thought to function antagonistically to regulate the recruitment of MICAL-L1 to TREs and receptor recycling.

MICAL-like proteins also contain NPF motifs that facilitate their interaction with EHD proteins (Sharma *et al.*, 2009a). MICAL-L1 co-localises with EHD1 on TREs to mediate receptor recycling. Depletion of MICAL-

L1 results in the loss of EHD1 on TREs and subsequently impairs Tfr and β1 integrin recycling (Sharma *et al.*, 2009a). EHD1 knockdown has no effect on Rab8 localisation suggesting MICAL-L1 serves as a functional link between EHD1 and Rab8, recruiting both to TREs and thereby facilitating receptor recycling (Sharma *et al.*, 2009a).

MICAL-L1 has also been reported to have roles in delivery of cargo from TREs to the plasma membrane. Sikora et al., used RUSH assays to monitor the secretion of plasma membrane cargos, TNFα and E-cadherin. Knockdown of MICAL-L1 resulted in a reduction of TNFα and E-cadherin delivery to the cell surface. Expression of shRNA-resistant GFP-MICAL-L1 rescued TNFα levels at the plasma membrane (Sikora *et al.*, 2021). Additionally, MICAL-L1 and Src have been shown to partially co-localise at TREs. Cells depleted for MICAL-L1 by siRNA show a reduction in Src levels at the plasma and a reduction in Src phosphorylation. This suggests that MICAL-L1 has roles in Src delivery to the cell surface and activation (Reinecke *et al.*, 2014).

1.2 SNAREs

1.2.1 The discovery of membrane fusion machinery

A crucial part of the secretory pathway is membrane fusion. Proteins destined for secretion are trafficked from one compartment to the next bound by vesicular membranes. The only way to progress is by fusion of the protein-containing vesicle with its target compartment.

In the late 1980s, work in the Rothman laboratory began to uncover the machinery required for membrane fusion. N-Ethylmaleimide was shown to inhibit transport between Golgi cisternae in a cell-free system which was rescued by addition of a cytosolic fraction (Block *et al.*, 1988). The basis of this assay was used to purify an N-Ethylmaleimide Sensitive Factor (NSF) which was further shown to be required for transport between Golgi stacks. Using an IgM antibody against NSF inhibited transport between stacks. Incubation of Golgi stacks with ATP and cytosol, but without NSF, led to an accumulation of uncoated vesicles suggesting NSF was required for membrane fusion (Malhotra *et al.*, 1988). Following this, two factors were identified that allowed NSF to associate with membranes. A binding assay showed that NSF association with membranes required addition of cytosol suggesting a soluble cytosolic factor was important in NSF membrane association. This factor could be separated from bulk protein by cytosolic fractionation and was inactivated by heat and trypsin but not NEM, demonstrating it was a protein distinct from NSF. The cytosolic factor was termed ‘soluble NSF attachment protein’ (SNAP). The binding of NSF to membranes, however, could be saturated in the presence of excess cytosol. This suggested an additional membrane bound factor is required for NSF membrane association. Pre-treatment of membranes with sodium carbonate (used to remove

peripheral proteins, but not integral membrane proteins) demonstrated the membrane bound factor was an integral membrane component (Weidman *et al.*, 1989).

The Rothman lab went on to clone and sequence NSF and found it to be equivalent to Sec18 in yeast which had previously been shown to mediate transport from the ER to the Golgi. Rothman used monoclonal antibodies against NSF in semi-intact cells to block NSF function. This inhibited ER to Golgi transport which was rescued by addition of highly purified NSF (Beckers *et al.*, 1989). Thus, NSF was also required for ER to Golgi transport leading to the hypothesis that this was a general mechanism for membrane fusion and not specific to intra-Golgi transport.

Further work to dissect this mechanism led to the isolation of three isoforms of SNAP from bovine brain cytosol - α-SNAP, β-SNAP, and γ-SNAP. Each isoform was shown to bind NSF to membranes and allow vesicular transport (Clary, Griff and Rothman, 1990). Using radioactively labelled α-SNAP in pulldown assays, Rothman went on to show that SNAPs can only bind NSF in the presence of the integral membrane component. Further velocity sedimentation studies demonstrated that NSF, SNAPs, and the integral membrane component, form a multisubunit 20S complex and the dissociation of this complex was coupled with ATP hydrolysis (Wilson *et al.*, 1992). Additional crosslinking studies uncovered a 30-40 kDa integral membrane receptor was the α-SNAP binding component in the complex and demonstrated that SNAPs bind to the multisubunit SNAP receptor (SNARE) membrane complex as an adaptor for NSF association with membranes (Whiteheart *et al.*, 1992).

At the same time, identification and cloning of SNARE proteins was taking place in the labs of Scheller, Südhof, and Jahn. Scheller used a polyclonal antibody raised against purified cholinergic synaptic vesicles from *Torpedo californica* to screen a cDNA library generated from the electromotor nucleus. This led to the identification of vesicle-associated membrane protein, VAMP1. Scheller suggested it had roles in neurotransmitter packaging, transport, and release (Trimble, Cowan and Scheller, 1988). Subseqently, Südhof went on to clone synaptobrevin (also known as VAMP2) from mammalian synaptic vesicles and demonstrated its homology to VAMP1 (Südhof *et al.*, 1989).

A pivotal discovery in understanding SNARE function was made in the Montecoccu lab. Montecoccu et al., found that injection of Botulinum Toxin serotype B (BoNT/B) and Tetanus toxin light chains into neurons inhibits neurotransmitter release. They went on to incubate purified synaptic vesicles with both toxins and found a single band disappeared from the SDS-PAGE protein pattern, which they identified as synaptobrevin (Schiavo *et al.*, 1992). Südhof and Jahn quickly confirmed the discovery. By incubating isolated synaptic vesicles with the Tetanus toxin, they were able to demonstrate that the toxin specifically cleaves synaptobrevin resulting in near complete degradation of the protein as assayed by immunoblotting. No other synaptic proteins were affected by the toxin. Thus, they concluded

synaptobrevin was central in neurotransmitter release and hypothesised its involvement the membrane fusion step itself, potentially as part of a membrane fusion complex (Link *et al.*, 1992).

Identification of other proteins thought to be involved in vesicle fusion occurred shortly after. Scheller was interested in synaptotagmin, a protein previously identified as a regulator of neurotransmitter release and sought to identify its interacting partners. An anti-synaptotagmin antibody was used in pulldown assays on a crude fraction from rat brain. This led to the identification of syntaxin A and B. They identified a hydrophobic C-terminus thought to serve as a membrane anchor and were able to extract syntaxin from membranes using detergent demonstrating it was an integral membrane protein. However, co-immunoprecipitation with anti-synaptotagmin on salt-washed vesicle fraction (disturbs vesicle-membrane interactions) did not pull down syntaxin. This demonstrated that syntaxin was on a different membrane compartment. Using immunofluorescence, they showed syntaxin was concentrated on a domain of the plasma membrane at the site of neurotransmitter release suggesting syntaxin plays a role in the docking of vesicles at the pre-synaptic terminal (Bennett, Calakos and Scheller, 1992).

Additional members of the syntaxin family were identified by screening cDNA libraries with syntaxin cDNA probes. Immunofluorescence studies were used to localise the isoforms and found, whilst the majority were localised to the plasma membrane, syntaxin 5 localised to either the Golgi or an ER-Golgi intermediate compartment. This suggested the same general machinery is used in multiple membrane trafficking pathways (Bennett *et al.*, 1993). A few years later, Botulinum toxin serotype C (BoNT/C) was shown to cleave syntaxin proteins suggesting they were part of the hypothesised membrane fusion complex (Schiavo *et al.*, 1995).

The identification of SNAP-25 by the Wilson lab provided additional insight into the molecular mechanism of membrane fusion. cDNA clones of a 25kDa neuronal specific mRNA, termed SNAP-25, were isolated and characterised. Using protein fractionation and light and electron microscopy, it was shown that SNAP-25 was concentrated in pre-synaptic terminals suggesting a role in synaptic function (Oyler *et al.*, 1989). Südhof and Jahn also found that Botulinum Toxin serotype A (BoNT/A) cleaves SNAP-25 and inhibited neurotransmitter release (Blasi *et al.*, 1993). This led to the proposal that SNAP-25 was also a component of the putative membrane fusion complex.

At this point, proteins that were thought to be involved in membrane fusion had been identified and characterised. However, the mechanism by which they facilitated fusion was unknown. A ground breaking discovery that was fundamental to our mechanistic understanding of membrane fusion came from Rothman in 1993 (Söllner *et al.*, 1993; Söllner *et al.*, 1993b). NSF and SNAP were used to extract SNAP receptors (SNAREs) from brain homogenate. Three proteins were purified from this assay and identified as SNAP25, VAMP, and syntaxin. Syntaxin and SNAP25 had been shown to associate with the plasma

membrane and VAMP was known to associate with vesicles suggesting a simple mechanism for vesicle targeting and docking. Rothman went on to show that in the absence of NSF and α-SNAP, the three SNAREs can assemble into a stable complex (Söllner *et al.*, 1993b). Using co-immunoprecipitation experiments in the presence of α-SNAP, NSF, and ATP, Rothman demonstrated that ATP hydrolysis by NSF results in the dissociation of the SNARE complex (Söllner *et al.*, 1993). This work led to the generation of the SNARE hypothesis for vesicle targeting which suggested that specific SNAREs reside on vesicles (v-SNAREs) and would form a unique match with the corresponding SNAREs on the target membrane (t-SNAREs). The direct and specific binding of v-SNAREs and t-SNAREs forms a stable complex which would dock the vesicle to the target membrane (Rothman and Warren, 1994).

Despite the discovery of the SNARE complex, its function in membrane fusion remained unclear. In 1998, Rothman used reconstituted lipid assays to demonstrate that the interaction of v-SNAREs and t-SNAREs on separate lipid bilayers was enough to bridge the two membranes. He found that spontaneous membrane fusion occurred a physiological temperatures leading to the hypothesis that SNARE complexes help to drive membrane fusion (Weber *et al.*, 1998). Whilst this model was still in dispute, further evidence that SNARE complexes drive membrane fusion was provided by Scheller in 1999. Scheller permeabilised PC12 cells in a 'cracked-cell' assay to show that a 65 amino acid fragment of SNAP25 rescues norepinephrine release after inhibition by Botulinum toxin E (Chen *et al.*, 1999). This rescue correlated with SNARE complex formation leading him to propose SNARE complex formation drives membrane fusion. Rothman went on to confirm that SNAREs define compartmental specificity. Using liposome assays, they tested the ability of three t-SNAREs known to mediate either ER to Golgi fusion, homotypic fusion of vacuoles, or fusion with the plasma membrane to form complexes with a library of v-SNAREs in all possible combinations. In doing so, they found a pattern of specificity established by SNARE proteins, as predicted by the SNARE hypothesis (J. A. McNew, Parlati, *et al.*, 2000).

The SNARE hypothesis has been crucial to our understanding of vesicle trafficking. The model in which SNAREs to provide specificity to vesicle targeting and docking, bridge two membranes, and ultimately drive membrane fusion is now widely accepted.

1.2.2 SNARE structure

SNAREs are a superfamily of small proteins of which there are approximately 39 in humans, 17 of which are thought to be involved in post-Golgi trafficking. SNAREs have a simple domain structure (figure 1-2) consisting of N-terminal domains, an evolutionary conserved SNARE motif, and a membrane-anchored C-terminal domain which is connected to the SNARE motif via a flexible linker (Jahn and Scheller, 2006).

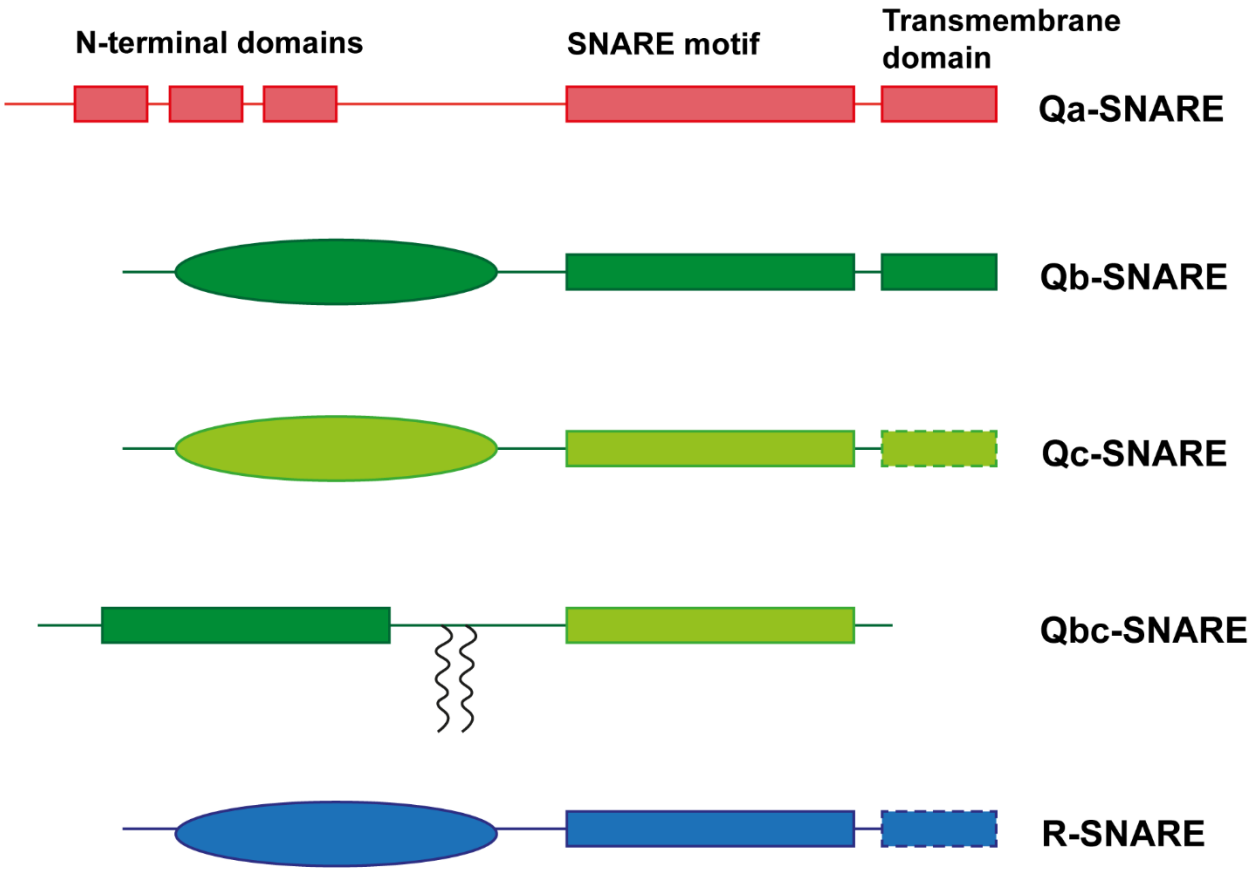

Figure 1-2: SNARE domain structure. *Figure adapted from Jahn and Scheller, 2006. Nature Reviews Molecular Cell Biology.* Qa-SNAREs (red) have N-terminal antiparallel three-helix bundles known as Habc domains. Various N-terminal domains of Qb-SNAREs (dark green), Qc-SNAREs (light green), and R-SNAREs (blue) are represented by an oval shape. All SNARE subfamilies contain at least one SNARE motif. Qbc-SNAREs contain two SNARE motifs joined by a flexible linker which is commonly S-acylated (zig zag lines). Dotted lines on transmembrane domains represent that some SNAREs lack C-terminal transmembrane domain.

1.2.2.1 SNARE motif

The SNARE motif is a short stretch of 60-70 amino acids arranged in heptad repeats. The SNARE subfamily, SNAPs, have two SNARE motifs joined by a flexible linker. The SNARE motif is the main site of interaction between SNAREs and necessary for driving fusion. The SNARE motif has an intrinsic α-helical structure. Upon interaction with other SNAREs, the SNARE motifs from each SNARE form elongated coiled coils of four intertwined parallel alpha helices known as an alpha helical core complex or the SNARE complex (figure 1-3). Each of the four alpha helices is provided by a different SNARE motif and as such, four SNARE motifs are required to form the SNARE complex (Jahn and Scheller, 2006). The SNARE complex consists of 16 stacked layers of interacting side chains which is mostly hydrophobic apart from a central '0' layer which contains 3 glutamines (Q) and 1 arginine (R), each contributed by a different SNARE motif. As a result, SNAREs have been classified into Qa, Qb, Qc, and R-SNAREs. One of each type of SNARE is required for a fusion-competent alpha helical core complex. As SNAPs can have two SNARE motifs and contribute both the alpha helical core complex, they can be classified as Qbc-SNAREs (Fasshauer *et al.*, 1998).

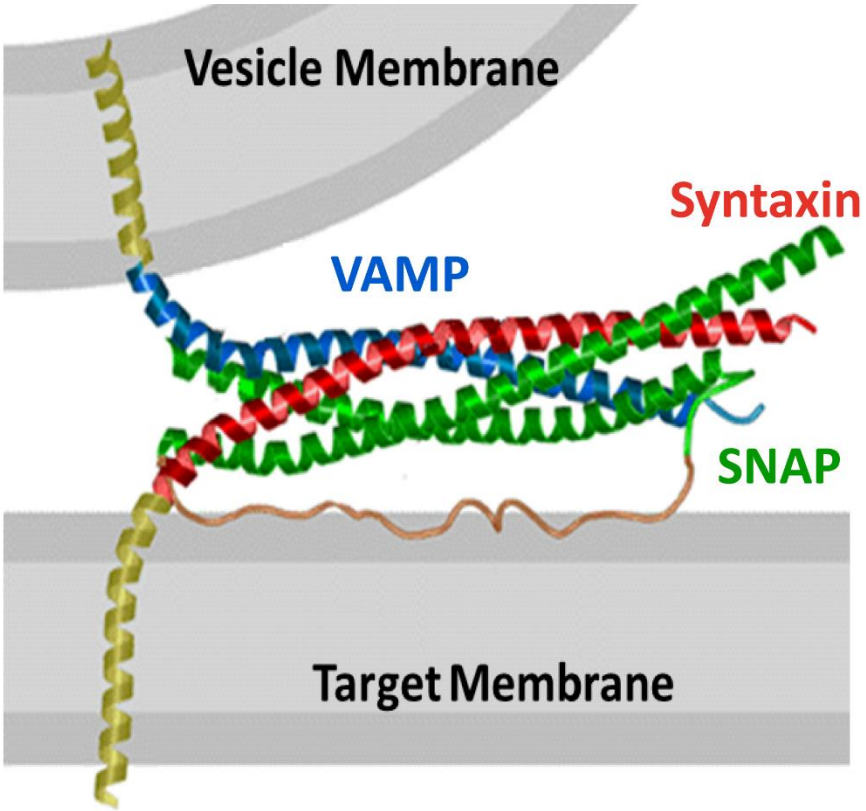

Figure 1-3 SNARE complex schematic. *Figure adapted from Sutton et al., 1998. Nature.* Formation of a SNARE complex required 4 SNARE motifs contributed by SNAREs associated with the vesicle and target membranes. The 4 coiled-coil SNARE motifs zip up to form an alpha helical core complex. VAMPs (blue) contribute 1 SNARE motfi to the complex and is associated with the vesicle membrane. Syntaxins (red) contribute 1 SNARE motif to the complex and are associated with the target membrane. The majority of vamps and syntaxins are embedded into the membrane via a transmembrane domain (yellow). SNAPs (-23, -25, -29; green) contribute 2 SNARE motifs to the complex and are associated with the target membrane through post-translational modification of a linker between the two SNARE motfis.

1.2.2.2 N-terminal domains

SNAREs can have various N-terminal domains which are independently folded. Syntaxins have N-terminal Habc domains which are antiparallel three helix bundles. These domains provide a regulatory mechanism to SNARE function by folding over the SNARE motif to form a closed configuration. This prevents the interaction with other SNAREs and the formation of a SNARE complex. Sec/Munc (SM) proteins have been shown to bind the Habc domains to hold the SNARE in a closed confirmation. For example, Munc18-1 has been shown to bind STX1 at its Habc domain to regulate synaptic vesicle fusion. Deletion of the Habc domain of STX1 results in a loss of Munc18-1 and a decrease in a pool of readily releasable vesicles suggesting that the Habc domains can also function to stabilise and chaperone SM proteins (Zhou, Zhiping P Pang, *et al.*, 2013). Some syntaxins also have an N-terminal peptide that precedes the Habc domains and has also been shown to bind SM proteins. Munc18-1 can also bind STX1 at its N-terminal peptide which has been shown to be essential for fusion. STX1 mutants lacking the N-terminal peptide are unable to rescue synaptic vesicle fusion in STX1-deficient neurons (Zhou, Zhiping P. Pang, *et al.*, 2013). Additionally, Vps45 has been shown to bind the STX16/Tgl2 N-terminal peptide and this binding is necessary to permit SNARE complex assembly (Bryant and James, 2001).

Some R-SNAREs (including Ykt6, VAMP7, and Sec22b) have long N-terminal domains arranged in an α-β-α sandwich configuration known as longin domains (Daste, Galli and Tareste, 2015). These domains are also able to fold over the SNARE motif thus negatively regulating membrane fusion. In the case of Ykt6, the login domain not only folds over the SNARE motif but also masks a farnesyl residue which prevents Ykt6 farnesylation and membrane anchoring (Fukasawa *et al.*, 2004). Longin domains can also interact with other proteins to regulate SNARE sorting. For example, VAMP7 interacts with the adaptor complex AP-3 for sorting into late endosomes (Martinez-Arca *et al.*, 2003)

SNAREs belonging to the SNAP subfamily, have more divergent N-terminal domains and few of the structures are known. Uniquely, yeast homologue of SNAP23, Vam7 contains a phosphoinositide-binding PX domain which allows its association with vacuole membranes (ML *et al.*, 2001) and promotes SNARE complex formation (Xu and Wickner, 2012).

1.2.2.3 C-terminal domains

The majority of the syntaxins and VAMPs have single C-terminal transmembrane domains (TMD) for membrane anchoring. There have been shown to be certain requirements of the SNARE transmembrane domains that are important in the ability of the SNARE to drive membrane fusion. VAMP2 with mutations affecting TMD length results in neurosecretory deficits in PC12 cells (Fdez *et al.*, 2010) suggesting a length requirement for membrane fusion. Additionally, the flexibility of the TMD has been shown to be essential

for complete fusion. Mutating core residues of synaptobrevin-2 TMD diminished Ca^{2+}-dependent exocytosis in adrenal chromaffin cells (Dhara *et al.*, 2016).

There are a number of SNAREs without a transmembrane domain, including SNAPS 23, 25, 29, and 47, syntaxins 11 and 19, and Ykt6. SNAP23 and 25 are S-acylated on cysteine residues in the linker between their two SNARE motifs (Greaves *et al.*, 2010). SNAP29 and 47 do not contain S-acylated cysteine residues in the linker and are thought to associate with membranes through their SNARE binding partners (Itakura, Kishi-Itakura and Mizushima, 2012; Kuster *et al.*, 2015). Unusually for Qa-SNAREs, STX11 and STX19 have been shown to be S-acylated on cysteine residues in the C-terminus (Hellewell *et al.*, 2014; Ampah *et al.*, 2018). Ykt6 contains a C-terminal CAAX box which is both S-acylated and farnesylated (Fukasawa *et al.*, 2004). Post-translational lipid modification of SNAREs is also important in SNARE trafficking and function. Ykt6 S-acylation induces a confirmational change that exposes the SNARE motif allows complex formation, thus positively regulating Ykt6 function (Fukasawa *et al.*, 2004; Wen *et al.*, 2010; Gordon *et al.*, 2017). SNAP25 cycles between recycling endosomes/TGN and the plasma membrane. Mutating specific cysteine residues in the SNAP25 S-acylation motif enhanced its localisation to recycling endosomes and the TGN suggesting S-acylation is key in regulating SNAP25 trafficking (Greaves and Chamberlain, 2011).

1.2.3 Q-SNARE acceptor complexes

Q-SNAREs at the target membrane have been proposed to form a pre-assembled acceptor complex (Qabc complex) which can subsequently binds the vesicle-associated R-SNARE. The presence of an acceptor complex allows for the rapid formation of SNARE complexes and fusion and is supported by the fact vesicles can fuse with the plasma membrane after arriving with no measurable delay (Ninomiya *et al.*, 1997). Using single-molecule fluorescence resonance energy transfer (smFRET), it has been shown that STX1 and SNAP25 can form a binary complex supported by lipid bilayers with conformational variability. The conformational variability can be locked into a single configuration by the addition of synaptobrevin or SM protein Munc18-1. This suggests that Q-SNAREs are able to form an acceptor complex with accessory proteins on the target membrane which readily binds R-SNAREs (Weninger *et al.*, 2008). Moreover, formation of a STX1, SNAP25, Munc18-1 complex *in vitro* has been shown to be an efficient acceptor complex for synaptobrevin, which is resistant to disassembly by NSF. Synaptobrevin binding to the complex results in the rapid formation of a fully zippered SNARE complex and changes the conformation of complex such that Munc18-1 is bound to the N-terminus of STX1 (Jakhanwal *et al.*, 2017). This is further supported by use of ultrahigh-resolution microscopy demonstrating the presence of the STX1/SNAP25/Munc18-1 complex in the intact plasma neuronal membrane (Pertsinidis *et al.*, 2013).

The presence of an acceptor complex has been widely debated. The reactive nature of SNAREs means they readily form ‘dead-end’ complexes for example, a STX1, SNAP25 complex with a 2:1 stoichiometry.

This makes identify SNARE complex intermediates challenging. Previous studies have suggested that Munc18-1 displaced SNAP25 in STX1/SNAP25 heterodimers and that NSF readily dissociated a STX1/SNAP25 complex. It was proposed that acceptor complex formation begins with a Munc18-1/STX1 heterodimer (Ma *et al.*, 2013). Alternatively, another model proposed that Munc18-1 linked STX1 and synaptobrevin forming an acceptor complex for SNAP25 (Ma *et al.*, 2015). Support for the proposal that R-SNAREs bind SM proteins prior to assembly with its SNARE binding partners comes from the identification of a conserved R-SNARE binding site on Vps33 which accelerated SNARE complex formation and fusion (Parisotto *et al.*, 2014; Baker *et al.*, 2015).

1.2.4 SNARE-mediated fusion

SNAREs interact through their SNARE motif to drive membrane fusion. The widely accepted model of membrane fusion is known as the 'zippering hypothesis'. The main piece of evidence for this model came from Sutton et al., who resolved the crystal structure of the SNARE complex (Sutton *et al.*, 1998). In this model, 4 SNARE motifs interact and 'zip up' from the N-terminal end of the motif to the C-terminal end. In doing so, the SNAREs form an extremely stable parallel four helical bundle in a trans-configuration known as the trans-SNARE complex. The zipping reaction brings the membranes into close proximity and exerts a mechanical force on the membrane thought to overcome the energy barrier for fusion. For successful fusion to occur, at least one SNARE motif from each classification (Qa, Qb, Qc, R) must be present. At least one SNARE motif must be provided by both target and vesicle membrane. SNAREs can form less stable complexes such as Qaaaa, Qabab, Qaabc, or even anti-parallel QabcR complexes. However, it is thought that such complexes do not drive membrane fusion but act as inhibitory complexes to regulate fusion. Fusion is thought to be a stepwise process that undergoes a series of intermediates. Hemifusion is a state in which trans-SNARE complexes have formed and the outer leaflets of the membrane are continuous but no aqueous pore has formed. Following hemifusion, the inner membrane leaflets fuse and an aqueous pore is formed known as fusion pore opening. The fusion pore then enlarges and allows content mixing. Following fusion, the SNARE complex forms a cis-configuration in which all four SNAREs are associated with the same membrane. SNARE complexes are subsequently dissembled by NSF and SNAP proteins. This allows SNAREs to be recycled for future SNARE complex formation and fusion (reviewed in Jahn and Scheller, 2006).

1.2.5 Post-Golgi Qa-SNAREs

The syntaxins (STX) are a subset of SNAREs and are defined as Qa-SNAREs. There are 17 members of the STX subfamily which localise to different intracellular compartments (figure 1-4).

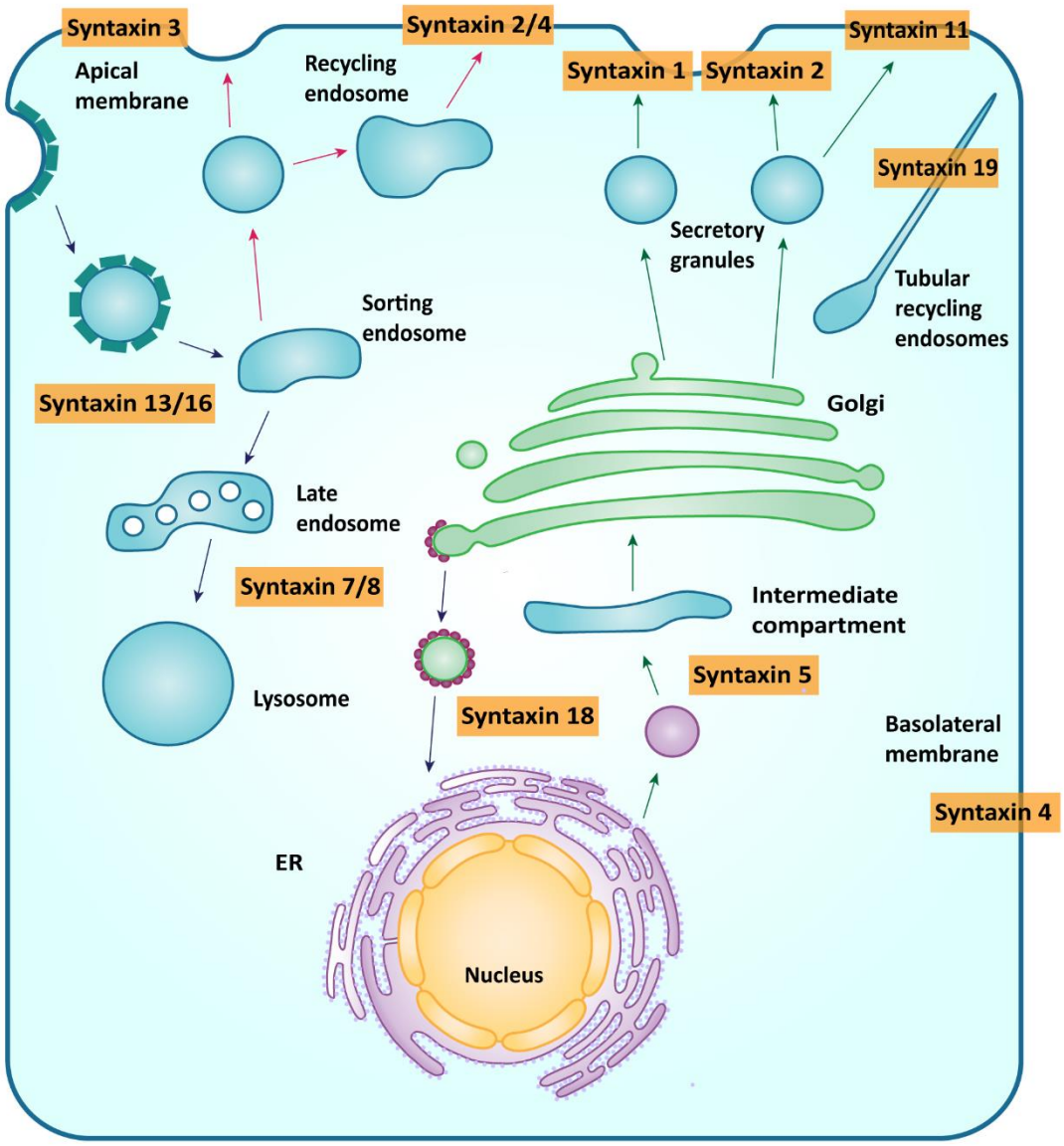

Figure 1-4: Comparmental specificity of syntaxins. Sytaxins mediate fusion at different intracellular compartments. Syntaxin 1 and 2 have been shown to mediate fusion of secretory vesicles with the plasma membrane. Syntaxin 3 localises to and mediates fusion at the apical membrane. Syntaxin 4 mediates fusion of recycling endomes with the plasma memrbane and mediates fusion at the basolateral membrane in epithelial cells. Syntaxin 5 mediates trafficking from the ER to the Golgi. Syntaxin 7 and 8 mediate endosomal/lysosomal fusion. Syntaxin 11 mediates fusion at the plasma membrane. Syntaxin 13 and 16 mediate recycling/early endosomal fusion. Syntaxin 19 localises to tubular recycling endosomes.

Of note, STXs 1A, 1B, 2, 3, 4, and 11 have been shown to mediate fusion at the plasma membrane. STXs 1A and 1B are largely enriched in brain tissues and mediate synaptic vesicle fusion at the plasma membrane for neurotransmitter release. There are also been reports of syntaxin 1A playing a role in insulin granule exocytosis (Liang *et al.*, 2017). STX2 also mediates fusion with the plasma membrane and has been shown to mediate exosome secretion in colorectal cancer (Wang *et al.*, 2021). Other studies have shown STX2 can act as an inhibitory SNARE which forms 'dead-end' complexes to regulate insulin

granule exocytosis and zymogen granule exocytosis in pancreatic acinar cells (Zhu *et al.*, 2017; Dolai, Liang, Orabi, Holmyard, *et al.*, 2018). STX3 localises to the apical plasma membrane in epithelial cells and is required for epithelial cell polarity (Sharma *et al.*, 2006). It has also been shown to localise to Weibel-Palade bodies and mediate von Wilibrand factor secretion in endothelial cells (Schillemans *et al.*, 2018). In contrast, STX4 has been shown to localise to the basolateral membrane in epithelial cells where it plays a role in basolateral protein delivery (Torres *et al.*, 2011). It has also been widely studied for its role in GLUT4 trafficking and insulin secretion (Hou and Pessin, 2007).

1.2.5.1 STX11

STX11 has also been shown to mediate fusion with the plasma membrane. STX11 lacks a C-terminal transmembrane domain and is S-acylated on cysteine residues at its C-terminus (Zhang *et al.*, 2018). Despite the lack of the transmembrane domain, STX11 has been shown to localise to the plasma membrane at the immunological synapse in cytotoxic T-lymphocytes where it mediates the secretion of cytolytic granules (Halimani *et al.*, 2014). Mutations in STX11 give rise to the primary immunodeficiency disorder Familial Hemophagocytic Lymphohistiocytosis type 4 (FHL4). Patients with this disorder have deficient cytotoxic T-lymphocyte degranulation (Bryceson *et al.*, 2007; Marsh *et al.*, 2010). Analysing patient mutations has revealed that mutations in the S-acylation domain of STX11 impair cytotoxic T-lymphocyte degranulation suggesting that S-acylation is essential for STX11 function (Hellewell *et al.*, 2014). Knockdown of STX11 results in a block of cytolytic granule fusion with the plasma membrane. Additionally, dual colour evanescent wave imaging revealed that STX11 traffics through a subpopulation of recycling endosomes to the immunological synapse where it clusters and functions as a platform for arriving cytolytic granules and subsequently drives their fusion (Halimani *et al.*, 2014). It has been shown that other SNAREs such as VAMP8, and SM protein, Munc18-2 are required for STX11 delivery to the plasma membrane. VAMP8 localises to Rab11a-positive recycling endosomes in cytotoxic T-lymphocytes. After stimulation, VAMP8 traffics and fuses recycling endosomes the plasma membrane where it deposits STX11. Knockdown in VAMP8 blocks recycling endosome and cytolytic granule fusion at the immunological synapse (Marshall *et al.*, 2015a). In cytotoxic T-lymphocytes lacking Munc18-2, STX11 is lost from the plasma membrane suggesting a role for Munc18-2 in chaperoning STX11 (Dieckmann *et al.*, 2015). The interaction between Munc18-2 and STX11 is also important for STX11-mediated fusion. Munc18-2 has been shown to bind STX11 at an N-terminal KDR peptide. Mutations in this peptide have been identified in patients with FHL4 (Muller *et al.*, 2014). Additionally, Munc18-2 has been shown to be required for complete fusion driven by STX11 in cytotoxic T-lymphocytes. Using a reconstituted cell-cell fusion assay, it has been shown that STX11 can mediate lipid mixing, but not content mixing, resembling hemifusion. Addition of Munc18-2 stimulated complete fusion. Complete fusion was not achieved by the addition of Munc18-2 mutants that cannot bind STX11 (Spessott *et al.*, 2017a).

STX11-mediated fusion is also required for platelet secretion. Platelets from FHL4 patients deficient in STX11 show defects in agonist-induced platelet secretion (Ye *et al.*, 2012). Similar to cytolytic granule secretion, Munc18-2 interaction with STX11 is thought to be important in platelet secretion. Neonatal platelets have reduced levels of STX11 and Munc18-2 and have impaired platelet secretion compared to adult platelets with normal STX11 and Munc18-2 levels (Caparrós-Pérez *et al.*, 2017). Platelets with mutations in Munc18-2 and STX11 show significantly reduced levels of platelet secretion compared to platelets with mutations in STX11 alone, suggesting a role for Munc18-2 in the regulation of STX11-mediate fusion (Al Hawas *et al.*, 2012). To drive platelet secretion, STX11 is thought to complex with VAMP8 and SNAP23 at the plasma membrane and dynamic cycling of STX11 S-acylation has been shown to regulate platelet secretion (Al Hawas *et al.*, 2012; Zhang *et al.*, 2018).

1.2.5.2 STX19

STX19 is an unusual Qa-SNARE thought to mediate post-Golgi trafficking. It was originally identified *in silico* through database searches of mouse cDNA with homology to syntaxins. It has highest homology with STX11 (38 % amino acid identity) and contains a conserved glutamine residue predicted to be at the central '0' layer in the alpha helical core SNARE complex (Wang *et al.*, 2006). It has a simple domain structure predicted to consist of an N-terminal peptide followed by Habc regulatory domains and the evolutionarily conserved SNARE motif (figure 1-5). Analysis using mass-spectrometry identified SNAPs 23, 25, and 29, and VAMPs 3 and 8 as SNARE binding partners for STX19 suggesting STX19 is able to form SNARE complexes with these SNAREs (Gordon *et al.*, 2010).

Through co-localisation studies, endogenous STX19 was shown to localise to Rab8/MICAL-L1 positive TREs in HeLa cells. STX19 was also found to co-localise with GPI-anchored cargo (CD55) that traffics through the Rab8-dependent recycling pathway. Overexpression of GFP-tagged STX19 in HeLa cells showed that GFP-STX19 localises to TREs and the plasma membrane.

Unusually for a Qa-SNARE, STX19 was found not to possess a transmembrane domain. Its C-terminus contains a highly conserved cysteine-rich patch which is S-acylated to allow its association to membranes (figure 1-3). This region contains a basic patch consisting of lysine (K) and arginine (R) residues followed by 3 cysteine pairs separated by tryptophan (W) and proline (P) residues (KYKKRNPCRVLCCWCCPCCSSK). Deletion of this region abolishes STX19 targeting to TREs and the plasma membrane. Similarly, replacing the cysteine-rich domain of STX19 with the transmembrane domain of STX13 targets the construct to the plasma membrane but localisation at the TREs is lost. The cysteine-rich region alone (coupled to a GFP tag) is also targeted to TREs and the plasma membrane. These data indicated that the cysteine-rich C-terminus of STX19 is capable of its targeting to TREs and the plasma membrane. Inhibition of S-acylation using 2-bromopalmitate resulted in the cytoplasmic localisation of STX19 full length and cysteine-rich

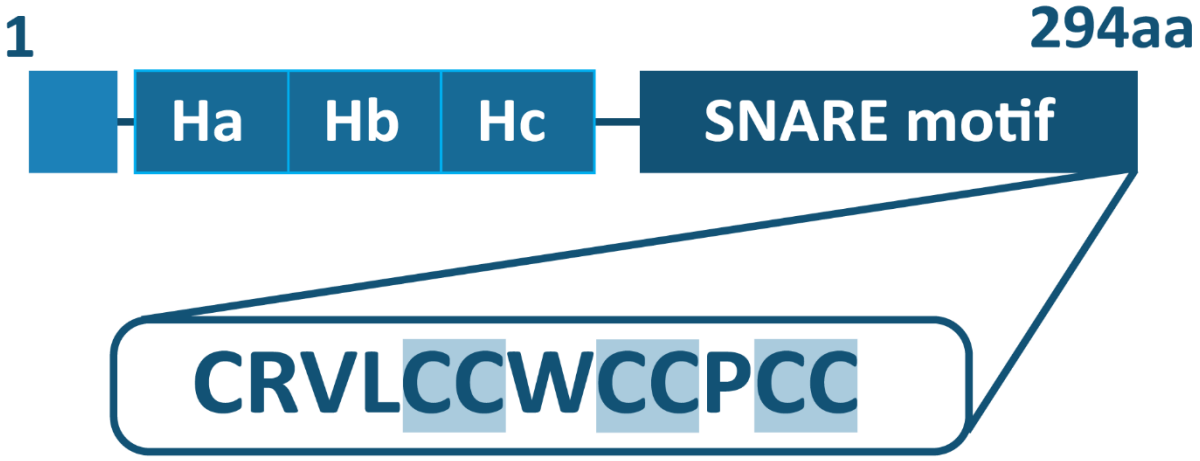

Figure 1-5: Domain structure of STX19. STX19 consists of 294 amino acids. It is predicted to have an N-terminal peptide followed by regulatory Habc domains. The Habc domains are connected to the evolutionarily conserved SNARE motif by a flexible linker. STX19 lacks a transmembrane domain but has a cysteine-rich path at the C-terminus. The sequence of the cysteine-rich patch is highlighted. The cysteine pairs that are S-acylated are highlighted by blue box.

region alone constructs. This shows that S-acylation is required for STX19 membrane targeting and association. Using an immunoprecipitation acyl-release assay coupled with mass spectrometry revealed that STX19 can be S-acylated at residues C284, C285, C287, C288, C290, and C291, relating to the 3 cysteine pairs described earlier. Despite the reversible nature of S-acylation, it was shown using knocksideways assays, that STX19 is stably associated with membranes (Ampah *et al.*, 2018).

Mutating the cysteine-rich region was also shown to affect the stability of STX19. Intensity levels of mutant constructs were reduced compared to wildtype constructs. Addition of proteasomal inhibitor MG132 to block degradation increased intensity levels of mutant constructs suggesting that when STX19 is not properly targeted to membranes it is readily turned over by ubiquitylation. Additionally, treatment of the cysteine-rich region only constructs with 2-BP demonstrated that levels are reduced in dose-dependent manner indicating that the cysteine-rich region is a degron when not S-acylated. Removal of the cysteine rich domain also results in reduced expression levels suggesting there is an additional degron upstream of the cysteine-rich region (Ampah *et al.*, 2018).

Localisation of STX19 to Rab8-positive TREs could suggest a role for STX19 in receptor recycling. However, a specific function for STX19 remains unclear. Wang et al., have previously used GST-pulldowns to identify an interaction between STX19 and EGF-R. It seems unlikely however that this would be a direct interaction as STX19 does not contain a binding domain for receptor tyrosine kinases. Overexpression of STX19 was shown to perturb EGF-R endocytosis using internalisation assays suggesting a role for STX19 in EGF-R trafficking (Wang *et al.*, 2006).

Subsequent studies have suggested a role for STX19 in constitutive secretion. Gordon et al., used a flow cytometry-based assay to measure constitutive secretion coupled with an siRNA SNARE library. Knockdown of STX19 resulted in a decrease in constitutive secretion. Additionally, analysis using total internal reflection fluorescence (TIRF) microscopy showed that there was a significant decrease in the number of fusion events at the cell surface in STX19-depleted cells (Gordon *et al.*, 2010). This suggests that STX19 has a role in mediating fusion of secretory vesicles with the plasma membrane. Furthermore, STX19 has been identified in a genome-wide RNAi screen to have a role in secretion of membrane-anchored cargo such as VSV-G (Simpson, Joggerst, Laketa, Verissimo, Cetin, Erfle, Bexiga, Singan, J.-K. Hériché, *et al.*, 2012).

Proximity-dependent biotinylation screens and yeast-two hybrid assays *(unpublished data, Ampah et al.,)* have identified potential interactors which may provide insight into the pathways STX19 plays a role in. These assays confirmed STX19 interaction with SNAPs 23, 25, and 29, and VAMPs 3 and 8. Insight into how STX19 function is regulated was also gained as Sec/Munc proteins, Munc18-1 and Munc18-2 were identified as potential interactors.

More unusual proteins such as ZW10-interactor (ZWINT) and Dystonin (DST) were predicted to interact with STX19. ZWINT is a kinetochore-associated protein that is required for Zeste-White 10 (ZW10) recruitment and microtubule attachment (H. Wang *et al.*, 2004; Woo Seo *et al.*, 2015). This function of ZWINT has been shown to be essential in mitotic checkpoint signalling (Kops *et al.*, 2005). Interaction with STX19 may suggest a role for STX19 in trafficking to kinetochore during mitosis. It remains unclear however why a kinetochore-associated protein would interact with a post-Golgi SNARE. DST is a large spectraplakin protein that crosslinks actin fibres and microtubules to mediate reorganisation of the cytoskeleton (Zhang, Yue and Wu, 2017). Spectraplakin proteins have been shown to link actin filaments at focal adhesions to microtubules which allows exocytosis of cargo in close proximity to focal adhesions (Wu, Kodama and Fuchs, 2008). Interaction with DST may suggest a role for STX19 in polarised trafficking, however, the function of this interaction remains unclear.

In vivo, STX19 has a limited tissue distribution. Wang et al., use RNA *in situ* hybridisation to demonstrate enrichment of STX19 in the epithelial lining of the stomach and the skin of mice (Wang *et al.*, 2006). This agrees with data from the Genotype-Tissue Expression (GTEx) project that shows STX19 mRNA is relatively highly expressed in epithelial tissues and the skin (Lonsdale *et al.*, 2013). A very specific tissue distribution may suggest a role for STX19 in specialised secretory pathways rather than general bulk secretion. Additionally, data from the International Mouse Phenotyping Consortium (IPMC) showed that STX19 knockout mice have decreased circulating insulin levels suggesting STX19 may play a role in specialised secretion (Dickinson *et al.*, 2016). However, the exact pathways STX19 functions in remains unknown.

1.3 Munc18 proteins

Munc18 proteins belong to the Sec/Munc (SM) family of proteins and are well-known to regulate SNARE function. These proteins are around ~60-80 kDa in size and have an arched 'clasp-like' structure (Südhof and Rothman, 2009). Munc18 proteins were originally identified as a mammalian homologue of *Caenorhabditis elegans* unc-18 proteins in GST-pulldowns with STX1 and rat brain homogenate. There are 3 isoforms of Munc18 in mammalian cells, Munc18-1, Munc18-2, and Munc18-3 and all have been shown to be able to bind post-Golgi SNAREs. Munc18-1 is predominantly expressed in brain tissues whilst Munc18-2 and Munc18-3 are expressed ubiquitously (J. McNew *et al.*, 2000).

1.3.1 Munc18 mechanisms of regulation

It was originally thought that Munc18 proteins were negative regulators of SNARE-mediated fusion. This hypothesis came from structural and *in vitro* data suggesting that STX1 was not able to bind Munc18-1 whilst in a SNARE complex (Pevsner *et al.*, 1994; Misura, Scheller and Weis, 2000). Munc18-1 was found to bind the Habc domain of STX1 (Dulubova *et al.*, 1999; Yang *et al.*, 2000). Studies using NMR spectroscopy demonstrated that, in isolation, STX1 forms a closed confirmation. STX1 mutants that are locked in an open confirmation were unable to bind Munc18-1 (Dulubova *et al.*, 1999). Furthermore, STX1 bound to Munc18-1 was unable to form SNARE complexes with its SNARE binding partners (Yang *et al.*, 2000). These studies led to the hypothesis that Munc18-1 binds the Habc domain of STX1 to hold it in a closed confirmation. STX1 is therefore unable to form SNARE complexes and thus Munc18-1 negatively regulates fusion.

Subsequent studies however revealed a second STX binding mode for Munc18 proteins. Munc18-1 was shown to co-elute with STX1 when it is associated in a SNARE complex using gel filtration and this was dependent on the N-terminal peptide of STX1 (Dulubova *et al.*, 2007). This binding mode was subsequently identified as important for SNARE complex formation. Using FRET-based biochemical reconstitution assays, binding of Munc18-1 to the N-terminal peptide of STX1 was shown to be the initiation factor for SNARE complex formation (Rathore *et al.*, 2010). Ma et al., used optical tweezers to pull apart SNARE complexes and observe how they re-assemble complexes in a stepwise manner. This revealed that Munc18-1 binding to the N-terminal of STX1 stabilises a half-zippered SNARE complex (Ma *et al.*, 2015). Similarly, Munc18-1 has been shown to catalyse the stepwise zippering of STX1, VAMP2, and SNAP25 using single-molecule force spectroscopy. Munc18-1 forms an intermediate template complex with STX1 and VAMP2 by holding the N-terminals of STX1 and VAMP2 together whilst keeping the C-terminals part so that SNAP25 can associate to induce full zippering (Jiao *et al.*, 2018).

Formation of SNARE complexes mediated by Munc18-1 is critical for membrane fusion. Rescue experiments in syntaxin-deficient neurons demonstrated that Munc18-1 binding to the STX1 N-terminal is critical for synaptic exocytosis as expression of N-terminal peptide mutants of STX1 was unable to rescue vesicle fusion (Zhou, Zhiping P. Pang, *et al.*, 2013). Similarly, Shen et al., used a 'clogged' Munc18-1 protein in which the N-terminal peptide of STX1 was fused to the N-terminal binding pocket of Munc18-1 preventing its association with the N-terminal peptides of native STX1 proteins. 'Clogged' Munc18-1 was shown to be defective in promoting SNARE complex formation and failed to mediate spontaneous and evoked synaptic exocytosis in induced neuronal cells (Shen *et al.*, 2018). This demonstrated Munc18-1 binding to STX1 was essential for STX1-mediated fusion.

Studies have shown that these two STX1 binding modes of Munc18-1 have different functions. Using quantitative colocalization and fluorescence lifetime imaging microscopy (FLIM) to analyse mutant STX1 locked in the open confirmation demonstrated that interaction of Munc18-1 with STX1 in two different confirmations is spatially distinct. Munc18-1 was shown to bind STX1 at its Habc domain to hold it in a closed confirmation as it traffics through the Golgi and towards the plasma membrane. This is thought to prevent ectopic SNARE complex formation. Munc18-1 was shown to bind the open confirmation of STX1 at the plasma membrane (Medine *et al.*, 2007; Rickman *et al.*, 2007). This suggests that the two different binding modes of Munc18-1 are important in regulating STX1 function by preventing inappropriate SNARE complex formation until STX1 reaches the membrane where it then facilitates complex formation. In support of this, Schollmeier et al., used liposome fusion assays to measure the assembly of Q-SNAREs on liposomes and subsequent SNARE complex formation between Q- and R- SNARE liposomes. They found that Munc18-1 binds STX1 in a closed confirmation until Munc18-1 binds VAMP2. This results in a confirmational switch in which Munc18-1 stimulates the formation of the SNARE complex (Schollmeier *et al.*, 2011). Additionally, the two distinct binding modes were shown to be important in synaptic exocytosis. Expression of STX1 mutants in STX1-deficient neurons revealed that N-terminal binding was critical for exocytosis. However, deletion of the Habc domain resulted in a loss of Munc18-1 and a decrease in the readily releasable pool of vesicles suggesting that Habc binding stabilises Munc18-1 (Zhou, Zhiping P. Pang, *et al.*, 2013). These studies demonstrate that the two different binding modes perform distinct functions yet both binding modes are important for the proper regulation of fusion.

Alternatively, it has also been suggested that the N-terminal and Habc binding modes might be two steps with the same function. Using SDS-resistant SNARE complexes *in vitro*, it was shown that STX1 was able to form a complex with SNAP25 and VAMP2 but not when STX1 is pre-mixed with Munc18-1. This suggested that STX1 bound to Munc18-1 was unable to bind the SNARE complex which is in agreement with previous *in vitro* studies discussed earlier. However, deletion of the STX1 N-terminal peptide allowed SNARE complex formation when STX1 mutants were pre-mixed with Munc18-1. This suggested that the

N-terminal peptide binding mode was responsible for preventing SNARE complex formation. The authors hypothesised a model in which Munc18-1 first binds the STX1 N-terminal peptide to lock in the interaction and Munc18-1 subsequently binds the Habc domain to hold it in a closed confirmation and negatively regulate fusion (Burkhardt *et al.*, 2008).

Whilst most of the published literature on the mechanisms of SNARE regulation by Munc18 relates to the Munc18-1 and STX1 interaction, other studies have shown that the N-terminal binding mode is utilised by other Munc18 isoforms. Munc18-2 has been shown to bind STX11 and regulate its function. Structural analysis of Munc18-2 demonstrated that the Munc18-2 binding site of STX11 is at its N-terminal peptide (Hackmann *et al.*, 2013). Additionally, patients with FHL4 have mutations in the N-terminal peptide of STX11 and this has been shown to abrogate Munc18-2 binding (Müller *et al.*, 2014). Munc18-2 binding of STX11 was also shown to be essential for STX11-mediate fusion. In liposome assays, STX11 was unable to mediate completion fusion until the addition of Munc18-2 (Spessott *et al.*, 2017a).

Similarly, Munc18-3 has been shown to bind the N-terminal peptide of STX4. STX4 mediates the formation of invadopodia during tumour cell invasion. This function was shown to be regulated by Munc18-3. Expressing the STX4 N-terminal peptide alone out competes Munc18-3 binding to the native STX4 and decreased invadiopodia formation and cell invasion (Brasher *et al.*, 2017). Two different binding modes have also been reported for STX4/Munc18-3. GST-pulldowns were used to investigate the STX4/Munc18-3 interaction. C-terminally tagged STX4-GST was able to pulldown Munc18-3 through interaction via the N-terminal peptide. N-terminally tagged GST-STX4 was no longer able to bind Munc18-3 at the N-terminal peptide but was still able to pulldown Munc18-3. This suggested there was an additional binding site for Munc18-3 and therefore, it is possible that Munc18-3 has two different STX4 binding modes.

1.3.2 Munc18-1

Munc18-1 was the first Munc18 isoform identified. It is primarily expressed in neurons and neuroendocrine cells. Munc18-1 is well characterised to have roles in regulating STX1-mediated synaptic vesicle fusion as discussed. This function of Munc18-1 is essential as Munc18-1 knockout in mice abolishes neurotransmitter release (Verhage *et al.*, 2000). As well as regulating SNARE complex formation, Munc18-1 was identified to play a role in vesicle docking. Chromaffin cells from Munc18-1 null mice have a 10-fold reduction in the number of large-dense core vesicles docked at the plasma membrane (Voets *et al.*, 2001). Overexpression of Munc18-1 in neurons results in an increase in the number of vesicles docks at the synaptic terminal (Toonen *et al.*, 2006). The role of Munc18-1 in vesicle docking may depend on its SNARE interacting partners. Proteolytic cleavage of STX1 using Botulinum Toxin serotype C was also shown to impair vesicle docking (Wit *et al.*, 2006), whilst SNAP25 expression in Munc18-1 deficient neurons rescues the docking phenotype but not fusion (de Wit *et al.*, 2009). This suggests that Munc18-

1 regulates vesicle docking through interaction with STX1 and SNAP25. However, chromaffin cells from SNAP25 null mice do not have docking phenotypes (Sørensen *et al.*, 2003). It has been suggested that Munc18-1 interaction with other proteins may also regulate vesicle docking. Munc18-1 was shown to interact with Rab3. Expression of a gain of function Munc18-1 mutation was shown to increase interaction with Rab3 and the density and exocytosis of secretory granules at the cell surface in chromaffin cells (Graham *et al.*, 2008). Similarly, Munc18-1 was shown to interact with Doc2 using GST-pulldowns. Addition of excess STX1 prevented pulldown of Munc18-1 using GST-Doc2 despite STX1 and Doc2 binding to Munc18-1 at different sites. This suggested Doc2 binding to Munc18-1 competes with STX1 to regulate vesicle docking. (Verhage *et al.*, 1997).

An additional role for Munc18-1 as a molecular chaperone has also been reported. Munc18-1 mutations result in early onset epileptic encephalopathies (EOEE). Neurons from patients with EOEEs have been shown to have form lewy body-like structures containing α-synuclein. Munc18-1 mutants that cause EOEEs were shown to co-aggregate with α-synuclein and Munc18-1 knockouts increased the number of α-synuclein aggregates. Aggregates formed by a Parkinson's disease α-synuclein mutant (α-synuclein^{A30P}) were reduced by expression of wildtype Munc18-1 (Chai *et al.*, 2016). This suggested a key role for Munc18-1 as a molecular chaperone that assists the folding of α-synuclein.

Owing to its role in synaptic transmission, Munc18-1 mutations give rise to wide spectrum of encephalopathies. All patients have a form of intellectual disability whilst 85 % have a form of epilepsy (Stamberger, Weckhuysen and Jonghe, 2017). Mutations in Munc18-1 were first identified in patients with early infantile epileptic encephalopathy. The characteristics of this disease are intractable seizures and psychomotor retardation. Patients have a very poor prognosis with a 50 % mortality rate (Saitsu *et al.*, 2008). Since then, Munc18-1 mutations have been identified as causative in a wide range of EOEEs including West syndrome (Otsuka *et al.*, 2010), Lennox-Gastaut syndrome (Allen *et al.*, 2013), and Dravet syndrome (Carvill *et al.*, 2014). Moreover, Munc18-1 haploinsufficiency modelled in mice was shown to cause psychiatric and motor dysfunction, cortical hyperexcitability, and seizures. This was a result of reduced cortical inhibitory neurotransmission (Chen *et al.*, 2020). Munc8-1 mutations have also been identified in patients without EOEE including mental retardation (Hamdan *et al.*, 2009), atypical Rhett syndrome (Cogliati *et al.*, 2019), and intellectual disability without epilepsy (Hamdan *et al.*, 2011).

1.3.3 Munc18-2

Munc18-2 is expressed ubiquitously but enriched in epithelial cells and cells of the immune system (Tellam, McIntosh and James, 1995; Ziegler *et al.*, 1996). Munc18-2 has been shown to mediate numerous exocytotic pathways including apical trafficking in epithelial cells (Vogel *et al.*, 2017), and degranulation in cells of the immune system (Brochetta *et al.*, 2008).

Mutations in Munc18-2 give rise to microvillus inclusions disease (MVID). Microvillus inclusions disease (MVID) is a life-threatening, congenital enteropathy characterised by severe diarrhoea, malabsorption, and a failure to thrive (Schneeberger *et al.*, 2018). The only current treatment options are intravenous feeding and intestinal transplantation (Comegna *et al.*, 2018). Biopsy and electron microscopy are used analyse the ultrastructure of patient enterocytes to diagnose MVID. Ultrastructural characteristics of MVID include accumulation of subapical vesicles, loss of microvilli at the apical surface, and the presence of microvilli inclusions (MVIs) in the cytoplasm (Michail *et al.*, 1998; Schneeberger *et al.*, 2018). MVID has been modelled using Munc18-2 deficient intestinal organoids (Mosa *et al.*, 2018). Subcellularly, enterocytes in Munc18-2 deficient organoids showed subapical accumulation of vesicles, complex tubulovesicle structures, and shorter, wider, less dense microvilli. This phenotype could be rescued by expression of wildtype Munc18-2 but not by MVID patient variant Munc18-2 P477L (Mosa *et al.*, 2018). This suggested a role for Munc18-2 in the trafficking of apically targeted vesicles.

Similarly, Munc18-2 was shown to interact with STX3 and is required for fusion of vesicles with the apical membrane using a CaCo2 Munc18-2 knockout cell line. Coaffinity purification experiments demonstrated that STX3 is pulled down from cell lysates in wild type cells but not Munc18-2 knockout cells. Loss of Munc18-2 in CaCo2 cells disrupts enterocyte polarity, result in a loss of apical microvilli and, subapical vesicle accumulation. Additionally, apical membrane-localised proteins, NHE3 and GLUT5, were cytoplasmic in Munc18-2 depleted cells suggesting Munc18-2 regulates apical trafficking (Vogel *et al.*, 2017). Myo5B has also been shown to work in concert with Rab8 and Rab11 to regulate apical trafficking. In Myo5B knockout cells, NHE3 and GLUT5 are mislocalised from the apical membrane to the cytoplasm. Myo5B knockout was also shown significantly reduce the interaction between STX3 and Munc18-2 (Vogel *et al.*, 2015). Taken together, this suggested Munc18-2 functions in a Myo5B/STX3/Rab8/Rab11 pathway to regulate apical trafficking in epithelial cells.

Mutations in Munc18-2 also lead to Familial Hemophagocytic Lymphohistiocytosis 5 (FHL5) (zur Stadt *et al.*, 2009; Vogel *et al.*, 2017) FHL5 is an autosomal recessive disease characterised by a severe hyperinflammatory phenotype and chronic enteropathies (Vogel *et al.*, 2017). FHL5 usually manifests within the first year of life and is fatal unless treated with haematopoietic stem cell transplant (Cetica *et al.*, 2010). Natural killer (NK) and cytotoxic T-lymphocytes have been shown to have significantly reduced killing activity towards target cells (zur Stadt *et al.*, 2009). Enterocytes from FHL5 patients also show subcellular characteristic reminiscent of MVID (Vogel *et al.*, 2017; Mosa *et al.*, 2018). The hyperinflammatory phenotype and reduction in NK and cytotoxic T-lymphocyte killing activity can be attributed towards a role for Munc18-2 in the exocytosis of secretory granules in immune cells.

Lymphoblasts and natural killer (NK) cells isolated from FHL5 patients have impaired cytotoxic granule exocytosis (Côte *et al.*, 2009). FHL5 Munc18-2 mutations results in loss of degranulation in cytoxtic T-lymphocytes. STX11 plasma membrane localisation is lost from FHL5 cytotoxic T-lymphocytes lacking Munc18-2 suggesting that Munc18-2 mediates STX11 trafficking to the plasma membrane where it allows the fusion of cytotoxic granules (Dieckmann *et al.*, 2015). Furthermore, knockdown of Munc18-2 in primary cytotoxic T-lymphocytes coupled with cell killing assays demonstrated that loss of Munc18-2 significantly reduced cytotoxic activity. Munc18-2 was found to bind STX11 both *in vitro* and *in vivo* and be essential for complete STX11-mediated fusion (Spessott *et al.*, 2017a). Taken together, these data demonstrate a role for Munc18-2 in regulating STX11-mediated exocytosis of cytotoxic granules.

Similarly, Munc18-2 was found to localise to secretory granules in mast cells and redistribute to lamellipodia upon mast cell stimulation (Martin-Verdeaux *et al.*, 2003). Conditional knockout of Munc18-2 in mast cells of mice demonstrated a role for Munc18-2 in mast cell granule exocytosis. Exocytosis was abolished in Munc18-2 depleted cells (Gutierrez *et al.*, 2018). In similar studies, combinatorial knockdowns of both Munc18-2 and STX3 resulted in an additive inhibitory effect on granule exocytosis. However, knockdown of Munc18-2 alone inhibited secretory granule translocation to the cell surface whilst STX3 knockdown inhibited granule fusion suggesting distinct roles for both proteins in secretory granule exocytosis (Brochetta *et al.*, 2014). Overall, several studies demonstrate Munc18-2, in combination with STX3, plays a role in the exocytosis of secretory granules in mast cells.

An additional role for Munc18-2 in platelet secretion has been associated with FHL5. Munc18-2 levels in FHL5 patient platelets are significantly reduced and platelets show defective thrombin-stimulated secretion of serotonin, ADP/ATP, and platelet factor 4 (Al Hawas *et al.*, 2012). As such, Munc18-2 is thought to regulate platelet exocytosis. Conditional knockout of Munc18-2 in megakaryocytes was performed in mice. These mice showed haemostatic defects and prolonged arterial and venous bleeding times. Platelets from Munc18-2 conditional knockout mice were shown to have impaired exocytosis of alpha, dense, and lysosomal granules. *In vitro* studies demonstrated that Munc18-2 deficient platelets have defective aggregation and impaired thrombus formation (Cardenas *et al.*, 2019). Taken together, these data suggested Munc18-2 is essential for regulated exocytosis in platelets and platelet participation in thrombosis.

1.3.4 Munc18-3

Munc18-3 is ubiquitously expressed and has been shown to bind exclusively to STX4 (Tellam, McIntosh and James, 1995; Thurmond *et al.*, 1998). Through this interaction, Munc18-3 has been shown to regulate a number of exocytotic pathways involving STX4-mediated fusion at the plasma membrane.

In some cell types, Munc18-3 regulates trafficking at the apical membrane. Munc18-3 localises to the apical membrane in rat parotid acinar cells where it interacts with STX4. Isoproterenol treatment stimulates amylase release from acinar cells and induces translocation of Munc18-3 to the plasma membrane. Using antibodies against Munc18-3 to block its function resulted in a dose-dependent decrease in isoproterenol-stimulated amylase release from cells suggesting that Munc18-3 regulates amylase secretion through interaction with STX4 at the plasma membrane (Imai, Nashida and Shimomura, 2004).

Munc18-3 is also required for apical trafficking and cell polarity in intestinal epithelial cells. Knockdown of Munc18-3 in CaCo2 cells significantly reduced the apical localisation of GM1 ganglioside, an apical marker, and Rab11, known to mediate apical trafficking of vesicles. Cells depleted for Munc18-3 also did not form a polarised monolayer and formed mostly cell islands. In accordance with its role in epithelial cell polarity, heterozygous or biallelic variants of Munc18-3 have been shown to give rise to very early onset inflammatory bowel disease (VEOIBD). VEOIBD is characterised by intestinal inflammation in children less than 6 years of age. Patients often also present with bilateral sensorineural hearing loss (Ouahed *et al.*, 2021).

In contrast, Munc18-3 has also been reported to regulate trafficking at the basolateral membrane. STX4 localises to the basolateral membrane of polarised MDCK cells. Immunoprecipitation studies demonstrated that Munc18-3 interacts with STX4 via its N-terminal peptide. Loss of the STX4 N-terminal peptide results in the loss of STX4 at the basolateral membrane suggesting that Munc18-3 plays a role in the basolateral targeting of STX4 (Reales *et al.*, 2011). Other studies suggest Munc18-3 is required for STX4 stability at the basolateral membrane. Knockdown of Munc18-3 reduces the expression but not the localisation of STX4, though it does reduce the basolateral localisation of β1-integrin. However, introducing N-terminal mutations in STX4 that affect Munc18-3 binding and basolateral sorting mislocalises STX4 to the cytoplasm. This suggests that Munc18-3 stabilises STX4 at the plasma membrane rather being responsible for its membrane targeting (Torres *et al.*, 2011).

Munc18-3 has also been shown to mediate basolateral exocytosis in pathophysiological conditions. Under normal conditions, zymogen granules are secreted from the apical surface of pancreatic acinar cells (Gaisano and Gorelick, 2009). Stimulation of pancreatic acinar cells with supraphysiological levels of the intestinal hormone cholecystokinin mimics pancreatitis (Dolai, Liang, Orabi, Xie, *et al.*, 2018). In these cells, zymogen granules pathophysiologically fuse with the basolateral membrane and apical exocytosis is blocked (Gaisano and Gorelick, 2009). Munc18-3 depletion was shown to impair the formation of the basolateral SNARE complex, STX4-SNAP23-VAMP8 in mouse pancreatic acinar cells which in turn reduces basolateral exocytosis of zymogen granules in pancreatitis-modelled cells (Dolai, Liang, Orabi, Xie, *et al.*,

2018). Displacement of Munc18-3 from the basolateral membrane prevented basolateral exocytosis of zymogen granules which were re-directed to the apical membrane (Gaisano, Sheu and Whitcomb, 2004).

Moreover, Munc18-3 function has been widely studied in the regulation of insulin-stimulated GLUT4 trafficking in adipocytes and skeletal muscle cells. However, its exact role remains controversial.

Overexpression studies suggested Munc18-3 acts a negative regulator of GLUT4 vesicle fusion. Expression of a Munc18-3 peptide unable to bind STX4 in 3T3-L1 adipocytes prevents the exocytosis of GLUT4-vesicles with the plasma membrane which accumulated under the cell surface (Thurmond *et al.*, 1998, 2000). Expression of full length Munc18-3 was also shown to reduce glucose transport in adipocytes. Use of Munc18-3 antibodies to block its function stimulated GLUT4 translocation to the plasma membrane suggesting that Munc18-3 negatively regulates GLUT4 vesicle translocation (Macaulay *et al.*, 2002). Consistent with this, overexpression of Munc18-3 in skeletal muscle was also shown to inhibit GLUT4 translocation to the membrane (Khan *et al.*, 2001). Overall, these studies suggest Munc18-3 function inhibits GLUT4 vesicle translocation and fusion at the plasma membrane.

In contrast, depletion studies suggest a positive role for Munc18-3 in GLUT4 trafficking. Heterozygous Munc18-3 knockout mice showed a reduction in insulin-stimulated GLUT4 translocation in skeletal muscle suggesting Munc18-2 positively regulates GLUT4 translocation (Oh *et al.*, 2005; Jain *et al.*, 2012). Moreover, Munc18-3 was shown to be phosphorylated in response to insulin receptor activation. Expression of Munc18-3 wildtype and phosphomimetic mutants, but not phosphodefective mutants, in Munc18-3 depleted adipocytes rescues GLUT4 vesicle exocytosis (Jewell *et al.*, 2011). Phosphorylation of Munc18-3 was suggested to be important in repositioning of Munc18-3 on STX4 such that it allows STX4 to form an open confirmation and form SNARE complexes to mediate GLUT4 vesicle fusion (D'Andrea-Merrins *et al.*, 2007; Smithers *et al.*, 2008).

Finally, Munc18-3 regulation of GLUT4 vesicle trafficking has been implicated in insulin resistance. Insulin resistance is the inability of cells to response to insulin which can be caused by impaired GLUT4 translocation or activity (Nelson, Robinson and Buse, 2002). Insulin resistance can be induced in cells using glucosamine. Cells exposed to glucosamine have increased O-linked glycosylation levels and impaired translocation of GLUT4. It was shown that Munc18-3 is O-linked glycosylated in response to glucosamine treatment. O-linked glycosylation of Munc18-3 impairs its translocation to the plasma membrane and the results in defective GLUT4 translocation (Nelson, Robinson and Buse, 2002; Chen *et al.*, 2003).

1.4 Research question

STX19 is a poorly characterised Qa-SNARE. Previous studies have characterised its localisation and membrane targeting in HeLaM cells and suggested a possible role secretion of soluble and membrane

anchored cargo (Gordon *et al.*, 2010; Ampah *et al.*, 2018). However, it remains unclear which pathways and processes STX19 functions in and how STX19 function is regulated. The main aim of this study was to gain insight into the regulation and function of STX19. To address this aim, we used cell-based mitochondrial re-routing assays to validate and characterise STX19 protein-protein interactions and used overexpression studies to analyse effects of STX19 expression on SNARE binding partners and compartmental markers. As STX19 has a limited tissue distribution and is relatively highly expressed in epithelial tissues and the skin (Wang *et al.*, 2006; Lonsdale *et al.*, 2013; Toufighi *et al.*, 2015), we have also established a physiologically relevant cell model in which STX19 function can be studied. Through these studies, we have gained insight into the molecular interactions which may regulate STX19 function, identified STX19 overexpression phenotypes which provide clues into which pathways STX19 may function in, and characterised STX19 localisation in a physiological model.

Chapter 2

Materials and Methods

2.1 Bacterial culture and transformation

2.1.1 Bacterial culture

Plated bacterial cultures were grown at 37 °C in a HeraTherm incubator (Thermo Scientific, Massachusetts, US) and maintained on agar plates (1.5 % agar, 1 % tryptone, 1 % sodium chloride, 0.5 % yeast extract, ddH_2O). See table 2-1 for all buffer recipes used for bacterial culture and transformation. Where required, kanamycin (50 µg/mL) or ampicillin (100 µg/mL) were added for selection purposes (see table 2-3). 20 mg/mL X-gal was used to coat set plates for blue/white screening on TOPO cloned transformants.

Liquid cultures were grown at 37 °C at 220 rpm in a KS4000 iControl shaking incubator (IKA-Werke, Staufen, Germany) and maintained in LB medium (1 % tryptone, 0.5 % yeast extract, 0.5 % sodium chloride, ddH_2O). Where required, kanamycin (50 µg/mL) or ampicillin (100 µg/mL) were added for selection purposes. Small bacterial cultures (2-50 mL) were pelleted by centrifugation for 15 minutes at 3000 rpm in a Rotina 46R centrifuge (Hettich Zentrifugen, Tuttlingen, Germany). Large bacterial cultures (>50 mL) were pelleted by centrifugation for 10 minutes at 5000 xg in a Beckman Avanti J-25 centrifuge (Beckman Coulter, California, US).

Bacterial strains used in this thesis include DH5α (plasmid amplification of large-scale DNA purification) and One Shot™ Mach1™ T1 Phage-Resistant Chemically Competent E. coli (Invitrogen, California, US) (TOPO cloning for construct generation).

2.1.2 Bacterial transformation

Competent bacteria were thawed on ice. 2 µL of ~100 ng DNA was added to 50 µL of competent bacteria and incubated on ice for 20 minutes. The bacteria were heat shocked at 42 °C for 42 seconds and incubated on ice for a further 2 minutes. 1 mL of LB media was added and the bacteria were incubated in a KS4000 iControl shaking incubator at 220 rpm, 37 °C for 1 hour. Bacteria were pelleted by centrifugation using a Sigma-Aldrich 1 -15p microcentrifuge (Missouri, US) at 10,000 rpm for 5 minutes. The supernatant was discarded and bacteria re-suspended in 100 µL LB media. The re-suspended bacteria was spread onto an agar plate containing the appropriate selection antibiotic using a cell spreader and incubated overnight at 37 °C in a HeraTherm incubator.

2.1.3 Bacterial inoculation

Bacterial colonies from agar plates were picked and used to inoculate 3 mL of LB media containing 1 µg/µL of the appropriate selection antibiotic. Bacteria was cultured overnight at 37 °C in a shaking incubator. 200 µL of the resulting bacterial culture was used to inoculate 250 mL of LB media containing 1 µg/µL of

the appropriate selection antibiotic. Cultures were incubated overnight in a shaking incubator at 220 rpm, 37 °C.

2.1.4 Plasmid isolation

Plasmid DNA was isolated from bacterial cultures using GeneJET mini-, midi-, or maxi-prep kits (Thermo Scientific, Massachusetts, US) following the manufacturers' protocol. The concentration of the purified plasmid DNA was assessed using Thermo Scientific Nanodrop Lite spectrophotometer. Purified plasmid DNA was stored at -20 °C.

2.2 Mammalian cell culture and transfection

2.2.1 Mammalian cell culture

HeLa-M and HEK293 cells were grown in Dulbecco's Modified Eagle Medium (DMEM) (Sigma Aldrich, Missouri, US) supplemented with 10 % Fetal Bovine Serum (Gibco, California, US), and 1 % penicillin/streptomycin (Sigma Aldrich, Missouri, US) at 37 °C in a 5 % CO_2 humidified incubator. All buffers used for mammalian cell culture and transfection are listed in table 2-2. Cells were passaged at 80-90 % confluency. To passage the cells, cells were washed with sterile PBS (Gibco, California, US). Cells were then incubated for 5 minutes at 37 °C with 1 mL trypsin (Sigma Aldrich, Missouri, US) for detachment and re-suspended in 10 mL of fresh media. Cell lines were maintained by re-plating a 1:10 ratio of cells and fresh media.

Adult Human Epidermal Keratinocytes (HEKa) were grown in EpiLife medium (Gibco, California, US) supplemented with 1 % Human Keratinocyte Growth Supplement (HKGS) (Gibco, California, US) and 1 % penicillin/streptomycin (Sigma Aldrich, Missouri, US) at 37 °C in a 5 % CO_2 humidified incubator. Cells were passaged at <80 % confluency. Cells were washed with 9 mL trypsin (Sigma Aldrich, Missouri, US) and incubated with 3 mL trypsin at room temperature. After detachment, Cells were washed with 9 mL of trypsin neutraliser solution (Gibco, California, US). Cells were then transferred to a 50 mL falcon tube and centrifuged at 180 x g for 7 minutes. The supernatant was removed and the pellet re-suspended in 12 mL EpiLife medium. Cells were then plated in a T75 flask at a density of 2.5 x 10^3 cells / cm^2. The culture medium was replaced every 2 days until the culture is 50 % confluent and every day >50 % confluency.

2.2.2 Cryopreservation and cell line revival

HeLaM and HEK293 cells for freezing were washed once with sterile PBS (Gibco, California, US) and incubated with 1 mL trypsin for 5 minutes at 37 °C. Cells were re-suspended in 10 mL of DMEM and pelleted by centrifugation at 1500 rpm for 5 minutes. The supernatant was removed and cells were re-suspended in 1 mL ice-cold DMEM containing 10 % DMSO (Sigma Aldrich, Missouri, US). Cells were

transferred to cryovials and frozen using an isopropanol bath at -80 °C before long term storage in liquid nitrogen.

Frozen cells were quickly thawed in a water bath at 37 °C and re-suspended in 10 mL of DMEM. Cells were pelleted by centrifugation at 1500 rpm for 5 minutes. The supernatant was discarded and the pellet re-suspended in 10 mL of DMEM. Cells were plated onto a 10 cm dish containing 10 mL of DMEM and kept in culture.

HEKa cells for freezing were washed once with 3 mL trypsin (Gibco, California, US) and incubated with 9 mL trypsin for 7-8 minutes minutes at room temperature. Cells were re-suspended in 9 mL of trypsin neutraliser and pelleted by centrifugation at 180 x g for 7 minutes. The supernatant was removed and cells were re-suspended in 1 mL EpiLife medium containing 10 % DMSO (Sigma Aldrich, Missouri, US). Cells were transferred to cryovials and frozen using an isopropanol bath at -80 °C before long term storage in liquid nitrogen.

Frozen HEKa cells were quickly thawed in a water bath at 37 °C until a sliver of ice remains. Cells were re-suspended to a density of 1.24×10^4. 5 mL of the cell re-suspension was added to T25 culture flask and incubated at 37 °C in a 5 % CO_2 humidified incubator.

2.2.3 Adult Human Epidermal Keratinocyte calcium-induced differentiation

HEKa cells were seeded at a density of 2.5×10^3 cells / cm^2 and incubated for 48 hours at 37 °C in a 5 % CO_2 humidified incubator. The culture media was removed and replaced with 10 mL EpiLife medium containing 10 % HKGS, 1.2 mM $CaCl_2$, and 10 ng/µL EGF. Cells were incubated at 37 °C in a 5 % CO_2 humidified incubator for 96 hour until cells form epithelial sheet-like clusters.

2.2.4 Cell transfection

2.2.4.1 Transient transfection

Cells for transfection were seeded into 12 well plates (Thermo Scientific, Massachusetts, US). 0.6×10^5 HeLaM cells were seeded per well with 1 mL DMEM. Cells were incubated overnight at 37 °C. Prior to transfection, the DMEM was replaced with 1 mL antibiotic-free DMEM.

Plasmid DNA was transfected into cells using either polyethylenimine (PEI), Lipofectamine 2000 (Invitrogen, California, US), or FuGENE HD (Promega, Madison, USA). PEI was used at a ratio of 1 µg DNA to 5 µL PEI. Lipofectamine 2000 was used at a ratio of 1 µg DNA to 2.5 µL Lipofectamine 2000. FuGENE HD was used at a ratio of 1 µg DNA to 3 µL FuGENE HD. For PEI and Lipofecatmine 2000 transfections,

plasmid DNA and transfection reagents were diluted in separate microcentrifuge tubes containing 25 µL Opti-MEM® (Gibco, California, US) per well. Both tubes were incubated at room temperature for 5 minutes. The transfection reagent mix was added to the plasmid DNA mix, mixed gently by pipetting, and incubated at room temperature for 20 minutes. For FuGENE HD transfections, plasmid DNA was diluted in a microcentrifuge tube containing 25 µL Opti-MEM®. FuGENE HD was added directly to the tube containing the diluted DNA and incubated for 10 minutes at room temperature. The resulting transfection mixes (in all cases) were added dropwise to cells before swirling to mix. Cells were incubated overnight at 37 °C.

All expression constructs used in this thesis are listed in table 2-4.

2.2.4.2 siRNA transfection

$2.0x10^5$ HeLaM cells per well were seeded onto a 6 well plate (Thermo Scientific, Massachusetts, US) with 2 mL antibiotic-free DMEM and allowed to adhere for 2 – 4 hours. Cells were transfected using Lipofectamine RNAiMAX (Invitrogen, California, US). 5 µL of 20 µM siRNA was diluted in 150 µL Opti-MEM®. In a separate microcentrifuge tube, 6 µL of Lipofectamine RNAiMAX was diluted in 34 µL Opti-MEM®. Both microcentrifuge tubes were incubated at room temperature for 5 minutes. The diluted Lipofectamine RNAiMAX was added to the siRNA, mixed gently by pipetting, and incubated at room temperature for 20 minutes. The siRNA transfection mix was added dropwise to cells before swirling to mix. Cells were incubated at 37 °C.

For single hit knockdowns, cells were analysed after 48 hours after transfection. For double hit knockdowns, cells were trypsinised 48 hours after initial transfection. Cells were then seeded at $2x10^5$ cells per well onto 6 well plates with 2 mL antibiotic-free DMEM and allowed to adhere for 2 – 4 hours. Cells were transfected with siRNA following the same protocol as the initial transfection and incubated at 37 °C for a further 48 hours. For analysis by microscopy, cells were trypsinised 24 hours after the second transfection and seeded at $1x10^5$ cells per well onto 15 mm No. 1 round coverslips (VWR, Pennsylvania, US) in 12 well plates and incubated for a further 24 hours. Cells were analysed 96 hours after initial transfection.

2.2.5 Generation of stable cell lines by viral transduction

2.2.5.1 Transfection of HEK293 cells for viral production

HEK293 cells were grown using standard cell culture methods described above and transfected at 70 – 90 % confluency. Prior to transfection, cells were washed with sterile PBS and 6 mL antibiotic-free DMEM

was added. Cells were incubated at 37 °C for 2 – 4 hours. Lentiviral transduction was used to generate a stable HeLaM cell line expressing the Dharmacon SMARTvector lentiviral tet-inducible shRNA (Dharmacon, Colorado, US). Cells were transfected with Dharmacon SMARTvector containing the tet-inducible shRNA sequence, psPax2 lentiviral packaging vector, and pMD2.G VSV-G expressing envelope plasmid. Retroviral transduction was used to generate a stable HeLaM cell line expressing HA-VAMP8. Cells were transfected pLXIN-MOD vector containing HA-VAMP8, pUMVC packaging vector, and pMD2.G VSV-G envelope. For both transductions, polyethylenimine (PEI) (Sigma-Aldrich, Missouri, US) was used to transfect cells at a ratio of 1 µL PEI to 5 µg total DNA. A total of 10.5 µg DNA was transfected.

All plasmid DNA was diluted in 400 µL Opti-MEM® in a microcentrifuge tube. 52.5 µL PEI was diluted in 400 µL Opti-MEM® in a separate microcentrifuge tube. Both were incubated at room temperature for 5 minutes. The diluted PEI was added to the DNA, mixed gently by pipetting, and incubated at room temperature for 20 minutes. The transfection mix was added dropwise to the cells before swirling to mix. The cells were incubated overnight at 37 °C.

Cells were washed once with sterile PBS and 15 mL antibiotic-free DMEM was added. Cells were incubated for a further 24 hours at 37 °C. HeLaM cells were seeded at $2x10^5$ cells per well onto a 6 well plate with 2 mL antibiotic-free DMEM to achieve 50 % confluency for viral transduction the following day.

2.2.5.2 Harvesting viral media and viral transduction of HeLaM cells

The viral media was harvested from the HEK293 cells using a 20 mL syringe. 17 µL of 5 mg/mL polybrene (Sigma-Aldrich, Missouri, US) was added directly to the syringe and gently mixed. The media was filtered through a 0.45 µM filter (Merck Millipore, Massachusetts, US). 2 mL of the viral media was added to each well of HeLaM cells. Excess viral media was stored at -80 °C for future use. HeLaM cells were incubated with the viral media at room temperature for 20 minutes and then centrifuged at 2500 rpm for 90 minutes. Cells were incubated overnight at 37 °C.

The cells were expanded into T75 flasks in antibiotic-free DMEM and incubated overnight at 37 °C. For selection of cells of virally transduced cells, the media was replaced with DMEM containing the appropriate antibiotic selection (puromycin for lentiviral transductions, G418 for retroviral transductions; see table 2-3). Cells were treated with the antibiotic every 3 – 4 days for the generation and maintenance of the stable cell line.

2.3 Mitochondrial re-routing assays

2.3.1 Knocksideways assay

HeLaM cells were seeded at $0.85x10^5$ cells per well in a 12 well plate and incubated overnight at 37 °C. Cells were transfected according to the protocol in section 2.2.4.1 with Pmito, FKBP-myc-STX19, and any potential interacting protein tagged with GFP. The constructs were transfected in a ratio of 0.5 µg Pmito to 0.9 µg FKBP-myc-STX19 to 0.1 µg interacting protein. Cells were incubated overnight at 37 °C. To induce mitochondrial re-routing, cells were treated with 1 µg/mL rapamycin (see table 2-3) in 1 mL fresh media and incubated at 37 °C for 30 minutes. Cells were fixed using 4 % PFA and analysed using immunofluorescence microscopy as per the protocol in section 2.4.

2.3.2 Mitochondrial re-routing assay

$0.85x10^5$ HeLaM cells or $1.2x10^5$ Cos7 cells per well were seeded in a 12 well plate and incubated overnight at 37 °C. Cells were transfected according to the protocol in section 2.2.4.1 with a STX19 construct in which the C-terminal S-acylation domain had been replaced with the transmembrane domain of monoamine oxidase (STX19-mito, see section 2.6.6). Cells were co-transfected with a GFP/mCherry-tagged potential interactor. The constructs were transfected in a ratio of 0.9 µg STX19-mito to 0.1 µg potential interactor. Cells were incubated overnight at 37 °C. Cells were fixed using 4 % PFA and analysed using immunofluorescence microscopy as per the protocol in section 2.4.

2.4 Immunofluorescence microscopy

2.4.1 Immunofluorescence fixation and staining

Cells were grown on 15 mm No. 1 round coverslips (VWR, Pennsylvania, US) in 12 well plates. For Total Internal Reflection Fluorescence microscopy (TIRF), cells were grown in 35 mm glass bottom dishes (Ibidi, Gräfelfing, Germany).

Cells were rapidly fixed by adding 0.5 mL 4 % paraformaldehyde (PFA) to directly to the cell culture media in each well to avoid osmotic shock. The media was aspirated and cells were fixed using 1 mL 4 % PFA at room temperature for 15 minutes. The cells were quenched with 1 mL 0.1 M glycine at room temperature for 5 minutes. Cells were permeabilised with 0.1 % saponin with 5 % FBS at room temperature for 10 minutes and blocked using 1 % bovine serum albumin (BSA) at room temperature for 30 minutes. All buffer recipes are listed in table 2-5.

All antibody incubation steps were performed in 1 % BSA. Cells were incubated with primary antibodies at room temperature for 30 minutes. Cells were washed 3 times in 1 % BSA. Cells were incubated with secondary antibodies at room temperature for 30 minutes. Cells were washed twice with 1 % BSA and once with 1XPBS. See table 2-6 for a full list of antibodies used in this study. Coverslips were mounted onto microscope slides using ProLong Gold Mounting Media (Invitrogen, California, US) and sealed with clear nail polish. For TIRF microscopy, 1 mL of 1 x PBS was added to the 35 mm dish. Microscope slides and dishes were stored at 4 °C.

Epifluorescence microscopy was performed using an Olympus BX61 epifluorescence microscope (Olympus, Tokyo, Japan) equipped with 40x and 60x oil objectives, 488 nm, 594 nm, and 647 nm lasers and a Hamamatsu orca ER CCD detector (Hamamatsu Photonics, Hertfordshire, UK). Images were processed using ImageJ.

TIRF microscopy was performed using a Ti-NS N-STORM microscope (Nikon, Tokyo, Japan) equipped with a CFI Plan Apo TIRF 60x oil objective (Nikon, Tokyo, Japan) and an Andor iXion ultra EM-CCD camera (Andor Technologies, Belfast, Northern Ireland). For TIRF imagining, 488 nm, 594 nm, or 647 nm lasers are directed at the sample at an angle greater than the critical angle of the laser line. This results in total internal reflection of the laser line and creates an imaging field at 100 nm depth from the cell surface. Images were processed using ImageJ.

2.4.2 Anti-HA antibody uptake assays

HeLaM cells stably transduced with HA-VAMP8 were incubated with mouse anti-HA antibodies diluted 1:100 in DMEM culture media for 30 minutes at 37 °C in a 5 % CO_2 humidified incubator. Cells were then fixed and stained using the immunofluorescence protocol in section 2.4.

2.5 Flow cytometry secretion assay

HeLaM cells stably transduced with pQCXIP-S1-eGFP-FM4-FCS-hGH were used in this assay. This construct contains a signal sequence (S1), eGFP, four FM aggregation domains, furin cleavage site (FCS) and human growth hormone (hGH). This construct is trapped in the ER until release by treatment with D/D solubiliser. D/D solubiliser disrupted the FM domains interactions and as such, the construct can traffic to the plasma membrane and be secreted by the cells (Gordon *et al.*, 2021).

Cells were grown in 6-well dishes and transfected with either StrepSTX19 or StrepNSP6 in duplicate. Untransfected cells were set up for use as a negative control. 24 hours after transfection, cells were washed once with sterile PBS and detached using 1 mL trypsin for 5 minutes at 37 °C. Cells were re-

suspended in 1 mL DMEM with or without 1 µg/mL D/D solubiliser. Cells were incubated at 37 °C for 2.5 hours before fixing with 4 % PFA. Cells were stained following the protocol in section 2.4. As the cells are in suspension, cells were pelleted using centrifugation at 1200 rpm for 3 minutes at 4 °C between each stage.

Flow cytometry data was collected using the Attune NxT Flow Cytometer (Invitrogen, Waltham, Massachusetts, US) equipped with 488 nm and 594 nm lasers. Forward and side scatter gating was used to gate cell populations. The 594 nm laser was used to gate transfected cell populations and the 488 nm laser was used to measure GFP fluorescence intensity in transfected and untransfected cell populations. Data was analysed using FloJo (Treestar, Oregon, US).

2.6 Molecular biology

2.6.1 Casting agarose gels, gel electrophoresis, and gel purification

50 ml 1 % agarose gels were used for gel electrophoresis. 0.5 g agarose was added to 50 mL 1XTBE (90 mM Tris-borate, 2 mM EDTA, pH 8.0) and heated using a microwave swirling at 30 second intervals until all the agarose was dissolved. The gel was cooled with running water and 2 µL SYBR safe DNA gel stain (Invitrogen, California, US) was added and swirled to mix. The gel was poured into a gel tank containing the appropriate sized combs and allowed to set.

5 – 15 µL samples were loaded into the gel alongside Quick-Load purple 2-log DNA ladder (New England Biolabs, Massachusetts, US). 1XTBE was used a running buffer. A current of 80 mA was passed through the gel for DNA separation using a Fisher Biotech Scientific electrophoresis system power pack (Fisher Biotech Scientific, Pittsburgh, US). Once separated, DNA bands were excised using a razor blade.

DNA was extracted from excised bands using the Monarch® DNA gel extraction kit (New England Biolabs, Massachusetts, US) according to the manufacturers' instructions.

2.6.2 Primer design and polymerase chain reaction (PCR)

Primers were designed using Serial Cloner software 2.6.1. 15 – 20 base pairs were selected from the start (5' primer) or end (3' primer) of the DNA to be cloned ensuring a 40 – 60 % G-C content and a 60 – 70 °C melting temperature. Appropriate restriction sites corresponding to the vector to be used were included in the primer sequence. Primers were generated by Sigma-Aldrich. See table 2-8 for a full list of primers used in this thesis.

Quick-Load® Taq 2X Master Mix (New England Biolabs, Massachusetts, US) for all PCR reactions. 1 µL of 100 µM 5' and 3' primers were combined with 1 µL template DNA and 22 µL dH_2O. PCR amplification was carried out using a BioRad T100 ThermoCycler (BioRad, California, US). Samples were initially heated to 94 °C for 1 minute. Denaturing took place at 92 °C for 30 seconds, annealing took place at 55 – 65 °C for 1 minute, and extension took place at 72 °C for 1.5 minutes. The reaction was cycled through 30 times before a polishing step at 72 °C for 10 minutes.

PCR products were resolved on a 1 % agarose gel (see section 2.6.1) alongside Quick-Load purple 2-log DNA ladder and DNA extracted as above.

2.6.3 TOPO-TA cloning of PCR products

PCR products were cloned into TOPO vectors using TOPO-TA cloning kit (Invitrogen, California, US). 1 µL of salt solution, 1 µL TOPO vector, and 4 µL PCR product were combined and incubated at room temperature for 10 minutes. 4 µL of the mixture was added to 50 µL One Shot™ Mach1™ T1 Phage-Resistant Chemically Competent E. coli and incubated on ice for 10 minutes. The bacteria were heat shocked at 42 °C for 42 seconds and incubated on ice for a further 2 minutes. The bacteria were spread onto ampicillin agar plates coated with 120 µL 20 mg/mL X-Gal and incubated overnight at 37 °C.

White colonies were picked and cultured in 3 mL LB media containing 1 µg/µL ampicillin overnight at 37 °C. Plasmids were isolated using GeneJET mini-prep kit according to manufacturers' instructions. The plasmid DNA was digested using EcoRI enzyme restriction digest (see section 2.6.4 for protocol) and NEBuffer EcoRI (New England Biolabs, Massachusetts, US). Digested DNA was separated using gel electrophoresis (see section 2.6.1) and purified using Monarch® DNA gel extraction kit (New England Biolabs, Massachusetts, US) according to the manufacturers' instructions. Insert DNA was sequenced at the University of Sheffield Core Genomic facility.

2.6.4 Restriction Digests

All restriction digests were carried out using enzymes and buffers from New England Biolabs, Massachusetts, US. See table 2-9 for a full list of restriction enzymes and buffers used in this thesis.

15 µL restriction digests were performed using 0.5 µL of each restriction enzyme, 1.5 µL of the appropriate restriction buffer, 5 µL DNA (approx. 400 ng), and 7.5 µL ddH_2O.

30 µl restriction digests were performed using 1.5 µL of each restriction enzyme, 3 µL of the appropriate restriction buffer, 24 µL DNA (approx. 800 ng). Amount of DNA was adjusted depending on DNA concentration. Any remaining volume was made up with ddH_2O.

Restriction digest mixtures were incubated at 37 °C for 1 hour. Samples were then resolved on a 1 % agarose gel and DNA extracted as per the protocol in section 2.6.1.

2.6.5 Ligation and transformation

All ligation reactions used T4 ligase and T4 ligase buffer (New England Biolabs, Massachusetts, US). For a 20 µL reaction, 2 µL T4 ligase buffer, 50 ng vector DNA, 50 ng insert DNA, 1 µL T4 ligase was used and the remaining volume made up with ddH_2O. The mixture was incubated at room temperature for 30 minutes.

DH5α bacterial cells were transformed with ligated DNA. 5 µL of ligated DNA was added to 50 µL bacteria and incubated on ice for 20 minutes. The bacteria were heat shocked at 42 °C for 42 seconds and incubated for a further 2 minutes on ice. 1 mL of LB media was added to the bacteria and incubated in a shaking incubator at 220 rpm for 1 hour at 37 °C. The bacteria was pelleted by centrifugation at 10 000 rpm for 5 minutes using a Sigma 1 – 15p microcentrifuge. The supernatant was discarded and the pellet re-suspended in the remaining 100 µL LB media. The bacteria were spread onto an agar plate containing the appropriate antibiotic for selection and incubated overnight at 37 °C. Insert and vector only controls were used to ensure proper ligation had taken place. Colonies were picked and used to inoculate 3 mL of LB media containing the 1 µg/µL of the appropriate antibiotic for selection. Plasmids were isolated from the resultant culture using the GeneJET mini-prep kit according to manufacturers' instructions. Plasmid DNA was sequenced to confirm correct vector insertion at the University of Sheffield Core Genomic facility.

2.6.6 Constructs generated for use in this thesis

The STX19-mito, STX19-mito KDR-AAA, and STX19-mito SNARE domain deletion constructs were generated using a STX19 template DNA and a STX16-HA-MAO construct. The STX16-HA-MAO construct was a kind gift from Dr Sean Munro (University of Cambridge). The construct consists of STX16 in a pcDNA3.1+ vector backbone containing a HA tag, monoamine oxidase transmembrane domain, and MITO-APEX – used for visualisation by electron microscopy. GFP-ZWINT and GFP-DST constructs were generated using DNA for a fragment of the protein that were predicted to interact with STX19 based on commercial yeast-two hybrid screens (Ampah and Peden, unpublished) and the pEGFP-C3 vector. Primers designed for these constructs can be found in table 2-8. The template DNA was amplified using PCR and TOPO cloned as per the protocols described in sections 2.6.2 and 2.6.3. The insert DNA was excised and purified from the vector using EcoRI and NEBuffer EcoRI (New England Biolabs, Massachusetts, US) as per the protocol in section 2.6.4. and sequenced (University of Sheffield Genome Sequencing Facility) to ensure the correct sequences had been amplified. The inserts and vectors were digested as per the protocol in section 2.6.4. Table 2-10 shows a full list of the inserts, the corresponding vectors, and the

enzymes and buffers used for the restriction digest reactions. The digested DNA was separated by gel electrophoresis and purified from the gel as per the protocols in section 2.6.1. The purified vector and insert were ligated and used to transform DH5α bacterial cells using the protocol described in section 2.1.2.

2.7 Protein chemistry

2.7.1 Cell lysis and sample preparation

Cells were placed on ice and washed twice with ice-cold 1XPBS. Plates were placed at an angle on the ice to drain off any excess PBS. Cells were then incubated on ice with 200 µL HEPES lysis buffer (50 mM HEPES, 150 mM NaCl, 1.5 mM $MgCl_2$, 1 mM EDTA, 10 % glycerol, 0.5 % Triton X-100, 1XPCI) per well of a 6 well plate for 20 minutes. See table 2-13 for buffer recipes. Cells were removed from the bottom of the plate using a cell scraper and placed into 1.5 mL microcentrifuge tubes. Samples were incubated on ice for 45 minutes vortexing briefly at 15 minute intervals. Samples were centrifuged at 15 000 rpm for 20 minutes at 4 °C.

The supernatant was transferred to new ice-cold 1.5 mL centrifuge tubes. Protein concentration was assessed using the BioRad DC protein concentration assay as described in section 2.7.2. 4X Laemmli buffer was added to the samples such that the final concentration of Laemmli buffer was 1X. Samples were boiled at 95 °C for 5 minutes and stored at -20 °C.

2.7.2 BioRad DC protein concentration assay

Protein concentration was determined using reagents from BioRad DC protein concentration assay kit (BioRad, California, US) expect where mentioned.

Protein standards ranging from 0 mg/mL – 2 mg/mL were prepared using Albumin (Thermo Scientific, Massachusetts, US) diluted in HEPES lysis buffer. 5 µL of each protein standard and samples were loaded into a 96 well plate in triplicate. 1 mL of reagent A was combined with 20 µL reagent S. 25 µL of the resultant reagent was added to the wells containing the protein standards and samples. 200 µL of reagent B was added to the wells and the plate was incubated in the dark at room temperature for 15 minutes. Absorbance was read at 740 nm using a FLUO star omega plate reader (BMG Labtech, Ortenburg, Germany). A standard curve was generated using the protein standards concentrations and absorbances. Sample concentration was determined using the standard curve.

2.7.3 Casting acrylamide gels

15 % acrylamide gels were prepared according to the recipes in table 2-12. See table 2-11 for buffer recipes used in gel casting. Spacer and short plates were washed with liquid detergent and rinsed in ethanol. Plates were assembled and clamped in BioRad casting frames. Approximately 3.5 – 4 mL of separating gel was poured in between the plates until the gel reached 1.5 cm below the top of the plates. Approximately 1 mL of isopropanol was added and the gel left to set at room temperature for 30 minutes.

Isopropanol was removed and the gel washed 3 times with ddH_2O ensuring all water is removed after the final wash. Approximately 1 mL of stacking gel was poured in between the plates until the gel reached the top of the plate and a 0.75 mm BioRab comb inserted into the gel. The gel was left to set at room temperature for 30 minutes. The comb was removed prior to use.

2.7.4 Sodium dodecyl sulfate–polyacrylamide gel electrophoresis (SDS-PAGE)

All equipment used for SDS-PAGE was part of the Mini-PROTEAN® Tetra Vertical electrophoresis system (BioRad, California, US) expect where mentioned.

Cast gels were loaded into Mini-PROTEAN® electrophoresis cassette and the cassette filled with 1XTGS running buffer (25 mM Tris, 192 mM Glycine, 0.1 % SDS, ddH2O, pH 8.3). See table 2-13 for all buffer recipes. Wells that were not to contain samples were loaded with 15 µL of 1X Laemmli buffer using round tip or flat tip gel loading tips. Precision Plus Protein WesternC (BioRad, California, US) standard was diluted 1 in 4 with ddH_2O and 8 µL was loaded into the gel where appropriate. 10 – 15 µL of sample was loaded in the gel depending on protein concentration, see section 2.7.2 for the BioRad DC protein concentration assay protocol. The loaded cassette was placed into the gel tank and the tank was filled with 1XTGS running buffer to the line indicated on the tank. A current of 100 V was passed through the system using the Fisher Biotech Scientific electrophoresis system powerpack (Fisher Biotech Scientific, Pittsburgh, US) for 15 minutes or until the samples passed into the separating gel. The current was increased to 200 V for 45 minutes or until the laemlli buffer exited the gel. The gels were removed from the tank and washed with ddH_2O before staining or use in protein transfer.

2.7.5 Coomassie staining SDS-PAGE gels

The gels were submerged in Quick Blue Stain (Avidity Science, Wisconsin, US) and placed on a Stuart Scientific platform shaker (Bibby Scientific, Staffordshire, UK) overnight. Stained gels were rinsed in ddH_2O and imaged using the GelDoc EZ Imager (BioRad, California, US).

2.7.6 Protein transfer

Proteins were transferred onto 0.45 µM nitrocellulose membranes (Whatman, Maidstone, UK) using a wet blotting method. Low molecular weight transfer buffer was used for low molecular weight proteins (25 mM Tris Hydrochloride, 192 mM Glycine, 20 % Methanol, ddH2O). High molecular weight transfer buffer containing 0.1 % SDS was used for proteins >100 kDa in weight. See table 2-13 for buffer recipes.

A transferred cassette was prepared with transfer sponges, Whatman chromatography paper (Whatman, Maidstone, UK), the SDS-PAGE gel, and the nitrocellulose membrane in a tray filled with transfer buffer. All components of the transfer cassette were soaked in transfer buffer. Proteins were transferred overnight at 4 °C with a 100 mA of current using a BioRad PowerPac HC (BioRad, California, US).

2.7.7 Staining nitrocellulose membranes with Ponceau S

To visualise protein bands, membranes were briefly stained with Ponceau S solution (0.1 % Ponceau S, 5 % acetic acid, see table 2.12) (Sigma-Aldrich, Missouri, US). Membranes were rinsed with ddH_2O to remove excess staining solution and left to dry on Whatman chromatography paper.

2.7.8 Immunoblotting

Membranes were blocked using a milk blocking buffer (5 % non-fat dry skimmed milk in 1XPBS with 1 % tween-20, see table 2-13) for 30 minutes at room temperature on a Stuart Scientific Platform Shaker. All antibodies used for immunoblotting were diluted in blocking buffer, see table 2-6 for a full list of antibodies used in this thesis. Membranes were incubated with primary antibodies for 1 hour at room temperature. For antibodies that require a higher concentration, membranes were placed on an antibody incubate plate on top of parafilm. 1 mL of antibody diluted in blocking buffer was pipetted on to the membrane. For antibodies that used a lower concentration, membranes were incubated with 3 – 5 mL antibody diluted in blocking buffer and placed on a Stuart Scientific platform shaker.

All membrane washes took place in blocking buffer. Membranes were washed 3 times briefly followed by 3 times for 5 minutes on a platform shaker. After washing, membranes were incubated with 3 – 5 mL secondary antibodies conjugated to HRP and Precision Protein Streptactin HRP (5000x) (BioRad, California, US) diluted in blocking buffer for 1 hour at room temperature on a platform shaker. Membranes were washed as above apart from the final 5 minute wash which was in 1XPBST.

2.7.9 Protein detection

Membranes were incubated with Clarity Western ECL Substrate (BioRad, California, US) as per manufacturers' protocol at room temperature for 5 minutes in the dark. Excess substrate was removed and membranes enclosed in plastic. Membranes were imaged using LI-COR C-DiGit blot scanner (LI-COR Biosciences, Nebraska, US) at high sensitivity.

Table 2-1: Bacterial culture buffers

Buffer	Composition	Recipe
Agar plates	1 % Tryptone 0.5 % Yeast extract 0.5 % NaCl 1.5 % Agar ddH2O	5 g Tryptone (Sigma-Aldrich, T7293-1KG) 2.5 g Yeast extract (Sigma-Aldrich, Y1625) 5 g NaCl (Fisher Chemical, S/3120/60) 7.5 g Agar (Sigma-Aldrich, 05040-1KG) 250 mL ddH2O Powders were dissolved in ddH2O before autoclaving, antibiotics were added once media had cooled to the touch but not set Store plates at 4 °C
LB media	1 % Tryptone 0.5 % Yeast extract 0.5 % NaCl ddH2O	5 g Tryptone (Sigma-Aldrich, T7293-1KG) 2.5 g Yeast extract (Sigma-Aldrich, Y1625) 5 g NaCl (Fisher Chemical, S/3120/60) 250 mL ddH2O Powders were dissolved in ddH2O before autoclaving Store at room temperature
X-Gal	20 mg/ml X-Gal Dimethylsulfoxide (DMSO)	200 mg X-Gal (Invitrogen, 15520034) 10 mL DMSO (Sigma-Aldrich, 472301) Divide into aliquots and store at -20 °C

Table 2-2: Mammalian cell culture and transfection buffers

Buffer	Composition	Recipe
Complete dulbecco's modified eagle's medium (DMEM)	DMEM containing 2 mM L-Glutamine, sodium pyruvate, and phenol red 10 % FBS 1 % 100 µg/mL penicillin/streptomycin	500 mL DMEM (Sigma-Aldrich, D5796) 50 mL FBS (Gibco, 10500064) 5 mL penicillin/streptomycin (Sigma-Aldrich, P4333-100ML) FBS and penicillin/streptomycin was filtered through a 0.22 µM stericup (Merck Millipore, scgvu05re) in a tissue culture hood and added to the DMEM For antibiotic-free media used in transfections, only FBS was filtered

		and added to DMEM Store at 4 °C
EpiLife Medium	EpiLife medium containing 60 µM calcium chloride 1 % Human Keratinocyte Growth Supplement (HKGS) 1 % 100 µg/mL penicillin/streptomycin	500 mL EpiLife media (Gibco, MEPI500CA) 5 mL HKGS (Gibco, S0015) 5 mL penicillin/streptomycin (Sigma-Aldrich, P4333-100ML) HKGS and penicillin/streptomycin was filtered through a 0.22 µM stericup (Merck Millipore, scgvu05re) in a tissue culture hood and added to the media. Store at 4 °C.
Tryspin-EDTA	Trypsin-EDTA containing 2.5 g porcine trypsin and 0.2 g EDTA	As supplied (Sigma-Aldrich, T4049) Store at 4 °C
Trypsin neutraliser solution	Trypsin neutraliser solution containing 0.5% newborn bovine serum as a trypsin inhibitor	As supplied (Gibco, R002100) Store at 4 °C
Sterile 1XPBS	Phosphate buffered saline pH 7.4	As supplied (Gibco, 10010-056) Store at 4 °C
Opti-MEM	Opti-MEM reduced serum media buffered with HEPES and sodium bicarbonate	As supplied (Gibco, 11520386) Store at 4 °C
Lipofectamine 2000		As supplied (Invitrogen, 11668027) Store at 4 °C
FuGENE HD transfection reagent		As supplied (Promega, E2311) Store at 4 °C
Lipofectamine RNAiMAX		As supplied (Invitrogen, 13778075) Store at 4 °C
PEI	1 mg/mL polyethylenimine (PEI) ddH2O	50 mg PEI (Polysciences Inc, 23966-1) 45 mL ddH2O Add PEI to ddH2O and adjust pH to 2.0 using 12 M HCl Dissolve PEI for 2 hours using a magnetic stirrer Adjust pH to 7.0 using 10 M NaOH Adjust final volume of the solution to 50 mL and Filter through a 0.22 µM filter (Insight Biotechnologies, sc-358816) Store at -20 °C

Polybrene	0.05 % Hexadimethrine bromide ddH2O	50 mg Hexadimethrine bromide (Sigma-Aldrich, H9268-10G) 10 mL ddH2O Filter through a 0.22 µM filter (Insight Biotechnologies, sc-358816) Store at -20 °C

Table 2-3: Antibiotics

Antibiotic stock	Working concentration	Composition	Recipe
Ampicillin 100 mg/mL	100 µg/mL	100 mg/mL Ampicillin sodium salt ddH2O	1 g Ampicillin sodium salt (Fisher Bioreagents, BP1760-5) 10 mL ddH2O Filter through a 0.22 µM filter (Insight Biotechnologies, sc-358816) Store at -20 °C
Kanamycin 50 mg/mL	50 µg/mL	50 mg/mL Kanamycin disulfate salt ddH2O	0.5 g Kanamycin disulfate salt (Merck, EC 223-347-1) 10 mL ddH2O Filter through a 0.22 µM filter (Insight Biotechnologies, sc-358816) Store at -20 °C
Puromycin 10 mg/mL	1 µg/µL	As supplied	Puromycin Dihydrochloride (Gibco, A1113803) Store at -20 °C
Rapamycin 10 mg/mL	1 µg/mL	10 mg/mL Rapamycin ddH2O	0.1 g Rapamycin (Fisher BioReagents, BP2963-1) 10 mL ddH2O Filter through a 0.22 µM filter (Insight Biotechnologies, sc-358816) Store at -20 °C
Neomycin (G418) 50 mg/mL	100 µg/mL	As supplied	G418 solution (Roche, 4727878001)

Table 2-4: Expression constructs

Construct	Vector	Insert	Tag	Insert species
FKBP-GFP	pIRES-Neo	FKBP-GFP		*Aequorea victoria*
FKBP-myc-STX19$^{1-272}$	pIRES-Neo	FKBP STX19 without tail	Myc	Human
FKBP-myc-STX19$^{1-294}$	pIRES-Neo	FKBP STX19 full length	Myc	Human
GFP-DST	pEGFP-C3	DST Y2H fragment	EGFP	Human
GFP-Munc18-1	pEGFP-C3	Munc18-1	EGFP	Human
GFP-Munc18-2	pEGFP-C3	Munc18-2	EGFP	Human
GFP-Munc18-3	pCMV3-N-GFPSpark	Munc18-3	GFPSpark	Human
GFP-Rac1	pEGFP-C3	Rac1	EGFP	Human
GFP-STX11	pEGFP-C3	STX11 full length	EGFP	Human
GFP-STX19	pEGFP-C3	STX19 full length	EGFP	Human
GFP-STX19$^{275-294}$	pEGFP-C3	STX19 tail	EGFP	Human
GFP-ZWINT	pEGFP-C3	ZWINT Y2H fragment	EGFP	Human
HA-STX19	pIRES-Neo	STX19	HA	Human
HA-STX19$^{1-272}$	pIRES-Neo	STX19 without tail	HA	Human
HA-STX19$^{1-277}$/ STX13$^{251-276}$	pIRES-Neo	STX19 without tail STX13 transmembrane domain	HA	Human
HA-VAMP8	pLXIN retroviral	VAMP8	2XHA	Human
Pmito	pMito (Gift from Steve Royle, plasmid #59352 Addgene Adapted from pEYFP-Mitotrap plasmid #46942	pMito-mCherry-FRB	mCherry	Yeast
StrepNSP6	pIRES-Neo2	NSP6	Strep tag	Sars-CoV2
StrepSTX19	pIRES-Neo2	STX19 full length	Strep tag	Human
StrepSTX19$^{KDR-AAA}$	pIRES-Neo2	STX19 KDR mutant	Strep tag	Human
StrepSTX19$^{\Delta 218-272}$	pIRES-Neo2	STX19 without SNARE domain	Strep tag	Human
STX16mito	pcDNA3.1+	STX16 without transmembrane domain Monoamine oxidase transmembrane domain	HA Mito-APEX	Human
STX19mito	pcDNA3.1+	STX19 without tail Monoamine oxidase transmembrane domain	HA Mito-APEX	Human
STX19mito$^{KDR-AAA}$	pcDNA3.1+	STX19 KDR mutant without tail	HA Mito-APEX	Human

		Monoamine oxidase transmembrane domain		
STX19mito$^{\Delta 219-294}$	pcDNA3.1+	STX19 without SNARE domain and tail Monoamine oxidase transmembrane domain	HA Mito-APEX	Human
ZWINT-FLAG	pCMV3	ZWINT full length	FLAG	Human
FLAG-ZWINT	pCMV3	ZWINT full length	FLAG	Human

Table 2-5: Immunofluorescence microscopy buffers

Buffer	**Composition**	**Recipe**
4 % PFA	4 % PFA 1xPBS ddH2O	20 mL 10 % Formaldehyde, methanol-free, ultra pure (Polysciences Inc. 04018-1) 5 mL 10XPBS (Fisher Bioreagents, BP399-4) 25 mL ddH2O Store at room temperature, use within 3 days or make fresh
Methanol	Methanol	As supplied (Fisher Scientific, M/4056/17) Store at room temperature
Glycine	0.1 M Glycine 1XPBS	0.75 g Glycine (Fisher Scientific, G/0800/60) 100 mL 1XPBS Store at room temperature
Saponin	0.1 % Saponin 5 % FBS 1XPBS	1 g Saponin (Sigma-Aldrich, S4521) 50 mL FBS (Gibco, 16140071) 950 mL 1XPBS Store at 4 °C
Triton-X 100	0.1 % Triton-X 100 1XPBS	1 % Triton-X 100: 500 µl Triton-X 100 (Sigma-Aldrich, X100-500ML) 49.5 mL 1xPBS 0.1 % Triton-X 100: 1 mL 1 % Triton-X 100 (Sigma-Aldrich, X100-500ML) 10 mL 1XPBS Store at 4 °C
1XPBS	10xPBS ddH2O	100 mL 10XPBS (Fisher Bioreagents, BP399-4) 900 mL ddH2O Store at room temperature

Table 2-6: Primary and secondary antibodies

Antigen	Source	Application	Type
Primary antibodies			
β-Catenin	Kind gift from Kai Erdmann	IF: 1/200	Mouse mAb
CD59	Sigma Aldrich Cat No. SAB4700207	IF: 1/200	Mouse mAb
CD63	BD Bioscience Cat No. 555988 Clone H5C6	IF: 1/200	Mouse mAb
Dystonin	Santa Cruz Biotechnology Cat No. sc-13776	IF: 1/100	Goat pAb
E-Cadherin	Kind gift from Kai Erdmann	IF: 1/200	Mouse mAb
FLAG tag	Cell Signalling Technology Cat No. 14793S Clone D6W5B	IF: 1/400	Rabbit mAb
FLAG tag	Cell Signalling Technology Cat No. 8146S Clone 9A3	IF: 1/400	Mouse mAb
HA tag	BioLegend Cat No. 901502 Clone HA.11	IF: 1/400 WB: 1/1000	Mouse mAb
LAMP1	Abcam Cat No. ab24170	IF: 1/200	Rabbit pAb
LC3	MBL International Cat No. M152-3 Clone 4E12	IF 1:200	Mouse mAb
MICAL-L1	Abnova Cat No. H00085377-B01P	IF: 1/200	Mouse pAb
Myc tag	A. Peden Clone 9E10	IF: 1/400	Mouse mAb
P62	Kind gift from Jason King BD Transduction Laboratories Cat No. 610833 anti-P62 Ick ligand	IF: 1/200	Mouse mAb
pAkt	Kind gift from Jason King Cell Signalling Technologies Cat No. 4051 Clone S473	IF: 1/200	Mouse mAb
Rab8	Cell signalling technology Cat No. 6975	IF: 1/400	Rabbit mAb
Rac1	Kind gift from Daniel Humphries	IF: 1/200	Mouse mAb
SNAP29 11	Made in house, raised against the full-length protein Purified from cell culture media (Gordon *et al.*, 2010)	IF: 1/3	Mouse pAb
SNAP29 5	Made in house, raised against the full-length protein Purified from cell culture media (Gordon *et al.*, 2010)	IF: 1/3	Mouse pAb
STX19	Made in house, raised against the full-length protein (Ampah *et al.*, 2018)	IF: 1/600	Rabbit pAb
VAMP3	A. Peden	IF: 1/200	Rabbit pAb
VAMP4	A. Peden	IF: 1/500	Mouse mAb
VAMP7	A. Peden Clone 6C3 IgG2B	IF: 1/100	Mouse mAb
VAMP8A	A. Peden	IF: 1/200	Rabbit pAb
VAMP8B	A. Peden	IF: 1/200	Rabbit pAb
ZWINT	Abcam Cat No. ab174266	IF: 1/400	Rabbit mAb

Secondary antibodies			
Alexa Fluor 488	Invitrogen Molecular Probes Cat No. A32723	IF: 1/1000	Goat anti-mouse
Alexa Fluor 488	Invitrogen Molecular Probes Cat No. A32731	IF: 1/1000	Goat anti-rabbit
Alexa Fluor 594	Invitrogen Molecular Probes Cat No. A32742	IF: 1/1000	Goat anti-mouse
Alexa Fluor 594	Invitrogen Molecular Probes Cat No. A32740	IF: 1/1000	Goat anti-rabbit
Alexa Fluor 647	Invitrogen Molecular Probes Cat No. A32728	IF: 1/1000	Goat anti-mouse
Alexa Fluor 647	Invitrogen Molecular Probes Cat No. A32733	IF: 1/1000	Goat anti-rabbit
StrepTactin XT Conjugate DY-488	IBA Cat No. 2-1562-050	IF: 1/1000	
StrepTactin XT Conjugate DY-594	IBA Cat No. 2-1565-050	IF: 1/1000	
HRP-conjugated (FC specific fragment)	Jackson ImmunoResearch Laboratories Cat no: 115-035-008	WB: 1/5000	Anti-mouse
HRP-conjugated (FC specific fragment)	Jackson ImmunoResearch Laboratories Cat no: 111-035-008	WB: 1/5000	Anti-rabbit
StrepTactin HRP conjugate	BioRad Cat no: 161-0380	WB: 1/8000	

Table 2-7: Gel electrophoresis buffers

Buffer	**Composition**	**Recipe**
Agarose gel	1 % agarose 1XTBE	0.5 g agarose (Fisher Bioreagents, BP1356-100) 5 mL 10XTBE (Sigma-Aldrich, T4415-4L) 45 mL ddH2O
1XTBE	90 mM Tris-borate 2 mM EDTA ddH2O pH 8.0	100 mL 10XTBE (Sigma-Aldrich, T4415-4L) 900 mL ddH2O Store at room temperature
SYBR safe DNA gel stain		As supplied (Invitrogen, S33102)

Table 2-8: Primers

Primer name	Sequence (5' to 3')
STX19-mito in pcDNA3.1+ vector backbone containing HA-tag, MAO TM domain, MITO-APEX	
3' KpnI BamHI STX19-mito	CggatccggtaccTACAGCTAGTCCAAATTTCTC
5' NheI STX19-Mito	GCgctagcATGAAAGACCGACTTCAAGAAC
STX19-mito KDR-AAA in pcDNA3.1+ vector backbone containing HA-tag, MAO TM domain, MITO-APEX	
3' KpnI BamHI STX19-mito	CggatccggtaccTACAGCTAGTCCAAATTTCTC
5' XhoI STX19-mito KDR-AAA	ctcgagATGTACCCCTACGACGTCCCCGACTACGCAGCAGCAGCACTTCAAGAACTAAAGCAGAGAACAAAGG
STX19-mito SNARE domain deletion in pcDNA3.1+ vector backbone containing HA-tag, MAO TM domain, MITO-APEX	
3' NotI STX19-mito SD del.	GCggccgcTTATACAGCTAGTCCAAATTTCTC
5' NheI STX19-mito	GCgctagcATGAAAGACCGACTTCAAGAAC
GFP-ZWINT in pEGFP-C3	
3' EcoRI ZWINT Y2H fragment	GCgaattcTTAAACCTCCGCCAGATGCTGC
5' XhoI ZWINT Y2H fragment	GCctcgagCTGCAGAACATCCTGGCTCAG
GFP-DST in pEGFP-C3	
3' EcoRI DST Y2H fragment	GCGgaattcTTATGCCCTCCATGGTACC
5' XhoI DST Y2H fragment	GCctcgagACAGGTGATGAAGTT

Table 2-9: Restriction enzymes and buffers

Enzyme	Source
EcoRI	New England Biolabs, R010T
KpnI	New England Biolabs, R0142S
BamHI	New England Biolabs, R0136S
NheI	New England Biolabs, R0131S
XhoI	New England Biolabs, R0146S
NEBuffer EcoRI	New England Biolabs, B0101
NEBuffer 2.1	New England Biolabs, B7202S
NEBuffer 3.1	New England Biolabs, B7203S

Table 2-10: Restriction digests for construct generation

Construct	Vector	Enzymes used in restriction digest	Restriction digest buffer
STX19-mito	pcDNA3.1+ backbone containing HA-tag, MAO TM domain, MITO-APEX	KpnI NheI	NEBuffer 2.1
STX19-mito KDR-AAA	pcDNA3.1+ backbone containing HA-tag, MAO TM domain, MITO-APEX	KpnI XhoI	NEBuffer 1.1
STX19-mito SNARE domain deletion	pcDNA3.1+ backbone containing HA-tag, MAO TM domain, MITO-APEX	NotI NheI	NEBuffer 2.1
GFP-ZWINT	pEGFP-C3	XhoI EcoRI	NEBuffer 3.1
GFP-DST	pEGFP-C3	XhoI EcoRI	NEBuffer 3.1

Table 2-11 SDS-PAGE gel buffers

Buffer	Composition	Recipe
Separating buffer	1.5 M Tris base 0.4 % SDS pH 8.8	90.8 g Trizma (Sigma-Aldrich, T1503/93352-1KG) 2 mL 20 % SDS (Fisher Bioreagents, BP1311-200) 400 mL ddH2O Adjust pH to 8.8 using concentrated HCl Make up final volume to 500 mL with ddH2O Store at 4 °C
Stacking buffer	0.5 M Tris base 0.4 % SDS pH 6.8	30.3 g Trizma (Sigma-Aldrich, T1503/93352-1KG) 2 mL 20 % SDS (Fisher Bioreagents, BP1311-200) 400 mL ddH20 Adjust pH to 8.8 using concentrated HCl Make up final volume to 500 mL with ddH2O Store at 4 °C
30 % Acrylamide	30% Acrylamide/Bis 37.5:1	As supplied (BioRad, 1610158) Store at 4 °C
20 % SDS	20 % Sodium dodecyl sulfate solution	As supplied (Fisher Bioreagents, BP1311-200) Store at room temperature
10 % APS	10 % Ammonium persulfate in ddH2O	0.1 g APS (Sigma-Aldrich, A3678-25G) 1 mL ddH2O Divide into aliquots for long term storage at -20 °C or <3 week storage at 4 °C

TEMED	Tetramethylethylenediamine ~ 99 %	As supplied (Sigma-Aldrich, T7024) Store at 4 °C

Table 2-12 SDS-PAGE gel casting recipes

15 % separating gel - 20 mL for 4 gels	
ddH2O	4.8 mL
Separating buffer	5 mL
30 % Acrylamide	10 mL
20 % SDS	50 µL
10 % APS	100 µL
TEMED	10 µL

Stacking gel - 5 mL for 4 gels	
ddH2O	3.5 mL
Separating buffer	700 µL
30 % Acrylamide	800 µL
20 % SDS	50 µL
10 % APS	100 µL
TEMED	5 µL

Table 2-13 Cell lysis, SDS-PAGE, transfer, and immunoblotting buffers

Buffer	**Composition**	**Recipe**
HEPES lysis buffer	50 mM HEPES 150 mM NaCl 1.5 mM MgCl2 1 mM EDTA 10% glycerol 0.5% Triton X-100 1X Protease cocktail inhibitor (PCI) pH 7.5	5.95 g HEPES (Sigma-Aldrich, H3375) 4.38 g NaCl (Fisher Chemical, S/3120/60) 0.07 g MgCl2 (Thermo Fisher Scientific, R0971) 0.165 g EDTA (Sigma-Aldrich, E9884) 50 mL Glycerol (Fisher Chemical, G5516-500ML) 2.5 mL Triton-X 100 (Sigma-Aldrich, X100-500ML) 500 mL ddH2O 1X cOmplete™, Mini, EDTA-free Protease Inhibitor Cocktail (Roche, 11873580001) PCI to be added fresh before use - do not add to stock solution. Dilute PCI from 25 X stock to 1X concentration in final volume of lysis buffer required for experiment Store at 4 °C

HEPES wash buffer	50 mM HEPES 150 mM NaCl 1.5 mM MgCl2 1 mM EDTA 10% glycerol 1X Protease cocktail inhibitor (PCI) pH 7.5	5.95 g HEPES (Sigma-Aldrich, H3375) 4.38 g NaCl (Fisher Chemical, S/3120/60) 0.07 g MgCl2 (Thermo Fisher Scientific, R0971) 0.165 g EDTA (Sigma-Aldrich, E9884) 50 mL Glycerol (Fisher Chemical, G5516-500ML) 500 mL ddH2O PCI to be added fresh before use - do not add to stock solution. Dilute PCI from 25 X stock to 1X concentration in final volume of wash buffer required for the experiment Store at 4 °C
1XTGS running buffer	25 mM Tris 192 mM Glycine 0.1 % SDS ddH2O pH 8.3	100 mL 10XTGS (BioRad, 161-0772) 900 mL ddH2O Store at room temperature
4XLaemmli buffer	250 mM Tris-HCl 40% glycerol 20% βmercaptoethanol 8% SDS 1% bromophenol blue pH 6.8	As supplied (BioRad, 161-0747) Diluted to 1X with sample Store at room temperature
1XTransfer buffer	25 mM Tris Hydrochloride 192 mM Glycine 20 % Methanol ddH2O + 0.1 % SDS for high MW transfer	15 g Tris Hydrochloride (Fisher Chemical, 1185-53-1) 72 g Glycine (Fisher Chemical, G/0800/60) 1 L Methanol (Fisher Chemical, M/4056/17) 4 L ddH2O + 5 mL 20 % SDS for high MW transfer buffer (Fisher Bioreagents, BP1311-200) Store at room temperature
Ponceau S	0.1% Ponceau-S powder 5% acetic acid	0.5 g Ponceau S powder (Sigma-Aldrich, P3504) 25 mL Acetic acid (Romil-SpS Super Purity Solvents, H014P) 475 mL ddH2O Filter through 0.2 µM filter (Insight Biotechnologies, sc-358816) Store at room temperature
Blocking buffer	5 % non-fat dry skimmed milk powder 1 % Tween-20 1XPBS	30 g skimmed milk powder (Sigma-Aldrich, 0166-500G) 600 µL Tween-20 (AppliChem Pancreac, A4974,0500) 60 mL 10XPBS (Fisher Bioreagents, BP399-4) 540 mL ddH2O Store at 4 °C, use within 3 days or make fresh

Chapter 3

Investigating the interacting

partners of STX19

3.1 Introduction

Underpinning all physiological processes is the ability of proteins to interact with one another. To fully appreciate the function of a protein, it is crucial to understand the proteins it interacts with. Therefore, screening of potential interactors of STX19 was key to gain insight into the pathways and processes STX19 plays a role in. Previous work in our lab used biochemical approaches to screen for protein interactors. This included the use of a commercial yeast-two hybrid assay and proximity-dependent biotinylation assays (BioID) coupled to mass-spectrometry. A yeast-two hybrid screen was performed using a human colon library and STX19 as a bait. 70 unique interactors of STX19 were identified. This was shortlisted to 26 proteins based on functional relevance to STX19. From BioID approaches, 54 proteins were shortlisted as potential STX19 interactors. Figure 3-1 shows a Venn diagram of potential interactors of interest for this study and the assays they were identified in. Shortlisted interactors were also compared to a publicly available protein-protein interaction database BioGRID which identifies interactions through affinity capture-mass spectrometry. Other SNAREs already predicted to complex with STX19 were identified in the screens including SNAPs 23, 25, 29, and VAMPs 3 and 8. We chose 4 of the interactors (Munc18-1, Munc18-2, ZWINT, and DST) shortlisted by either yeast-two hybrid, BioID, or both that were also were present on the database and carried these forward as most likely to be genuine STX19 interactors for further validation and investigation.

Two of the proteins we chose to investigate were Munc18-1 and -2. Munc18 proteins (Munc18-1, Munc18-2, and Munc18-3) belong to the Sec/Munc family of proteins and are well-known regulators to SNARE function (Südhof and Rothman, 2009). Munc18-1 and -2 were identified as potential interactors of STX19 in BioID assays and are listed on BioGRID. Munc18-3 was not identified as a potential STX19 interactor in any of the screens performed and is not listed on BioGRID. Munc18-1 is highly enriched in brain tissues and known to interact with STX1 to regulate neurotransmitter and neuropeptide secretion (Deák *et al.*, 2009; Jiao *et al.*, 2018; Puntman *et al.*, 2021). As a result, mutations in Munc18-1 give rise to severe encephalopathies and neurodevelopmental disorders (Abramov, Guiberson and Burré, 2021). More recent studies have also indicated a potential role for Munc18-1 in the first phases of insulin secretion (Oh *et al.*, 2012; Zhang *et al.*, 2020).

Munc18-2 is known to interact with STX11 in cytotoxic T lymphocytes and natural killer cells. Mutation in Munc18-2 or STX11 in these cell types resulted in impaired exocytosis of cytotoxic granules giving rise to Familial Hemophagocytic Lymphohistocytosis 4/5 (FHL4/FHL5) – a hyperinflammatory disorder (Spessott *et al.*, 2015, 2017a). STX11 has been shown to interact with Munc18-2 via an N-terminal KDR peptide which is conserved in STX19 and mutation in this peptide abolished Munc18-2 interaction (Müller *et al.*, 2014). Munc18-2 is also enriched in epithelial cells, similarly to STX19, where it has been

shown to interact with STX3 to regulate apical trafficking of cargo proteins such as sodium/hydrogen-exchanger 3 (NHE3) and cystic fibrosis transmembrane conductance regulator (CFTR) (Riento *et al.*, 2000; Vogel *et al.*, 2015). Mutations in Munc18-2 give rise to enteropathies in FHL4 patients through disrupted apical exocytosis and result in microvillus inclusions in intestinal organoids which can be used to model Microvillus Inclusions Disease (MVID) (Vogel *et al.*, 2017; Mosa *et al.*, 2018). Whilst STX3 also contains the conserved N-terminal KDR peptide, it is not yet clear if this is the binding site for Munc18-2. Given that STX19 is highly homologous to STX11, contains the N-terminal KDR peptide, and is also enriched in epithelial cells, we predict that Munc18-2 is a genuine STX19 interactor. Therefore, we chose to investigate this interaction further. We also chose to investigate the interaction between STX19 and Munc18-1, however given that Munc18-1 is enriched in brain tissues and has roles in neurotransmitter release, it is unlikely that this interaction is physiologically relevant. Since Munc18-3 was not predicted to interact with STX19, we used this protein as a negative control.

One of the shortlisted interactors from previous biochemical analysis was ZW10-interactor (ZWINT). ZWINT was identified as a potential interactor of STX19 through yeast-two hybrid screening and is listed as an interactor BioGRID. Previous co-immunoprecipitation studies in the lab also demonstrated ZWINT is immunoprecipitated with STX19 but not STX7. ZWINT is predicted to interact with STXs 3, 11, and 18, and SNAPs 25 and 29 (Lee *et al.*, 2002; Huttlin *et al.*, 2015, 2017). It is known for its role as a spindle assembly checkpoint protein where it recruits Zeste-White 10 (ZW10) to the kinetochore for proper kinetochore-microtubule attachment (H. Wang *et al.*, 2004; Kops *et al.*, 2005). Given no known role for STX19 in mitosis, it remains unclear why STX19 would interact with ZWINT. However, protein complexes at kinetochores have previously been reported to have moonlighting functions in membrane trafficking. The NRZ (Nag1, RINT-1, and ZW10) have been shown to act as a tethering complex in ER-to-Golgi trafficking. This complex interacts with STX18 to mediate vesicle docking (Tagaya *et al.*, 2014). Additionally, membrane trafficking components have been shown to have roles in proper formation of the outer kinetochore. SNAP29 has been shown to be essential in stabilising ZWINT association with the kinetochore and knockdown of SNAP29 results in the loss of ZWINT at kinetochores, ultimately impacting microtubule attachment to kinetochores (Morelli *et al.*, 2016a). ZWINT is also implicated in a number of epithelial cancers including breast, lung, colorectal, and hepatocellular cancers with gene upregulation correlating with poor prognosis (Ying *et al.*, 2018; Peng *et al.*, 2019; Yi *et al.*, 2020; Zhou, Shen and Zhang, 2020; Akabane *et al.*, 2021). Given that ZWINT was identified in yeast-two hybrid screens and was immunoprecipitated with STX19, we chose to investigate this interaction further to gain insight into why STX19 might interact with a kinetochore protein.

Dystonin (DST, also known as bullous pemphigoid antigen 1, BPAG1) was identified as a potential interactor of STX19 in both yeast-two hybrid screens and BioID assays. DST is a member of the spectraplakin protein family which are well known for their roles in cross linking actin fibres and microtubules to regulate various cellular processes such as polarisation, migration, cell division, and cell adhesion (Zhang, Yue and Wu, 2017). DST has a number of isoforms including a neuronal-specific isoform, a muscle-specific isoform, and an epithelial-specific isoform (Ali *et al.*, 2017). The epithelial-specific isoform localises to hemidesmosomes in keratinocytes which attach cells to the basal lamina and has roles in restricting keratinocyte migration and maintaining keratinocyte polarisation (Hamill *et al.*, 2009; Michael *et al.*, 2014). Mutations in this isoform give rise to the skin blistering disease, Epidermolysis Bullosa (Pulkkinen and Uitto, 1998; Ali *et al.*, 2017). Spectraplakin proteins have also been shown to link actin filaments to microtubules in close proximity of focal adhesions to co-ordinate polarised exocytic trafficking. There is growing evidence that small GTPases regulate vesicle delivery to enriched sites of exocytosis at focal adhesions however, it remains unclear how vesicle fusion machinery is recruited to these sites (Grigoriev *et al.*, 2007; Fourriere *et al.*, 2019). We hypothesised that DST acts a cytoskeletal linker to target vesicle delivery to enriched sites of exocytosis and a scaffold to recruit the necessary fusion machinery including STX19. To investigate this hypothesis, we chose to further validate and characterise the potential interaction between STX19 and DST.

To further characterise the interactions of shortlisted proteins, we used two different mitochondrial re-routing cell-based assays, a knocksideways assay and a mitochondrial targeting assay. These assays allowed the efficient and cost-effective study of protein-protein interactions in a more physiologically relevant setting. The mitochondria are a suitable candidate for re-routing studies as it has well-defined protein target signals, a large membrane area ideal for housing exogenous proteins, and insertion of exogenous proteins does not affect mitochondrial function (Robinson, Sahlender and Foster, 2010). Both of our methods re-route overexpressed STX19 to the mitochondria however, the mechanism of re-routing differs. We can determine if STX19 interacts with another protein by co-expressing the potential interactor or probing for the endogenous protein with an antibody. If interaction with STX19 occurs, the potential interactor should also localise to the mitochondria (providing its endogenous localisation is not mitochondrial) following STX19 re-routing.

The knocksideways assay was originally developed to cause rapid inactivation of proteins as a means to study protein function (Robinson, Sahlender and Foster, 2010). Robinson et al., used the knocksideways assay to inactivate AP-1 thus highlighting its role in retrograde trafficking. Transfection of three constructs is required for studying protein interaction using the knocksideways assay. A) a Pmito construct consisting of the import signal of the yeast mitochondrial outer membrane protein,

Tom70p, which inserts the targets the construct to the mitochondria, followed by an mCherry tag for visualisation, and an FRB domain. B) a protein of interest conjugated to an FKBP tag. C) a potential interacting protein construct (or antibody raised against the potential interactor). Under normal circumstances, the FRB and FKBP domains do not interact. However, upon rapamycin treatment, both tags interact with the rapamycin molecules which re-routes the protein of interest to the mitochondria (depicted in figure 3-2). Should the co-transfected potential interactor also re-route to the mitochondria post-rapamycin treatment, we can determine this is via interaction with the protein of interest.

We also made use of a mitochondrial-targeting assay in which the protein of interest can be re-routed or targeted to the mitochondria without rapamycin treatment. In this assay, the membrane target sequence of the protein of interest is removed so that it no longer localises to the membranes it would usually reside on (unless cytoplasmic) and is conjugated to the C-terminal transmembrane domain of monoamine oxidase (MAO) – a mitochondrial-localised enzyme. This domain contains the mitochondrial target sequence for MAO and effectively targets the protein of interest to the mitochondria. Re-routing using this method has been successfully tested for numerous members of the Ras protein superfamily (Gillingham *et al.*, 2019).

3.1.1 Chapter aims

Our aim for this research was to gain insight into the function of STX19 by investigating its protein-protein interactions. We sought to achieve this aim by:

1. Validating the mitochondrial re-routing assays as useful cell-based tools for studying protein-protein interactions.
2. Characterising STX19 interactions with shortlisted candidates from biochemical interaction screens using mitochondrial re-routing assays.

3.1.2 Summary of results

Through our efforts using mitochondrial re-routing assays to study protein-protein interactions, we found that Munc18-2 is re-routed to the mitochondria through an interaction with STX19. This interaction takes place at an N-terminal KDR motif in STX19. Overexpression of STX19 results in the re-localisation of Munc18-2 from the cytoplasm to the plasma membrane and tubular recycling endosomes (TREs). Mutation in the KDR motif abolished Munc18-2 re-localisation to membranes demonstrating that the KDR motif of STX19 is responsible for Munc18-2 recruitment. Munc18-1 was also re-routed to the mitochondria through interaction with STX19, however it was not recruited to STX19 membranes upon STX19 overexpression. This suggests that whilst both Munc18-1 and -2 have

the ability to bind STX19, it is likely the interaction with Munc18-2 is most physiologically relevant. We have also shown that ZWINT interacts with STX19 however, this interaction only takes place when STX19 is present on membranes rather than when STX19 is targeted to the mitochondria. Overexpression of STX19 and ZWINT demonstrate co-localisation at distinct domains of the plasma membrane. These data suggest that STX19 and ZWINT are interacting partners and their interaction takes place at the plasma membrane. Finally, we were able to demonstrate interaction between DST and STX19 using the knocksideways assay. We also found that DST is re-routed to the mitochondria through interaction with STX16-mito.

3.2 Results

3.2.1 STX19 mitochondrial re-routing in the knocksideways assay

To first demonstrate how the knocksideways system works, we transfected HeLaM cells with FKBP-GFP and Pmito. 24 hours post-transfection, cells were treated with 1 µg/mL rapamycin to induce re-routing. Untreated cells were used as a negative control. In untreated cells, FKBP-GFP displayed a nuclear and cytoplasmic localisation, whilst Pmito labelled the mitochondria. There was no co-localisation of the two constructs (figure 3-3A). Following rapamycin treatment, FKBP-GFP was effectively re-routed to the mitochondria as cells displayed a classic mitochondrial staining pattern that co-localised with Pmito (figure 3-3B). This demonstrates that our knocksideways protocol was successful in re-routing FKBP-tagged GFP to the mitochondria upon rapamycin treatment.

In order to re-route STX19 to the mitochondria using the knocksideways assay, we made use of two STX19 constructs generated previously in the lab. Both constructs contain an FKBP tag for re-routing and a myc tag for visualisation. One construct includes a truncated version of STX19 lacking the C-terminal S-acylation domain (FKBP-myc-STX19$^{1-272}$). This construct is cytoplasmic as it was lacking the domain that targets STX19 to membranes. The second includes the full length STX19 (FKBP-myc-STX19$^{1-294}$) which localises to tubular recycling endosomes (TREs) and the plasma membrane.

To test if the STX19 constructs are re-routed to the mitochondria using the knocksideways assay, HeLaM cells were co-transfected with Pmito and either FKBP-myc-STX19$^{1-272}$ or FKBP-myc-STX19$^{1-294}$. 24 hours post-transfection, cells were treated with 1 µg/mL rapamycin to induce re-routing to the mitochondria. Untreated cells were used as a negative control.

We first assessed re-routing of the truncated FKBP-myc-STX19$^{1-272}$ construct. In untreated cells expressing FKBP-myc-STX19$^{1-272}$ and Pmito, FKBP-myc-STX19$^{1-272}$ displayed cytoplasmic staining which appears to be enriched towards the plasma membrane but not predicted to be associated with the membrane itself. Pmito displays a mitochondrial staining pattern that did not co-localise with FKBP-

myc-STX19$^{1-272}$ (figure 3-4A). Following rapamycin treatment, FKBP-myc-STX19$^{1-272}$ displays a mitochondrial staining pattern. Pmito also labelled the mitochondria. Pmito and FKBP-myc-STX19$^{1-272}$ demonstrate good co-localisation at the mitochondria (figure 3-4B). Therefore, upon treatment with rapamycin, FKBP-myc-STX19$^{1-272}$ is successfully re-routed to the mitochondria. The FKBP-myc-STX19$^{1-272}$ mitochondrial staining appeared to be granular in comparison to the smooth labelling of Pmito. It would be tempting to speculate that the granular cytoplasmic staining prior to rapamycin treatment may be the labelling of STX19-positive vesicles and upon rapamycin treatment, the vesicles are re-routed to the mitochondria. This, however, would require additional investigation.

To understand if STX19 that is associated with membranes can be re-routed to the mitochondria, we used our full length FKBP-myc-STX19$^{1-294}$ construct in the knocksideways assay. In untreated cells transfected with FKBP-myc-STX19$^{1-294}$ and Pmito, FKBP-myc-STX19$^{1-294}$ localises to TREs and the plasma membrane. There is also a punctate staining pattern in the cytoplasm. We could speculate the puncta are STX19-positive vesicles or trafficking compartments, but no experiments were conducted to confirm this. Nevertheless, the TRE and plasma membrane staining is representative of overexpressed STX19 staining. Pmito displayed a classic mitochondrial staining pattern which did not co-localise with FKBP-myc-STX19$^{1-294}$ (figure 3-5A). Following treatment with rapamycin, FKBP-myc-STX19$^{1-294}$ staining was lost from TREs and the plasma membrane. Instead, FKBP-myc-STX19$^{1-294}$ displayed a punctate pattern distributed throughout the cytoplasm largely towards the periphery of the cell. This was not consistent with the classic mitochondrial staining pattern demonstrated by FKBP-GFP after rapamycin treatment. Pmito did demonstrate mitochondrial localisation however, Pmito was also present in the STX19 puncta towards the periphery of the cell (figure 3-5B).

Since there was no clear mitochondrial staining from FKBP-myc-STX19$^{1-294}$, we can determine that FKBP-myc-STX19$^{1-294}$ is not re-routed to the mitochondria in the knocksideways system. However, FKBP-myc-STX19$^{1-294}$ includes the STX19 C-terminal S-acylation domain which targets the proteins to TREs and the plasma membrane. Therefore, we reasoned that instead of re-routing STX19 to the mitochondria, STX19 is pulled out of microdomains at the plasma membrane and forms clusters with mitochondria under the cell surface. STX19 is still in contact with the mitochondria but the mitochondria have been pulled towards the plasma membrane.

Overall, we have demonstrated that STX19 can be re-routed to the mitochondria using the knocksideways assay but only when the protein lacks its C-terminal S-acylation domain. Use of the full length STX19 protein in this assay results in an unusual phenotype of STX19 and Pmito-positive clusters most likely at the cell surface. These data have been published (Ampah *et al.*, 2018).

3.2.2 STX19 mitochondrial re-routing using the monoamine oxidase (MAO) C-terminal transmembrane domain

In order to simplify our cell-based interaction assays, we set out to determine if STX19 can be targeted to the mitochondria by the MAO transmembrane domain. Compared to the knocksideways assay, this assay requires transfection of less constructs and does not require rapamycin treatment. We generated a construct (STX19-mito) using a pcDNA3.1+ vector backbone containing STX19 lacking the C-terminal S-acylation domain ($STX19^{1-272}$), a HA tag for visualisation, and the MAO C-terminal transmembrane domain. The C-terminal S-acylation domain of STX19 was omitted from this construct to prevent targeting to TREs and the plasma membrane and allow efficient mitochondrial re-routing. A STX16-mito construct was used as a negative control as STX16 is not predicted to interact with any of the shortlisted proteins we were investigating. This construct includes STX16 lacking its C-terminal transmembrane domain, a HA tag, and the MAO transmembrane domain. The construct was kindly provided by Prof. Sean Munro at the University of Cambridge. Schematics of the STX19-mito and STX16-mito constructs are depicted in figure 3-6A.

To assess the localisation of STX19-mito, the construct was expressed in HeLaM cells. Cells were co-stained with anti-HA mouse antibodies and anti-STX19 rabbit antibodies. Staining for the HA tag demonstrates localisation of the construct to the mitochondria and staining for STX19 demonstrates STX19 is present in the construct and has not been lost or degraded.

Upon analysis of transfected cells, the anti-HA labelling demonstrated a mitochondrial staining pattern which smoothly labelled the mitochondria with very little cytoplasmic staining suggesting that the STX19-mito construct is effectively targeted to mitochondria. Anti-STX19 labelling also demonstrated a mitochondrial staining pattern that co-localises with the anti-HA stain. In addition, there was puncta in the anti-STX19 stain that did not label the mitochondria and was not present in the anti-HA labelling. We presume that these puncta are either the endogenous STX19 protein or non-specific staining of the anti-STX19 antibody (figure 3-6B).

Based on these data, we can determine that the STX19-mito construct effectively targets STX19 to the mitochondria.

3.2.3 Validating STX19 interaction with Munc18 proteins

To determine if mitochondrial re-routing assays are useful for studying protein-protein interactions, we set out to investigate if Munc18 proteins are re-routed to the mitochondria through interaction with STX19. Munc18 proteins are well-known regulators of SNARE function and biochemical analysis predicted that Munc18-1 and Munc18-2, but not Munc18-3, interact with STX19. Based on this, we

were confident these interactions were genuine and therefore, chose Munc18 proteins as candidates to test if interacting proteins are also re-routed to the mitochondria in our assays. We predicted that Munc18-1 and Munc18-2 would re-route to the mitochondria via interaction with STX19, but Munc18-3 would not interact with STX19 and not re-route to the mitochondria.

3.2.3.1 Knocksideways assay with Munc18 proteins

First, we used the knocksideways assay to re-route STX19 to the mitochondria and determine if Munc18-1, -2, and -3 are also re-routed. We chose to use the truncated construct of STX19, (FKBP-myc-STX19$^{1-272}$ in these assays based on our previous observations that this construct is efficiently re-routed to the mitochondria. Overexpression of Munc18 proteins was used due to the limited availability of reliable Munc18 antibodies. During experimental optimisation, we found that expressing the interacting protein at low levels was important to reduce the cytoplasmic pool of the protein. This enabled clear observation of mitochondrial re-routing of the interacting protein.

3.2.3.1.1 GFP-Munc18-1 re-routes to the mitochondria with FKBP-myc-STX19$^{1-272}$

To determine if STX19 is able to re-route Munc18-1 to the mitochondria, HeLaM cells were transfected with Pmito, FKBP-myc-STX19$^{1-272}$, and GFP-Munc18-1. 24 hours post-transfection, cells were treated with 1 μg/mL rapamycin for 15 minutes before fixing and staining with anti-myc antibodies. Untreated cells were used as a negative control. In untreated cells, GFP-Munc18-1 and FKBP-myc-STX19$^{1-272}$ localise to the cytoplasm and Pmito localises to the mitochondria (figure 3-7A). Line scan analysis demonstrates no co-localisation between the constructs (figure 3-7C). In cells treated with rapamycin, GFP-Munc18-1 shows a pool of cytoplasmic staining as well as staining at the mitochondria. FKBP-myc-STX19$^{1-272}$ and Pmito are both localised to the mitochondria (figure 3-7B). Line scan analysis demonstrates co-localisation between all three constructs through correlating peaks of fluorescent intensity (figure 3-7D). These data suggest that GFP-Munc18-1 is re-routed to the mitochondria following rapamycin treatment through interaction with STX19.

3.2.3.1.2 GFP-Munc18-2 re-routes to the mitochondria with FKBP-myc-STX19$^{1-272}$

To determine if STX19 is able to re-route Munc18-2 to the mitochondria, HeLaM cells were transfected with Pmito, FKBP-myc-STX19$^{1-272}$, and GFP-Munc18-2. 24 hours post-transfection, cells were treated with 1 μg/mL rapamycin for 15 minutes before fixing and staining with anti-myc antibodies. Untreated cells were used as a negative control. In untreated cells, GFP-Munc18-2 and FKBP-myc-STX19$^{1-272}$ localise to the cytoplasm and Pmito localises to the mitochondria (figure 3-8A). Line scan analysis demonstrates no co-localisation between the constructs (figure 3-8C). In cells treated with rapamycin, GFP-Munc18-2, FKBP-myc-STX19$^{1-272}$ and Pmito localise to the mitochondria (figure 3-8B). Line scan

analysis demonstrates co-localisation between all three constructs through correlating peaks of fluorescent intensity (figure 3-8D). These data suggest that GFP-Munc18-2 is re-routed to the mitochondria following rapamycin treatment through interaction with STX19.

3.2.3.1.3 GFP-Munc18-3 does not re-route to the mitochondria with FKBP-myc-STX19$^{1-272}$

To determine if STX19 is able to re-route Munc18-3 to the mitochondria, HeLaM cells were transfected with Pmito, FKBP-myc-STX19$^{1-272}$, and GFP-Munc18-3. 24 hours post-transfection, cells were treated with 1 µg/mL rapamycin for 15 minutes before fixing and staining with anti-myc antibodies. Untreated cells were used as a negative control. In untreated cells, GFP-Munc18-3 and FKBP-myc-STX19$^{1-272}$ localise to the cytoplasm and Pmito localises to the mitochondria (figure 3-9A). Line scan analysis demonstrates no co-localisation between the constructs (figure 3-9C). In cells treated with rapamycin, GFP-Munc18-3 remains cytoplasmic whilst FKBP-myc-STX19$^{1-272}$ and Pmito localise to the mitochondria (figure 3-9B). Line scan analysis demonstrates co-localisation between FKBP-myc-STX19$^{1-272}$ and Pmito through correlating peaks of fluorescent intensity and no co-localisation with GFP-Munc18-3 (figure 3-9D). These data suggest that GFP-Munc18-3 does not re-route to the mitochondria and therefore, does not interact with STX19. This demonstrates that the knocksideways assay is a useful tool for studying protein-protein interactions as there is no non-specific re-routing of proteins that do not interact with the protein of interest to the mitochondria.

3.2.3.1.4 GFP-Munc18-2 is re-routed to the mitochondrial clusters with FKBP-myc-STX19$^{1-294}$

Our previous experiments suggested interaction between the truncated STX19 construct and Munc18-2. Subsequently, we aimed to determine if Munc18-2 was able to interact with the full length STX19 construct. To do so, HeLaM cells were transfected with Pmito, FKBP-myc-STX19$^{1-294}$, and GFP-Munc18-2. 24 hours post-transfection, cells were treated with 1 µg/mL rapamycin for 15 minutes before fixing and staining with anti-myc antibodies. Untreated cells were used as a negative control. In untreated cells, GFP-Munc18-2 shows a cytoplasmic/nuclear localisation, FKBP-myc-STX19$^{1-294}$ localises to the plasma membrane and displays a punctate staining pattern, and Pmito localises to the mitochondria (figure 3-10A). Line scan analysis demonstrates no co-localisation between the three constructs (figure 3-10C). Treatment with rapamycin results in the re-routing of GFP-Munc18-2 to puncta throughout the cytoplasm that co-localise with FKBP-myc-STX19$^{1-294}$ and Pmito (figure 3-10B). Co-localisation was supported by line scan analysis (figure 3-10D). We suggest that these puncta are the STX19/mitochondrial clusters that were induced following rapamycin treatment as described previously. There was a pool of cytoplasmic GFP-Munc18-2 suggesting that not re-routing is not 100 % efficient. Nevertheless, GFP-Munc18-2 was re-routed into STX19/mitochondrial clusters at the cell surface through interaction with STX19.

These data are in line with the knocksideways assay using the truncated FKBP-myc-STX19$^{1-272}$ construct. Therefore, Munc18-2 is able to interact with both the full-length STX19 protein that is associated with membranes and the truncated STX19 protein.

Overall, these data support STX19 interaction with Munc18-2 as predicted by biochemical analysis. This demonstrates that the knocksideways assay is a useful, cell-based tool to validate protein-protein interactions.

3.2.3.2 Mitochondrial targeting assay with Munc18 proteins

As the knocksideways assay proved to be useful in studying protein-protein interactions, we wanted to determine if the mitochondrial targeting assay was also a good strategy to study interaction. This assay is simpler than the knocksideways assay as it only requires transfection of two constructs and does not require rapamycin treatment. Therefore, it would be a more efficient method to study interaction than the knocksideways assay.

3.2.3.2.1 GFP-Munc18-1 and -2, but not GFP-Munc18-3, are re-routed to the mitochondria with STX19-mito

To determine if the mitochondrial targeting assay was able to re-route interacting proteins to the mitochondria, we performed similar experiments transfecting cells with either STX19-mito or STX16-mito and either GFP-Munc18-1, -2, or -3. STX16-mito was used a negative control as STX16 is regulated by SM protein, Vps45, and no interaction between STX16 and Munc18-1, -2, or -3 is predicted (Struthers *et al.*, 2009). Based on our previous experiments, we hypothesised that STX19-mito would be able to re-route Munc18-1 and Munc18-2, but not Munc18-3 to the mitochondria.

Upon co-transfection with STX19-mito, both GFP-Munc18-1 and GFP-Munc18-2 showed a mitochondrial localisation (figures 3-11A and 3-11C). Therefore, STX19-mito is able to re-route Munc18-1 and Munc18-2 to the mitochondria. This was supported by line scan analysis which shows correlating fluorescent intensity traces for both constructs. Co-transfection with STX16-mito did not re-route GFP-Munc18-1 or GFP-Munc18-2 to the mitochondria and both proteins displayed cytoplasmic localisation (figures 3-11B and 3-11D). Line scan analysis shows there is no co-localisation between STX16-mito and GFP-Munc18-1 or -2. This suggests that the mitochondrial re-routing of GFP-Munc18-1 and -2 occurs specifically through interaction with STX19.

Upon co-transfection with STX19-mito or STX16-mito, Munc18-3 demonstrated cytoplasmic localisation and was not re-routed to the mitochondria. Line scan analysis shows no co-localisation with STX19-mito/STX16-mito and GFP-Munc18-3 (figures 3-11E and 3-11F). These data were in line with biochemical analysis and previous knocksideways experiments suggesting that Munc18-3 does

not interact with STX19. This validates the use of the mitochondrial targeting assay as it does not re-route non-interacting proteins to the mitochondria.

Mitochondrial re-routing of GFP-Munc18-1, -2, and -3 was quantified by counting the number of cells that were A) transfected with both STX19-mito or STX16-mito and GFP-Munc18-1, -2, or -3 and B) demonstrated mitochondrial re-routing of the Munc18 proteins (figure 3-11G). The number of cells showing re-routing was expressed as a percentage of the total number of transfected cells. GFP-Munc18-1, -2, and -3 demonstrated mitochondrial re-routing in 95, 93, and 18 % of cells transfected with STX19-mito respectively. 0 % of cells transfected with either GFP-Munc18-1, -2, or -3 and STX16-mito demonstrated mitochondrial re-routing. These data show that a large proportion of cells transfected with STX19-mito are able to re-route protein interactors to the mitochondria validating the use of this assay for studying protein-protein interactions. 18 % of cells demonstrated re-routing with Munc18-3, is it likely that Munc18-3 does have the ability to interact with STX19 despite no previous predicted interaction. However, the percentage of cells with Munc18-3 re-routing is lower than that of Munc18-1 and Munc18-2 suggesting the interaction is weaker and likely not physiologically relevant. Additionally, statistical analysis suggested no significance between the number of cells with Munc18-3 re-routing between STX19-mito and STX16-mito transfected samples. At very low levels of expression, it can be difficult to determine true mitochondrial staining by eye. An automated pipeline to identify mitochondrial staining using a mitochondrial marker and quantify the number of cells may provide more precise measurements.

Altogether, these data suggest that the mitochondrial targeting assay is able to re-route interacting proteins to the mitochondria through interaction with the bait protein making it a useful tool for studying protein-protein interactions. As predicted, STX19-mito re-routed GFP-Munc18-1 and GFP-Munc18-2, but not GFP-Munc18-3 to the mitochondria further supporting STX19 interaction with Munc18-1 and Munc18-2.

3.2.3.3 Overexpressed STX19 recruits Munc18-2 to tubular recycling endosomes (TREs).

As mitochondrially-targeted STX19 is able to re-route Munc18 proteins to the mitochondria, we next asked the question if STX19 would be able to recruit Munc18-1 and Munc18-2 to membranes, specifically TREs. Investigating if STX19 is able to recruit Munc18 proteins will determine if binding of Munc18 proteins to STX19 can take place at membranes and may provide insight into the regulatory mechanisms of STX19 function. When Munc18 proteins are expressed alone, they are cytoplasmic suggesting the levels of SNARE interacting partners are too low to recruit Munc18 proteins to membranes. However, overexpression increases protein levels, therefore, we hypothesised that

overexpression of STX19 and Munc18 proteins would induce recruitment of interacting Munc18 proteins to membranes.

To address this, we overexpressed HA-tagged STX19 and GFP-tagged Munc18-1, Munc18-2, or Munc18-3 in HeLaM cells and analysed their localisation. As expected, STX19 localises to TREs and the plasma membrane. GFP-Munc18-1 did not co-localise with HA-STX19 and localises to the cytoplasm (figure 3-12A). Line scan analysis suggests there is no co-localisation between HA-STX19 and GFP-Munc18-1 (figure 3-12D). Similarly, GFP-Munc18-3 localises to the cytoplasm and did not co-localise with STX19 on TREs (figure 3-12C). Line scan analysis suggests there is no co-localisation between HA-STX19 and GFP-Munc18-3 (figure 3-12F). Upon co-expression with STX19, GFP-Munc18-2, shows localisation on TREs and the plasma membrane (figure 3-12B). Line scan analysis supports co-localisation of the two proteins through correlating fluorescent intensity traces (figure 3-12E).

Quantification of the number of cells with Munc18 membrane recruitment was performed in a similar fashion to the STX19-mito experiments. The number of cells expressing both GFP-Munc18-1, -2, or -3 and HA-STX19 were counted and the percentage of these cells demonstrating GFP-Munc18 localisation to STX19-positive TREs was determined. Cells expressing GFP-Munc18-1, -2, or -3 exhibited STX19-positive TRE localisation in 18, 92, and 0 % of cells transfected with HA-STX19 respectively (figure 3-12G). This suggests that a large proportion of cells transfected with HA-STX19 show Munc18-2 localisation on TREs suggesting that the STX19 is able to recruit Munc18-2 to specific membranes. The cells with Munc18-1 localisation to TREs could also indicate recruitment by STX19 however, this may be non-specific due to overexpression.

These data suggest that STX19 overexpression recruits Munc18-2 to TREs and the plasma membrane. Both Munc18-1 and Munc18-2 were shown to interact with STX19 in mitochondrial re-routing experiments. However, the proportion of cells with Munc18-2 recruitment to TREs is much greater compared to Munc18-1. This suggests that the interaction between STX19 and Munc18-2 is physiologically relevant, and it is likely that Munc18-2 but not Munc18-1 is involved in the functional regulation of STX19.

3.2.3.4 Mapping the interaction between STX19 and Munc18-2

As previous experiments demonstrated that mitochondrial re-routing is a useful tool for demonstrating protein-protein interactions, we questioned if these assays could be used to further characterise the interactions by mapping the domains of STX19 with which Munc18-2 interacts. We hypothesised that if the site of interaction on STX19 is altered, STX19-mito mutant constructs would no longer be able to re-route the interacting protein to the mitochondria. This led to the development

of two additional STX19-mito constructs: STX19-mito$^{\Delta 219\text{-}294}$, and STX19-mito$^{KDR\text{-}AAA}$ (figure 3-14A). The STX19-mito$^{\Delta 219\text{-}294}$ construct lacks the coiled-coil SNARE domain. This domain is highly conserved in SNARE proteins and is well known for its interaction with other proteins particularly SNAREs. There are no previous reports of Munc18 proteins interacting with SNARE domains and as such, we used this construct as a control. STX19-mito$^{KDR\text{-}AAA}$ contains a mutation in an N-terminal KDR motif (amino acids 2-4). This KDR motif is well conserved across STX1A, 1B, 3, and 19, whilst STX2 and 4 have an RDR motif (figure 3-13A). The KDR motif in STX19 is also conserved across several species including monkey and mouse, with the exception of chicken which contains an RDR motif. (figure 3-13B). Munc18-2 has previously been shown to interact with STX11 via this KDR motif (Müller *et al.*, 2014). Since STX11 shares high homology with STX19, we predicted that Munc18-2 would also bind STX19 at the N-terminal KDR motif and as such, the STX19-mito$^{KDR\text{-}AAA}$ construct would no longer re-route Munc18-2 to the mitochondria. To address this hypothesis, HeLaM cells transfected with either STX19-mito (original construct with no mutations), STX19-mito$^{\Delta 219\text{-}294}$ or STX19-mito$^{KDR\text{-}AAA}$ and GFP-Munc18-2.

As a positive control, HeLaM cells were transfected with STX19-mito and GFP-Munc18-2. STX19-mito and GFP-Munc18-2 both localise to the mitochondria (figure 3-14B). This was supported by line scan analysis which shows correlation between the fluorescent intensity traces for both constructs. Therefore, this suggests that GFP-Munc18-2 is re-routed to the mitochondria through interaction with STX19-mito.

To determine if the SNARE domain of STX19 is the site of Munc18-2 interaction, HeLaM cells were transfected with STX19-mito$^{\Delta 219\text{-}294}$ and GFP-Munc18-2. Both STX19-mito$^{\Delta 219\text{-}294}$ and GFP-Munc18-2 localise to the mitochondria (figure 3-14C). Co-localisation at the mitochondria was supported by line scan analysis which showed correlation between the two fluorescent intensity traces. Therefore, this suggests that STX19-mito$^{\Delta 219\text{-}294}$ is able to re-route GFP-Munc18-2 to the mitochondria and the SNARE domain of STX19 is not the site of interaction for Munc18-2.

To determine if the N-terminal KDR motif is the site of Munc18-2 interaction, HeLaM cells were transfected with STX19-mito$^{KDR\text{-}AAA}$ and GFP-Munc18-2. STX19-mito$^{KDR\text{-}AAA}$ localises to the mitochondria and GFP-Munc18-2 localises to the cytoplasm (figure 3-16D). The line scan analysis suggests no co-localisation between STX19-mito$^{KDR\text{-}AAA}$ and GFP-Munc18-2. Therefore, STX19-mito$^{KDR\text{-}AAA}$ was unable to re-route GFP-Munc18-2 to the mitochondria. This suggests that the N-terminal KDR motif of STX19 is the site of interaction for GFP-Munc18-2.

The number of cells co-expressing the STX19-mito constructs and GFP-Munc18-2 and demonstrating GFP-Munc18-2 mitochondrial re-routing was quantified. The percentage of cells with GFP-Munc18-2

re-routing in cells expressing STX19-mito, STX19-mito$^{KDR-AAA}$, and STX19-mito$^{\Delta 219-294}$ was 92, 98, and 1.5 % cells respectively (figure 3-14E).

Overall, these data suggests that use of mutant constructs in combination with mitochondrial re-routing is effective for mapping domains of interaction. Using this method, we have identified an N-terminal KDR motif which is responsible for the interaction of STX19 and Munc18-2.

3.2.3.5 The N-terminal KDR motif of STX19 recruits Munc18-2 to membranes

Our previous data have suggested that STX19-mito is able to re-route Munc18-2 via interaction with the STX19 N-terminal KDR motif. Our data also suggests that overexpression of STX19 recruits Munc18-2 to the plasma membrane and TREs. We therefore sought to determine if the KDR motif of STX19 is responsible for the interaction that recruits Munc18-2 to specific membranes. To do so, HeLaM cells were transfected with a KDR-AAA mutant HA-STX19 construct (HA-STX19$^{KDR-AAA}$) and GFP-Munc18-2. HA-STX19$^{KDR-AAA}$ localises to the plasma membrane and TREs, however, GFP-Munc18-2 demonstrates a cytoplasmic localisation and is not recruited to membranes (figure 3-15A). Line scan analysis suggests no co-localisation between the two proteins (figure 3-15B). Therefore, this suggests that the KDR motif of STX19 is the site of interaction with Munc18-2 required for its recruitment to the plasma membrane and TREs. This supports our hypothesis that Munc18-2 is the most likely Munc18 protein to regulate STX19 function through its interaction with the KDR motif.

3.2.4 Investigating STX19 interaction with kinetochore protein, ZWINT

ZWINT was identified as an interactor of STX19 through yeast-two hybrid screening, BioID analysis and is listed as an interactor on BioGRID. ZWINT was also pulled down with STX19, but not STX7, in previous co-immunoprecipitation experiments. ZWINT is a small 277 amino acid protein which contains a coiled-coil domain and an ZW10 interaction domain (figure 3-16). Given that ZWINT has a documented role in kinetochore-microtubule attachment through its ZW10 interaction domain, it is unclear why ZWINT would interact with STX19. Therefore, we aimed to further validate and characterise this interaction using our mitochondrial re-routing assays.

3.2.4.1 ZWINT interacts with full-length STX19

Firstly, we used the knocksideways assay to determine if interaction with STX19 was able to re-route ZWINT to the mitochondria. FKBP-myc-STX19$^{1-272}$ or FKBP-myc-STX19$^{1-294}$ and Pmito were co-transfected into HeLaM cells. 24 hours post-transfection, cells were treated with 1 µg/mL rapamycin for 15 minutes before fixation. Untreated cells were used as a negative control. Cells were stained with anti-myc and anti-ZWINT antibodies to assess the localisation of endogenous ZWINT.

In untreated cells, ZWINT and FKBP-myc-STX19$^{1-272}$ localise to the cytoplasm and Pmito localises to the mitochondria (figure 3-17A). Line scan analysis suggests there is no co-localisation between FKBP-myc-STX19$^{1-272}$, Pmito and ZWINT (figure 3-17C). Following rapamycin treatment, FKBP-myc-STX19$^{1-272}$ re-routes to the mitochondria and co-localises with Pmito as expected. Surprisingly, ZWINT is not re-routed to the mitochondria and remains cytoplasmic (figure 3-17B). Line scan analysis suggests that there is co-localisation between FKBP-myc-STX19$^{1-272}$ and Pmito, but not with ZWINT (figure 3-17D). These data suggest that FKBP-myc-STX19$^{1-272}$ does not interact with ZWINT and is unable to re-route ZWINT to the mitochondria.

Additionally, we performed the knocksideways assay using the full length FKBP-myc-STX19$^{1-294}$ construct to determine if ZWINT interacts with STX19 that is associated with membranes. In untreated cells, FKBP-myc-STX19$^{1-294}$ localises to the plasma membrane and TREs and Pmito localises to the mitochondria. ZWINT showed two differing patterns of localisation. In some cells, ZWINT localises to the cytoplasm. However, in other cells, ZWINT was localised to the nucleus and large puncta in the cytoplasm (figure 18-A). No experiments were carried out to determine the identity of the puncta and co-staining with different markers would be required. We found that analysing cells with different staining patterns did not affect the outcome of the experiment. Line scan analysis suggests there is no co-localisation between FKBP-myc-STX19$^{1-294}$, Pmito, and ZWINT (figure 3-18C). Following rapamycin treatment, FKBP-myc-STX19$^{1-294}$ localises to puncta distributed at the plasma membrane. A pool of Pmito remains at the mitochondria however, there is also a pool of Pmito co-localised with FKBP-myc-STX19$^{1-294}$ puncta. Therefore, treatment with rapamycin induces STX19/mitochondrial clusters at the cell surface as seen with previous experiments. A pool of ZWINT staining remains at the nucleus and cytoplasm. However, ZWINT also localises to FKBP-myc-STX19$^{1-294}$ and Pmito puncta (figure 3-18B). Line scan analysis suggests co-localisation of FKBP-myc-STX19$^{1-294}$, Pmito and ZWINT at these puncta (figure 3-18D). These data suggest that the ZWINT puncta seen without rapamycin treatment are not the same puncta that co-localise with FKBP-myc-STX19$^{1-294}$ and Pmito after treatment. Prior to treatment, the puncta are larger in size and smaller in number than the puncta seen in cells that were treated with rapamycin. This suggests that after rapamycin treatment, STX19 is able to re-route ZWINT into STX19/mitochondrial clusters at the cell surface and provides evidence towards the interaction between STX19 and ZWINT.

Overall, these data suggest that STX19 is only able to interact with ZWINT when it localises to membranes. ZWINT is not re-routed to the mitochondria in assays using the truncated version of STX19 however, it is pulled into STX19/mitochondrial clusters in assays using the full-length STX19.

3.2.4.2 Endogenous ZWINT does not re-route to the mitochondria with STX19-mito

Our knocksideways assay showed varying results depending on the presence of the C-terminal S-acylation domain on STX19. STX19 constructs lacking the S-acylation domain failed to re-route ZWINT to the mitochondria. To confirm that ZWINT does not interact with STX19 lacking this domain, we assessed the interaction using the mitochondrial targeting STX19-mito assay. HeLaM cells were co-transfected with either STX19-mito or STX16-mito and stained with anti-HA to detect STX19-mito/STX16-mito and anti-ZWINT antibodies to assess the localisation of endogenous ZWINT. STX16-mito was used as a negative control as STX16 is not predicted to interact with ZWINT. Since the STX19-mito construct lacks the C-terminal S-acylation domain, we predicted that ZWINT would not re-route to the mitochondria.

Both STX19-mito and STX16-mito localise to the mitochondria. In cells expressing STX19-mito, ZWINT localises to the cytoplasm (figure 3-19A). Line scan analysis suggests no co-localisation between STX19-mito and ZWINT (figure 3-19C). In cells expressing STX16-mito, ZWINT localises to the cytoplasm. As expected, there was no mitochondrial localisation of ZWINT in these cells (figure 3-19B). Line scan analysis suggests no co-localisation between STX16-mito and ZWINT (figure 3-19D). These data support our earlier finding using the knocksideways assay and suggest that ZWINT does not interact with STX19 lacking the C-terminal S-acylation domain.

3.2.4.3 Overexpressed ZWINT pulls STX19-mito to the plasma membrane

To further explore the potential interaction between STX19 and ZWINT, we decided to overexpress a FLAG-tagged ZWINT construct. ZWINT-FLAG localises to the cytoplasm and regions of the plasma membrane, particularly membrane protrusions. The ZWINT antibody previously used did not show plasma membrane staining. Therefore, we reasoned that the ZWINT-FLAG construct may be highlighting a pool of ZWINT localisation that is not seen by the antibody. Since STX19 also localises to the plasma membrane including in membrane protrusions, we hypothesised that ZWINT-FLAG may interact with STX19 at the plasma membrane and so carried out mitochondrial targeting STX19-mito assays with ZWINT-FLAG.

HeLaM cells were co-transfected with either STX19-mito or STX16-mito and ZWINT-FLAG. Cells were then fixed and stained with anti-HA and anti-FLAG antibodies. In cells expressing STX19-mito, ZWINT-FLAG shows a plasma membrane localisation. STX19-mito localises to the mitochondria and to regions of the plasma membrane highlighted by the insert (figure 3-20A). Line scan analysis suggests co-localisation of STX19-mito and ZWINT-FLAG at the plasma membrane (figure 3-20C). In cells expressing STX16-mito, ZWINT-FLAG localises to the plasma membrane and the cytoplasm and STX16-mito

localises to the mitochondria. There is no localisation of STX16-mito at the plasma membrane or co-localisation with ZWINT-FLAG as confirmed by line scan analysis (figure 3-20B and 3-20D).

Overall, these data suggest that ZWINT-FLAG is able to interact with STX19-mito and pull it, along with mitochondria it is associated with, onto the plasma membrane. As STX16-mito is not pulled to the plasma membrane upon co-transfection with ZWINT-FLAG, it is likely that membrane localisation of STX19-mito is specific to its interaction with ZWINT.

3.2.4.4 HA-STX19 co-localises with ZWINT-FLAG at distinct domains of the plasma membrane

We had seen previously that ZWINT-FLAG localises to the plasma membrane and is enriched in membrane protrusions. Overexpressing STX19 also results in STX19 localisation at the plasma membrane. We therefore questioned if overexpressed STX19 and ZWINT-FLAG are localised to similar regions of the plasma membrane. To address this, HeLaM cells were transfected with HA-STX19 and ZWINT-FLAG. Cells were then fixed and stained with anti-HA and anti-FLAG antibodies.

Upon co-expression of the two constructs, we found that ZWINT-FLAG and HA-STX19 are localised the same regions of the plasma membrane, highlighted by the insert (figure 3-21A) Line scan analysis suggests co-localisation between HA-STX19 and ZWINT-FLAG (figure 3-21C). HA-STX19 also localises to TREs however, there is no localisation of ZWINT-FLAG to TREs. Both HA-STX19 and ZWINT-FLAG also localise to similar puncta within the cytoplasm.

Both ZWINT and STX19 have coiled-coil domains which could be a site of interaction. We therefore questioned if the removal of the coiled-coil SNARE domain of STX19 would affect its co-localisation with ZWINT-FLAG on membranes. To address this HeLaM cells were transfected with HA-STX19$^{\Delta 218\text{-}272}$, a STX19 construct in which the SNARE domain is removed, and ZWINT-FLAG. Cells were then fixed and stained with anti-HA and anti-FLAG antibodies.

ZWINT-FLAG and HA-STX19$^{\Delta 218\text{-}272}$ localise to regions of the plasma membrane as highlighted by the insert (figure 3-21B). Line scan analysis suggests co-localisation between HA-STX19$^{\Delta 218\text{-}272}$ and ZWINT-FLAG (figure 3-21D). ZWINT-FLAG does not appear to localise to STX19-positive puncta however, this would require more thorough investigation. This shows that the lack of the SNARE domain of STX19 does not affect localisation of STX19 or ZWINT-FLAG.

Based on these data and the mitochondrial re-routing data suggesting STX19 interaction with ZWINT, we predict that ZWINT is a genuine interactor of STX19 and the function of this interaction occurs at the plasma membrane.

3.2.5 Investigating STX19 interaction with spectraplakin, DST

Dystonin (DST) was identified to be an interactor of STX19 in both yeast-two hybrid screens and BioID assays. DST is a large spectraplakin protein (~6000 – 7000 amino acids depending on splice variant), consisting of multiple domains and binding sites. At the N-terminal, calponin homology domains facilitate binding to actin, whilst a C-terminal GAR domain and SXIP motif facilitate binding to microtubules. DST also contains a number of spectrin repeats which serve as spacers between actin-binding and microtubule-binding domains, as well as functioning as a platform for the binding of structural and signalling proteins (figure 3-22). Yeast-two hybrid screening uncovered 4 clones of DST predicted to interact with STX19 which are mapped onto the DST schematic in figure 3-22. Due to the lack of reliable antibodies and difficulty transfecting full-length DST due to its large size, we generated a GFP-tagged construct using one of the clones (clone 4; GFP-DST). This construct was used in the mitochondrial re-routing assays to study its interaction with STX19. Based on the biochemical screening data, we predicted that STX19 would interact with GFP-DST and this interaction would re-route GFP-DST to the mitochondria in our mitochondrial re-routing assays.

3.2.5.1 Knocksideways assays suggest interaction between STX19 and DST

To determine if STX19 interacts with DST, we performed knocksideways assays to assess if GFP-DST is re-routed to the mitochondria through interaction with STX19. HeLaM cells were co-transfected with GFP-DST, FKBP-myc-STX19$^{1-272}$, and Pmito. 24 hours post-transfection, cells were treated with 1 µg/mL rapamycin. Cells were then fixed and stained with anti-myc antibodies. Untreated cells were used as a negative control.

In untreated cells, GFP-DST localises to the cytoplasm, though there appears to be an enrichment by the plasma membrane. FKBP-myc-STX19$^{1-272}$ localises to the cytoplasm but also seems to be enriched by the plasma membrane in similar locations to GFP-DST. Pmito localises to the mitochondria (figure 3-23A). Line scan analysis suggests no co-localisation between GFP-DST, FKBP-myc-STX19$^{1-272}$, and Pmito (figure 3-23C). Following rapamycin treatment, FKBP-myc-STX19$^{1-272}$, GFP-DST, and Pmito localise to the mitochondria, though the mitochondria do appear fragmented (figure 3-23B). Line scan analysis suggests co-localisation between GFP-DST, FKBP-myc-STX19$^{1-272}$, and Pmito (figure 3-23D). These data suggest that GFP-DST is re-routed to the mitochondria through interaction with STX19.

As our data suggests that the truncated STX19 construct may interact with GFP-DST, we questioned if full length STX19 which is associated with membranes could interact with GFP-DST. To address this, HeLaM cells were transfected with FKBP-myc-STX19$^{1-294}$, GFP-DST, and Pmito. 24 hours post-

transfection, cells were treated with 1 μg/mL rapamycin. Cells were then fixed and stained with anti-myc antibodies. Untreated cells were used as a negative control.

In untreated cells, GFP-DST localises to the cytoplasm, FKBP-myc-STX19$^{1-294}$ to the plasma membrane and has a punctate staining pattern. Pmito localises to the mitochondria (figure 3-24A). Line scan analysis suggests no co-localisation between GFP-DST, FKBP-myc-STX19$^{1-294}$, and Pmito (figure 3-24C). Following rapamycin treatment, FKBP-myc-STX19$^{1-294}$ and Pmito localise to STX19/mitochondrial clusters. GFP-DST also shows localisation in these structures and the cytoplasm (figure 3-24B). Line scan analysis suggests co-localisation of GFP-DST, FKBP-myc-STX19$^{1-294}$, and Pmito in these clusters (figure 3-24D). These data suggest that GFP-DST is re-routed into STX19/mitochondrial clusters following rapamycin treatment though interaction with full length STX19.

3.2.5.2 STX19-mito does not re-route GFP-DST to the mitochondria

Since GFP-DST appeared to interact with STX19 in knocksideways assays, we aimed to further validate the interaction using our mitochondrial targeting assay. HeLaM cells were transfected with either STX19-mito or STX16-mito and GFP-DST. Cells were then fixed and stained using anti-HA antibodies. Cells co-expressing GFP-DST and STX19-mito show a cytoplasmic localisation of GFP-DST and mitochondrial localisation of STX19-mito (figure 2-25A). Line scan analysis suggests no co-localisation between STX19-mito and GFP-DST (figure 3-25C). This suggests that GFP-DST was unable to interact with STX19-mito and be pulled onto the mitochondria. This was unexpected as GFP-DST was able to interact with the truncated version of STX19 (FKBP-myc-STX19$^{1-272}$) in the knocksideways assays. Surprisingly, cells co-expressing STX16-mito and GFP-DST demonstrated mitochondrial localisation of both constructs (figure 3-25B). Line scan analysis suggests co-localisation between GFP-DST and STX16-mito (figure 3-25D). Even though it was not previously predicted, these data suggest that STX16 interacts with DST making it an ineffective negative control for these experiments.

3.3 Discussion

3.3.1 Summary of results

The aims the beginning of this study were to:

1. Validate the mitochondrial re-routing assays as useful cell-based tools for studying protein-protein interactions.
2. Characterise STX19 interactions with shortlisted candidates from biochemical interaction screens using mitochondrial re-routing assays.

Using Munc18 proteins, we were able to validate mitochondrial re-routing assays as useful cell-based tools for studying protein-protein interactions Munc18-1 and -2 were predicted to interact with STX19 through biochemical studies and re-routing of these proteins via interaction with STX19. Munc18-1 was re-routed to the mitochondria in the mitochondrial targeting STX19-mito assay and Munc18-2 was re-routed to the mitochondria and to STX19/mitochondrial clusters in both the knocksideways and mitochondrial targeting assays. Munc18-3, which was not predicted to interact with STX19, was not re-routed to the mitochondria in either of these assays. This shows that the re-routing to the mitochondria is specific to protein interactors only. STX16-mito did not re-route any of the Munc18 proteins to the mitochondria demonstrating that the Munc18-1 and -2 interactions are specific to STX19.

In order to address our second aim to characterise the interactions of STX19, we were also able to exploit the mitochondrial targeting assay by generating mutant constructs of STX19 in order to map binding domains. From this, we showed that Munc18-2 interacts with STX19 at an N-terminal KDR motif. We also show that overexpression of STX19 recruits Munc18-2 to the plasma membrane and TREs and that this recruitment depends on interaction via the KDR motif.

Our data also suggests that ZWINT is a genuine interactor of STX19 but appears to only be able to interact with STX19 when it is associated with membranes. We also gained more confidence that DST is a real interactor of STX19, however further studies are needed to validate this interaction.

Overall, we have validated the use of mitochondrial re-routing assays as tools to study protein-protein interactions and we have further characterised some of the predicted interactors from biochemical screens.

3.3.2 Mitochondrial re-routing techniques are useful tools for studying protein-protein interactions

One of the main aims of this study was to determine how useful mitochondrial re-routing techniques are in studying protein-protein interactions. The knocksideways assay was originally developed by the Robinson lab as a means to rapidly inactivate proteins to study their function. Robinson uses the knocksideways assay to demonstrate that mitochondrial re-routing of adaptor protein AP-2 effectively abolishes clathrin-mediated endocytosis of transferrin (Robinson, Sahlender and Foster, 2010). Since then, mitochondrial re-routing techniques have proven a useful tool in studying membrane trafficking. The Munro lab used mitochondrial re-routing of 11 Rab GTPases coupled with proximity biotinylation to identify Rab GTPase effectors (Gillingham *et al.*, 2019). Mitochondrial re-routing of tumour protein D54 (TPD45) by the Royle lab led to the discovery of intracellular nanovesicles that contain selective cargos harbouring a dileucine motif (Larocque *et al.*, 2020).

Our hypothesis was that mitochondrial re-routing assays could be exploited to study protein-protein interaction. In these assays, a protein of interest is re-routed to the mitochondria. Co-expression with a potential interactor and observing if the interactor is also re-routed to the mitochondria validates interaction between the two proteins. We initially used Munc18 proteins as potential interactors to determine if this was possible as they are well-known interactors of SNAREs. As such, we were highly confident the interactions with Munc18-1 and Munc18-2 predicted by biochemical analysis were real. We were able to successfully demonstrate re-routing of Munc18-2 to the mitochondria through interaction with STX19 in both knocksideways (using full-length and truncated STX19 constructs) and mitochondrial targeting assays. Munc18-2 was not re-routed to the mitochondria using STX16-mito suggests that mitochondrial re-routing of Munc18-2 was specific to its interaction with STX19. Therefore, mitochondrial re-routing techniques can be a useful tool to validate protein interactions in cell-based assays. We were also able to use mitochondrial targeting assays to map the Munc18-2 binding site on STX19 to an N-terminal KDR motif, discussed in more detail in the following section. Therefore, we were able to demonstrate that mitochondrial re-routing assays are useful for mapping protein-protein interactions.

Surprisingly, use of a full-length STX19 construct in the knocksideways assay led to the formation of STX19/mitochondrial clusters as opposed to complete mitochondrial re-routing of full-length STX19. We propose that STX19 is pulled from its microdomains in the membrane and is forming clusters with mitochondria at or under the cell surface. Unlike biochemical assays, this provides insight into how protein-protein interactions occur between membrane associated proteins. For example, in our knocksideways assays studying the protein interaction between STX19 and ZWINT, we found that ZWINT was re-routed into STX19/mitochondrial clusters with the full-length STX19 construct but not re-routed to the mitochondrial with the truncated STX19 construct. This suggests that ZWINT is only able to interact with STX19 when it is associated with membranes. Therefore, mitochondrial re-routing assays can provide valuable insights to protein-protein interactions as they take place in a biological system.

We have shown that mitochondrial re-routing assays can be useful in studying protein-protein interactions, however, there are still some limitations to this system. We found during experimental optimisation that the amount of transfected DNA is crucial to observing mitochondrial re-routing of protein interactors. The assays require a large amount of STX19 on the mitochondria and a small amount of the protein interactor to induce successful re-routing. Initially, we co-transfected equal amounts of STX19 and Munc18 DNA and found that Munc18 proteins exhibit have strong cytoplasmic localisation and mitochondrial re-routing of Munc18-2 was limited. Re-routing of Munc18-2 was only observed in cells expressing very little Munc18-2 but highly expressing STX19. We reasoned that only

a small amount of Munc18-2 was being re-routed to the mitochondria and any protein that was on the mitochondria was being masked by the strong cytoplasmic pool of Munc18-2. Therefore, we altered the specific concentrations of STX19 and Munc18-2 transfected DNA to 0.9 µg : 0.1 µg DNA respectively and found that mitochondrial re-routing now occurred in 93 % of cells. This provides a limitation to the assay as it is likely DNA concentrations will need to be optimised for each protein of interest and their interactors depending on how well the constructs express. This can make imaging and quantification particularly challenging if a very low amount of the potential interactor is required to see re-routing as this also negatively impacts transfection efficiency and the number of cells expressing both constructs.

Another limitation is that mitochondrial re-routing may depend on the strength of the interaction between two proteins. Pulling a protein from its endogenous localisation to the mitochondria based solely on the interaction with another protein may be challenging if there is a weak interaction between the two proteins.

Overall, the mitochondrial re-routing assays used in this study have shown to be useful for validating and mapping protein-protein interactions. We have also shown that these assays provide insight into the biological context of protein-protein interactions by allowing interactions to be studied in a cell-based system.

3.3.3 Munc18-2 interacts with STX19 via an N-terminal KDR motif

One of the aims of this study was to investigate potential protein interactors of STX19 that were identified by biochemical screens. Munc18-2 was identified in BioID screens and is listed as a potential interactor of BioGRID. Munc18-2 interacts with STX11 which is highly homologous to STX19 and is enriched in epithelial tissues, similar to STX19, where it regulates apical trafficking (Vogel *et al.*, 2015). We therefore hypothesised that Munc18-2 may interact with STX19 to regulate its function. As discussed, our data suggests Munc18-2 interacts with STX19 in knocksideways and mitochondrial targeting assays using full length and truncated STX19 constructs.

Further exploitation of the mitochondrial targeting assay using mutant STX19-mito constructs allowed us to map the domain of interaction to an N-terminal KDR motif in STX19. This KDR motif is conserved in other members of the syntaxin family including STX1A, 1B, 3, and 11 (STX2 and 4 contain an RDR motif). Previous literature has demonstrated STX11 interacts with Munc18-2 also at its N-terminal KDR motif (Hackmann *et al.*, 2013; Müller *et al.*, 2014; Spessott *et al.*, 2017a) . Originally, Munc18 proteins were thought to bind syntaxins at their Habc domain which folds over the SNARE domain and holds the SNARE in a closed confirmation (Dulubova *et al.*, 1999). This was thought to inhibit SNARE complex

formation and therefore, negatively regulate fusion. However, there is now literature to show that Munc18 proteins can also bind syntaxins at an N-terminal peptide and that this binding mode serves to facilitate SNARE complex formation, rather than inhibit it. This has previously been demonstrated for Munc18-1 interaction with STX1 (Dulubova *et al.*, 2007; Khvotchev *et al.*, 2007; Burkhardt *et al.*, 2008; Deák *et al.*, 2009), Munc18-3 interaction with STX4 (Aran *et al.*, 2009), and Vps45 interaction with Tgl2 (Eisemann *et al.*, 2020). A current model suggests that there are two distinct binding modes of Munc18 proteins to syntaxins – the N-terminal peptide binding mode and the Habc domain binding model. The Habc domain binding mode would serve to hold the SNARE in a closed confirmation whilst it is trafficking through the cell. Once in the appropriate place, the binding mode would switch to the N-terminal binding mode, perhaps regulated by an unknown factor. This would allow the Munc18 protein to facilitate complex formation, prevent diffusion of SNAREs, or actively pull apart SNARE complexes to facilitate fusion pore opening (Dulubova *et al.*, 2007). To support this, Rickmann et al., demonstrated that the two binding modes occur in spatially distinct cellular localisations, with the 'closed' Habc domain binding mode occurring predominantly on intracellular membranes and the 'open' N-terminal peptide occurring predominantly at the cell surface (Rickman *et al.*, 2007). Additionally, Spessott et al., report that STX11 alone mediates lipid mixing, but not cytoplasmic mixing, in cell-cell fusion assays, however, addition of Munc18-2 stimulates complete fusion. This is prevented by Munc18-2 N-terminal peptide mutants that cannot bind STX11 (Spessott *et al.*, 2017a). It would be interesting to determine if Munc18-2 has dual binding modes for STX19 by generating a STX19 Habc domain deletion or a closed confirmation mutant construct and determining if Munc18-2 is still re-routed to the mitochondria.

Based on the literature and our results suggesting Munc18-2 binds STX19 at the same N-terminal peptide, we hypothesise that Munc18-2 regulates STX19 function by holding it in an open confirmation and facilitating STX19 SNARE complex formation. Furthermore, our data suggests that the N-terminal KDR peptide of STX19 is able to recruit Munc18-2 to the plasma membrane and TREs. Rathore et al., have previously shown that the N-terminal peptide of STX1 is able to physically recruit Munc18-1 to the SNARE bundle to facilitate complex formation and conclude that the N-terminal peptide acts as an initiation factor for the assembly of a fusion competent SNARE complex (Rathore *et al.*, 2010). This further supports our hypothesis that Munc18-2 positively regulates the function of STX19.

Further studies are required to confirm this hypothesis such as co-immunoprecipitation of Munc18-2 with STX19 and STX19 KDR-AAA mutants. Co-immunoprecipitation of STX19/STX19 KDR-AAA mutants and its SNARE binding partners in the presence of GFP-Munc18-2 will also provide insight into how Munc18-2 binding affects the ability of STX19 to form SNARE complexes. Our assays were carried out in a cell-based system, therefore we could not completely rule out interaction via a bridging protein.

Further *in vitro* interaction studies using purified proteins would be able to determine if this is a direct interaction.

To investigate the impact of Munc18-2 binding on STX19-mediated fusion, we would also use a flow-cytometry based assay to measure constitutive secretion. This assay has been used previously to identify a role for STX19 in secretion. It is well-known that overexpression of SNAREs can drive the fusion they mediate, therefore, we plan to overexpress STX19 and STX19 KDR-AAA mutants alongside GFP-Munc18-2 and measure the effect on constitutive secretion.

Finally, we overexpressed Munc18-2 in our assays. Whilst negative controls demonstrate STX19 interaction with Munc18-2 is specific and not a consequence of overexpression, it would be necessary to use an antibody for Munc18-2 to assess interaction with the endogenous protein. Antibodies were not used in these studies due to the lack of availability of good Munc18-2 antibodies.

Overall, using mitochondrial re-routing assays, we have validated the interaction between STX19 and Munc18-2 and mapped the domain of interaction to an N-terminal KDR peptide. Based on the literature, we hypothesise that the N-terminal binding mode of Munc18-2 on STX19 serves to facilitate STX19-mediated fusion, though further experiments are required to confirm this. We have shown that using mitochondrial re-routing assays to map interaction domains can provide insights into the nature of protein-protein interactions and into the regulation of STX19 function.

3.3.4 Munc18-1 interacts with the truncated version of STX19

Munc18-1 was identified as a potential interactor through BioID screens and is listed on BioGRID. In order to validate the interaction between STX19 and Munc18-1, Munc18-1 was overexpressed in mitochondrial re-routing assays with STX19. From our assays, we showed that Munc18-1 was re-routed to the mitochondria in the knocksideways assay with the truncated STX19 construct. We also observed mitochondrial re-routing with the truncated STX19-mito construct. This suggests that Munc18-1 has the ability to bind STX19. Munc18-1 is highly expressed in nervous tissues and has been well documented to have roles in regulating SNAREs mediating fusion at neuronal synapses (Dulubova *et al.*, 2007; Lonsdale *et al.*, 2013). As STX19 is relatively highly expressed in epithelial tissues and has very low expression in nervous tissues, we hypothesis that the interaction between STX19 and Munc18-1 is not physiologically relevant. Furthermore, Munc18-1 showed localisation to TREs in 18 % of cells upon co-expression with HA-STX19 compared to 92 % of cells showing Munc18-2 localisation to TREs. This supports the idea that whilst Munc18-1 may be able to bind STX19, the interaction is not physiologically relevant.

3.3.5 ZWINT interacts with STX19 on membranes

One of the proteins that was identified as a potential interactor in biochemical screens was ZWINT. This protein was identified in BioID screens, yeast-two hybrid screens, and is listed on BioGRID. Additionally, co-immunoprecipitation experiments performed previously by the lab showed ZWINT was immunoprecipitated STX19 but not STX7. We therefore predicted that ZWINT is likely a genuine interactor of STX19.

ZWINT is a kinetochore-localised protein that recruits ZW10 and facilitates spindle formation during mitosis. Why STX19, as a post-Golgi Qa-SNARE, would interact with a kinetochore-localised protein remains unclear. Previous large-scale interaction studies have identified ZWINT as a potential interactor of STX3, 11, and 18, and SNAP29 (Hutchins *et al.*, 2010; Hein *et al.*, 2015; Huttlin *et al.*, 2015). We sought to validate the interaction between ZWINT and STX19 through mitochondrial re-routing assays as a first step to understanding why a kinetochore protein would interact with STX19.

We found that endogenous ZWINT is re-routed into STX19/mitochondrial clusters in knocksideways assays using the full-length STX19 construct but is not re-routed to the mitochondria with the truncated STX19 construct. Additionally, we found endogenous ZWINT does not re-route to the mitochondria in mitochondrial targeting assays using STX19-mito which contains the truncated version of STX19. This suggests that ZWINT only interacts with STX19 when it is associated with specific membranes. We rationalised three possible reasons for this: A) ZWINT interacts with the C-terminal S-acylation domain of STX19 which has been removed in truncated constructs to prevent membrane association of STX19, B) the interaction between ZWINT and STX19 is not strong enough to pull ZWINT onto the mitochondria but ZWINT may able to interact with STX19 at the plasma membrane prior to rapamycin treatment and thus is pulled into clusters during re-routing C) interaction between ZWINT and STX19 occurs through an unknown bridging protein that is localised only at the membrane. Additional studies *in vitro* using purified proteins should be carried out to confirm STX19 and ZWINT interact directly. It would also be interesting to perform reconstituted liposome assays to determine if a lipid component is necessary for the interaction between ZWINT and STX19.

Our experiments using ZWINT-FLAG constructs also suggests that ZWINT and STX19 are in the same regions of the plasma membrane. Overexpression of ZWINT-FLAG and HA-STX19 demonstrates co-localisation of the two proteins in distinct domains of the plasma membrane. We also saw enrichment of ZWINT-FLAG and HA-STX19 in similar puncta in the cytoplasm. We could speculate that these puncta may be trafficking vesicles or endocytic compartments, but further investigation would be required. Removal of the STX19 SNARE domain did not alter ZWINT localisation to the plasma membrane. However, ZWINT and STX19 without its SNARE domain appeared to be less well co-

localised compared to the full length STX19 though confirmation of this would require quantification of intensity levels in specific puncta and analysis using Pearson's correlation coefficient. It is likely that ZWINT has membrane targeting independent from STX19, however, overexpression of STX19 drives its co-localisation with STX19 in distinct regions of the membrane. ZWINT is thought to interact with other SNAREs at the plasma membrane including STX3 and 11 and therefore, ZWINT localisation to the plasma membrane may be facilitated by interaction with other proteins. Furthermore, using ZWINT-FLAG in mitochondrial targeting assays suggests ZWINT and STX19 are able to interact at the plasma membrane. ZWINT-FLAG was able to pull STX19-mito onto the plasma membrane. ZWINT-FLAG did not pull STX16-mito to the plasma membrane suggesting this is specific to STX19. Future mitochondrial targeting assays with STX19-mito mutant constructs would be useful to map a binding site for ZWINT on STX19. As we found ZWINT-FLAG was able to pull STX19-mito to the plasma membrane, it would also be interesting to determine if ZWINT-FLAG was able to pull a truncated HA-tagged STX19 construct in which the C-terminal S-acylation domain has been removed to the plasma membrane.

Localisation of ZWINT-FLAG to the plasma membrane was surprising as the anti-ZWINT antibody we used suggested endogenous ZWINT is cytoplasmic. An N-terminally-tagged FLAG-ZWINT also shows localisation at the plasma membrane (data not shown) suggesting the positioning of the tag is not affecting localisation. This suggests that the anti-ZWINT antibody is only binding to the cytoplasmic pool and not the pool of ZWINT at the plasma membrane. As ZWINT does not have a transmembrane domain, it may associate with membrane either through interactions with other proteins or it may undergo post-translational modifications that allow membrane association. It is possible that the antibody epitope is masked when ZWINT is associated with the plasma membrane or in complex with proteins at the plasma membrane.

These studies suggest that ZWINT is a valid interactor of STX19 and provides some insight into the nature of the interaction as data suggests the interaction can only occur at specific membranes. Considering their interaction and co-localisation, we hypothesise that the function carried out by the interaction of these two proteins takes place at the plasma membrane. What this function is remains unclear. ZWINT is well documented to recruit ZW10 to kinetochores for proper mitotic checkpoint signalling (H. Wang *et al.*, 2004). Previous studies have shown a role for SNAP29 in stabilising the association of ZWINT with the kinetochore for proper outer kinetochore formation and microtubule attachment (Morelli *et al.*, 2016a). It is possible that STX19 may stabilise ZWINT association with the plasma membrane through a similar mechanism. Previous studies have also shown a trafficking role for ZW10 in ER-Golgi transport. ZW10 is recruited to kinetochores by ZWINT where it forms the NRZ complex with RINT1 (Rad50 interactor 1) and NAG (neuroblastoma-amplified gene). The NRZ complex

then associates with STX18 to regulate retrograde vesicle transport from the Golgi to the ER. The components of the NRZ are structurally related to subunits of tethering complexes, such as the exocyst, suggesting that the NRZ complex is acting as a vesicle tether (Tagaya *et al.*, 2014) . Since ZWINT has the ability to recruit ZW10, we hypothesise that ZWINT is acting to recruit tethering complexes that link STX19 vesicles to the plasma membrane.

3.3.6 DST interacts with STX19 in the knocksideways assay but not in mitochondrial targeting assays

DST was identified as a potential interactor through BioID and yeast-two hybrid screening. DST (or BPAG1) belongs to the spectraplakin family of proteins which are large proteins (>500kDa) with the ability to cross-link actin filaments and microtubules. DST has alternative splicing variants which gives rise to four isoforms that have different tissue distribution. The neuronal isoform of DST (BPAG1n) has been previously shown to interact with components of trafficking machinery including clathrin and dynactin to mediate retrograde axonal trafficking. Additionally, there is an epithelial-isoform of DST (BPAG1e) which has been shown to play a role in keratinocyte motility. Since DST was pulled out in both biochemical and yeast-two hybrid screening, we thought it likely to be a genuine interactor of STX19. Based on literature showing DST has roles in regulating axonal transport and can be enriched in epithelial tissues, as is STX19, we predicted that DST may interact with STX19 to regulate trafficking. Therefore, we sought to validate the interaction between STX19 and DST using our mitochondrial re-routing assays.

We found that DST was re-routed to the mitochondria in the knocksideways assay with the truncated STX19 construct and into STX19/mitochondrial clusters with the full-length STX19 construct. This suggests there is a genuine interaction between STX19 and DST. However, unexpectedly, DST did not re-route to the mitochondria in the mitochondrial targeting assays with STX19-mito. In some of the experiments, mitochondrial re-routing of DST was apparent with STX19-mito, however this was in a very limited number of cells and proved difficult to repeat. As previously discussed, the amount of DNA transfected in these assays seems crucial to observing proper mitochondrial re-routing. Expressing a large amount of DST resulted in strong cytoplasmic staining which may have masked any mitochondrial re-routing however, we found achieving a good transfection efficiency with a very small amount of DST (0.1 µg) challenging. Nevertheless, one possible reason re-routing may be seen with the knocksideways assay and not the mitochondrial targeting STX19-mito assay could be that proteins are able to interact prior to re-routing in the knocksideways assay. It may be that DST and STX19 are able to interact primarily at the cell surface or in the cytoplasm (as would be the case with the truncated construct) and STX19 is able to re-route DST to the mitochondria after rapamycin treatment.

If STX19 is targeted to the mitochondria, it is possible that is not close enough to DST to interact with STX19 or the interaction with DST may not be strong enough to pull it onto the mitochondria.

The GFP-DST construct used in these assays was generated from a clone pulled out from the yeast-two hybrid screen predicted to interact with STX19. This clone is 749 amino acids in size which is substantially smaller than the 5497 amino acid full-length protein. Four clones were pulled out from yeast-two hybrid screening representing four potential binding sites. Since our construct was only made from one of these clones, it is highly likely the interaction between our construct and STX19 is weaker than the interaction between the full-length DST and STX19. It is plausible that interaction with two or more of the potential binding sites of DST would strengthen the interaction. This further supports our reasoning that a weak interaction may not be strong enough to pull DST to the mitochondria in the mitochondrial targeting STX19-mito assays. Further experiments should be carried out with DST constructs containing two or more of the predicted interaction sites. We had obtained various other DST constructs for use in these assays including constructs consisting of: DST actin-binding domain (ABD) – spectrin repeat (SR) 21, DST SR21 – SR41, DST SR21 – Gas2-related domain (GAR), and a full-length FLAG-tagged construct – all of which cover two or more of the predicted yeast-two hybrid fragments. However, due to the large size of these fragments, we found transfection particularly difficult and thus were unable to perform mitochondrial re-routing assays with these constructs. Further optimisation to achieve good transfection efficiency is required.

Surprisingly, we found that our DST construct was re-routed to the mitochondria upon co-transfection of STX16-mito. We remain unclear as to why this may be the case since STX16 was not predicted to interact with DST. Two possibilities for this result may be that A) there is no interaction between STX16 and DST and the re-routing is non-specific or B) there is a genuine interaction between STX16 and DST. We do not predict the former to be the case as we do not see non-specific mitochondrial re-routing with any of the other proteins we have assessed such as the Munc18 proteins and ZWINT. STX6 and 7 are listed as predicted DST interactors on BioGRID so it is possible that DST is interacting with other SNAREs including STX16. Additional experimental repeats are required to confirm mitochondrial re-routing of DST with STX16-mito is not an artefact.

Overall, we have shown that DST interacts with full-length and truncated STX19 constructs using the knocksideways assay. These data give us more confidence that DST is a genuine interactor, however, further studies should be carried out as discussed to completely validate this interaction.

A)

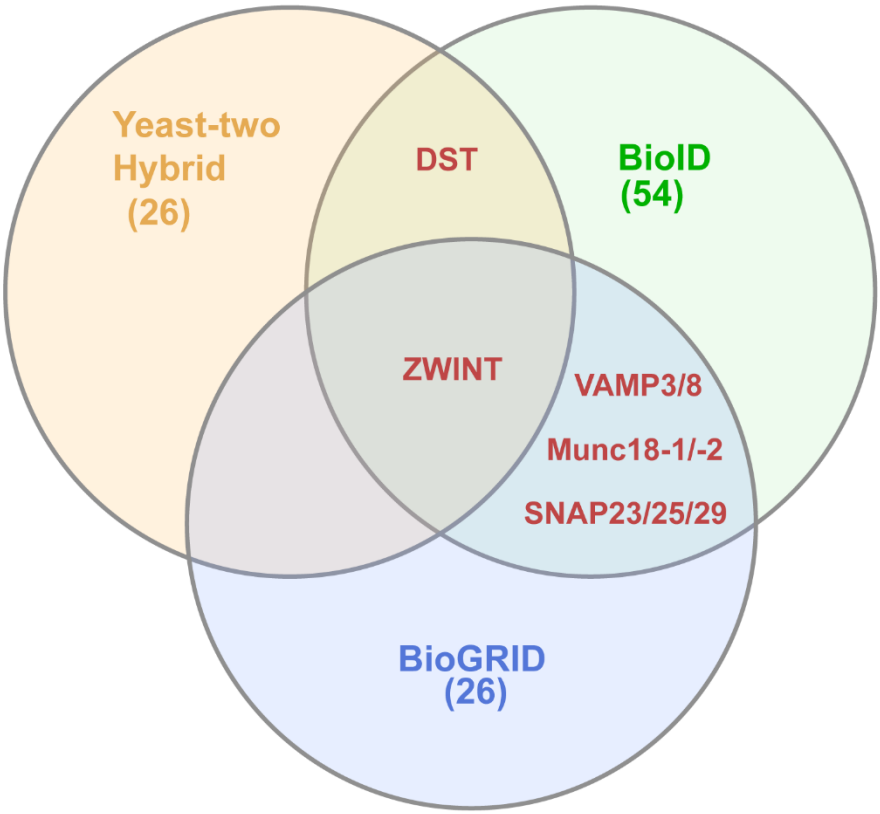

Figure 3-1: Potential STX19 interactors. A) A Venn diagram depicting the shortlisted number of potential interactors from yeast-two hybrid screening (yellow), proximity dependent biotinylation assays (BioID; green), and the number of potential STX19 interactors listed on BioGRID (blue). DST was identified as a potential interactor in yeast-two hybrid screening and BioID screening. ZWINT was identified as a potential interactor in yeast-two hybrid screening, BioID screening and is listed on BioGRID. VAMPs 3 and 8, SNAPs 23, 25, and 29, and Munc18-1, and -2 were identified in BioID screening and are listed on BioGRID.

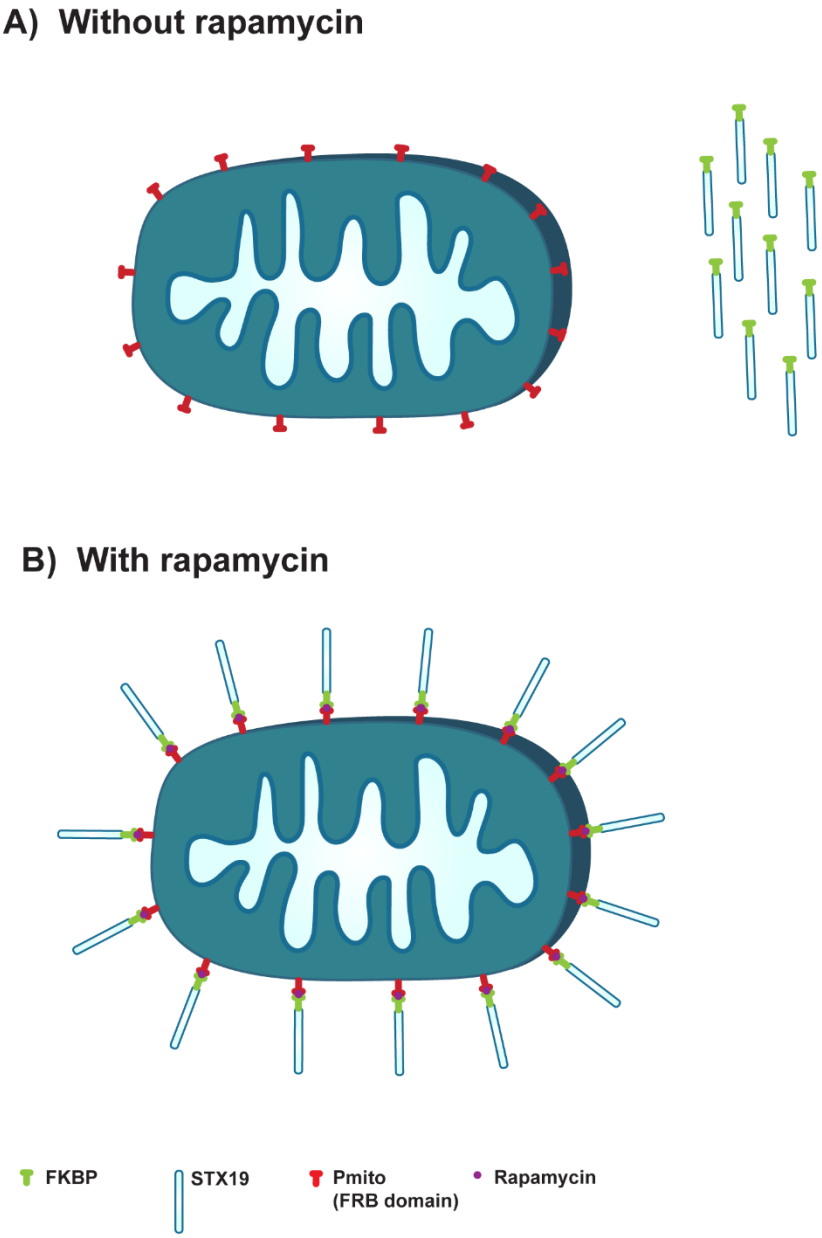

Figure 3-2: Knocksideways assay
An assay in which proteins can be re-routed onto the mitochondria through FKBP/FRB rapamycin-dependent interactions. The bait protein (Pmito) consists of a mitochondrial outermembrane target signal derived from Tom70, mCherry, and a FRB domain. This construct is targted to the mitochondria and as such labels the mitochondria with mCherry. An additional construct is generated consisting of the protein of interest, in this case STX19, a myc tag, and an FKBP tag. In this assay, both constructs are co-expressed in cells. **A)** In the absence of rapamycin, the FRB domain of the Pmito construct and the FKBP tag of the protein of interest construct do not interact. Pmito localises to the mitochondria and the protein of interest localises to its typical subcellular compartment. **B)** In the presence of rapamycin, both the FRB domain and FKBP tag interact with rapamycin molecules and the protein of interest can be re-routed to the mitochondria. We have generated two FKBP tagged constructs of STX19 for use in this assay. FKBP-myc-STX19$^{1-294}$ contains the full length STX19 protein. FKBP-myc-STX19$^{1-272}$ lacks the C-terminal cysteine rich domain of STX19 which is required for membrane targeting. Therefore, this construct has a cytoplasmic localisation in the absence of rapamycin.

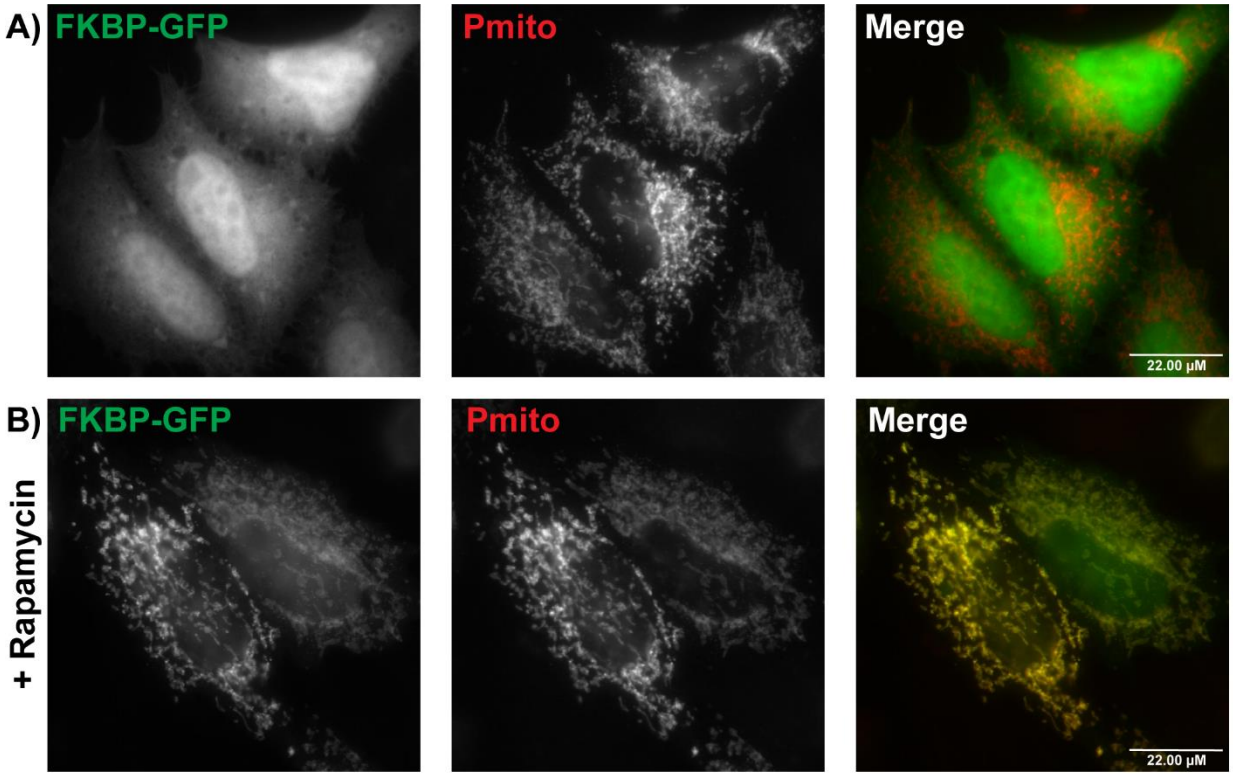

Figure 3-3: FKBP-GFP is re-routed to the mitochondria in knocksideways assay
HeLaM cells were transfected with FKBP-tagged GFP and Pmito. Cells were incubated with 1 µM rapamycin for 15 minutes at 37 °C. After rapamycin treatment, cells were fixed using 4 % PFA and stained using anti-myc antibodies. **A)** In the absence of rapamycin, FKBP-GFP localises to the cytoplasm and the nucleus, and Pmito localises to mitochondria. **B)** In the presence of rapamycin, both FKBP-GFP and Pmito localise to the mitochondria. Scale bar: 22.00 µM.

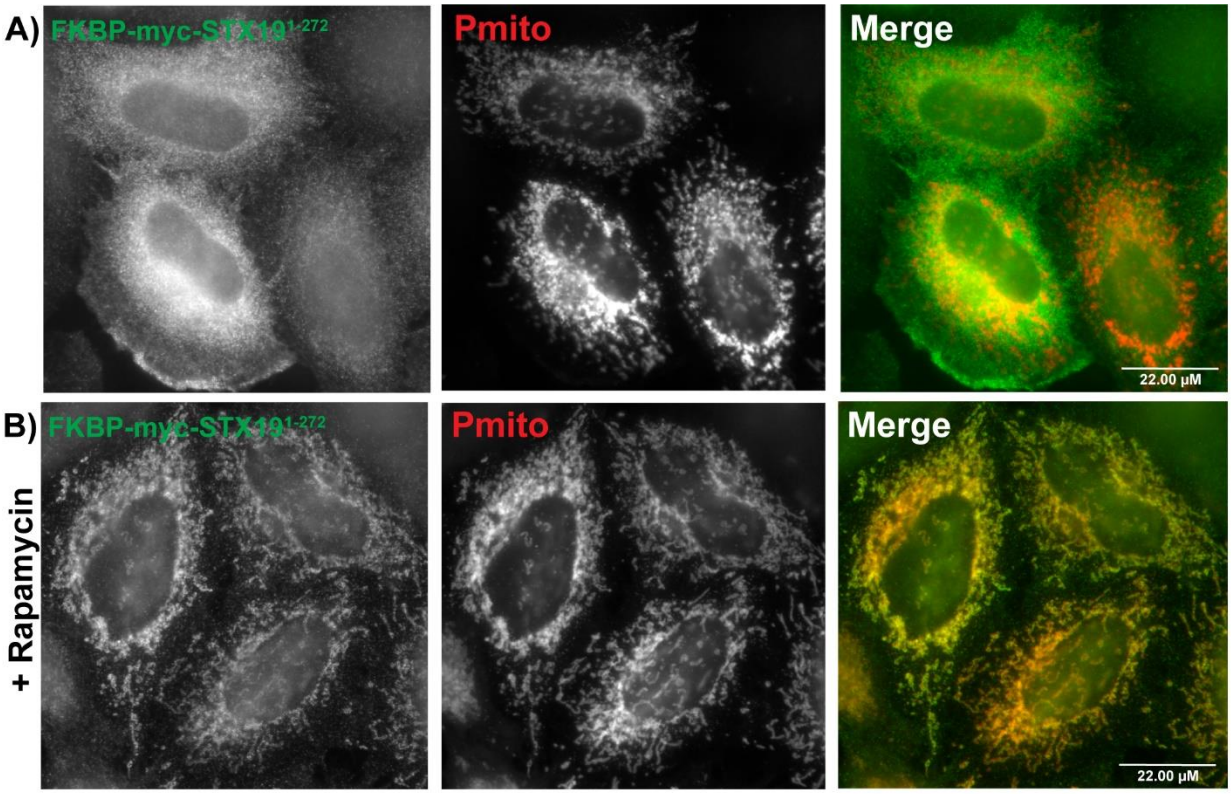

Figure 3-4: FKBP-myc-STX19$^{1-272}$ is re-routed to the mitochondria in knocksideways assay. HeLaM cells were transfected with FKBP-myc-STX19$^{1-272}$ and Pmito. Cells were incubated with 1 µM rapamycin for 15 minutes at 37 °C. After rapamycin treatment, cells were fixed using 4 % PFA and stained using anti-myc antibodies. **A)** In the absence of rapamycin, FKBP-myc-STX19$^{1-272}$ localises to the cytoplasm and Pmito localises to mitochondria. **B)** In the presence of rapamycin, FKBP-myc-STX19$^{1-272}$ is effectively re-routed to the mitochondria. Scale bar: 22.00 µM.

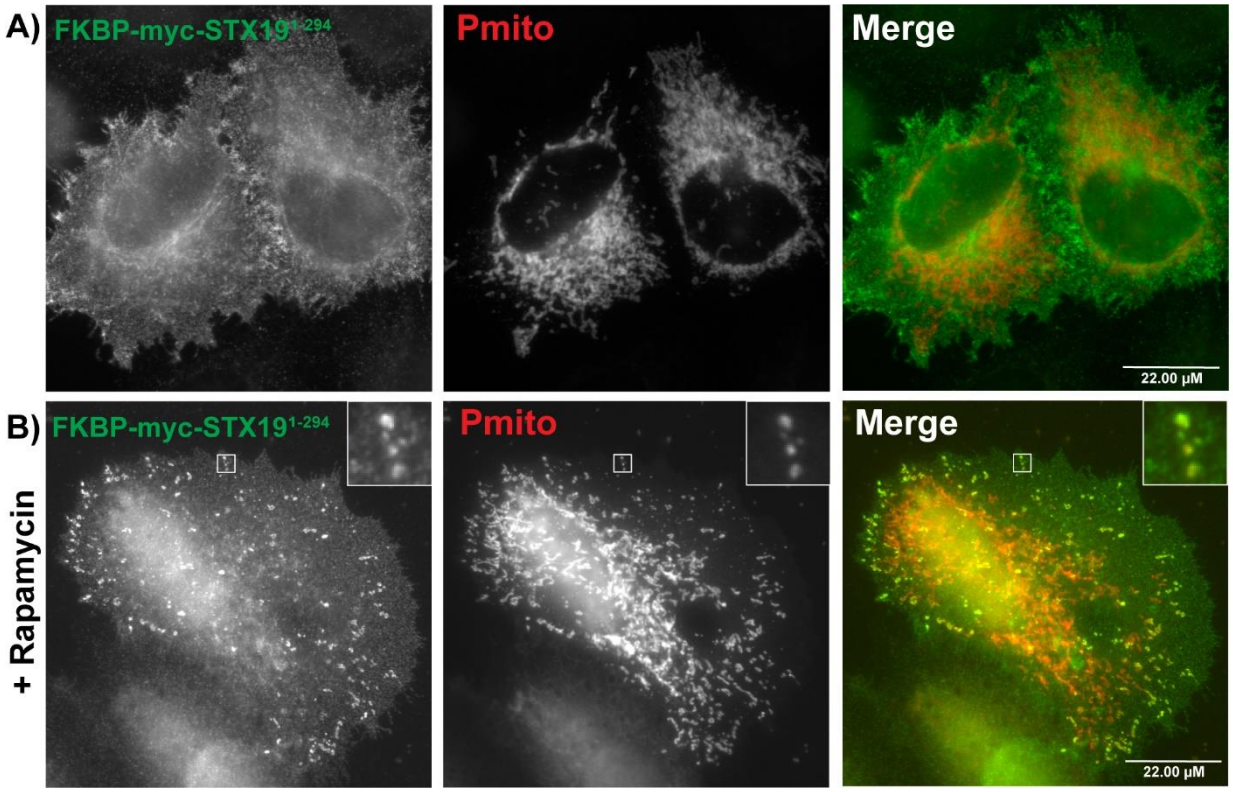

Figure 3-5: FKBP-myc-STX19$^{1-294}$ forms clusters with the mitochondria in knockside-ways assay. HeLaM cells were transfected with FKBP-myc-STX19$^{1-294}$ and Pmito. Cells were incubated with 1 µM rapamycin for 15 minutes at 37 °C. After rapamycin treatment, cells were fixed using 4 % PFA and stained using anti-myc antibodies. **A)** In the absence of rapamycin, FKBP-myc-STX19$^{1-294}$ localises to the plasma membrane, tubular recycling endosomes and the cytoplasm. Pmito localises to mitochondria. **B)** In the presence of rapamycin, FKBP-myc-STX19$^{1-294}$ forms clusters with mitochondria towards the periphery of the cell. Scale bar: 22.00 µM.

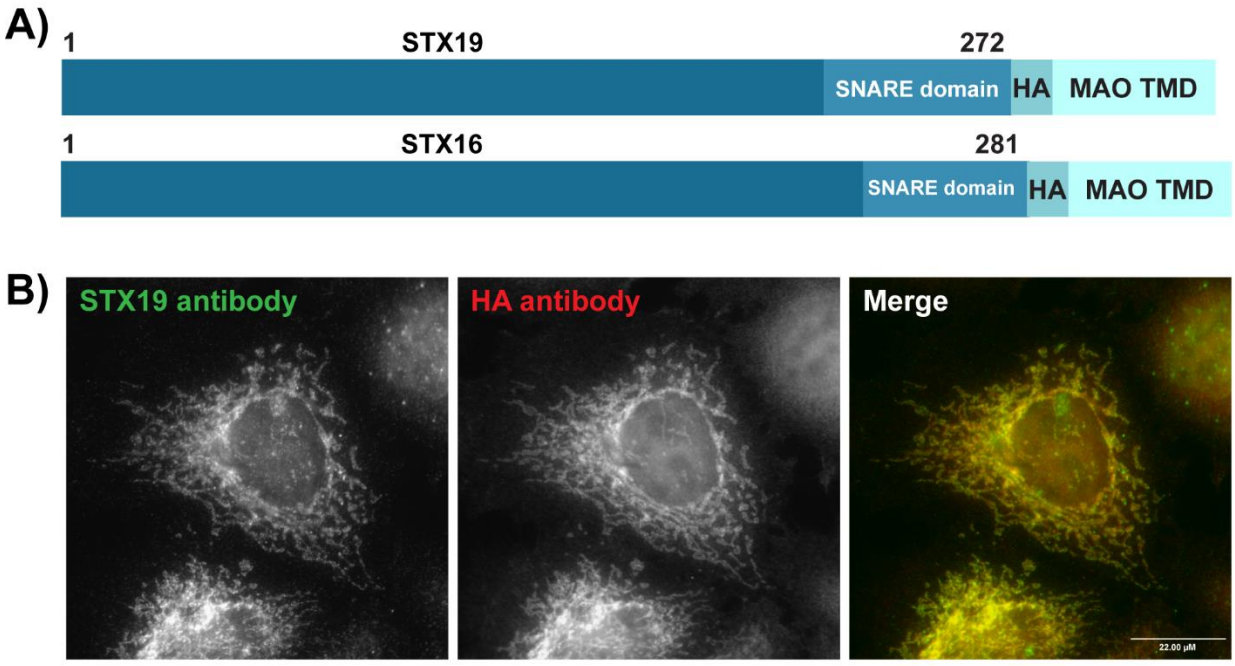

Figure 3-6: Mitochondrial re-routing constructs schematic and validation of STX-19mito. A) Schematics of STX19mito and STX16mito. The STX19mito and STX16 constructs consists of a truncated version of STX19 (STX19 1-272aa) which lacks the C-terminal cysteine-rich domain which is required for S-acylation and membrane association or a truncated version of STX16 (STX16 1-281aa) which lacks a transmembrane domain. Removing membrane association for each protein allows effective targeting to the mitochondria. A HA tag was included for visualisation by immunofluorescence staining. The constructs also include the transmembrane domain of monoamine oxidase (MAO TMD), mitochondria-localised enzyme. The MAO transmembrane domain targets the truncated STX19/STX16 to the mitochondria. **B)** HeLaM cells were transfected with STX19mito. Cells were then fixed using 4 % PFA and stained with anti-STX19 and anti-HA antibodies. The anti-HA antibody was used to detect the STX-19mito construct and the anti-STX19 antibody used to demonstrate the construct successfully targets STX19 to the mitochondria. Both antibodies demonstrate mitochondrial localisation of STX19.

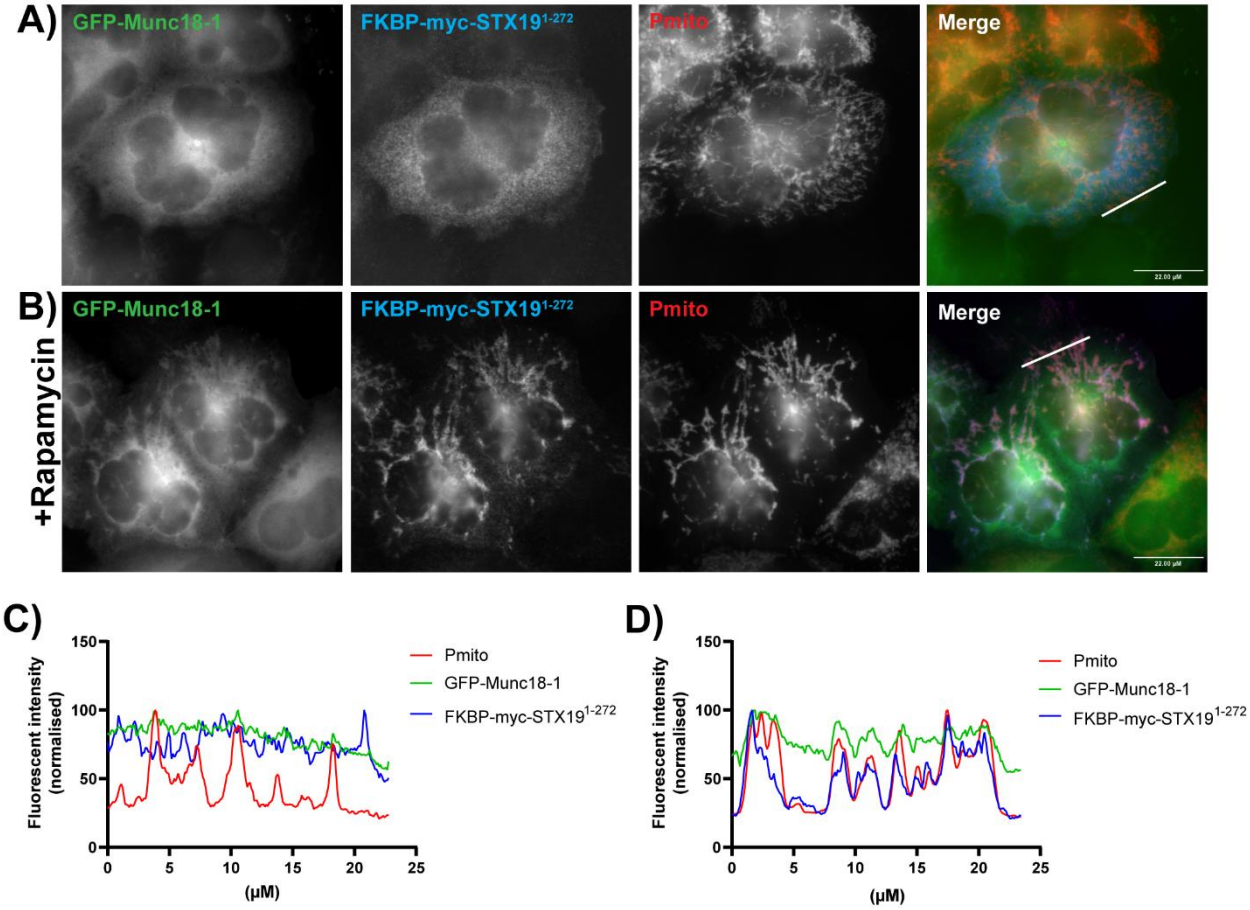

Figure 3-7: GFP-Munc18-1 is re-routed to the mitochondria by FKBP-myc-STX19$^{1-272}$ in knocksideways assay. HeLaM cells were transfected with GFP-Munc18-1, FKBP-myc-STX19$^{1-272}$ and Pmito the specific concentrations of 0.1 µg, 0.9 µg, 0.5 µg DNA respectively. Cells were incubated with 1 µM rapamycin for 15 minutes at 37 °C. After rapamycin treatment, cells were fixed using 4 % PFA and stained using anti-myc antibodies. **A)** In the absence of rapamycin, no co-localisation is seen between all three constructs. GFP-Munc18-1 and FKBP-myc-STX19$^{1-272}$ localises to the cytoplasm and Pmito localises to the mitchondria. **B)** In the presence of rapamycin, FKBP-myc-STX19$^{1-272}$ and GFP-Munc18-1 are re-routed to the mitochondria. A pool of GFP-Munc18-1 remains cytoplasmic. **C)** Line scan analysis of panel A demonstrating no co-localisation between all three constructs. **D)** Line scan analysis of panel B demonstrates co-localisation of Pmito, FKBP-myc-STX19$^{1-272}$, and GFP-Munc18-1 through corresponding peaks of intensity. Line scan analysis was performed using ImageJ. The white lines on the images represent the lines along which fluorescent intensity values were taken at 0.11 µM intervals. Fluorescence intensity values were normalised as a percentage of the highest value. Scale bar: 22.00 µM.

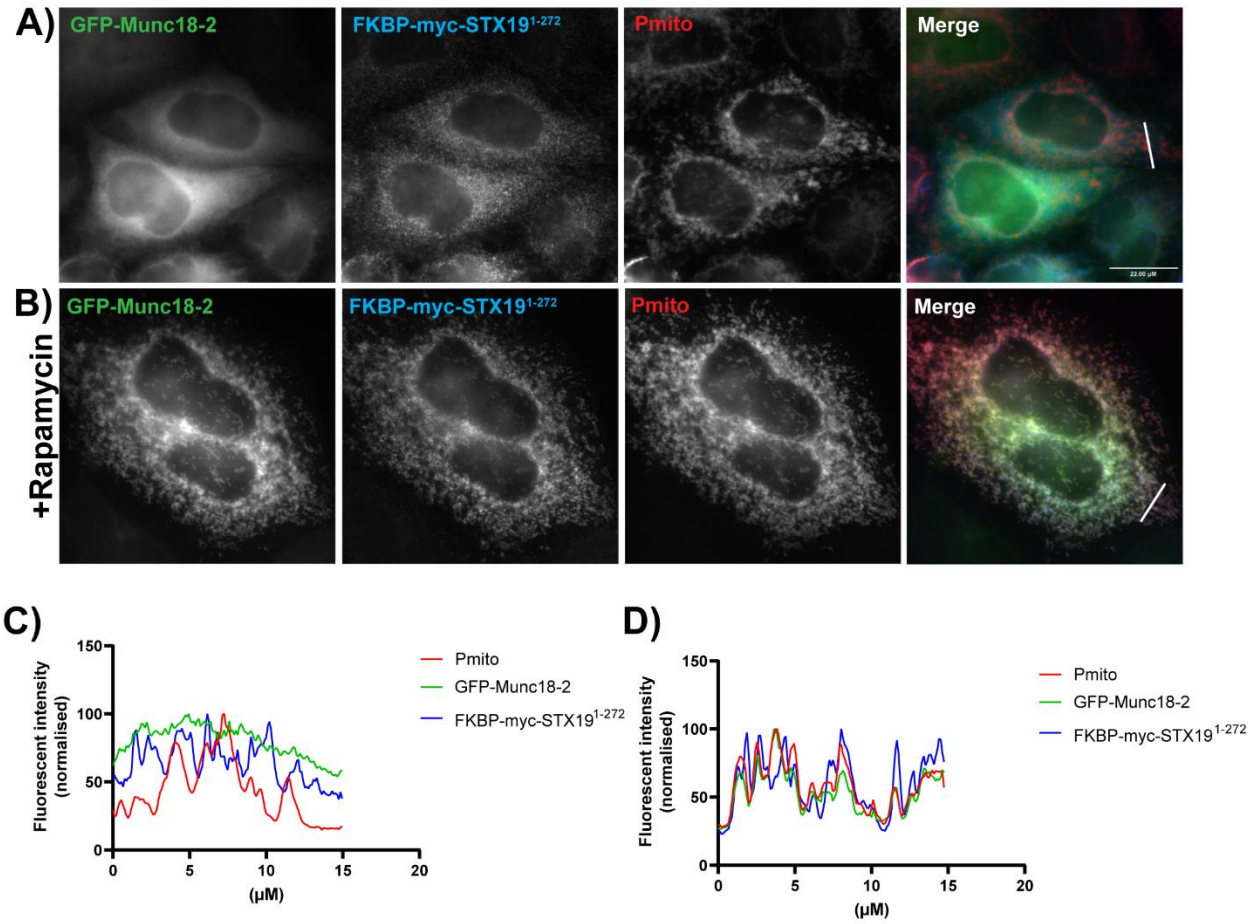

Figure 3-8: GFP-Munc18-2 is re-routed to the mitochondria by FKBP-myc-STX19$^{1-272}$ in knocksideways assay. HeLaM cells were transfected with GFP-Munc18-2, FKBP-myc-STX19$^{1-272}$ and Pmito at the specific concentrations of 0.1 µg, 0.9 µg, 0.5 µg DNA respectively. Cells were incubated with 1 µM rapamycin for 15 minutes at 37 °C. After rapamycin treatment, cells were fixed using 4 % PFA and stained using anti-myc antibodies. **A)** In the absence of rapamycin, no co-localisation is seen between all three constructs. GFP-Munc18-2 and FKBP-myc-STX19$^{1-272}$ localises to the cytoplasm and Pmito localises to the mitchondria. **B)** In the presence of rapamycin, FKBP-myc-STX19$^{1-272}$ and GFP-Munc18-2 are re-routed to the mitochondria. **C)** Line scan analysis of panel A demonstrating no co-localisation between all three constructs. **D)** Line scan analysis of panel B demonstrates co-localisation of Pmito, FKBP-myc-STX19$^{1-272}$, and GFP-Munc18-2 through corresponding peaks of intensity. Line scan analysis was performed using ImageJ. The white lines on the images represent the lines along which fluorescent intensity values were taken at 0.11 µM intervals. Fluorescence intensity values were normalised as a percentage of the highest value. Scale bar: 22.00 µM.

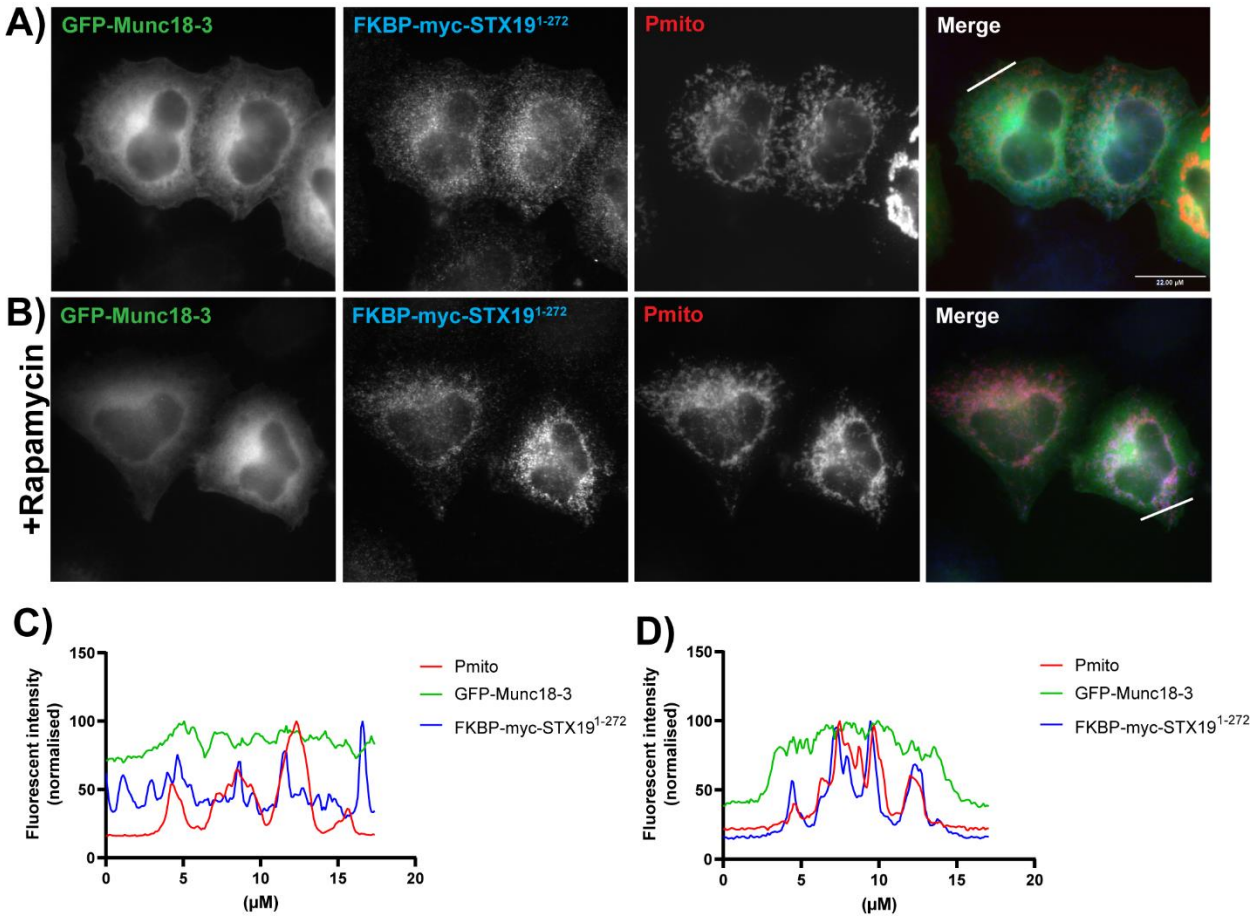

Figure 3-9: GFP-Munc18-3 is not re-routed to the mitochondria by FKBP-myc-STX-19$^{1-272}$ in knocksideways assay. HeLaM cells were transfected with GFP-Munc18-3, FKBP-myc-STX19$^{1-272}$ and Pmito at the specific concentrations of 0.1 µg, 0.9 µg, 0.5 µg DNA respectively. Cells were incubated with 1 µM rapamycin for 15 minutes at 37 °C. After rapamycin treatment, cells were fixed using 4 % PFA and stained using anti-myc antibodies. **A)** In the absence of rapamycin, no co-localisation is seen between all three constructs. GFP-Munc18-3 and FKBP-myc-STX19$^{1-272}$ localises to the cytoplasm and Pmito localises to the mitchondria. **B)** In the presence of rapamycin, FKBP-myc-STX19$^{1-272}$ is re-routed to the mitochondria, GFP-Munc18-3 remains cytoplasmic. **C)** Line scan analysis of panel A demonstrating no co-localisation between all three constructs. **D)** Line scan analysis of panel B demonstrates co-localisation of Pmito and FKBP-myc-STX19$^{1-272}$ through correspondig peaks of intensity and shows no co-localisation with GFP-Munc18-3. Line scan analysis was performed using ImageJ. The white lines on the images represent the lines along which fluorescent intensity values were taken at 0.11 µM intervals. Fluorescence intensity values were normalised as a percentage of the highest value. Scale bar: 22.00 µM.

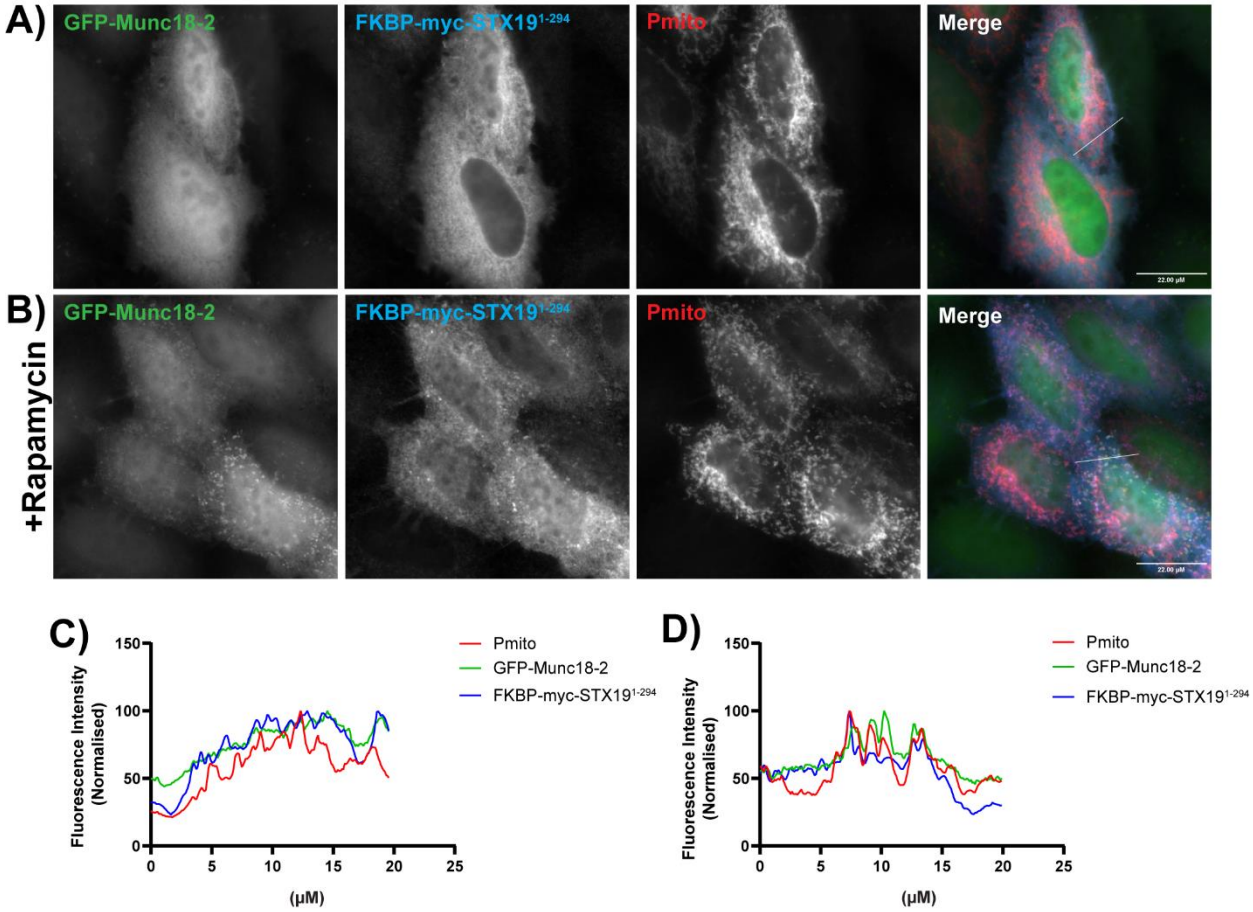

Figure 3-10: GFP-Munc18-2 is re-routed to mitochondrial clusters with FKBP-myc-STX19$^{1-294}$ in knocksideways assay. HeLaM cells were transfected with GFP-Munc18-2, FKBP-myc-STX19$^{1-294}$ and Pmito at the specific concentrations of 0.1 µg, 0.9 µg, 0.5 µg DNA respectively. Cells were incubated with 1 µM rapamycin for 15 minutes at 37 °C. After rapamycin treatment, cells were fixed using 4 % PFA and stained using anti-myc antibodies. **A)** In the absence of rapamycin, no co-localisation is seen between all three constructs. GFP-Munc18-2 localises to the cytoplasm. **B)** In the presence of rapamycin, FKBP-myc-STX19$^{1-294}$ co-localises with the mitochondria and mitochondrial clusters, GFP-Munc18-2 is re-routed into mitochondrial clusters with FKBP-myc-STX19$^{1-294}$ and Pmito. **C)** Line scan analysis of panel A demonstrating no co-localisation between all three constructs. **D)** Line scan analysis of panel B demonstrates co-localisation of all three constructs through corresponding peaks of intensity when the line dissects mitochondrial clusters. Line scan analysis was performed using ImageJ. The white lines on the images represent the lines along which fluorescent intensity values were taken at 0.11 µM intervals. Fluorescence intensity values were normalised as a percentage of the highest value. Scale bar: 22.00 µM.

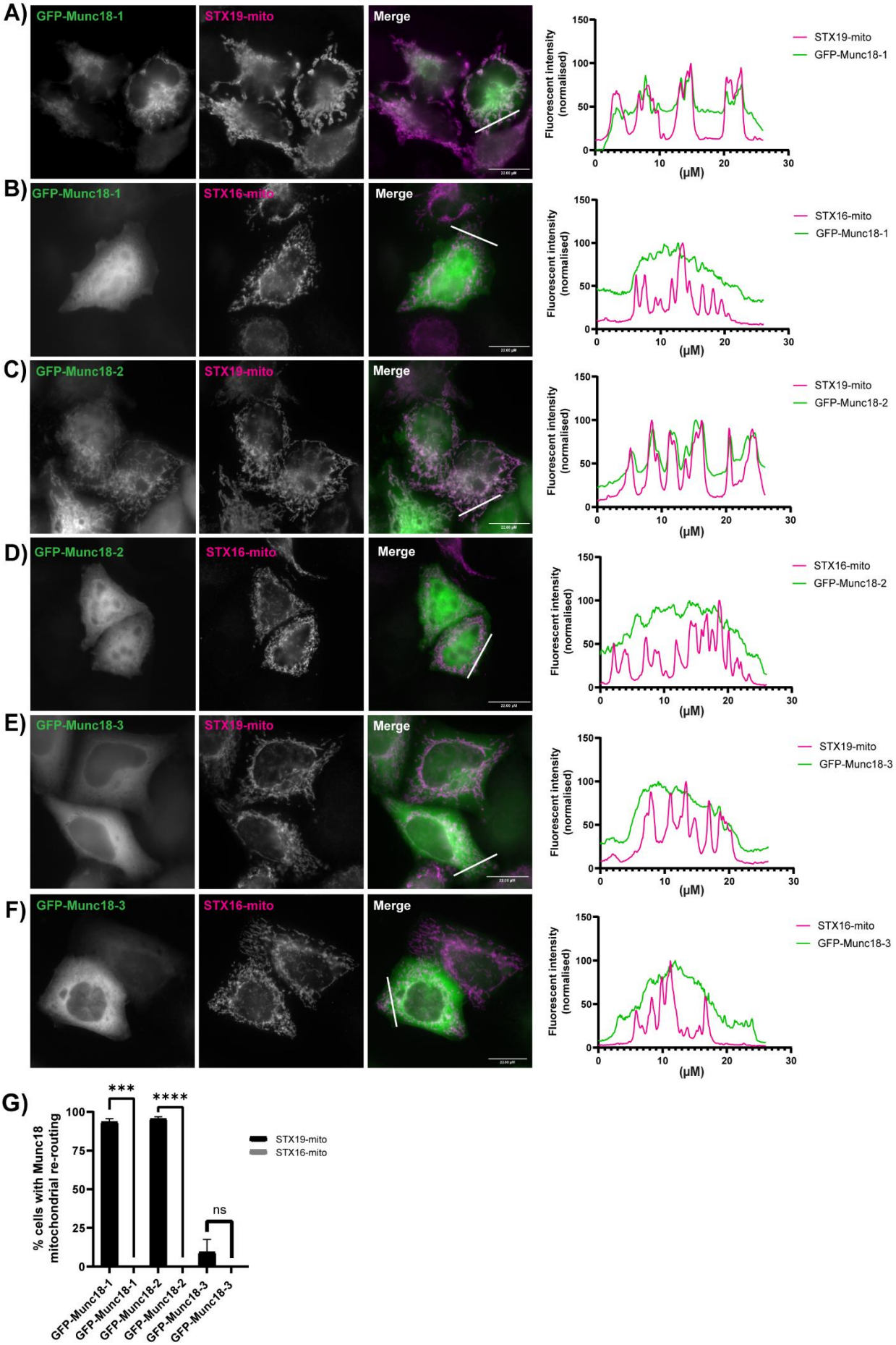
A)
GFP-Munc18-1
STX19-mito
Merge
STX19-mito
GFP-Munc18-1
B)
GFP-Munc18-1
STX16-mito
Merge
STX16-mito
GFP-Munc18-1
C)
GFP-Munc18-2
STX19-mito
Merge
STX19-mito
GFP-Munc18-2
D)
GFP-Munc18-2
STX16-mito
Merge
STX16-mito
GFP-Munc18-2
E)
GFP-Munc18-3
STX19-mito
Merge
STX19-mito
GFP-Munc18-3
F)
GFP-Munc18-3
STX16-mito
Merge
STX16-mito
GFP-Munc18-3
Fluorescent intensity (normalised)
(μM)
G)
% cells with Munc18 mitochondrial re-routing
STX19-mito
STX16-mito
***
****
ns
GFP-Munc18-1
GFP-Munc18-1
GFP-Munc18-2
GFP-Munc18-2
GFP-Munc18-3
GFP-Munc18-3

Figure 3-11: STX19-mito re-routes GFP-Munc18-1 and GFP-Munc18-2, but not GFP-Munc18-3 to the mitochondria HeLaM cells were transfected with either STX19-mito or STX16-mito, and GFP-Munc18-1, -2, or 3. Cells were then fixed using 4 % PFA and stained using anti-HA antibodies. **A)** GFP-Munc18-1 and STX19-mito both localise to mitochondria. Co-localisation confirmed by corresponding peaks of intensity on the line scan analysis of the merged immunofluorescent image. **B)** GFP-Munc18-1 demonstrates a cytoplasmic localisation whilst STX16-mito localises to the mitochondria. Line scan analysis of the merged immunofluorescent image demonstrates no co-localisation between the two constructs. **C)** GFP-Munc18-2 and STX19-mito localise to mitochondria. Co-colocalisation confirmed by corresponding peaks on intensity of the line scan analysis of the merged immunofluorescent image. **D)** GFP-Munc18-2 demonstrates a cytoplasmic localisation whilst STX16-mito localises to the mitochondria. Line scan analysis of the merged immunofluorescent image demonstrates no co-localisation between the two constructs. **E)** GFP-Munc18-3 demonstrates a cytoplasmic localisation whilst STX19-mito localises to the mitochondria. Line scan analysis of the merged immunofluorescent image demonstrates no co-localisation between the two constructs. **F)** GFP-Munc18-3 demonstrates a cytoplasmic localisation whilst, STX16-mito localises to the mitochondria. Line scan analysis of the merged immunofluorescent image demonstrates no co-localisation between the two constructs. **G)** Quantification of the number of cells that co-express either STX19-mito or STX16-mito and GFP-Munc18-1, -2, or -3. Approximately 90 cells co-expressing both contructs were counted over three repeats and assessed for mitochondrial re-routing of GFP-Munc18-1, -2, or -3. The percentage of cells with mitochondrial re-routing compared to the total number of cells expressing both constructs was determined and the average percentage across three repeats was plotted. GFP-Munc18-1, -2, and -3 demonstrated re-routing in 95, 93, and 18 % of cells expressing STX19-mito respectively, compared to 0 % for all three Munc18 isoforms in cells expressingSTX16-mito. Paired t-tests for each Munc18 isoform were performed using GraphPad Prism, (* $P < 0.05$/**** $P < 0.0001$). Scale bar: 22.00 µ M. Line scan analysis of the immunofluorescent microscopy images using ImageJ, % intensity represents the fluorescent intensity (normalised against the highest intensity measurment) for a given point along the white line indicated in the corresponding microscopy images. Data points were taken at 0.11 µM intervals along the line.

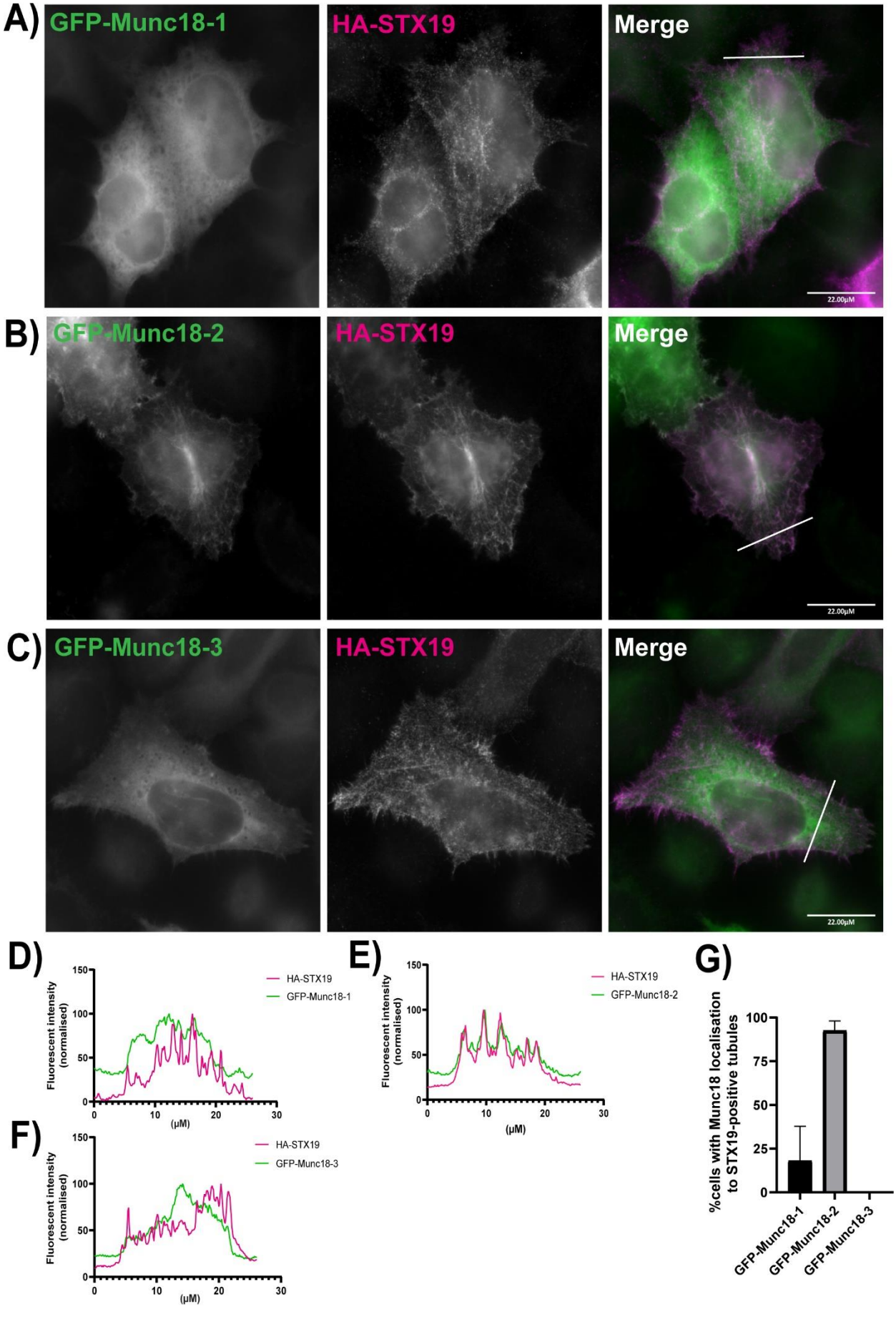
A)
GFP-Munc18-1
HA-STX19
Merge
22.00µM
B)
GFP-Munc18-2
HA-STX19
Merge
22.00µM
C)
GFP-Munc18-3
HA-STX19
Merge
22.00µM
D)
Fluorescent intensity (normalised)
HA-STX19
GFP-Munc18-1
(µM)
E)
Fluorescent intensity (normalised)
HA-STX19
GFP-Munc18-2
(µM)
F)
Fluorescent intensity (normalised)
HA-STX19
GFP-Munc18-3
(µM)
G)
%cells with Munc18 localisation to STX19-positive tubules
GFP-Munc18-1
GFP-Munc18-2
GFP-Munc18-3

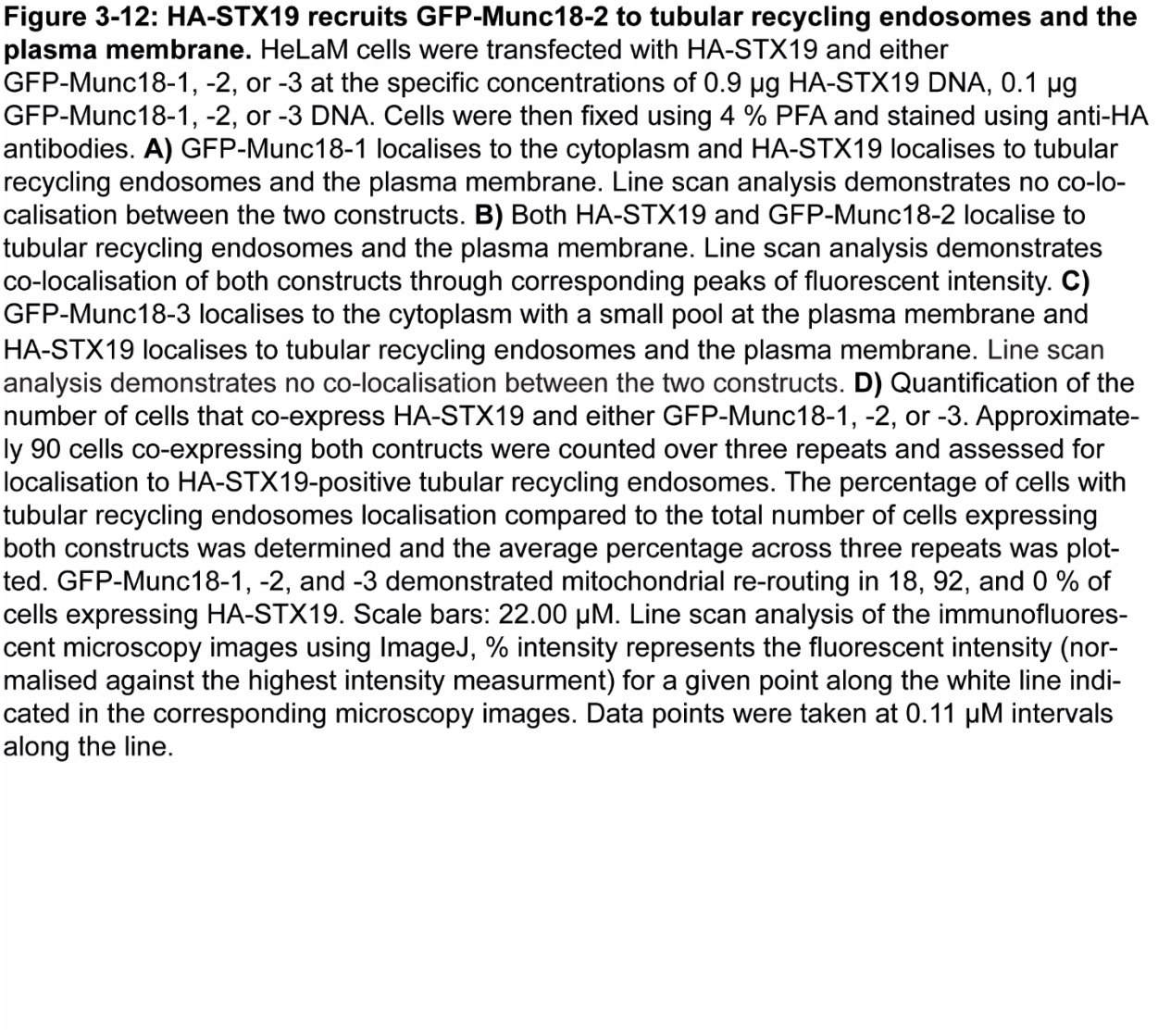

Figure 3-12: HA-STX19 recruits GFP-Munc18-2 to tubular recycling endosomes and the plasma membrane. HeLaM cells were transfected with HA-STX19 and either GFP-Munc18-1, -2, or -3 at the specific concentrations of 0.9 µg HA-STX19 DNA, 0.1 µg GFP-Munc18-1, -2, or -3 DNA. Cells were then fixed using 4 % PFA and stained using anti-HA antibodies. **A)** GFP-Munc18-1 localises to the cytoplasm and HA-STX19 localises to tubular recycling endosomes and the plasma membrane. Line scan analysis demonstrates no co-localisation between the two constructs. **B)** Both HA-STX19 and GFP-Munc18-2 localise to tubular recycling endosomes and the plasma membrane. Line scan analysis demonstrates co-localisation of both constructs through corresponding peaks of fluorescent intensity. **C)** GFP-Munc18-3 localises to the cytoplasm with a small pool at the plasma membrane and HA-STX19 localises to tubular recycling endosomes and the plasma membrane. Line scan analysis demonstrates no co-localisation between the two constructs. **D)** Quantification of the number of cells that co-express HA-STX19 and either GFP-Munc18-1, -2, or -3. Approximately 90 cells co-expressing both contructs were counted over three repeats and assessed for localisation to HA-STX19-positive tubular recycling endosomes. The percentage of cells with tubular recycling endosomes localisation compared to the total number of cells expressing both constructs was determined and the average percentage across three repeats was plotted. GFP-Munc18-1, -2, and -3 demonstrated mitochondrial re-routing in 18, 92, and 0 % of cells expressing HA-STX19. Scale bars: 22.00 µM. Line scan analysis of the immunofluorescent microscopy images using ImageJ, % intensity represents the fluorescent intensity (normalised against the highest intensity measurment) for a given point along the white line indicated in the corresponding microscopy images. Data points were taken at 0.11 µM intervals along the line.

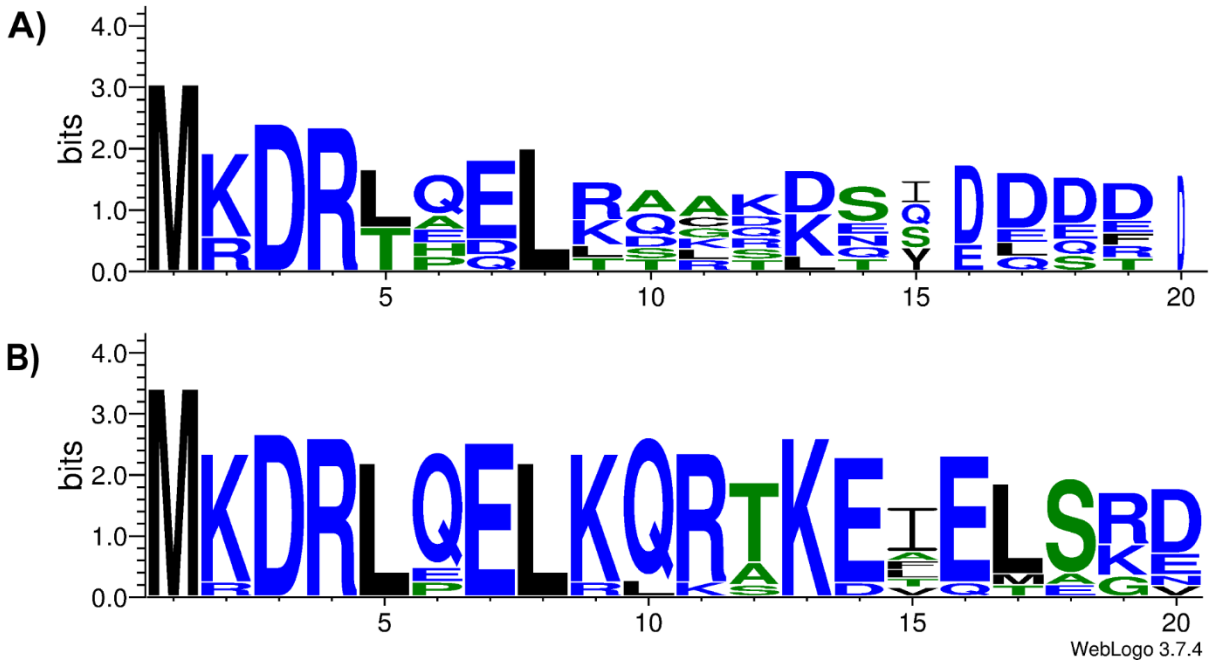

Figure 3-13: The N-terminal KDR motif is conserved in syntaxins and in STX19 in different species. Sequence information was obtain from UniProt. Sequence alignments were generated using Clustal Omega alignment software. Graphical representation of the first 20 amino acids of the alignments were generated using WebLogo3. **A)** Alignment of the first 20 amino acids of STXs 1A, 1B, 2, 3, 4, 11, and 19. STXs 1A, 1B, 3, 11, and 19 all have the conserved KDR motif whilst STXs 2 and 4 have a partially conserved RDR motif. **B)** Alignment of the first 20 amino acids of STX19 in different species. Species include human, monkey, mouse, chicken, cow, dog, cat, platypus, horse, and spotted gar fish. The KDR motif is well-conserved throughout all species with the exception of chicken which contains an RDR motif.

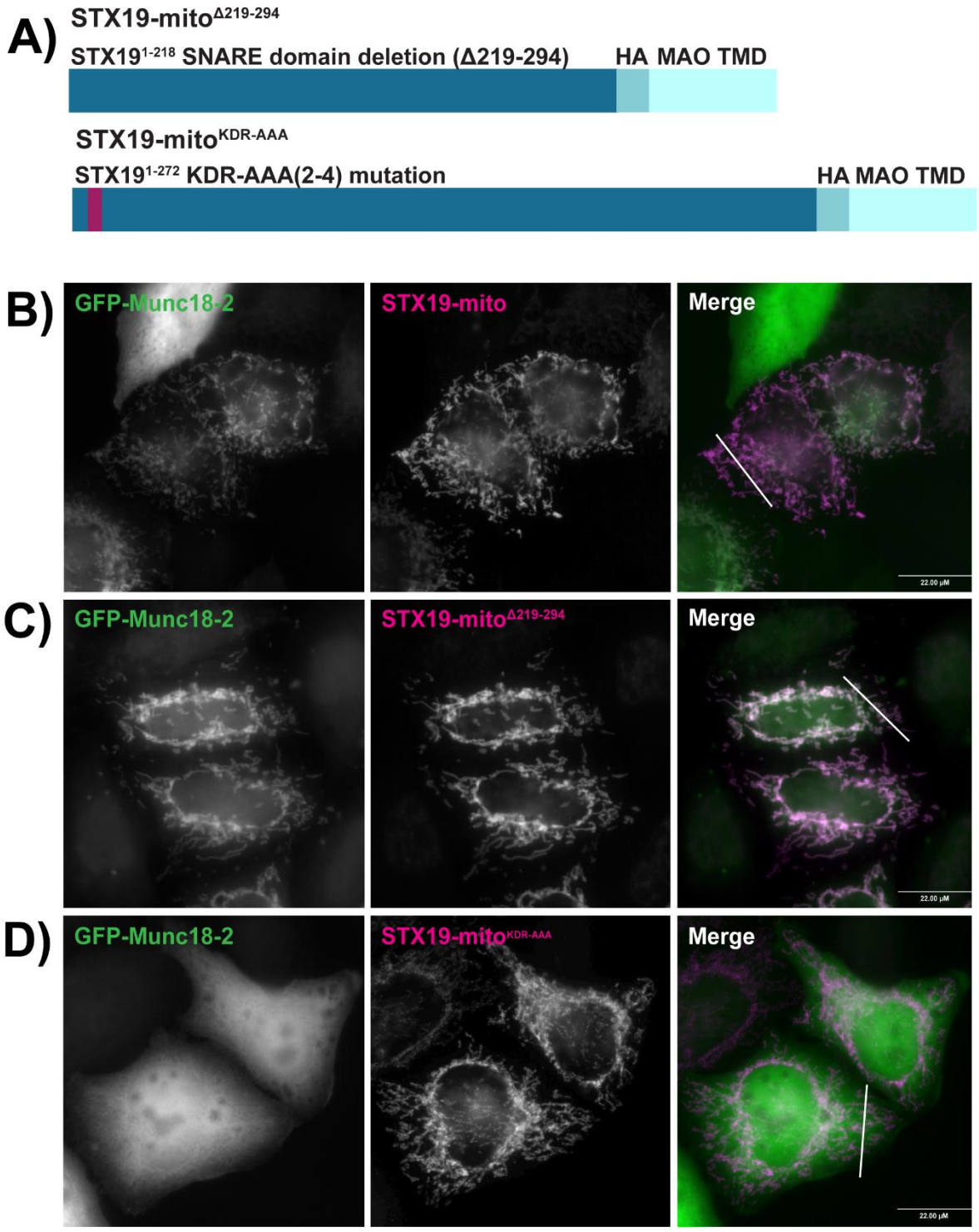
A)
STX19-mito$^{\Delta 219-294}$
STX19$^{1-218}$ SNARE domain deletion (Δ219-294)
HA MAO TMD
STX19-mito$^{KDR-AAA}$
STX19$^{1-272}$ KDR-AAA(2-4) mutation
HA MAO TMD
B)
GFP-Munc18-2
STX19-mito
Merge
C)
GFP-Munc18-2
STX19-mito$^{\Delta 219-294}$
Merge
D)
GFP-Munc18-2
STX19-mito$^{KDR-AAA}$
Merge

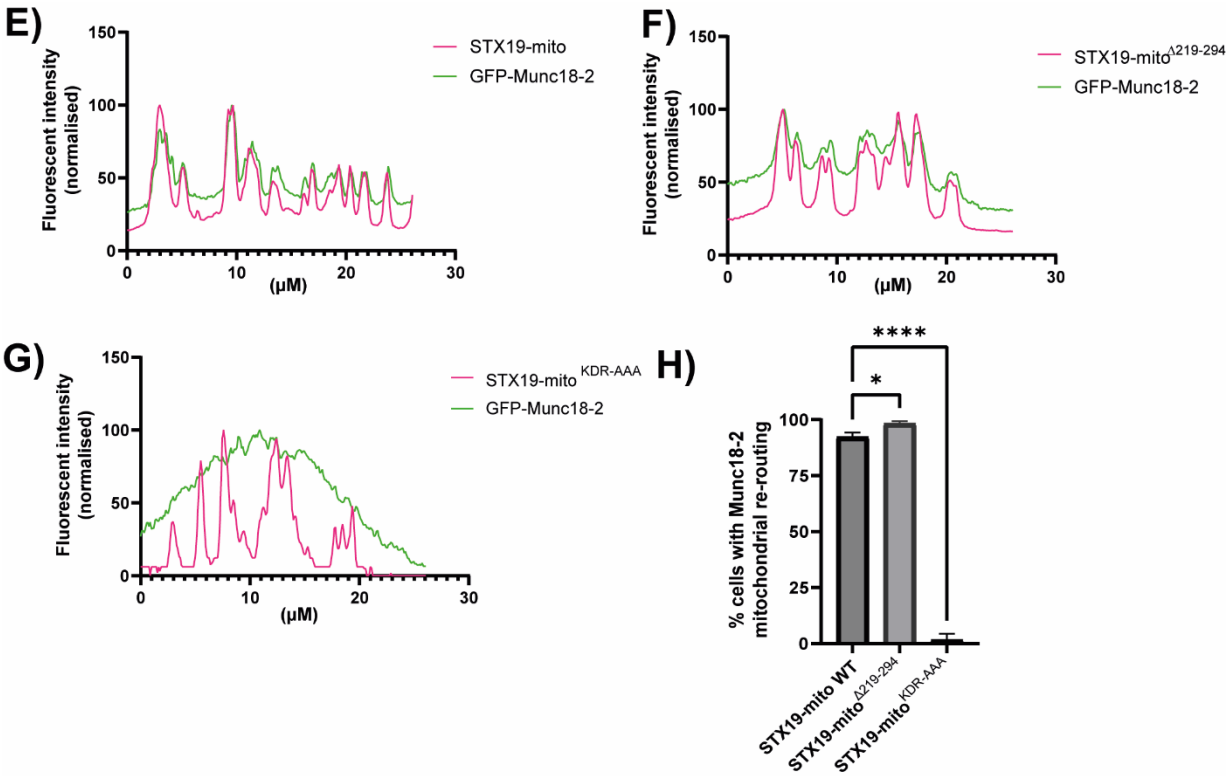

Figure 3-14: STX19-mito re-routes GFP-Munc18-2 to the mitochondria via an N-terminal KDR motif. A) Schematics depicting STX19-mito mutant constructs. STX19-mito$^{\Delta 219-294}$ consists of a truncated version of STX19 in which the C-terminal cysteine rich domain that allows membrane association and the SNARE domain has been deleted. STX19-mito$^{KDR-AAA}$ consists of a truncated version of STX19 in which the C-terminal cysteine rich domain that allows membrane association has been removed and a KDR motif at the N-terminal (amino acids 2-4) have been mutated to alanines. Both constructs also contain a HA tag for visualisation and the monoamine oxidase (MAO) transmembrane domain for mitochondrial localisation. **B-E)** HeLaM cells were transfected with either STX19-mito, STX19-mito$^{\Delta 219-294}$, or STX19-mito$^{KDR-AAA}$ and GFP-Munc18-2 at the specific concentrations of 0.9 μg STX19-mito construct DNA and 0.1 μg GFP-Munc18-2 DNA. Cells were then fixed using 4 % PFA and stained using anti-HA antibodies. **B)** Both STX19-mito and GFP-Munc18-2 demonstrates a mitochondrial localisation. Line scan analysis demonstrates co-localisation of both constructs through corresponding peaks of fluorescent intensity. **C)** Both STX19-mito$^{\Delta 219-294}$ and GFP-Munc18-2 localise to the mitochondria. Line scan analysis demonstrates co-localisation of both constructs through corresponding peak of fluorescent intensity. **D)** STX19-mito$^{KDR-AAA}$ localises to the mitchondria and GFP-Munc18-2 localises to the cytoplasm. Line scan analysis demonstrates no co-localisation between the two constructs. **E)** Quantification of the number of cells that co-express either STX19-mito, STX19-mito$^{\Delta 219-294}$, or STX19-mito$^{KDR-AAA}$ and GFP-Munc18-2. Approximately 90 cells co-expressing both contructs were counted over three repeats and assessed for mitochondrial re-routing of GFP-Munc18-2. The percentage of cells with mitochondrial re-routing compared to the total number of cells expressing both constructs was determined and the average percentage across three repeats was plotted. GFP-Munc18-2 demonstrated mitochondrial re-routing in 92, 98, and 1.5 % of cells expressing STX19-mito, STX19-mito$^{\Delta 219-294}$, and STX19-mito$^{KDR-AAA}$ respectively. One way ANOVA was performed using GraphPad Prism (* P <0.05/**** P < 0.0001). Immunofluorescence images: Scale bar: 22.00 μM. Line scan analysis of the immunofluorescent microscopy images using ImageJ, % intensity represents the fluorescent intensity (normalised against the highest intensity measurment) for a given point along the white line indicated in the corresponding microscopy images. Data points were taken at 0.11 μM intervals along the line.

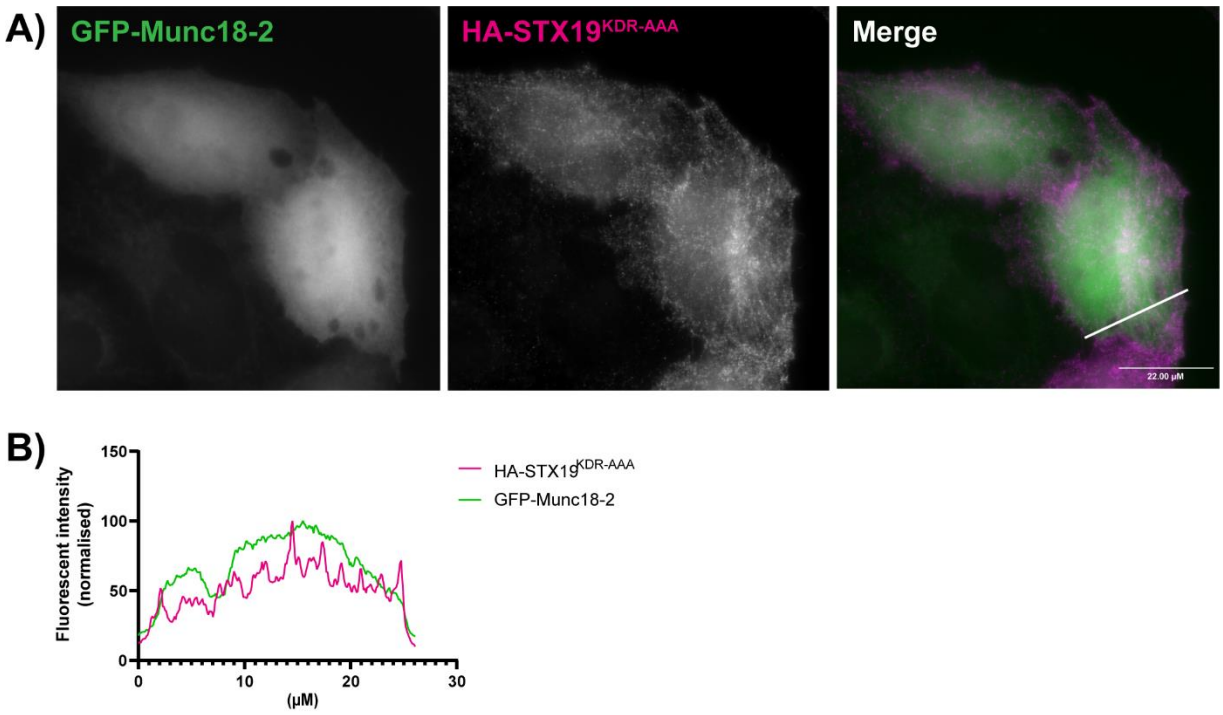

Figure 3-15: HA-STX19$^{KDR-AAA}$ does not recruit GFP-Munc18-2 to tubular recycling endosomes and the plasma membrane. HeLaM cells were transfected with HA-STX19 and either GFP-Munc18-2 at the specific concentrations of 0.9 µg and 0.1 µg DNA respectively. Cells were then fixed using 4 % PFA and stained using anti-HA antibodies. **A)** GFP-Munc18-2 localises to the cytoplasm and HA-STX19 localises to tubular recycling endosomes and the plasma membrane. **B)** Line scan analysis demonstrates no co-localisation between the two constructs. Scale bar: 22.00 µM. Line scan analysis of the immunofluorescent microscopy images using ImageJ, % intensity represents the fluorescent intensity normalised against the highest intensity measurment for a given point along the white line indicated in the corresponding microscopy images. Data points were taken at 0.11 µM intervals along the line.

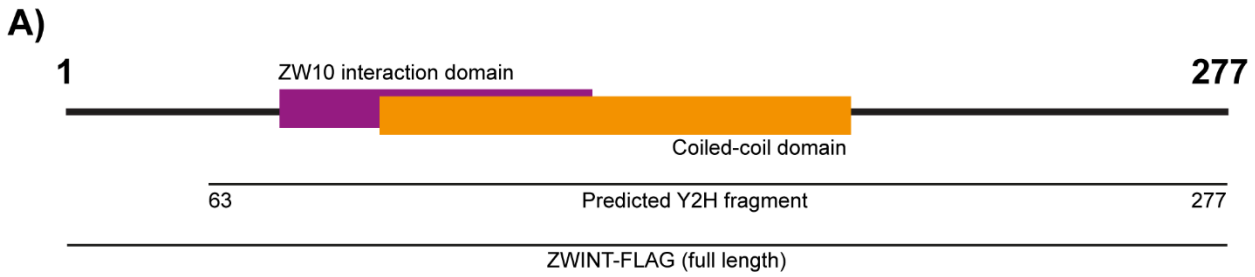

Figure 3-16: Schematic of ZWINT domains and mapping of fragments predicted to interact with STX19 through yeast-two hybrid screening. Human ZWINT consists of 277 amino acids. The ZW10 interaction domain (purple rectangle) is positioned at amino acids 85 – 155. The coiled-coil domain (orange rectangle) is positioned at amino acids 104 – 217. The fragment predicted to interact with STX19 through yeast-two hybrid screening is positioned at amino acids 63 – 277. A full length FLAG-tagged ZWINT construct was used for further interaction studies.

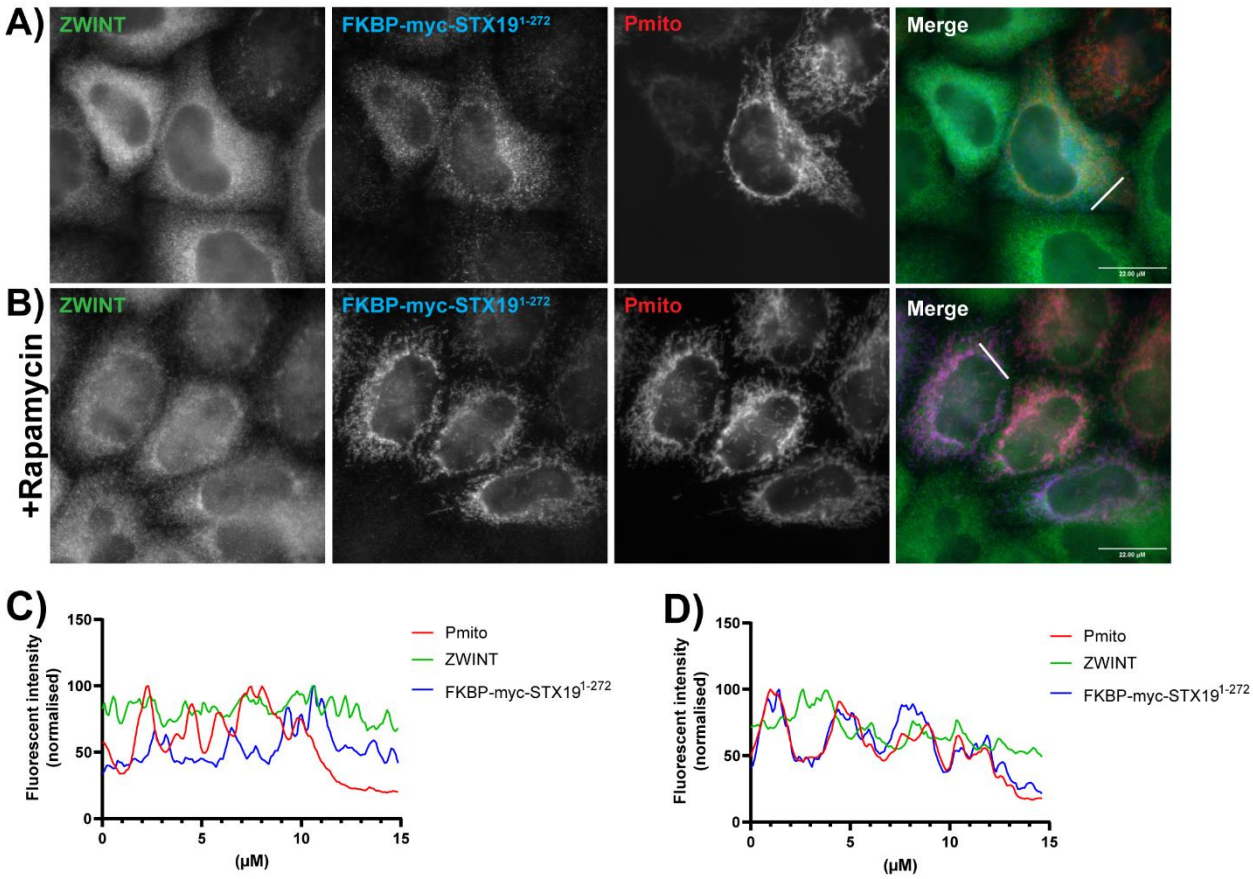

Figure 3-17: Endogenous ZWINT is not re-routed to the mitochondria with FKBP-myc-STX19$^{1-272}$ in knocksideways assay. HeLaM cells were transfected with FKBP-myc-STX19$^{1-272}$ and Pmito at the specific concentrations of 0.9 µg and 0.5 µg DNA respectively. Cells were incubated with 1 µM rapamycin for 15 minutes at 37 °C. After rapamycin treatment, cells were fixed using 4 % PFA and stained using anti-myc and anti-ZWINT antibodies. **A)** In the absence of rapamycin, no co-localisation is seen between all three constructs. ZWINT localises to the cytoplasm. **B)** In the presence of rapamycin, ZWINT remains cytoplasmic. A pool of ZWINT is enriched perinuclearly but this pool does not co-colocalise with the mitochondria. FKBP-myc-STX19$^{1-272}$ is re-routed to the mitochondria and co-localises with Pmito. **C)** Line scan analysis of panel A demonstrating no co-localisation between all three proteins. **D)** Line scan analysis of panel B demonstrates co-localisation between FKBP-myc-STX19$^{1-272}$ and Pmito through corresponding peaks of intensity but no-colocalisation with ZWINT. Line scan analysis was performed using ImageJ. The white lines on the images represent the lines along which fluorescent intensity values were taken at 0.11 µM intervals. Fluorescence intensity values were normalised as a percentage of the highest value. Scale bar: 22.00 µM.

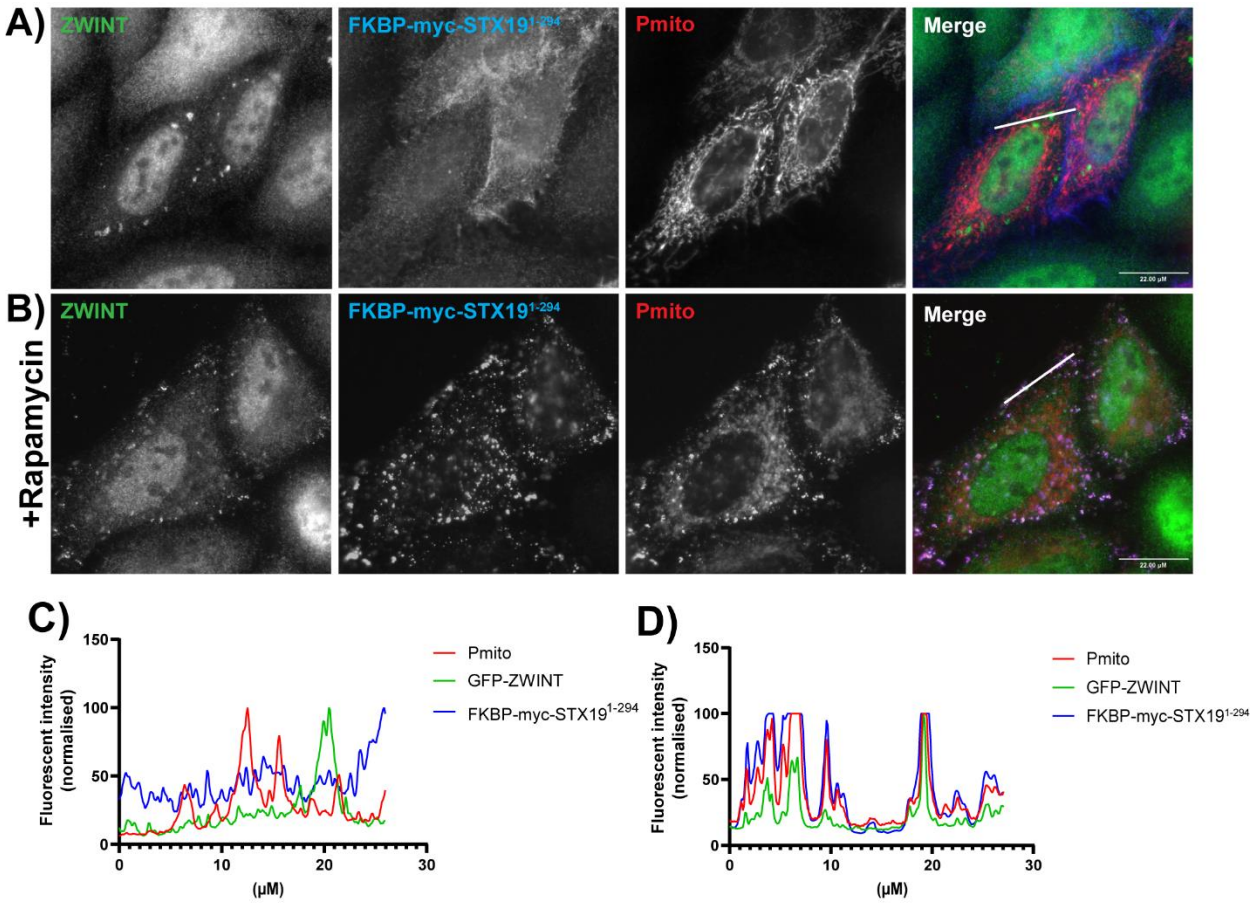

Figure 3-18: Endogenous ZWINT is re-routed to mitochondrial clusters with FKBP-myc-STX19$^{1-294}$ in knocksideways assay. HeLaM cells were transfected with FKBP-myc-STX19$^{1-294}$ and Pmito at the specific concentrations of 0.9 µg and 0.5 µg DNA respectively. Cells were incubated with 1 µM rapamycin for 15 minutes at 37 °C. After rapamycin treatment, cells were fixed using 4 % PFA and stained using anti-myc and anti-ZWINT antibodies. **A)** In the absence of rapamycin, no co-localisation is seen between all three constructs. ZWINT localises to the nucleus, the cytoplasm and unknown puncta. **B)** In the presence of rapamycin, ZWINT is re-routed into mitochondrial clusters with FKBP-myc-STX19$^{1-294}$ and Pmito. A pool of ZWINT remains in the cytoplasm and the nucleus. **C)** Line scan analysis of panel A demonstrating no co-localisation between all three proteins. **D)** Line scan analysis of panel B demonstrates co-localisation of all three proteins through corresponding peaks of intensity when the line dissects mitochondrial clusters. Line scan analysis was performed using ImageJ. The white lines on the images represent the lines along which fluorescent intensity values were taken at 0.11 µM intervals. Fluorescence intensity values were normalised as a percentage of the highest value. Scale bar: 22.00 µM.

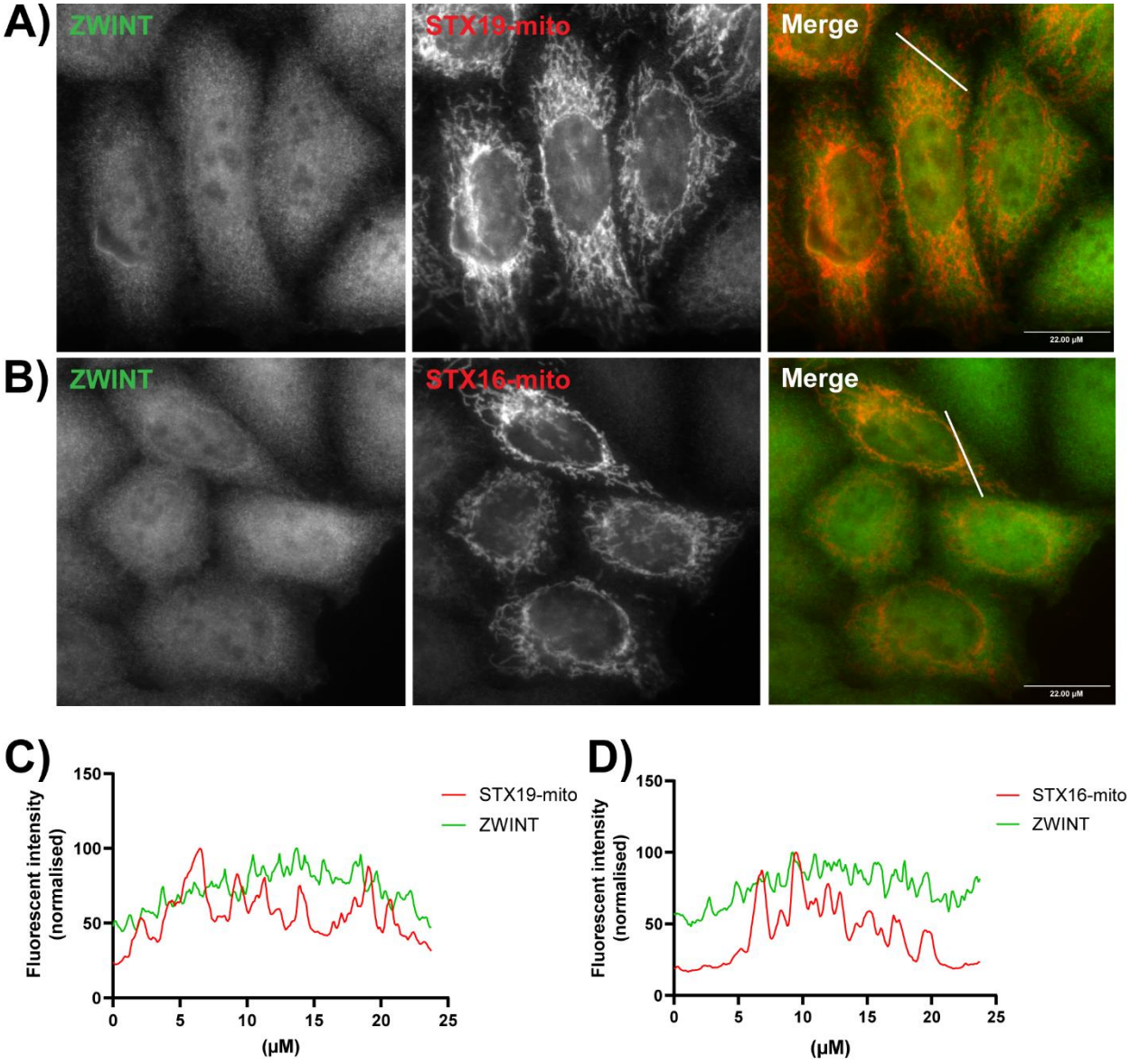

Figure 3-19: STX19-mito does not re-route endogenous ZWINT to the mitochondria. HeLaM cells were transfected with either STX19-mito, or STX16-mito . Cells were then fixed using 4 % PFA and stained using anti-HA and anti-ZWINT antibodies. **A)** ZWINT localises to the cytoplasm and the nucleus. STX19-mito localises to the mitchondria. **B)** ZWINT localises to the cytoplasm and the nucleus. STX16-mito localises to the mitchondria. **C)** Line scan analysis of panel A, STX19-mito and ZWINT, shows no co-localisation. **D)** Line scan analysis of panel B, STX16-mito and ZWINT, shows no co-localisation. Scale bar: 22.00 µM. Line scan analysis of the immunofluorescent microscopy images using ImageJ, % intensity represents the fluorescent intensity normalised against the highest intensity measurment for a given point along the white line indicated in the corresponding microscopy images. Data points were taken at 0.11 µM intervals along the line.

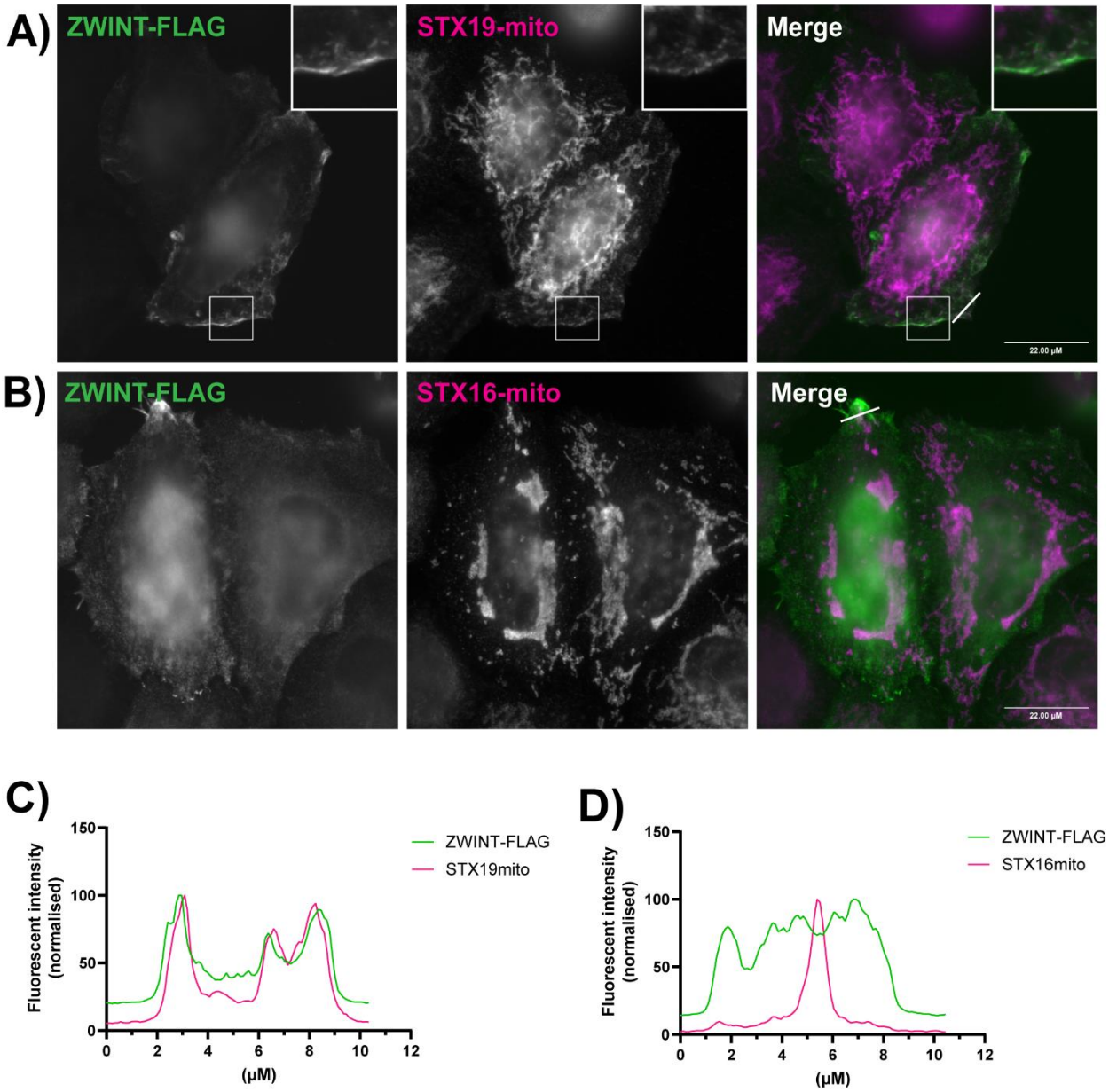

Figure 3-20: STX19-mito co-localises with a pool of ZWINT-FLAG at the plasma membrane. HeLaM cells were transfected with either STX19-mito, or STX16-mito and ZWINT-FLAG at the specific concentrations of 0.9 µg and 0.1 µg DNA respectively. Cells were then fixed using 4 % PFA and stained using anti-HA and anti-FLAG antibodies. **A)** ZWINT localises to distinct domains of the plasma membrane as well as a pool in the cytoplasm. STX-19-mito localises to the mitchondria with a pool of STX19-mito staining in the same domains as ZWINT-FLAG at the plasma membrane. Staining of ZWINT-FLAG and STX19-mito at the plasma membrane is highlighted by the insert. **B)** ZWINT-FLAG localises to distinct domains of the plasma membrane and appears to be enriched in protrusions at the membrane as well as a pool of cytoplasmic localisation. STX16-mito localises to the mitchondria. **C)** Line scan analysis of STX19-mito and ZWINT-FLAG shows show co-localisation between the two constructs through corresponding peaks of fluorescent intensity. **D)** Line scan analysis of STX16-mito and ZWINT shows no co-localisation. Scale bar: 22.00 µM. Line scan analysis of the immunofluorescent microscopy images using ImageJ, % intensity represents the fluorescent intensity normalised against the highest intensity measurment for a given point along the white line indicated in the corresponding microscopy images. Data points were taken at 0.11 µM intervals along the line.

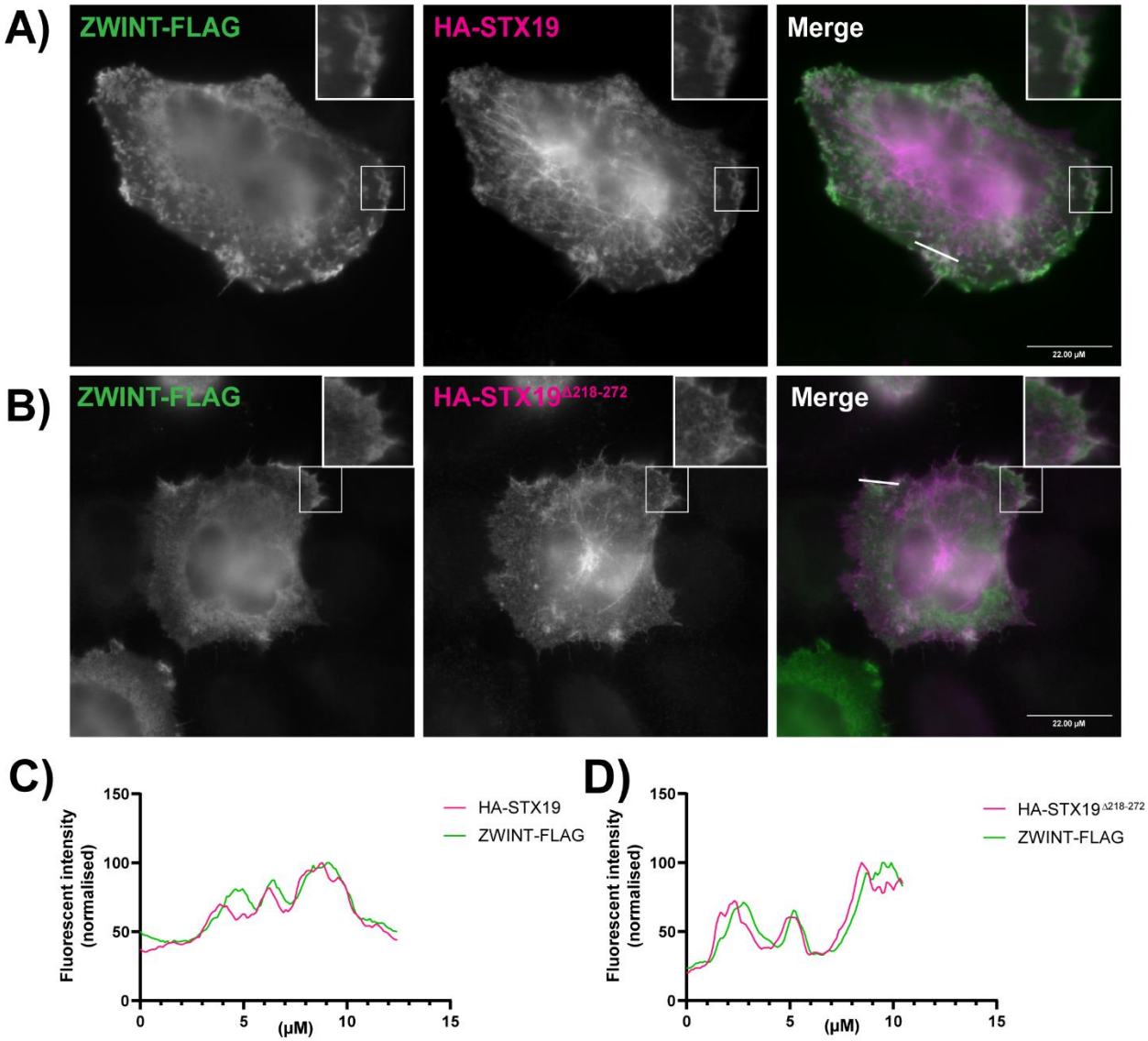

Figure 3-21: HA-STX19 co-localises with a pool of ZWINT-FLAG at the plasma membrane. HeLaM cells were transfected with either HA-STX19, or HA-STX19$^{\Delta 218-272}$, a construct in which the SNARE domain of STX19 has been deleted and ZWINT-FLAG at the specific concentrations of 0.9 µg and 0.1 µg DNA respectively. Cells were then fixed using 4 % PFA and stained using anti-HA and anti-FLAG antibodies. **A)** ZWINT localises to distinct domains of the plasma membrane as well the cytoplasm and unknown puncta. HA-STX19 localises to the same domains of the plasma membrane as ZWINT-FLAG as well as tubular recycling endosomes and the cytoplasm. Staining of ZWINT-FLAG and HA-STX19 at the plasma membrane is highlighted by the insert. **B)** ZWINT-FLAG localises to domains of the plasma membrane as well as the cytoplasm. HA-STX19$^{\Delta 218-272}$ also localises to the same domains of the plasma membrane as ZWINT-FLAG, as well as tubular recycling endosomes and the cytoplasm. Staining of ZWINT-FLAG and HA-STX19$^{\Delta 218-272}$ at the plasma membrane is highlighted by the insert. **C)** Line scan analysis of HA-STX19 and ZWINT-FLAG shows show co-localisation between the two constructs through corresponding peaks of fluorescent intensity. **D)** Line scan analysis of HA-STX19$^{\Delta 218-272}$ and ZWINT-FLAG shows co-localisation between the two constructs through corresponding peaks of fluorescent intensity. Scale bar: 22.00 µM. Line scan analysis of the immunofluorescent microscopy images using ImageJ, % intensity represents the fluorescent intensity normalised against the highest intensity measurment for a given point along the white line indicated in the corresponding microscopy images. Data points were taken at 0.11 µM intervals along the line.

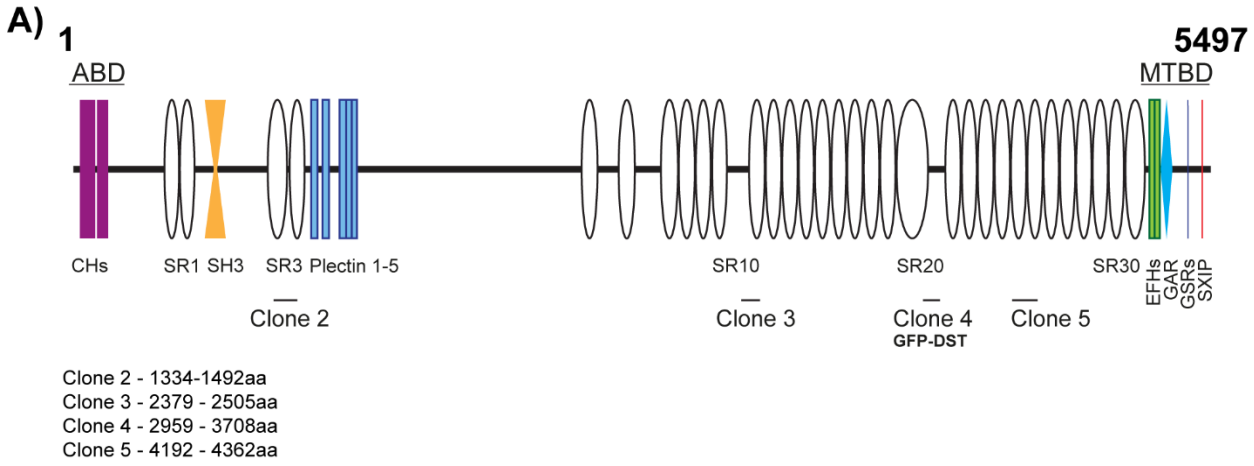

Figure 3-22: Schematic of DST domains and mapping of fragments predicted to interact with STX19 through yeast-two hybrid screening. A) Human Dystonin (DST) consists of 5497 amino acids. The actin-binding domain (ABD) at the N-terminus consists of calponin-homology domains 1 and 2 (CHs) indicated by purple rectangles. 32 spectrin repeats (SR) are indicated by white ovals with black outlines. The Src-homology 3 domain is represent by yellow triangles and the plectin domains (1-5) by blue rectangles. The microtubule-binding domain at the C-terminus consists of EF-hands 1 and 2 (green rectangles), Gas2-related domain (blue diamond), Gly-Ser-Arg (GSR) repeats (dark blue line) and an SxIP motif (red line). The location of the clones predicted to interact with STX19 through yeast-two hybrid screening are indictated by black lines below the main schematic. The amino acid position of the clones is shown below the schematic. Clone 1 overlapped with clone 5 and so was not included. Clone 4 was used to generate a GFP-DST construct used in further interaction studies.

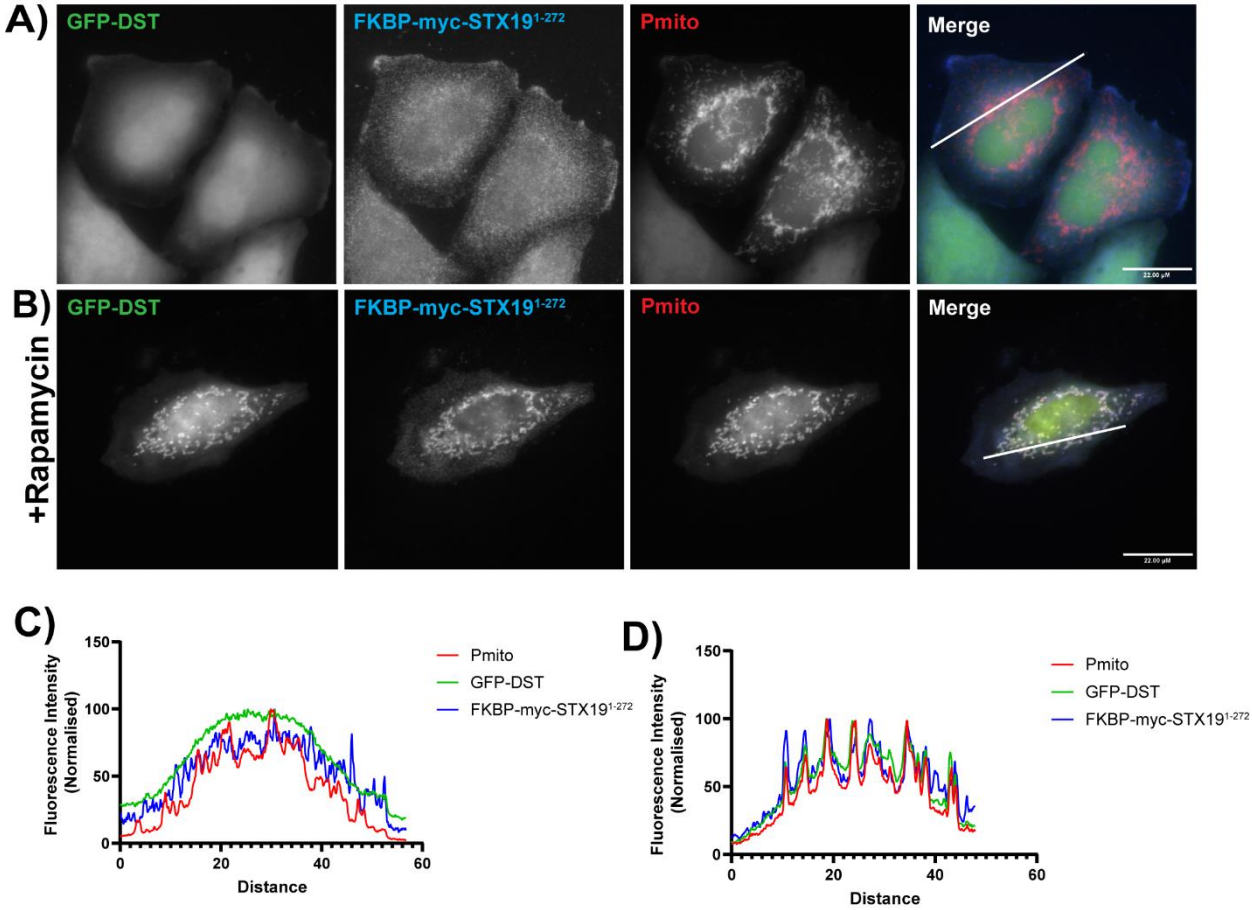

Figure 3-23: GFP-DST is re-routed to the mitochondria by FKBP-myc-STX19$^{1-272}$ in knocksideways assay. HeLaM cells were transfected with GFP-DST, FKBP-myc-STX-19$^{1-272}$ and Pmito at specific concentrations of 0.1 µg, 0.9 µg, and 0.5 µg DNA respectively. Cells were incubated with 1 µM rapamycin for 15 minutes at 37 °C. After rapamycin treatment, cells were fixed using 4 % PFA and stained using anti-myc antibodies. **A)** In the absence of rapamycin, no co-localisation is seen between all three constructs. GFP-DST and FKBP-myc-STX19$^{1-272}$ localises to the cytoplasm and Pmito localises to the mitchondria. **B)** In the presence of rapamycin, FKBP-myc-STX19$^{1-272}$ and GFP-DST are re-routed to the mitochondria. A pool of GFP-Munc18-1 remains cytoplasmic. **C)** Line scan analysis of panel A demonstrating no co-localisation between all three constructs. **D)** Line scan analysis of panel B demonstrates co-localisation of Pmito, FKBP-myc-STX19$^{1-272}$, and GFP-DST through corresponding peaks of intensity. Line scan analysis was performed using ImageJ. The white lines on the images represent the lines along which fluorescent intensity values were taken at 0.11 µM intervals. Fluorescence intensity values were normalised as a percentage of the highest value. Scale bar: 22.00 µM.

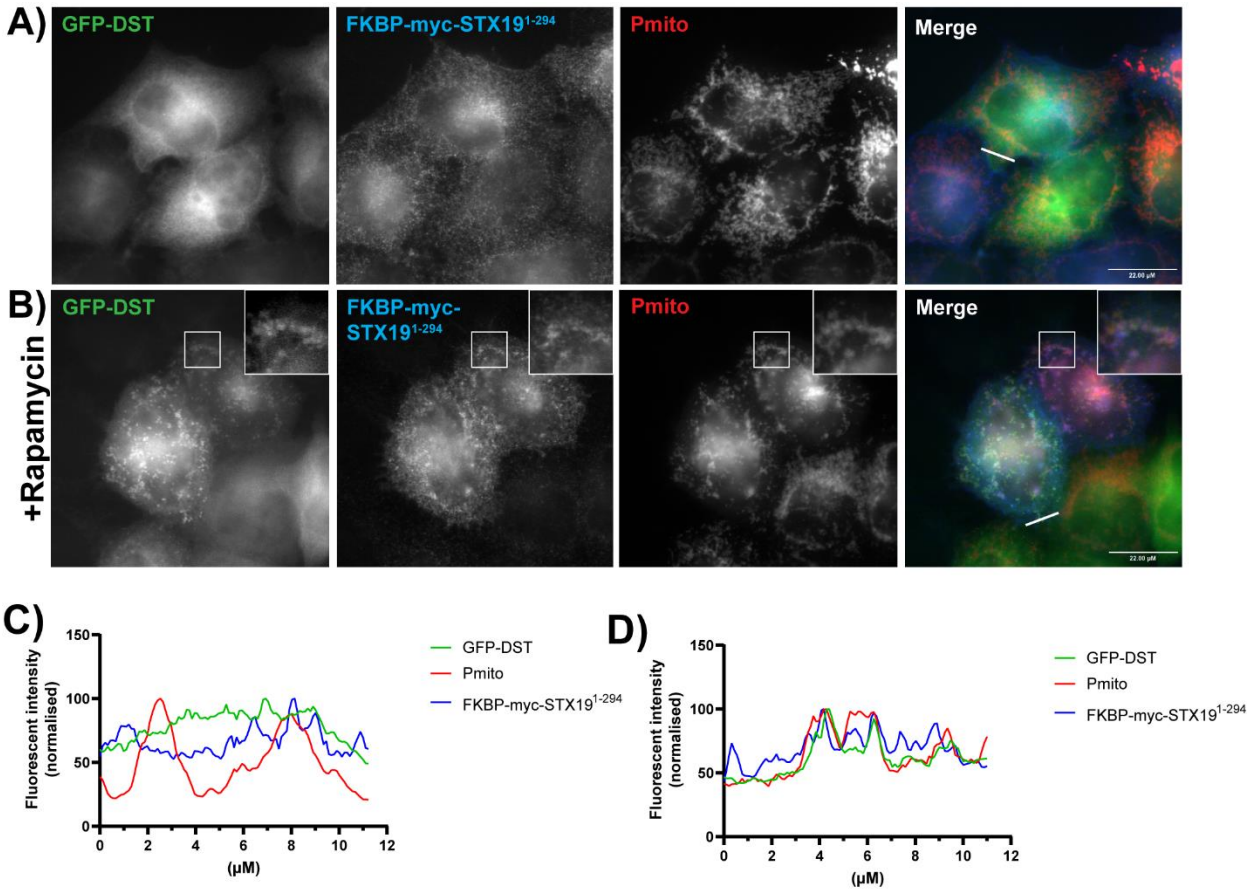

Figure 3-24: GFP-DST is re-routed to mitochondrial clusters with FKBP-myc-STX-19$^{1-294}$ in knocksideways assay. HeLaM cells were transfected with GFP-DST, FKBP-myc-STX19$^{1-294}$ and Pmito at the specific concentrations of 0.1 µg, 0.9 µg, and 0.5 µ g DNA respectively. Cells were incubated with 1 µM rapamycin for 15 minutes at 37 °C. After rapamycin treatment, cells were fixed using 4 % PFA and stained using anti-myc antibodies. **A)** In the absence of rapamycin, no co-localisation is seen between all three constructs. GFP-DST localises to the cytoplasm. **B)** In the presence of rapamycin, FKBP-myc-STX19$^{1-294}$ co-localises with the mitochondria and mitochondrial clusters, GFP-DST is re-routed into mitochondrial clusters with FKBP-myc-STX19$^{1-294}$ and Pmito. **C)** Line scan analysis of panel A demonstrating no co-localisation between all three constructs. **D)** Line scan analysis of panel B demonstrates co-localisation of all three constructs through corresponding peaks of intensity when the line dissects mitochondrial clusters. Line scan analysis was performed using ImageJ. The white lines on the images represent the lines along which fluorescent intensity values were taken at 0.11 µM intervals. Fluorescence intensity values were normalised as a percentage of the highest value. Scale bar: 22.00 µM.

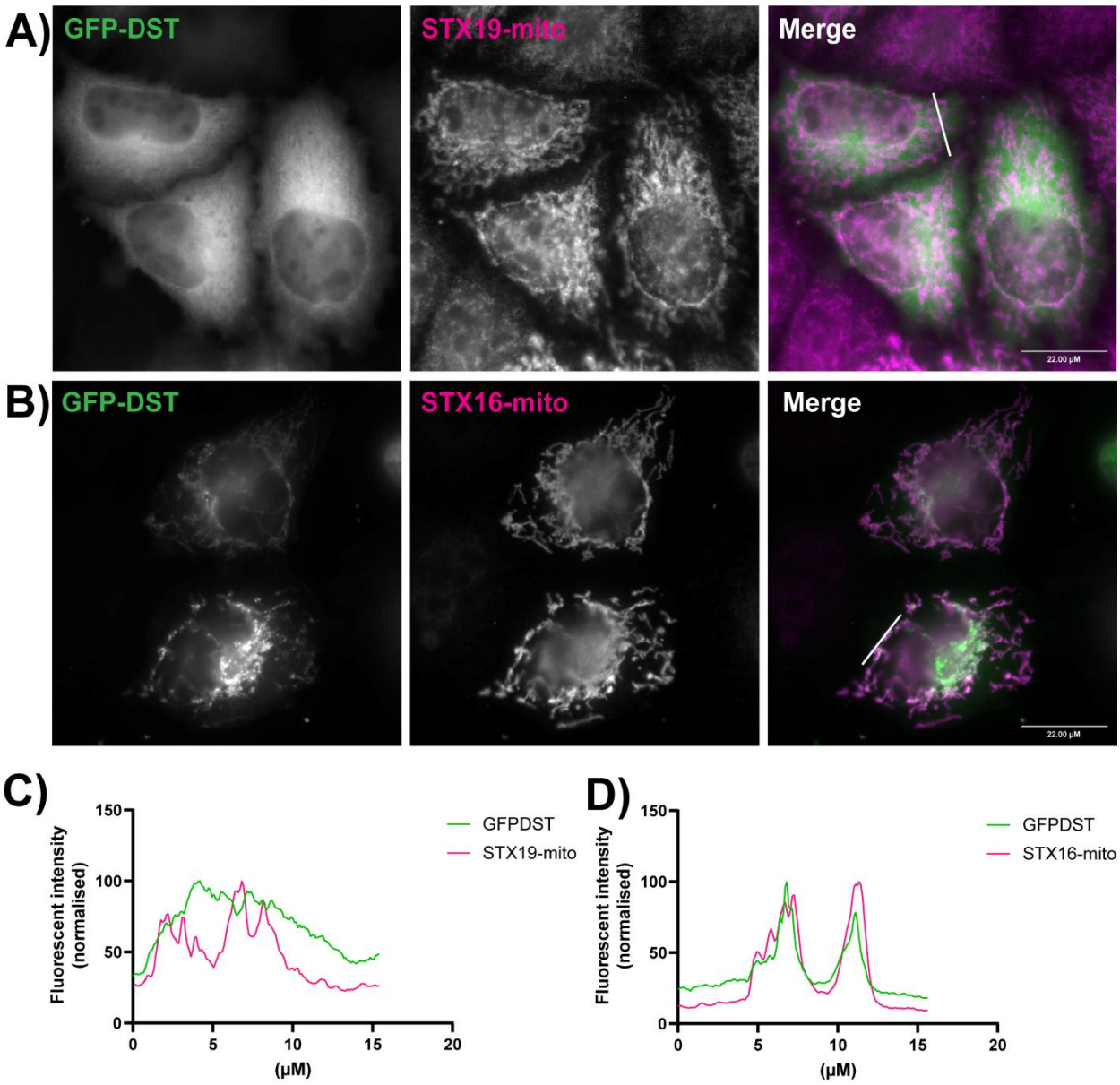

Figure 3-25: STX19-mito does not re-route GFP-DST to the mitochondria. HeLaM cells were transfected with either STX19-mito, or STX16-mito and GFP-DST at the specific concentrations of 0.9 µg STX19-mito construct DNA and 0.1 µg GFP-Munc18-2 DNA. Cells were then fixed using 4 % PFA and stained using anti-HA antibodies. **A)** GFP-DST localises to the cytoplasm. STX19-mito localises to the mitchondria. **B)** Both STX16-mito and GFP-DST localise to the mitochondria. **C)** Line scan analysis of STX19-mito and GFP-DST shows no co-localisation between the two constructs. **D)** Line scan analysis of STX16-mito and GFP-DST demonstrates co-localisation between the two constructs through corresponding peaks of intensity. Scale bar: 22.00 µM. Line scan analysis of the immunofluorescent microscopy images using ImageJ, % intensity represents the fluorescent intensity (normalised against the highest intensity measurment) for a given point along the white line indicated in the corresponding microscopy images. Data points were taken at 0.11 µM intervals along the line.

Chapter 4

Elucidating the pathways and processes STX19 is involved in

4.1 Introduction

To date, very little is known about the function of STX19. Wang et al., first provided insight into the function of STX19 using GST pulldown screens to demonstrate that EGF-R antibodies co-precipitated STX19 expressed in human embryonic kidney 293 cells. However, using STX19 antibodies in pulldowns did not result in significant co-immunoprecipitation of EGF-R. Additionally, overexpression of STX19 in A431 cells was shown to perturb EGF-R internalisation. These data suggested a role for STX19 in the regulation of EGF-R trafficking. It is unclear how STX19 could interact directly with the tyrosine kinase receptor as STX19 does not have any known domains which would allow it to bind the receptor (Wang *et al.*, 2006).

Gordon et al. identified STX19 as a SNARE required for constitutive secretion using a quantitative flow-cytometry based assay to measure constitutive secretion coupled with a SNARE-library siRNA screen. Furthermore, a genome-wide RNAi screen identified STX19 as a protein required for of ER-PM transport of the VSV-G protein (Simpson, Joggerst, Laketa, Verissimo, Cetin, Erfle, Bexiga, Singan, J. K. Hériché, *et al.*, 2012). These data suggest that STX19 has a role in the secretion of soluble and membrane-anchored cargo. To further dissect the role of STX19 in secretion, STX19 was knocked down using siRNA and fusion of exocytic vesicles with the plasma membrane was measured using total internal fluorescence (TIRF) microscopy. This led to a reduction in the number of fusion events at the plasma membrane, which suggests that STX19 is might function in the fusion of post-Golgi transport vesicles with the plasma membrane (Gordon *et al.*, 2010). STX19 does not have a proteinaceous transmembrane domain but instead associates with the membrane via lipid anchor. It is still unclear and debated in the field if SNAREs with lipid anchors are able to physically drive membrane fusion or have a regulatory role (Zhou, Bacaj T, *et al.*, 2013; Chang *et al.*, 2016a; Spessott *et al.*, 2017b).

Additionally, STX19 may regulate fusion at the plasma membrane. STX19 has also been shown to complex with other SNAREs including SNAPs 23, 25, and 29, and VAMPs 3 and 8 through analysis of STX19 interactors by mass-spectrometry (Gordon *et al.*, 2010). These SNAREs are able to drive fusion at the plasma membrane (C. Wang *et al.*, 2004; Morelli *et al.*, 2014; Kubo *et al.*, 2015; Mehlmann, Uliasz and Lowther, 2019). Additionally, Ampah et al., demonstrated that overexpressed STX19 localises to the plasma membrane and tubular recycling endosomes. STX19 localisation at these specific membranes requires S-acylation of a cysteine-rich C-terminal domain that allows its association with membranes. Further investigation using knocksideways assays suggested that STX19 is not cycling on and off but is stably associated with the plasma membrane and tubular recycling endosomes (Ampah *et al.*, 2018). Taken together, this may suggest a role for STX19 at the plasma membrane. Our hypothesis is that STX19 may mediate fusion of secretory vesicles with the plasma membrane in complex with its SNARE binding partners. However, the molecular mechanisms by which STX19 may mediate fusion remains unclear.

To determine where endogenous STX19 localises, Ampah et al., also performed localisation studies using a polyclonal STX19 antibody. These studies demonstrate localisation of endogenous STX19 to tubular recycling endosomes only. Co-localisation studies demonstrated that the tubular recycling endosomes are positive for Rab8, MICAL-L1 (figure 4-1A and B), and cargo such as MHC-I proteins and GPI-anchored proteins (CD55 and CD59) (Ampah *et al.*, 2018). At this tubular recycling endosomal compartment, Rab8 and MICAL-L1 are known to regulate clathrin-independent cargo and receptor recycling (Sharma *et al.*, 2009a). MICAL-L1 is a Rab8 effector that links Rab8 to tubular recycling endosomes to regulate its function. Both Rab8 and MICAL-L1 have been shown to mediate recycling of receptors, (such as β-intergrin receptors) and GPI-anchored cargo through this pathway (Hattula *et al.*, 2006; Sharma *et al.*, 2009b; Rahajeng *et al.*, 2012). Additionally, Wang et al., demonstrated that STX19 overexpression perturbs EGF-R internalisation (Wang *et al.*, 2006). Taken together, this suggests STX19 may have a role in receptor recycling.

Rab8 and MICAL-L1 have also been shown to play roles in exocytosis and trafficking to the plasma membrane (Grigoriev *et al.*, 2011; Sikora *et al.*, 2021). Rab8 is well-documented to have roles in trafficking to the plasma membrane in processes such as polarisation (Sato *et al.*, 2007; Bravo-Cordero *et al.*, 2016)and ciliogenesis (Lu *et al.*, 2015), and has been shown to be important for the docking and fusion of vesicles at the cell surface (Grigoriev *et al.*, 2011). MICAL-L1 has previously been shown to regulate Src trafficking from the endocytic recycling compartment (ERC) to the plasma membrane (Reinecke *et al.*, 2014) and more recently, has been shown to be required for the delivery of cargo, such as TNFα and E-cadherin, to the cell surface (Sikora *et al.*, 2021). Taken together, these data suggest that the tubular recycling endosomal compartment is able to mediate both receptor recycling and delivery to the cell surface. It remains unclear if localisation of STX19 to this compartment is due to its involvement in receptor recycling, delivery to the plasma membrane, or whether STX19 is recycling through this compartment.

Previous studies have suggested a role for STX19 in constitutive secretion. However, its tissue expression and regulation by ubiquitinylation suggest STX19 functions in a specialised secretory pathway rather than bulk secretion. STX19 has a very restricted tissue distribution. Wang et al., reported expression of STX19 in the stomach lining and skin of mice (Wang *et al.*, 2006) and analysis by the GTEx Tissue Expression Project (Lonsdale *et al.*, 2013) show STX19 is expressed only in epithelial tissues and the skin at relatively low levels (figure 4-2A). Data from the International Mouse Phenotyping Consortium shows STX19 expression in mouse stomach, lung, skin, and transverse colon tissues (figure 4-2 B-E; Dickinson *et al.*, 2016). STX19 is also thought to undergo post-translational regulation. STX19 has a degron present in its C-terminal S-acylation domain thus any protein that is not appropriately S-acylated is degraded. STX19 is also thought to contain a second degron upstream of the C-terminal domain as truncated STX19

constructs in which the C-terminal domain has been removed are also degraded. This suggests that STX19 levels are heavily regulated (Ampah *et al.*, 2018). Specific tissue distribution and post-translational regulation of STX19 suggests that STX19 is involved in the secretion of specialised cargo as opposed to playing a role in general secretion. Data from the International Mouse Phenotyping Consortium suggests knockout of STX19 in mice results in decreased circulating insulin levels (Dickinson *et al.*, 2016). This suggests STX19 may play a role in their trafficking, however the physiological processes STX19 is involved in remain unknown.

4.1.1 Chapter aims

Since there are still a number of outstanding questions, we sought to gain further insight into the function of STX19. The aims of the study were:

- To gain insight into the pathways STX19 plays a role in by determining how STX19 overexpression affects SNARE binding partners and compartmental markers
- Establish a physiologically relevant cell model for studying STX19 localisation and function

We sought to address the first aim by analysing the effects of overexpression of STX19 on constitutive secretion using a flow cytometry-based assay (Gordon *et al.*, 2021). Additionally, we aimed to analyse the effect of overexpression of STX19 on other SNAREs STX19 is thought to complex with using immunofluorescence microscopy, TIRF microscopy, and internalisation assays. Finally, we aimed to establish a physiologically relevant cell model for studying STX19 function and characterise the localisation of STX19 using immunofluorescence microscopy. STX19 is enriched in epithelial tissues and the skin. One of the interactors of STX19 highlighted in the previous chapter is DST which has an epithelial isoform enriched in keratinocytes. Additionally, STX19 has been shown to be upregulated 5-fold in differentiated keratinocytes (figure 4-3A; Toufighi *et al.*, 2015). Therefore, to gain further insight into STX19 function, we chose to use keratinocytes as a cell model.

4.1.2 Summary of results

Overall, we found that STX19 overexpression alters the steady state distribution of SNARE binding partner, VAMP8 and causes it to accumulate in enlarged structures. We found STX19 and VAMP8 are enriched in puncta at the cell surface and are co-localised in endocytic carriers following VAMP8 internalisation. This suggests overexpression of STX19 alters VAMP8 dynamics. We hypothesise that STX19 overexpression drives fusion of VAMP8-positive vesicles to STX19-positive compartments resulting in enlarged structures and VAMP8-positive vesicles to the cell surface. After fusion, both proteins are internalised through the same pathway. Additionally, we found co-localisation of STX19, VAMP8, and EGF-R in puncta in the cytoplasm suggesting these three proteins are trafficking the same pathways.

STX19 overexpression results in a loss of the key autophagy proteins, LC3 and P62, which could suggest a role for STX19 in autophagy-mediated pathways. We hypothesise that this could be the result of the altered distribution of VAMP8 and that STX19 overexpression results in the secretion of LC3 through an unconventional autophagy-mediated secretory pathway. However, it remains unclear if STX19 overexpression is physiologically relevant or is observed phenotypes are overexpression artefacts.

Finally, we were able to detect STX19 expression in keratinocytes upon calcium-induced differentiation. We observe that STX19 is enriched in highly polarised regions of the plasma membrane and localises to membrane protrusions of the cells that co-localise with pAKT. Membrane localisation in a physiologically relevant cell model supports our hypothesis that STX19 function occurs at the plasma membrane.

4.2 Results

4.2.1 Attempted knockdown of STX19 to study protein function did not prove successful

In order to gain insight into the function of STX19, we initially sought to knockdown STX19 and screen for any phenotypes in the localisation of STX19 SNARE binding partners, any trafficking machinery, or potential cargo. Despite previous successful attempts in the lab, we could not achieve a convincible level of knockdown using siRNA or tet-inducible shRNA. We first began with a STX19 esiRNA oligo and two different STX19 siRNA oligos (10 and 12). Using a double knockdown protocol, we were able to achieve good knockdown for our positive control, SNAP29 (figure 4-4A and B). However, using the same protocol resulted in a heterogenous level of knockdown for STX19 which would make studying function problematic. In cells treated with STX19 esiRNA, punctate staining in the cytoplasm and tubular recycling endosome (TREs) staining can be seen at an almost comparable level to mock treated cells (figure 4-4C). Cells treated with 50 nM oligo 10 siRNA also display a punctate staining in the cytoplasm. The TRE staining in treated cells appeared much dimmer and less visible than mock treated cells, however it was some staining was still visible (figure 4-4D). In an attempt to optimise STX19 knockdown, we also testing different concentrations of siRNA. Cells treated with 100 nM oligo 10 siRNA also showed punctate staining in the cytoplasm and TRE staining. Some cells appeared to have a reduction in staining at the TREs however, other cells demonstrated staining at the TREs that was comparable to mock treated cells (figure 4-4E). Finally, we attempted knockdown using a second oligo, oligo 12 at 100 nM concentration. Similar to oligo 10, cells treated with oligo 12 siRNA showed varying levels of TRE staining. Some cells seemed to have lost TRE staining but still have punctate staining in the cytoplasm, whilst other cells show staining at the TREs comparable to mock treated cells (figure 4-4F). We therefore, were unsuccessful in our attempts to knockdown STX19.

Another strategy we attempted to knockdown STX19 was using tet-inducible shRNA. In this system, cells are stably transduced with a plasmid containing shRNA downstream of a tet-inducible promoter (figure 4-5A). A GFP reporter is also downstream of the promoter in order to identify cells that should be expressing the shRNA. Addition of tetracycline or doxycycline results in the expression of GFP and shRNA. Our stable cell line shows GFP expression before the addition of doxycycline and addition of doxycycline did not alter the staining pattern of STX19. STX19 in cells treated with doxycycline was still clearly visible on TREs and in a punctate staining pattern in the cytoplasm similar to untreated cells (figure 4-5B and C). Therefore, we were unsuccessful in our attempts to use tet-inducible shRNA to knockdown STX19.

4.2.2 Overexpression of STX19 may alter the steady state levels of a GFP-tagged secretory reporter

Gordon et al., have previously shown that knockdown of STX19 lead to a reduction in secretion using a flow cytometry-based assay to measure secretion (Gordon *et al.*, 2010). It is well known in the field that overexpression of SNARE proteins can drive the fusion they mediate. We therefore speculated that overexpression of STX19 might enhance secretion kinetics. In order to gain insight into the involvement of STX19 in secretion, we overexpressed Strep-tagged STX19 in a flow-cytometry based assay for measuring constitutive secretion. In this assay, cells stably expressing a GFP-tagged mutant FKBP protein are used. This mutant protein forms large molecular assemblies in the ER. Treatment of cells with D/D solubiliser or rapamycin solubilises these assemblies and the GFP-tagged FKBP protein is freely able to traffic from the ER to the Golgi into secretory vesicles which ultimately fuse with the plasma membrane and release their content into the extracellular environment (figure 4-6A). Flow-cytometry is used to measure the amount of GFP fluorescence remaining after treatment as an indicator of constitutive secretion. A reduction in GFP fluorescence indicates secretion.

We compared overexpression of StrepSTX19 to untransfected cells and cells transfected with StrepNSP6. NSP6 is a Sars-CoV2 protein thought to block secretion. Untransfected cells without D/D solubiliser treatment show a clear peak of GFP fluorescence which shifts to the right when cells are treated with D/D solubiliser (figure 4-6B). This indicates a reduction in GFP intensity in these cells corresponding to constitutive secretion of GFP-FKBP.

StrepSTX19 transfected cells without D/D solubiliser show a broader peak of GFP fluorescence intensity compared to the untransfected control. This indicated that there is a larger proportion of cells with reduced GFP intensity than the untransfected control. This suggested that transfection of STX19 could be enhancing a ‘leak’ of the reporter from the cells despite no treatment with D/D solubiliser. Alternatively, transfection of STX19 may disrupt the cells reporter production. StrepSTX19 transfected cells that were treated with D/D solubiliser shows a higher number of cells at a lower GFP intensity suggesting that more cells are secreting GFP-FKBP compared to the untreated cells (figure 4-6C). For direct comparison of

untransfected, untreated cells and StrepSTX19 transfected, untreated cells, we overlaid the two histograms from these samples in one plot (figure 4-6F). StrepSTX19 transfected cells show a broader right-shifted peak of GFP intensity compared to untransfected cells. This suggests loss of GFP intensity in StrepSTX19 transfected cells.

To confirm that transfection of STX19 was responsible for this phenotype and it was not a non-specific artefact of the transfection method, we gated the cells that were untransfected in the StrepSTX19 sample and analysed their GFP intensity. Untransfected cells in the StrepSTX19 sample behaved similarly to cells in the untransfected sample. Cells without D/D solubiliser treatment show a clear peak of GFP intensity which shifts to the right with D/D solubiliser treatment indicating a reduction in GFP intensity and thus secretion of GFP-FKBP (figure 4-6D). This suggests that transfection of Strep-STX19 was responsible for the reduction in GFP intensity without D/D solubiliser. For direct comparison of untransfected cells in the untransfected sample without D/D solubiliser treatment and untransfected cells in the StrepSTX19 sample without D/D solubiliser treatment, we overlaid the two histograms in one plot (figure 4-6G). Both populations of cells show a clear peak at the same level of GFP-intensity. This suggests that there is no reduction in GFP intensity in the untransfected cells of the StrepSTX19 transfected sample and transfection of StrepSTX19 is responsible for the reduction in GFP intensity without D/D solubiliser treatment.

To confirm that this phenotype was due to transfection of STX19 and not general transfection, we also transfected cells with StrepNSP6. StrepNSP6 transfected cells without D/D solubiliser treatment show a clear peak of GFP intensity comparable to the untransfected control. StrepNSP6 transfected cells treated with D/D solubiliser show a peak of GFP intensity that does not considerably shift right (figure 4-6E). This suggests a block in secretion of GFP-FKBP. Nevertheless, the GFP intensity of the StrepNSP6 transfected cells without D/D solubiliser treatment was similar to the untransfected control and did not show the broader peak of GFP intensity as seen in StrepSTX19 transfected cells. This suggests the phenotype seen in StrepSTX19 transfected cells is due to the overexpression of STX19 specifically.

Overall, we found that overexpression of STX19 may result in a reduction in GFP intensity even without D/D solubiliser. This would make analysis of the effect of STX19 overexpression on secretion kinetics challenging to analyse.

4.2.3 Overexpression of STX19 leads to an altered steady-state distribution of VAMP8

Overexpression of STX19 results in its plasma membrane localisation and we predict that STX19 overexpression drives STX19-mediated fusion. Therefore, we reasoned that overexpression of STX19 may alter the localisation of its SNARE binding partners to mediate fusion. It has previously been shown that

STX19 is capable of interacting with VAMP3 and 8 (Gordon *et al.*, 2010). Therefore, we decided to investigate if STX19 overexpression affects their steady state distribution. We hypothesised that overexpression of STX19 may pull VAMPs 3 and 8 onto STX19-positive compartments to mediate fusion. In order to address this, we overexpressed StrepSTX19 in HeLaM cells and stained for various members of the VAMP family.

In cells expressing StrepSTX19, VAMP3 is enriched in the perinuclear region and shows a vesicular staining pattern throughout the cytoplasm. This is the expected staining pattern for VAMP3 and was not grossly altered in transfected cells (figure 4-7A). Similarly, VAMP4 is enriched in the perinuclear region and its staining pattern was not grossly altered in StrepSTX19 transfected cells (figure 4-7B). VAMP7 shows cytoplasmic staining with some enrichment in the perinuclear region. It is not entirely clear if this is specific or background staining, however, the VAMP7 staining pattern did not appear grossly altered in StrepSTX19 transfected cells (figure 4-7C). In non-transfected cells, VAMP8 shows enrichment in the perinuclear region and a diffuse vesicular staining throughout the cytoplasm. In StrepSTX19 transfected cells, the localisation of VAMP8 is altered. The perinuclear pool of VAMP8 is lost and VAMP8 localises to STX19-positive puncta distributed throughout the cytoplasm (figure 4-7D and E). STX19 and VAMP8 signals do not overlap completely but are in close proximity. Inserts on the immunofluorescent images highlighted puncta in which STX19 and VAMP8 are present. To confirm the validity of this phenotype, we used two different VAMP8 antibodies, VAMP8A and VAMP8B. Both antibodies demonstrated altered distribution of VAMP8 in StrepSTX19 transfected cells, suggesting this is a real phenotype. This suggests that overexpression of STX19 may be recruiting VAMP8 into these puncta. We hypothesise that STX19 may be driving the fusion of VAMP8-positive vesicles with this compartment and suggest the puncta are most likely swollen endosomes. Further investigation would be required to determine if the puncta are trafficking compartments and if they are secretory or endocytic.

We sought to determine if STX19 is recruiting VAMP8 into puncta is occurring via interaction with its SNARE domain. Thus, we removed the SNARE domain of STX19 (StrepSTX19$^{\Delta 218\text{-}272}$). This construct should not be able to interact with VAMP8 and drive membrane fusion. In this case, we predicted the altered distribution of VAMP8 would no longer be observed. We also chose to overexpress a STX19 KDR mutant construct (StrepSTX19$^{KDR\text{-}AAA}$) and analyse VAMP8 localisation. Based on our earlier observations, STX19 interacts with Munc18-2 via the N-terminal KDR motif, and we predict that this interaction facilitates STX19 interaction with other SNAREs. Therefore, we were interested to determine how overexpression of STX19 that is unable to bind Munc18-2 would affect the altered distribution of VAMP8 phenotype. HeLaM cells were transfected with either StrepSTX19, StrepSTX19$^{KDR\text{-}AAA}$, or StrepSTX19$^{\Delta 218\text{-}272}$. Cells were then fixed and stained using anti-VAMP8 antibodies.

As previously observed, overexpression of StrepSTX19 resulted in the loss of perinuclear staining for VAMP8 and causes VAMP8 to accumulate in structures which are most likely swollen endosomes (figure 4-8A). This supports our hypothesis that overexpression of STX19 drives fusion of VAMP8-positive vesicles to STX19-positive compartments. Overexpression of StrepSTX19$^{KDR\text{-}AAA}$ also led to a loss of perinuclear VAMP8 staining and results in the altered distribution of VAMP8 into STX19-positive puncta (figure 4-8B). This suggests that the KDR motif is not responsible for the interaction with VAMP8 and the inability of STX19 to bind Munc18-2 does not alter the VAMP8 phenotype. This however does not rule out the idea that Munc18-2 binding could strengthen STX19 interaction with other SNARES. Cells expressing StrepSTX19$^{\Delta 218\text{-}272}$ show a pool of VAMP8 staining at the perinuclear region (figure 4-8C). This suggests that STX19 is interacting with VAMP8 through its SNARE domain to recruit VAMP8 into STX19-positive puncta.

It is possible that expression level of STX19 effects the strength of the phenotype. This makes analysis of the phenotype more challenging and future repeats, quantification, and experiments to analyse steady state distribution of VAMP8 with different STX19 expression levels should be conducted.

Since StrepSTX19 and StrepSTX19$^{KDR\text{-}AAA}$ appeared to affect VAMP8 distribution, we sought to determine if other STX19 mutant constructs are able to reproduce this phenotype. The other STX19 constructs overexpressed included: GFP-STX19, HA-STX19, GFP-STX19$^{275\text{-}294}$, HA-STX19$^{1\text{-}277}$/STX13$^{251\text{-}276}$ and GFP-STX11. Description of these constructs can be found in table 4-1. Previous studies have predicted GFP-STX19 to act in a dominant-active manner as overexpression of GFP-STX19 results in the aggregation of Rab8 to the tips of membrane protrusions (supplementary figure 4-1). Therefore, we wanted to determine how GFP-STX19 expression may affect the distribution of VAMP8. We also chose to overexpress HA-STX19 to be certain that the Strep tag on our previous constructs was not responsible for the altered distribution of VAMP8. GFP-STX19$^{275\text{-}294}$ is a STX19 consisting of only the C-terminal tail of STX19. This tail includes the S-acylation domain required for membrane association. We predicted this would provide insight into if STX19 is causing the altered distribution of the VAMP8 through its C-terminal domain. HA-STX19$^{1\text{-}277}$/STX13$^{251\text{-}276}$ is a hybrid STX19/STX13 construct in which the C-terminal domain of STX19 has been replaced by the transmembrane domain of STX13. We predicted this would provide insight into if STX19 has to be localised to specific membranes to alter the distribution of VAMP8. Finally, we overexpressed GFP-STX11 and analysed the distribution of VAMP8 as a negative control. Descriptions of VAMP8 staining upon expression of these STX19 constructs can be found in Table 4-2. In these experiments, HelaM cells were transfected with one of the STX19 constructs. Cells were then fixed and stained using anti-VAMP8 antibodies.

Overexpression of GFP-STX19 altered the distribution of VAMP8. VAMP8 perinuclear staining is lost and instead VAMP8 localises to puncta distributed throughout the cell. VAMP8 does not co-localise with small bright GFP-STX19 puncta but there is some overlap between GFP-STX19 and VAMP8 in fainter, larger puncta (figure 4-9A). This suggests that GFP-STX19 is acting in a similar manner to Strep-STX19 to alter VAMP8 distribution. Small bright puncta in the GFP-STX19 channel are likely GFP that has been cleaved from the GFP-STX19 construct and degraded. Previous staining experiments using anti-STX19 antibodies have suggested this (data not shown).

Similarly, overexpression of HA-STX19 results in the altered distribution of VAMP8 where the perinuclear staining is lost and VAMP8 localises to puncta throughout the cell. HA-STX19 is not seen in distinct puncta, however, there are membranous structures which appear to be in close proximity to VAMP8-positive puncta (figure 4-9B). This suggests that the altered distribution of VAMP8 is specific to STX19 and is not affected by protein tags.

GFP-STX19$^{275\text{-}294}$ overexpression does not alter the distribution of VAMP8 which shows vesicular staining enriched in the perinuclear region in transfected cells (figure 4-9C). This VAMP8 staining pattern is comparable to non-transfected cells. This suggests that the C-terminal tail of STX19 alone is not sufficient to alter VAMP8 distribution.

Similarly, overexpression of HA-STX19$^{1\text{-}277}$/STX13$^{251\text{-}276}$ does not alter the distribution of VAMP8. HA-STX19$^{1\text{-}277}$/STX13$^{251\text{-}276}$ localises to the plasma membrane as well as showing vesicular staining in the cytoplasm. In transfected cells, VAMP8 shows vesicular staining in the cytoplasm which is enriched in the perinuclear region (figure 4-9D). The STX13 transmembrane domain does not target STX19 to TREs. Whilst the hybrid construct is also on the plasma membrane, we cannot be sure that it is in the same microdomains of the membrane that the C-terminal S-acylation domain would target STX19 to. Therefore, this data suggests that STX19 has to be on TREs or in specific microdomains of the membrane to alter the distribution of VAMP8.

Finally, overexpression of GFP-STX11 shows a cytoplasmic localisation, as well as a small number of bright puncta. In GFP-STX11 expressing cells, VAMP8 shows vesicular staining in the cytoplasm which is enriched in the perinuclear region (figure 4-9E). The steady-state distribution of VAMP8 is not altered in cells expressing GFP-STX11. This suggests the VAMP8 altered distribution phenotype is specific to STX19.

Overall, we find that overexpression of full-length STX19 constructs results in the altered steady-state distribution of VAMP8 regardless of tag. Additionally, the STX19 C-terminal tail domain alone is not sufficient to produce this phenotype. However, overexpression of the STX19/13 hybrid construct shows that STX19 must be on specific membranes to produce this phenotype. Finally, overexpression of GFP-

STX11 did not alter the steady-state distribution of VAMP8 suggesting this is specific to STX19 overexpression.

4.2.4 STX19 is enriched in similar structures to EGF-R and VAMP8

Previous studies have implicated STX19 in EGF-R trafficking. Wang et al., predicted interaction of STX19 and EGF-R and showed that overexpression of STX19 perturbs EGF-R internalisation (Wang *et al.*, 2006). Whilst it seems unlikely that STX19 would directly interact with EGF-R, it may play a role in its trafficking. Proximity-dependent biotinylation assays used to identify potential interactors of STX19 showed an enrichment for EGF-R and Girdin, a downstream effector of AKT that directly interacts with EGF-R to modulate its signalling (Ghosh, Garcia-Marcos and Farquhar, 2011). We therefore, hypothesised that STX19 may be recruiting VAMP8 to endosomal structures to mediate EGF-R trafficking. To address this, HeLaM cells were transfected with StrepSTX19. Cells were then fixed and stained using anti-VAMP8 and anti-EGF-R antibodies.

In StrepSTX19 transfected cells, VAMP8 distribution is altered from the perinuclear region to enlarged structures which are likely endosomes and some of which are STX19-positive, as we had seen previously. There was strong staining of EGF-R in the same structures as STX19. VAMP8 does not completely co-localise with the STX19/EGF-R puncta but seems to be in close proximity as highlighted by the insert (figure 4-10A). This suggests that overexpressed STX19 may be localised to EGF-R-positive compartments and recruiting VAMP8-positive vesicles into close proximity. As these experiments were conducted using widefield microscopy, it would be useful to analyse localisation using confocal or super-resolution microscopy and use Pearson's correlation coefficient to determine how well the STX19, EGF-R, and VAMP8 co-localise.

4.2.5 VAMP8 is present in STX19-positive puncta at the cell surface

Based on our previous findings, we hypothesised that STX19 overexpression is altering the distribution of VAMP8 driving fusion of VAMP8-positive vesicles to STX19-positive compartments forming enlarged endosomal structures and to the plasma membrane. In order to investigate STX19 and VAMP8 at the cell surface, we overexpressed STX19 and used total internal reflection fluorescence (TIRF) microscopy to observe STX19 and VAMP8 localisation at the surface of the cell. TIRF microscopy allowed us to image at a 100 nM depth from the cell surface. HeLaM cells were transfected with either StrepSTX19 or GFP-STX11. Cells were then fixed and stained using anti-VAMP8 antibodies and analysed by TIRF microscopy.

We found that STX19 and VAMP8 localise to a number of puncta distributed across the cell surface. We do not see complete overlap of STX19 and VAMP8 puncta however, there are a number of puncta which are enriched for both STX19 and VAMP8 (figure 4-11A). This demonstrates STX19 and VAMP8 are in close

proximity to one another in distinct regions of the plasma membrane. We also overexpressed GFP-STX11 and analysed VAMP8 localisation as a negative control (figure 4-11B). There was limited overlap between GFP-STX11 and VAMP8-positive puncta. These data support our hypothesis that overexpression of STX19 is recruits VAMP8 to the cell surface.

As previous results had shown EGF-R in STX19-positive puncta in close proximity to VAMP8, we wanted to determine if STX19, VAMP8, and EGF-R were enriched in the same regions at the cell surface. Therefore, we overexpressed StrepSTX19 and analysed localisation of VAMP8 and EGF-R using TIRF microscopy. From this, we observed localisation of STX19, VAMP8, and EGF-R to puncta in the TIRF field, highlighted by the insert (figure 4-12A). These puncta therefore may be at the cell surface or just below. Interestingly, a pool of these markers appears to be enriched in similar domains of the plasma membrane. However, it remains unclear if STX19, EGF-R, and VAMP8 co-localise in the same puncta or are only enriched in similar regions. Further analysis using higher resolution microscopy and Pearson's correlation coefficient would provide further insight. There were also puncta in which STX19 and VAMP8 were localised that did not display EGF-R enrichment (figure 4-12B). Some cells display patches of STX19 at the cell surface which are not enriched with VAMP8 but seem to be highly enriched with EGF-R (figure 4-12C). The variable results make it difficult to distinguish overlap between EGF-R, VAMP8, and STX19 is due to STX19 overexpression. There was, however, limited overlap between EGF-R, VAMP8 and GFP-STX11 at the cell surface (figure 4-12D). Taken together, this could suggest STX19 has a role in EGF-R delivery or recycling at the cell surface, but the nature of the patches (endocytic or secretory) remains unclear. Alternatively, STX19 may not be directly involved with EGF-R trafficking but could be recycling through the same pathways.

These data suggests that VAMP8 localises to STX19-positive puncta at the cell surface and suggests that overexpression of STX19 is altering VAMP8 distribution by pulling it away from the perinuclear region to the plasma membrane. Limited localisation of VAMP8 to GFP-STX11 positive puncta at the surface suggests this is specific to STX19.

Based on our data, we hypothesis that overexpression of STX19 may be altering the distribution of VAMP8 by A) recruiting and driving fusion of VAMP8-postive vesicles to STX19-positive compartments which are most likely endosomes which may be positive for EGF-R and B) recruiting and driving fusion of VAMP8-positive vesicles with the plasma membrane. VAMP8/EGF-R/STX19-positive structures are likely deeper in the cell and not at the cell surface. It is possible that co-localisation of EGF-R and STX19 at the cell surface may represent smaller trafficking vesicles in which VAMP8 is not present.

4.2.6 STX19 co-localises with VAMP8 in endocytic carriers

Based on our previous findings, our hypothesis is that STX19 overexpression leads to the recruitment and fusion of VAMP8-positive vesicles to the cell surface. We therefore reasoned that if there is more VAMP8 at the cell surface in STX19 transfected cells, there was likely to be a greater amount of VAMP8 internalisation and recycling. To address this, we generated a cell line stably expressing HA-VAMP8 and performed antibody uptake assays. HeLaM cells stably expressing HA-VAMP8 were transfected with either StrepSTX19, StrepSTX19$^{\Delta 218\text{-}272}$, or GFP-STX11. Cells were incubated with culture media containing anti-HA antibodies for 30 minutes to allow anti-HA antibody internalisation. Cells were then fixed and stained with secondary antibodies.

After antibody uptake, HA-VAMP8 localises to puncta in the cytoplasm. We found that these puncta were also highly enriched with StrepSTX19, highlighted by the insert (figure 4-13A). Line scan analysis suggests co-localisation of HA-VAMP8 and StrepSTX19 in these compartments (figure 4-13D). This suggests that StrepSTX19 and VAMP8 are present in the same endocytic carriers. We reasoned that this may be due to overexpressed STX19 pulling VAMP8 to the cell surface and subsequently both proteins recycled together in the same pathway. Which recycling pathways these are remains unclear. It would be interesting to determine if VAMP8 would usually traffic through this pathway or if STX19 overexpression alters the recycling kinetics of VAMP8.

Additionally, we also found that StrepSTX19$^{\Delta 218\text{-}272}$ co-localises with HA-VAMP8 in puncta distributed throughout the cell after antibody uptake, highlighted by the insert (figure 4-13B). Line scan analysis suggests co-localisation between HA-VAMP8 and StrepSTX19$^{\Delta 218\text{-}272}$ in these puncta (figure 4-13E). The intensity of StrepSTX19$^{\Delta 218\text{-}272}$ in VAMP8-positive puncta appears to be weaker than that of wildtype StrepSTX19. However, further investigation would be required to quantify the level of intensity for each construct to determine if there is a significant, reproducible difference.

GFP-STX11 does not co-localise with HA-VAMP8-positive puncta after antibody uptake (figure 4-13C and F). This suggests that VAMP8 internalisation is not altered to recycling pathways for any given overexpressed SNARE but is specific to STX19.

Overall, we have found that StrepSTX19 and HA-VAMP8 are present in the same endocytic carriers following antibody induced internalisation of VAMP8. We found that loss of the STX19 SNARE domain does not appear to effect VAMP8 internalisation through this pathway.

4.2.7 STX19 overexpression may alter the distribution of lysosomal markers

Based on previous findings, our hypothesis was that STX19 overexpression recruits and drives fusion of VAMP8-positive vesicles with STX19-positive compartments and the plasma membrane. VAMP8 has been

previously shown to mediate late endosome and lysosome fusion (Pryor *et al.*, 2004; Davis *et al.*, 2021). We therefore questioned if STX19 overexpression was altering lysosomal distribution. To address this, we sought to determine if STX19 overexpression had any effect on the distribution of lysosomal markers. HeLaM cells were transfected with StrepSTX19 and fixed and stained for lysosomal markers, CD63 and LAMP1 (Eskelinen, 2006; Pols and Klumperman, 2009).

In non-transfected cells, CD63 localises to late endosomes and lysosomes that are largely concentrated in the perinuclear area. There is also a pool of vesicular staining distributed throughout the cytoplasm. In StrepSTX19 transfected cells, there are reduced levels of CD63 and fewer CD63-positive puncta (figure 4-14A and B). StrepSTX19 puncta do not co-localise with CD63 puncta suggesting StrepSTX19 is not present in late endosomes or lysosomes. These data suggest that StrepSTX19 alters the distribution of CD63-positive puncta.

To determine if STX19 overexpression alters the distribution of lysosomes or the localisation of CD63 to lysosomes, we overexpressed STX19 and analysed the distribution of a second lysosomal marker, LAMP1. In non-transfected cells, LAMP1 localises to late endosomes and lysosomes that are largely concentrated in the perinuclear area. In StrepSTX19 transfected cells, there are fewer LAMP1-positive puncta which appear dispersed towards the periphery of the cell (figure 4-14C and D). These data suggest STX19 overexpression alters the distribution of lysosomes. However, it remains unclear if altered lysosomal distribution is a result of STX19 overexpression or if some cells naturally have different distributions of lysosomes. As such, it will be important to quantify of the number of CD63 and LAMP1-positive puncta, the intensity levels of CD63 and LAMP1, and the distance of puncta from the perinuclear region in future studies.

To further explore this potential distribution phenotype, we chose to overexpress the STX19 constructs described in Table 4-1. HeLaM cells were transfected with the STX19 constructs and fixed and stained using anti-CD63 antibodies. In GFP-STX19 transfected cells, CD63 localises to a number of puncta in the cytoplasm and a pool of puncta are concentrated in the perinuclear area (figure 15-A). There appears to be less vesicular staining of CD63 in GFP-STX19 transfected cells. This could suggest that CD63 is being recruited to lysosomes more so than in non-transfected cells, however this further investigation would be required to measure the amount of CD63 vesicular staining in the cytoplasm compared to the amount of CD63 associated with lysosomes. Additionally, there is a small amount of overlap between GFP-STX19 and CD63-positive puncta. Previous experiments in the lab have shown GFP, but not STX19, is present in these puncta (data not shown). This suggests the GFP is being cleaved from the GFP-STX19 construct and being turned over in lysosomes.

To confirm altered distribution of CD63 in StrepSTX19 transfected cells was not a result of strep tag expression, we also transfected cells with HA-STX19 and stained for CD63. There appear to be fewer CD63 puncta in HA-STX19 transfected cells compared to untransfected cells, particularly in the perinuclear region (figure 15-B). CD63 puncta in HA-STX19 transfected cells also are dispersed towards the periphery of the cell. Additionally, there is a less CD63 vesicular staining in the cytoplasm than untransfected cells. Therefore, this suggests the tags in these constructs is not responsible for the altered distribution of CD63.

We expressed GFP-STX19$^{275\text{-}294}$ to determine if the C-terminal S-acylation domain of STX19 alone was able to alter the distribution of CD63. In cells expressing GFP-STX19$^{275\text{-}294}$, CD63 localises to a number of puncta particularly concentrated around the perinuclear area, as well as a vesicular staining in the cytoplasm (figure 4-15C). We did not observe a great difference in CD63 staining between transfected and untransfected cells. Additionally, GFP-STX19$^{275\text{-}294}$ puncta co-localise with CD63 puncta suggesting this construct is being degraded in lysosomes. Therefore, we reasoned that altered distribution of CD63 relies on a domain of STX19 that has been removed from the GFP-STX19$^{275\text{-}294}$ construct.

Finally, a HA-STX19$^{1\text{-}277}$/STX13$^{251\text{-}276}$ hybrid construct was used to determine if STX19 has to be associated with tubular recycling endosomes in order to alter the distribution of CD63. HA-STX19$^{1\text{-}277}$/STX13$^{251\text{-}276}$ localises to the plasma membranes and shows vesicular staining enriched in the perinuclear area. CD63 localises to late endosomes and lysosomes, mostly concentrated in the perinuclear area (figure 4-15D). HA-STX19$^{1\text{-}277}$/STX13$^{251\text{-}276}$ does not alter the steady-state distribution of CD63. This suggests that STX19 needs to be localised to the tubular recycling endosomes or specific microdomains of the plasma membrane to alter the distribution of CD63. These data are summarised in table 4-2.

As we observed an altered LAMP1 distribution in StrepSTX19 transfected cells, we also chose to analyse the distribution of LAMP1 upon expression of the STX19 constructs. HeLaM cells were transfected for one of the STX19 constructs then fixed and stained using anti-LAMP1 antibodies. GFP-STX19, HA-STX19, and HA-STX19$^{1\text{-}277}$/STX13$^{251\text{-}276}$ transfected cells show dispersal of LAMP1-positive puncta at the cell periphery (figures 4-16A, B, and D). Cells transfected with GFP-STX19$^{275\text{-}294}$ show LAMP1-positive puncta mostly concentrated in the perinuclear region of the cells with less LAMP1-positive puncta towards the periphery of the cell (figure 4-16C). GFP-STX19$^{275\text{-}294}$ also shows co-localisation with LAMP1-positive puncta suggesting it is being turned over in lysosomes. These results differ slightly from we had previously seen with CD63. GFP-STX19 and HA-STX19$^{1\text{-}277}$/STX13$^{251\text{-}276}$ did not appear to alter the distribution of CD63 but did alter the distribution of LAMP1. However, these results should be taken with careful consideration as it is difficult to tell by eye if there is an increase in the number LAMP1-positive puncta at the cell periphery. Further investigation and quantification of both these phenotypes is required to truly understand the

effect the STX19 overexpression on the distribution of lysosomes. These data are summarised in table 4-2.

4.2.8 STX19 overexpression results in a striking change in the levels of autophagosomal markers

Based on previous data, we hypothesised that overexpression of STX19 is recruiting and driving fusion of VAMP8-positive vesicles to STX19-positive compartments and the plasma membrane. VAMP8 has a role in mediating the fusion of autophagosomes and lysosomes during autophagy in complex with STX17 and SNAP29 (Itakura, Kishi-Itakura and Mizushima, 2012). Additionally, STX19 was found to have two LIR motifs by peptide blot analysis suggesting it may have the ability to bind key the autophagy protein, LC3 (Gu *et al.*, 2019). As VAMP8 is involved in autophagy, we questioned how overexpression of STX19 affected the distribution of autophagosomes. To address this, we overexpressed StrepSTX19 or GFP-STX11 as a negative control, serum starved the cells to induce autophagy, and stained for proteins with a role in autophagy, LC3 and P62. LC3 is a key protein associated with autophagosomal membranes and involved in various aspects of the autophagy pathway including autophagosomal biogenesis (Kabeya *et al.*, 2000; Xie, Nair and Klionsky, 2008; Gu *et al.*, 2019) P62 interacts with LC3 and is involved in recruitment of protein aggregates into autophagosomes for degradation (Pankiv *et al.*, 2007). In untransfected cells, LC3 shows a punctate staining pattern likely to be autophagosomes or autolysosomes, and P62 shows a cytoplasmic staining where it localises prior to autophagosomal recruitment. Cells expressing StrepSTX19 demonstrate a striking reduction in staining of both LC3 and P62 (figures 4-17A and C). This suggests overexpression of STX19 alters the levels of LC3 and P62. GFP-STX11 has a punctate staining pattern as well as vesicular staining in the cytoplasm. The GFP-STX11 puncta co-localise with LC3 and P62 puncta (figures 4-17B and D) suggesting it is being turned over by autophagy.

To gain further insight how STX19 overexpression may result in loss of LC3 staining, we sought to determine if STX19 constructs described in table 4-1 also result in the same loss of LC3. HeLaM cells were transfected with one of the STX19 constructs. Cells were then fixed and stained using anti-LC3 antibodies.

Cells transfected with GFP-STX19 also show a striking loss of LC3-positive puncta (figure 4-18A). Future experiments with GFP or Strep-GFP transfected cells would be a useful control. Some cells transfected with HA-STX19 also demonstrate loss of LC3-positive puncta. There are however, transfected cells that still show LC3 staining, though there appears to be less LC3-positive puncta compared to untransfected cells (figure 4-18B). Therefore, quantification of this phenotype is necessary. This suggests that the overexpression of full-length STX19 constructs result in a loss of LC3 staining in some cells despite the tag. Cells transfected with the STX19 C-terminal tail construct, GFP-STX19$^{275-294}$, have punctate LC3 staining comparable to untransfected cells (figure 4-18C). This suggests the STX19 C-terminus alone is not sufficient to result in this phenotype and loss of LC3 staining must be mediated through a different domain

in STX19. HA-STX19$^{1-277}$/STX13$^{251-276}$ transfected cells also show punctate LC3 staining (figure 4-18D). This suggests that STX19 must be targeted to the specific membranes to result in loss of LC3 staining. These data are summarised in table 4-2.

Based on these data, one hypothesis is that STX19 overexpression may be recruiting LC3 containing structures to the cell surface and may ultimately lead to their secretion from the cell. During previous experiments, we analysed LC3 staining 24 hours post-transfection with STX19 which resulted in a large reduction in LC3 staining. We rationalised analysing LC3 expression at an earlier time point might allow to us to determine if LC3 localisation is altered prior to its loss. We predicted that if STX19 leads to the secretion of LC3, that LC3-positive compartments may be distributed towards or localise to the plasma membrane at an earlier time point. Therefore, we overexpressed STX19, serum starved the cells 6 hours post-transfection, and fixed and stained using anti-LC3 antibodies 12 hours post-transfection.

After 12 hours, cells expressing StrepSTX19 show a striking reduction in LC3-positive puncta compared to non-transfected cells similar to 24 hours post-transfection (figure 4-19A). However, cells expressing StrepSTX19 show cytoplasmic P62 staining 12 post-transfection (figure 19-C). This is in contrast to 24 hours post-transfection in which we saw a decrease in P62 staining. This suggests that loss of LC3-positive puncta preceeds loss of P62 staining. Therefore, it is unlikely that the loss of P62 staining is due to an upregulation of autophagy since LC3 would be required for this process. In cells expressing GFP-STX11, GFP-STX11 has a cytoplasmic localisation as well as puncta distributed throughout the cell (figures 4-19B and D). There is co-localisation between GFP-STX11 and LC3 and P62 puncta. This suggests that, as seen previously, GFP-STX11 is recruited into autophagosomes 12 hours post-transfection.

Overall, we found that overexpression of full-length STX19 constructs results in the loss of LC3 and P62 staining 24 hours post-transfection. We found that loss of LC3 occurs earlier than P62 as a reduction in LC3 expression can be seen 12 hours post-transfection. Taking this data in conjunction with the altered distribution of VAMP8 upon overexpression, one hypothesis may be that overexpression of STX19 is recruiting VAMP8-positive compartments such as LC3-positive autophagosomes to the plasma membrane and leading to their secretion. However, additional investigation will be required to gain more insight into the effect of STX19 overexpression on autophagy-dependant pathways.

4.2.9 Establishing a physiologically relevant cell model for STX19 studies

Previous studies and experiments in this chapter were conducted in HeLaM cells. However, physiologically, STX19 is enriched in epithelial tissues and the skin (Wang *et al.*, 2006; Lonsdale *et al.*, 2013). Therefore, to truly understand the function of STX19, it is necessary to study STX19 in a physiologically relevant cell model. Based on our experimental data, we predict that STX19 mediates

fusion at the plasma membrane as expressed STX19 localises to the plasma membrane and it interacts with SNAPs 23, 25, and 29, and VAMPs 3 and 8 which are known to be able to mediate fusion at the membrane. However, it is unclear where STX19 localises in epithelial and skin cells. Therefore, one of the aims of this study was to establish a physiologically relevant cell model to study STX19 function and characterise STX19 localisation. Analysis of gene expression changes during calcium-induced keratinocyte differentiation revealed a 5-fold upregulation of STX19 (figure 4-3A; Toufighi *et al.*, 2015). Based on this, we predicted that STX19 would be functioning in differentiated keratinocytes. Therefore, we decided to use keratinocytes as a relevant model of STX19 expression.

We first aimed to successfully induce differentiation in human epidermal keratinocytes. We based on our protocol on the study that identified STX19 upregulation in differentiated keratinocytes. Human epidermal keratinocytes were cultured at <50 % confluency in 0.05 mM calcium and 10 ng/µL EGF to maintain an undifferentiated state and then treated with 1.2 mM calcium to induce differentiation for 48 hours. Untreated keratinocytes have a small, elliptical, relatively flat morphology and are generally well distributed (figure 4-20A). After calcium treatment, the keratinocytes are clustered together in large masses. Cells towards the edges of the masses are much larger in size than those in the middle and untreated keratinocytes (figure 4-20B). This change in morphology suggests differentiation of the keratinocytes as they start to form an epithelial sheet. Further staining with keratinocyte differentiation markers would be important to confirm keratinocyte differentiation.

4.2.9.1 STX19 localises to distinct regions of the plasma membrane in differentiated keratinocytes

As STX19 is thought to be upregulated after calcium-induced differentiation, we aimed to determine where STX19 localises in differentiated keratinocytes and compare expression to undifferentiated keratinocytes. Undifferentiated and differentiated keratinocytes were stained for STX19 using anti-STX19 antibodies. Undifferentiated keratinocytes show a faint staining pattern which is likely background staining (figure 4-21A). This suggests there is very little STX19 expression in undifferentiated keratinocytes. In contrast, differentiated keratinocytes show STX19 specific staining at the plasma membrane in distinct polarised regions which generally appear to be at the edges of cells facing the extracellular environment (figure 4-21B). Additionally, 'fish scale-like' STX19 staining can be seen at the tips of cells that appear to be growing over each other (figure 4-21C). In some cells, we also observed STX19 localisation to tubular structures emanating from regions of the plasma membrane where STX19 is enriched (figure 4-21D).

4.2.9.2 VAMP3 and VAMP8 localise to the plasma membrane in differentiated keratinocytes

As we have shown, STX19 can localise to the plasma membrane in HeLaM cells and keratinocytes. Since STX19 is also able to interact with VAMP3 and 8 known to mediate fusion with the plasma membrane, we sought to understand if VAMP3 and VAMP8 localise to similar regions of the membrane as STX19 in keratinocytes. Unfortunately, we were unable to co-stain STX19 and VAMP3 and 8 as these antibodies are raised in the same species. However, we stained keratinocytes with antibodies against VAMP3 and 8 to determine if they localise to the plasma membrane. In undifferentiated keratinocytes, VAMP3 localises to the distinct regions of the plasma membrane and shows a pool of cytoplasmic staining. After differentiation, VAMP3 shows a polarised localisation at distinct regions of the plasma membrane that face the extracellular space and shows localisation to vesicular structures within the cytoplasm (figure 4-22A).

In undifferentiated keratinocytes, VAMP8 demonstrates vesicular staining. In differentiated keratinocytes, VAMP8 localises to distinct regions of the plasma membrane that face the extracellular space (figure 4-22B). Polarised localisation of VAMP8 to distinct regions of the plasma membrane in differentiated keratinocytes could corresponds to the localisation of STX19. It would be interesting to determine if STX19 and VAMP8 are localised to the same regions of the membrane.

4.2.9.3 STX19 does not co-localise with DST in differentiated keratinocytes

As discussed in the previous chapter, STX19 is thought to interact with DST. DST has an epithelial-specific isoform which is expressed in keratinocytes. The epithelial isoform of DST (BPAG1-e) has been shown to localise to hemidesmosomes which are structures that attach keratinocytes to the basal lamina (Borradori and Sonnenberg, 1999; Leung *et al.*, 2001; Litjens, JM and A, 2006). We hypothesised that STX19 may play a role in delivering proteins to hemidesmosomes required for cell attachment through interaction with DST. Therefore, we questioned if STX19 was localised to the same regions as DST in keratinocytes and addressed this by staining for STX19 and DST.

In undifferentiated and differentiated keratinocytes, DST localises to unique structures at the cell surface. These structures consist of a short section of membrane staining with a number of puncta just below (figures 4-23A and B). Based on current literature, we predict these structures are hemidesmosomes as this is where DST is known to localise in keratinocytes (Walko, Castañón and Wiche, 2015). In undifferentiated cells, STX19 shows very little expression as seen previously. In differentiated cells, STX19 is enriched in distinct regions of the plasma membrane that are protruding from the cells (figure 4-23C). There is no staining for STX19 in DST-positive structures and no staining for DST in STX19-enriched regions.

Therefore, these data suggest that STX19 is not localised to hemidesmosomes, and it is unlikely STX19 is involved in cargo delivery required for cell attachment.

4.2.9.4 STX19 localises adjacently to E-cadherin and β-catenin in membrane protrusions of differentiated keratinocytes

One of the important processes that occurs during keratinocyte differentiation is the formation of adherens junctions between cells. In the yeast-two hybrid screens to identify STX19 interactors perfomed previously in the lab, a number of proteins that are involved in formation of maintenance of adherens junctions were pulled down. These included Abl2 which preserves adherens junction integrity (Botros *et al.*, 2020), TRIO – a RhoGEF that complexes with RhoA and a calcium sensing receptor (CasR) at adherens junctions (Kruse *et al.*, 2019), and RASSF8 has been shown to regulate adherens junctions in *Drosophila* (Zaessinger *et al.*, 2015). We therefore hypothesised that STX19 may be mediating the trafficking of proteins to adherens junctions. To address this, we co-stained keratinocytes with STX19 and two markers of adherens junctions, E-cadherin and β-catenin.

In undifferentiated keratinocytes, E-cadherin and β-catenin localise to the plasma membrane between neighbouring cells (figures 4-24A and 4-25A). STX19 shows little expression in undifferentiated cells. In differentiated keratinocytes, E-cadherin and β-catenin largely localise to the membranes between neighbouring cells and E-cadherin shows a pool of staining at membranes facing the extracellular space STX19 is enriched in specific regions of the membrane facing the extracellular, however, STX19 is not in the same plasma membrane regions as E-cadherin or β-catenin (figures 4-24B and 4-25B). Additionally, E-cadherin and β-catenin are enriched membrane protrusions. STX19 is also enriched in the membrane protrusions. STX19 does not co-localise with E-cadherin and β-catenin in these structures but STX19 staining is in close proximity to E-cadherin and β-catenin (figures 4-24C and 4-25C). Since these structures are protruding from cells, it is unlikely E-cadherin and β-catenin are localised to adherens junctions in these structures.

Overall, these data suggest that STX19 does not localise to adherens junctions as it does not localise to membranes between cells with E-cadherin and β-catenin. Interestingly however, there appears to be an enrichment of STX19 staining in protruding structures from cells adjacent to E-cadherin and β-catenin. Previous studies have implicated E-cadherin in focusing membrane protrusion at the front of migrating cells (Grimaldi *et al.*, 2020) and have shown β-catenin enriched at the tip of membrane protrusions in cells undergoing epithelial-mesenchymal transitioning to regulate their migratory potential (Odenwald, Prosperi and Goss, 2013). Therefore, it is possible that STX19 is enriched in the tips of protrusions at the front edge of migrating keratinocytes in close proximity to E-cadherin and β-catenin.

4.2.9.5 STX19 does not co-localise with MICAL-L1 in keratinocytes

In HeLaM cells, STX19 localises to tubular recycling endosomes that are positive for MICAL-L1 (figure 4-1B). In differentiated keratinocytes, we have also observed localisation of STX19 to tubular structures emanating from regions of the membrane enriched in STX19. We therefore sought to determine if STX19 localises to MICAL-L1-positive tubules in keratinocytes by co-staining STX19 and MICAL-L1. In undifferentiated and differentiated cells, MICAL-L1 localises to short tubular structures towards the periphery of the cell (figure 4-26A and B). These tubular structures appear shorter compared to tubular recycling endosomes in HeLaM cells. It is unclear if the tubular structures in keratinocytes are similar to tubular recycling endosomes in HeLaM cells or if they carry out the same function. In undifferentiated keratinocytes, STX19 has very little expression (figure 4-26A). In differentiated keratinocytes, STX19 localises to distinct regions of the plasma membrane at the edge of the cell (figure 4-26B). This suggests that STX19 does not localise to MICAL-L1 tubular recycling endosomes in keratinocytes supporting our hypothesis that STX19 is functioning at the plasma membrane.

4.2.9.6 STX19 localises to the tips of membrane protrusions adjacent to Rac1 in differentiated keratinocytes

Another protein that localises to the tubular recycling endosome compartment in HeLaM cells is small GTPase, Rac1. Rac1 is known for its roles in regulating the actin cytoskeleton for the formation of lamellipodia, membrane ruffles, and focal adhesions in cell spreading and cell migration (Nobes and Hall, 1995; Price *et al.*, 1998; Parri and Chiarugi, 2010). Rab8 induces Rac1 activation to mediate cytoskeletal re-organisation in migrating cells (Bravo-Cordero *et al.*, 2016). Additionally, Rac1 has also been shown to regulate exocytosis in several cell types. Rac1 has been implicated in the control of neurotransmitter release in neurons where it is highly localised to secretory vesicles (Doussau *et al.*, 2000), as well as the exocytosis of secretory granules in mast cells (Price *et al.*, 1995) and amylase in pancreatic acini (Bi and Williams, 2005). Moreover, Rac1 has been shown to disrupt adherens junctions through clathrin-independent endocytosis of E-cadherin and activation of Rac1 has been shown to induce lamellipodia formation (Akhtar and Hotchin, 2017). Through this role, Rac1 has also been shown to mediate migration in keratinocytes (Ritto *et al.*, 2017). In HeLaM cells, STX19 co-localises with Rac1 on TREs and at the plasma membrane (figure 4-27A) including protruding structures we predict to be lamellipodia based on current literature. We therefore questioned if STX19 localised to lamellipodia in keratinocytes. To address this, undifferentiated and differentiated keratinocytes were co-stained for STX19 and Rac1. In undifferentiated cells, Rac1 localises to the plasma membrane (figure 4-27B). In differentiated cells, Rac1 localises to protruding structures at the membrane as well as showing some enrichment just before the tip of the

protrusion. STX19 appears to be enriched in the tip of the protrusion adjacent to Rac1 (figure 4-27C). These data suggest that STX19 has a polarised localisation in the tips of lamellipodia.

4.2.9.7 STX19 co-localises with CD59 at distinct regions of the plasma membrane in differentiated keratinocytes

Activation of Rac1 to induce lamellipodia formation relies in part on trafficking and recycling through clathrin-independent Arf6-positive pathways (Koubek and Santy, 2018). Arf6 works in concert with Rab8, MICAL-L1, and EHD1 to mediate clathrin-independent recycling of E-cadherin, integrins, and GPI-anchored proteins (Naslavsky, Weigert and Donaldson, 2004; Eyster *et al.*, 2009; Rahajeng *et al.*, 2012). Since we see localisation of STX19 to Rab8-positive-tubules in HeLaM cells (supplementary figure 4-1), we also questioned if STX19 localises to the same pathways in keratinocytes. One GPI-anchored protein that is endocytosed through this pathway is CD59 (Naslavsky, Weigert and Donaldson, 2004). We therefore chose to examine if STX19 and CD59 are localised to the same pathways in keratinocytes. Undifferentiated and differentiated keratinocytes were fixed and stained using anti-CD59 and anti-STX19 antibodies.

In HeLaM cells, GFP-CD59 localises to TREs and the plasma membrane. STX19 is co-localised on TREs and the membrane with CD59 (figure 4-28A). In undifferentiated keratinocytes, CD59 localises to the plasma membrane and show a punctate staining pattern which may be vesicular or endosomal compartments. (figure 4-28B). In differentiated keratinocytes, CD59 shows staining at distinct regions of the plasma membrane which co-localises with STX19 staining (figure 4-28C). These data suggest that STX19 is enriched in the same regions of the plasma membrane as cargo that is trafficked through the Arf6/Rab8 pathway.

4.2.9.8 STX19 localises in close proximity to activated Akt at the plasma membrane in differentiated keratinocytes

Rac1 signalling has been shown to be regulated by Akt in migrating epithelial cells (Yang *et al.*, 2011; Henderson *et al.*, 2015). Akt is a serine/threonine kinase and is a well-known effector of phosphsoinositide 3-kinases (PI3K) in the PI3K/Akt/mTOR signalling pathway (Revathidevi and Munirajan, 2019). Akt signalling has been implicated in keratinocytes migration as well as promoting keratinocyte differentiation and survival (Calautti *et al.*, 2005; Jiang *et al.*, 2020). As we have previously seen localisation of STX19 to the tips of membrane protrusions in close proximity to Rac1, we hypothesised that STX19 could be mediating the delivery of signalling components to the plasma membrane. To address this, we aimed to determine if STX19 was localised to similar regions of the membrane as Akt. We therefore, co-stained undifferentiated and differentiated keratinocytes with STX19 and phosphorylated-Akt (pAkt; active form).

In undifferentiated keratinocytes, both pAkt and STX19 show faint staining which suggests very little expression (figure 4-29A). In differentiated keratinocytes, STX19 shows enrichment in distinct regions of in membrane protrusions. In some cells, these regions do not show specific enrichment of pAkt (figure 4-29B). However, in others, pAkt is enriched in the same microdomains at the cell surface as STX19 (figure 4-29C). There is also some co-localisation between STX19 and pAkt puncta suggesting that STX19 function may be regulated by Akt phosphorylation or signalling. Taken together, these data suggest that STX19 is able to localise to the same regions of the membrane as pAKT. Excitingly, this could suggest a role for STX19 in the delivery of cargo in close proximity to Akt signalling.

4.3 Discussion

4.3.1 Summary of results

One of the aims of this chapter was to gain insight into the pathways and processes STX19 plays a role in. To address this aim, we analysed localisation of the R-SNARE, VAMP8, upon STX19 overexpression and markers of compartments VAMP8 is known to associate with. We found that STX19 alters the steady state distribution of VAMP8 and localises in the same regions of the plasma membrane as VAMP8. We also found that STX19 and VAMP8 co-localise in endocytic carriers following VAMP8 internalisation. We therefore hypothesised STX19 is recruiting and driving fusion of VAMP8-positive vesicles with STX19-positive compartments likely to be endosomes, and to the plasma membrane. Subsequently both proteins may be internalised through the same pathway or VAMP8 may be trafficking through a STX19-positive compartment. Additionally, we found that STX19 overexpression results in a reduction in the levels of key autophagy protein, LC3, under starvation conditions. We hypothesise that STX19 overexpression recruits and drive fusion of VAMP8-positive compartments at the cell surface where they are subsequently secreted. Further investigation is necessary to confirm these hypotheses. It remains unclear if the effects of STX19 overexpression suggest a role for STX19 in autophagy or if the observed phenotypes are simply due to an increased abundance of STX19.

Another aim of this chapter was to establish a physiologically relevant cell model in which STX19 function can be studied. We addressed this aim by staining for STX19 in differentiated keratinocytes and co-staining with other membrane markers. We found that STX19 localises to distinct polarised regions of the membrane and membrane protrusions in differentiated keratinocytes. As STX19 has a limited tissue distribution and is expressed at low levels, we hypothesise that STX19 is mediating fusion at the plasma membrane for the secretion of specialised cargo rather than bulk secretion. Co-localisation of Rac1 and STX19 in HeLaM cells and enrichment of STX19 in membrane protrusions in close proximity to Rac1 suggests STX19 localises near to regions of Rac1 acitivty. This suggests a localisation for STX19 in membrane protrusions or lamellipodia. Co-localisation of STX19 and pAkt at distinct regions of the

membrane suggests STX19 is localised in close proximity of Akt signalling. Alternatively, STX19 function may be regulated by Akt phosphorylation. Co-localisation of STX19 and CD59 suggests STX19 localises to regions of the membrane enriched in cargo recycling through an Arf6/Rac1/Rab8 pathway.

4.3.2 Overexpressed STX19 recruits VAMP8 to enlarged endosomes and partially co-localises with VAMP8 at the cell surface

Previous analysis of STX19 interactors by mass spectrometry have shown that STX19 interacts with VAMP8 (Gordon *et al.*, 2010). VAMP8 is known to localise to early endosomes, lysosomes, and the plasma membrane and the distribution between these compartments is carefully balanced (Jean *et al.*, 2015). We found that STX19 overexpression alters the steady-state distribution of VAMP8 from enrichment in the perinuclear region to distributed in STX19-positive puncta. Additionally, using TIRF microscopy, we observed co-localisation of STX19 and VAMP8 in puncta at the cell surface. We therefore hypothesised that STX19 overexpression alters the balanced distribution of VAMP8 recruiting VAMP8 to STX19 positive compartments and the plasma membrane.

It remains unclear if STX19 and VAMP8 are mediating fusion at the plasma membrane. VAMP8 is able to mediate fusion at the plasma membrane and has been shown to involved in exocytosis of secretory granules in pancreatic acini cells, muscin secretion in goblet cells, and fusion of recycling endosomes with the plasma membrane to facilitate T lymphocyte cytotoxicity (C. Wang *et al.*, 2004; Marshall *et al.*, 2015b; Cornick *et al.*, 2019). This indicates that VAMP8 has roles in regulated secretion. However, VAMP8 has been shown to zymogen granule secretion through a constitutive secretory-like pathway (Messenger *et al.*, 2014). As STX19 was predicted to be involved in constitutive secretion, it is possible the two SNAREs could act together in the same pathway. It would be interesting to determine if STX19 and VAMP8 can form fusion competent complexes to drive fusion in reconstituted liposome assays. Additionally, VAMP8-phluorin constructs would be useful to determine if there is an increased number of VAMP8-positive fusion events at the cell surface in STX19-transfected cells and if these events occur in STX19-positive puncta at the surface.

It is unclear if STX19 alters the distribution of VAMP8 through direct interaction or via an intermediate bridging protein. Initial experiments suggest removal of the STX19 SNARE domain does not impact the distribution of VAMP8 suggesting the STX19 SNARE domain could be involved in altering the distribution of VAMP8. Mutation of the STX19 N-terminal KDR motif appears to alter the steady state distribution of VAMP8 suggesting that this motif is not involved in altering VAMP8 distribution. We have shown in the previous chapter that Munc18-2 interacts with STX19 at the N-terminal KDR motif. It remains unclear if STX19 constructs with KDR mutations that are unable to bind Munc18-2 would be active or inhibitory SNAREs as a result. As these are initial experiments, additional repeats and quantification would be

required to further investigate which domains of STX19 are required in altering the steady state distribution of VAMP8. Studies in yeast suggest that tethering complexes and SNARE machinery should be considered an integrated molecular machine for driving fusion. Tethering complexes first mediate SNARE pairing and then drive the terminal stage of fusion (D'Agostino *et al.*, 2017). Therefore, it is possible that a tethering protein complex is required to mediate STX19/VAMP8 pairing prior to fusion. Future *in vitro* studies would be useful to determine if STX19 and VAMP8 interact directly.

Alternatively, VAMP8 has been shown to mediate fusion between recycling endosomes and the plasma membrane in T lymphocytes. STX11 localises to these recycling endosomes and the VAMP8-mediated fusion is required to deposit STX11 at the plasma membrane where it can drive exocytosis of cytotoxic granules. Knockdown of VAMP8 delays STX11 localisation to the plasma membrane and leads to an accumulation of STX11 in recycling endosomes (Marshall *et al.*, 2015b). Therefore, it could be possible that VAMP8 is supporting STX19 secretion at the plasma membrane rather than forming a complex with STX19 to drive fusion itself. It would be therefore interesting to understand how VAMP8 knockdown affects STX19 dynamics.

VAMP8 is also known to associated with early endosomes and has been shown to internalise through clathrin-dependant pathways into EEA1-positive endosomes (Jean *et al.*, 2015). STX19 however, localises to Rab8-positive tubular recycling endosomes that mediate recycling from clathrin-independent pathway (Roland *et al.*, 2007). Our antibody uptake assays in HA-VAMP8 stably expressing cells demonstrated that STX19 and VAMP8 localise to the same compartments suggesting STX19 and VAMP8 are in the same endocytic compartments. This suggests that STX19 and VAMP8 are internalised through the same pathways or VAMP8 is internalising through a STX19-positive compartment. The nature of these endocytic compartments remains unclear. Staining for EEA1 in our antibody uptake assays would indicate if these compartments are early endosomes. Based on our hypothesis that STX19 recruits VAMP8 to the plasma membrane, we would predict that an increased amount of VAMP8 at the surface would result in increased VAMP8 internalisation or recycling. Therefore, it would be interesting to quantify steady state cell surface levels of VAMP8 and the amount of VAMP8 internalisation in STX19-transfected and untransfected cells.

EGF-R is also known to internalise via clathrin-dependent pathways into early endosomes (Tomas, Futter and Eden, 2014) or via clathrin-independent pathways directed by ubquitinylation of EGF-R (Aguilar and Wendland, 2005). Our STX19 overexpression experiments demonstrated co-localisation of VAMP8, STX19, and EGF-R in puncta throughout the cell. This could suggest that STX19 and VAMP8 are co-localising at early endosomes. We have also seen enrichmentof STX19 and EGF-R in similar regions at the cell surface using TIRF microscopy. STX19 has been predicted to have a role in EGF-R trafficking and

overexpression of STX19 has been shown to impair EGF-R internalisation (Wang *et al.*, 2006). Whilst it is unlikely STX19 would directly interact with EGF-R to mediate its trafficking, presence of EGF-R and STX19 in the same microdomains at the cell surface suggests it is possible that STX19 could be regulating EGF-R trafficking. However, we did not observe VAMP8 co-localisation with STX19/EGF-R puncta at the cell surface. Overexpression of STX19 in combination with EGF-R internalisation and recycling assays would give us further insight into if STX19 plays a role in EGF-R trafficking. Co-staining for VAMP8 in these assays would indicate if VAMP8 may also be involved.

Based on these data, we hypothesise that overexpression of STX19 is driving fusion of VAMP8-positive vesicles to STX19-positive compartments and to the plasma membrane (figure 4-30). Subsequently, STX19 and VAMP8 are either internalised through the same pathways or VAMP8 is trafficking through a STX19-positive compartment. To gain further insight, it would be important to quantify the levels of VAMP8 at the cell surface in STX19-transfected and untransfected cells and characterise the pathways STX19 and VAMP8 are internalising through. What remains unclear is if the phenotypes we observe represent the physiological function of STX19 or are due to the increased abundance of STX19 in cells. Since STX19 is able to interact with VAMP8, overexpressed STX19 could pull VAMP8 to the membrane despite there being no interaction between VAMP8 and STX19 at the membrane under steady-state conditions. It would be interesting to determine what the effect of STX19 knockdown would be on the balanced distribution of VAMP8.

4.3.3 Overexpressed STX19 may result in altered lysosomal distribution

VAMP8 is also known to associate with lysosomes and has been shown to traffic from early endosomes to lysosomes in internalisation assays under starvation conditions (Jean *et al.*, 2015). We sought to understand how STX19 overexpression affects VAMP8-positive compartments such as lysosomes. By expressing STX19 and staining for lysosomal markers CD63 and LAMP1, we found that overexpression of STX19 may result in the dispersal of lysosomes towards the periphery of the cell. This would suggest STX19 alters the distribution of lysosomes. Since VAMP8 is associated with lysosomes, we would hypothesise that the altered distribution of lysosomes would be a result of the altered distribution of VAMP8. It would therefore be interesting to determine how STX19 overexpression effects VAMP8 trafficking to lysosomes using internalisation assays in starved conditions.

Variable results were obtained with expression of STX19 mutant constructs. Whilst full-length STX19 constructs appeared to affect the distribution of LAMP1, only HA-STX19 expression appeared to affect CD63 distribution and it was unclear if GFP-STX19 had the same effect. Additionally, the STX19/13 hybrid construct appeared to affect the distribution of LAMP1 but not of CD63. We found that the dispersal of lysosomes towards the periphery of the cell was a difficult phenotype to identify by eye. Therefore, it was

difficult to draw solid conclusions from these data. Further analysis would be required to quantify the number of CD63/LAMP1-positive puncta in STX19-transfected cells, as well as, measuring the distance of CD63/LAMP1-positive puncta from the centre point of the cell to truly understand if lysosomes are dispersed towards the cell periphery.

4.3.4 Overexpression of STX19 results in a loss of LC3 and P62 staining

Since we observed altered distribution of VAMP8 with STX19 overexpression, we sought to understand how overexpression of STX19 affects the autophagy pathway. VAMP8 resides on lysosomes and mediates fusion between lysosomes and autophagosomes in complex with STX17 and SNAP29 (Itakura, Kishi-Itakura and Mizushima, 2012). Knockdown of VAMP8 results in an accumulation of LC3-II suggesting an impairment in autophagic flux (Itakura, Kishi-Itakura and Mizushima, 2012). To explore how STX19 overexpression affects autophagosomal markers, we overexpressed STX19 and stained for LC3 and P62. LC3 is a key protein involved in the autophagy pathway and has two variations LC3-I and LC3-II. LC3-I is recruited to autophagosomal initiation membranes where it is lipidated to form LC3-II. Initiation membranes capture cargo as they grow and ultimately form autophagosomes. LC3-II facilitates the formation of autophagosomes by serving as a binding platform for other proteins containing LC3-interacting regions (LIR motifs) (Schaaf *et al.*, 2016; Melia, Lystad and Simonsen, 2020). Interestingly, STX19 has been identified to contain two LIR motifs suggesting STX19 could interact with LC3 (Gu *et al.*, 2019). Autophagosomes fuse with lysosomes to form autolysosomes and the hydrolyases contributes by lysosomes degrade the autophagosomal content. LC3-II is also degraded after autophagosomal-lysosomal fusion (Leidal *et al.*, 2020). P62 interacts with LC3 and mediates cargo recruitment into autophagosomes and is subsequently degraded itself by autophagy (Pankiv *et al.*, 2007; Leidal *et al.*, 2020).

Excitingly, we found that overexpression of STX19 resulted in the loss of LC3 and P62 staining at 24 hours post-transfection but only loss of LC3 staining occurs at 12 hours post-transfection. This suggests that the loss of LC3 proceeds the loss of P62. LC3 and P62 staining is not lost upon overexpression of STX11 suggesting the phenotype seen with STX19 is not due to a transfection artefact. We hypothesised that the loss of LC3 and P62 staining may be due to a number of reasons. A) Loss of LC3 staining may be due block in autophagosomal formation. We believed this to be unlikely as the formation of autophagosomes is predicted to arise from membranes STX19 is not associated with. The membranes from which initation membranes are derived from is debated within the field. It has been suggested that initiation membranes arise from either mitochondrial, ERGIC, ER, or Golgi membranes (Razi, Chan and Tooze, 2009; Van der Vaart and Reggiori, 2010; Cook *et al.*, 2014; Ge, Zhang and Schekman, 2014). Whilst this may still remain unclear, STX19 does not localise to these membranes. Therefore, it would be unlikely that STX19 has a role in autophagosome formation. Additionally, a block in autophagosome formation would result in the

accumulation of P62 in the cytoplasm as it would not be associated with autophagosomes and subsequently degraded.

B) A loss in LC3 and P62 staining could suggest an upregulation of autophagy. A loss of LC3 and P62 could indicate their degradation which occurs during autophagy. It is unlikely that STX19 is directly involved in fusion between lysosomes and autolysosomes as STX17 and SNAP29 are well characterised to mediate this fusion. However, future experiments to measure autophagic flux should be conducted to understand if STX19 is upregulating autophagy by another means. Since both P62 and LC3 are degraded by autophagy, it is important to measure degradation of these proteins rather than expression levels to measure autophagic flux (Yoshii and Mizushima, 2017). It would also be important to measure autophagic flux by measuring amount of LC3 associated with autophagosomes and autolysosome. This can be conducted through use of a GFP-mCherry tandem construct where GFP is quenched by the acidic lysosomal environment after autophagosomal-lysosomal fusion (Kimura, Noda and Yoshimura, 2007).

C) STX19 overexpression recruits autophagosomes or autolysosomes to the cell surface and leads to their secretion. An unconventional secretory pathway has been previously described that leads to the secretion of leaderless cytosolic proteins that cannot enter the conventional ER-Golgi secretory pathway (Ponpuak *et al.*, 2015). This pathway has also been shown to mediate the secretion of more complex cargo such as RNA viruses and extracellular vesicles (Sirois *et al.*, 2012; Pallet *et al.*, 2013; Teo, Leur and Sanyal, 2021). In this pathway, autophagosomes fuse with early endosomes to form amphisomes which then fuse with the membrane to release their contents (Ponpuak *et al.*, 2015). We hypothesise that STX19 is recruiting VAMP8-positive compartments to the plasma membrane and leading to their secretion. Recently, it has been shown that LC3 controls extracellular vesicle cargo loading and secretion and is in turn secreted itself. Additionally, proximity-dependent biotinylation proteomics to identify the LC3 secretome revealed that P62 can also be secreted (Leidal *et al.*, 2020). Therefore, it is possible that STX19 mediating the secretion of LC3 and P62 containing compartments. Interestingly, it has been shown that cargo secretion through this autophagy-dependent pathway is regulated by Rab8 (Dupont *et al.*, 2011). Considering STX19 localises to Rab8-positive tubular recycling endosomes, it would not be unreasonable to hypothesise STX19 is also involved in this pathway. STX3 and 4 in concert with SNAPs 23 and 29, and Sec22B have been suggested to mediate amphisome fusion with the plasma membrane (Kimura, Jia, Claude-Taupin, *et al.*, 2017). However, overexpression of STX19 could be recruiting VAMP8-positive compartments to the surface and mediating their fusion even though this might not occur physiologically.

Based on our findings, we hypothesise that the overexpression of STX19 recruits VAMP8-positive compartments to the plasma membrane (figure 4-30). Therefore, overexpressed STX19 may recruit autophagosomes or amphisomes to the plasma membrane resulting in their secretion via an autophagy-

dependent unconventional secretory pathway. Further experiments would be important to understand how STX19 results in the loss of LC3 and P62 staining. Firstly, it would be important to quantify the number of transfected cells with reduced LC3 and P62 staining by flow cytometry. Moreover, it would be interesting to mutate the two predicted LIR motifs in STX19 and determine if overexpression of this mutant construct would still have the same effects on LC3 and P62. As discussed previously, it will be important to measure autophagic flux using tandem GFP-mCherry-LC3 constructs as opposed to measuring LC3/P62 expression levels. Additionally, bafilomycin treatment is routinely used to inhibit autophagosome-lysosome fusion as a measure of autophagic flux. Bafilomycin inhibits V-ATPase which prevents lysosome acidification. It would therefore be interesting to determine what effect STX19 has on LC3 and P62 after bafilomycin treatment. To induce autophagy in our experiments, we serum starved the cells for 12 hours. Use of rapamycin to induce autophagy is a preferred method in the field and therefore, the experiments should be repeated with rapamycin to confirm STX19 overexpression directly affects autophagy. Finally, to determine if LC3 and P62 is being secreted from the cells by seeing if it is possible to detect LC3 and P62 in the culture media of STX19 transfected cells by western blot. It would also be interesting to determine if STX19 co-localises with LC3 and P62 at the plasma membrane using TIRF microscopy.

4.3.5 Characterising the localisation of STX19 in keratinocytes

We predict STX19 to be a post-Golgi SNARE that mediates fusion with the plasma membrane. This is based on previous literature suggesting a role for STX19 in constitutive secretion, the localisation of tagged STX19 to the plasma membrane, and its ability to interact with SNAREs known to mediate fusion with the membrane (Gordon *et al.*, 2010). These previous studies, however, were carried out in HeLaM cells. Data from Wang et al., and the GTex Project demonstrate that STX19 is enriched in epithelial tissues and the skin (Wang *et al.*, 2006; Lonsdale *et al.*, 2013). Additionally, STX19 has been shown to be upregulated 5-fold in keratinocytes during calcium-induced differentiation (figure 4-3A; Toufighi *et al.*, 2015). We therefore hypothesised that STX19 is involved in secretion of specialised cargo at the plasma membrane rather than general bulk secretion. The exact pathways and processes STX19 functions in however remains unknown. To gain insight into this, we first sought to set up a physiologically relevant cell model in which we could study the subcellular compartments STX19 localises to.

To address this, we analysed STX19 localisation in undifferentiated and differentiated keratinocytes. We found evidence of STX19 upregulation in differentiated keratinocytes. Undifferentiated keratinocytes show faint staining for STX19 which is likely to be background staining. In contrast, differentiated keratinocytes show a bright signal for STX19 at distinct polarised regions of the plasma membrane and at the tips of membrane protrusions. These data support our hypothesis that STX19 functions at the plasma

membrane as STX19 localises to the plasma membrane in a physiologically relevant cell model. Additionally, the distinct polarised localisation of STX19 suggests it is playing a role in specialised pathways as opposed to general secretion. This is in line with our idea that STX19 is involved in specialised pathways due to its specific enrichment in epithelial tissues.

We aimed to further characterise the regions of membrane STX19 is localised to by staining various markers. Since we had previously seen altered distribution of VAMP8 in HeLaM cells upon STX19 overexpression, we sought to understand where VAMP8 localises in keratinocytes. Unfortunately, we were unable to co-stain VAMP8 and STX19 as both antibodies were of the same species. We found however, that VAMP8 also localises to distinct regions of the plasma membrane. It would be interesting to determine if VAMP8 and STX19 are both at the same region of the membrane by co-staining.

Formation of adherens junctions is a key process that occurs during keratinocyte differentiation (Elsholz *et al.*, 2014). Adherens junctions consist of E-cadherin and β-catenin proteins linked to actin filaments (Hartsock and Nelson, 2008). As STX19 is upregulated upon differentiation, we sought to determine if STX19 was localised to adherens junctions. We did not find co-localisation of STX19 with E-cadherin or β-catenin at membranes making contact with other cells. Therefore, STX19 is not localised to adherens junctions. However, we observed enrichment of STX19 in membrane protrusions also enriched for E-cadherin. In migrating cells, cytoskeletal reorganisation results in the formation of membrane protrusions leading edge of the cell. E-cadherin has been shown to recycle from the membrane at the leading edge when adherens junctions are disassembled and suggested to focus membrane protrusion at the front of the cell (Brüser and Bogdan, 2017; Grimaldi *et al.*, 2020). This could suggest STX19 is localised to membrane protrusions in which E-cadherin is being recycled rather than directly associated with adherens junctions.

Moreover, Rac1 signalling activities are known to mediate E-cadherin recycling for disassembly of adherens junctions and re-organisation of the actin cytoskeleton for the turnover of focal adhesions and formation of membrane protrusions and lamellipodia (Nobes and Hall, 1995; Kurokawa *et al.*, 2004; Akhtar and Hotchin, 2017). In HeLaM cells, STX19 co-localises with Rac1 on TREs and at the plasma membrane suggesting they may be trafficking through the same pathways. In differentiated keratinocytes, STX19 shows enrichment at the tips of membrane protrusions in close proximity to Rac1. This suggests that STX19 might be localised to membrane protrusions at the just prior to leading edge of cells. Alternatively, Rac1 signalling is also known to regulate recycling endosome secretion of TNF in macrophages and has been shown to mediate secretion of Bmp2 and FGF21 from keratinocytes in knockout mice (Stanley *et al.*, 2014; Ueyama *et al.*, 2020). Therefore, it is possible STX19 could localise in close proximity to sites of Rac1-dependent secretion.

Similarly, Akt signalling is thought to mediate the function of Rac1 (Yang *et al.*, 2011; Henderson *et al.*, 2015). Akt has been shown to have many roles in keratinocytes including migration, differentiation, and survival (Calautti *et al.*, 2005; Jiang *et al.*, 2020). We have shown that STX19 co-localises with specific Akt puncta at the plasma membrane. This may suggest that STX19 is functioning in close proximity to Akt signalling. The fact that Akt functions in numerous pathways with overlapping components makes it difficult to distinguish what pathways Akt is signalling in when it is localised in the same puncta as STX19. Alternatively, it may that STX19 function is regulated by Akt phosphorylation. SNARE proteins have been previously shown to be regulated by phosphorylation. For example, phosphorylation of the Ykt6 SNARE domain has been proposed to act as a confirmational switch from an auto-inhibited confirmation to an active SNARE (Pradhipa Karuna *et al.*, 2020). Additionally, phosphorylation of the STX7 Habc domain by colony-stimulating factor 1 (CSF-1; a downstream effector of Akt) has been shown to promote its interaction with other SNAREs (Achuthan *et al.*, 2008). Phosphorylation of STX17 by TBK1 has been shown to be important in the formation of protein complex assemblies during autophagosomal initiation (Kumar *et al.*, 2019). Interestingly, proximity-dependent biotinylation screens have identified TBK1 as a potential interactor of STX19. It would be interesting to determine if STX19 co-localises with TBK1 in differentiated keratinocytes. In our experiments, we stained for pAkt, the phosphorylated active form. In future experiments, it would be interesting to determine if total Akt localises to the same regions of the plasma membrane as STX19 or if it is only the activated form of Akt.

Akt activation can occur downstream of EGF-R ligand binding and can be mediated by EGF-R recycling (Nishimura *et al.*, 2015). Therefore, STX19 may be regulating EGF-R trafficking at microdomains of the plasma membrane where Akt is activated. It would be interesting to determine if EGF-R is localised to the same regions of the plasma membrane as Akt and STX19. Additionally, one way in which Akt has been shown to regulate cell migration is through its downstream effector, Girdin (Weng *et al.*, 2006). Girdin is phosphorylated by Akt and is able to bind both actin and microtubules to mediate cytoskeletal re-organisation during migration (Enomoto *et al.*, 2005; Jiang *et al.*, 2008; Weng *et al.*, 2010). Girdin has also been shown to bind EGF-R to mediate cell migration or proliferation through different signalling pathways (Ghosh *et al.*, 2010). Proximity-dependent biotinylation assays and yeast-two hybrid screening identified Girdin as an interactor of STX19. It would therefore be interesting to determine if Girdin and STX19 localise in the same microdomains of the plasma membrane and the effect of STX19 overexpression on Girdin distribution.

Additionally, Rac1 is known to work in concert with Arf6 and Rab8 to mediate post-Golgi recycling of integrins and GPI-anchored proteins to the plasma membrane (Hattula *et al.*, 2006; Koubek and Santy, 2018). CD59 is a GPI-anchored protein that is known to recycle through this pathway and has been shown to mediate cytokine secretin in keratinocytes (Cai *et al.*, 2011). We have shown co-localisation of CD59

and STX19 to TREs and the plasma membrane in HeLaM cells suggesting there are recycling through the same pathway. In differentiated keratinocytes, STX19 and CD59 appear to be enriched in the same regions of the plasma membrane. This suggests that STX19 could be localising to membrane domains enriched in cargo trafficking through an Arf6/Rac1/Rab8-mediated pathway. Additionally, GPI-anchored cargo are sorted to the apical membrane in polarised epithelial cells (Zurzolo and Simons, 2016). Enrichment of STX19 in the same plasma membrane regions as CD59 could suggest STX19 is localised to the apical membrane.

Interestingly however, MICAL-L1 also localises to Rab8-positive TREs and is known to mediate CD59 recycling (Cai *et al.*, 2014). STX19 localises to the same TREs as MICAL-L1 in HeLa cells but not in differentiated keratinocytes. As we predict STX19 to play a role at the plasma membrane, it may be that its localisation to TREs in HeLaM cells is due to its recycling. In HeLaM cells, STX19 antibodies show the endogenous protein at TREs whilst it is the overexpressed STX19 that localises to the plasma membrane. Therefore, we reason that STX19 function is largely not occurring in HeLaM cells and instead it is being recycled through MICAL-L1-positive pathways. As STX19 is enriched in epithelial tissues and the antibody is able to detect STX19 at the plasma membrane in keratinocytes, we predict that STX19 is more functionally active in keratinocytes than HeLaM cells. Therefore, there may be less recycling of STX19 occurring in keratinocytes which may explain why we do not see localisation of STX19 to MICAL-L1 TREs in these cells.

We had previously predicted interaction with STX19 and DST through biochemical screens and our mitochondrial re-routing assays. Keratinocytes are enriched for an epithelial-specific isoform of DST. One of the predicted interaction fragments of DST pulled out from yeast-two hybrid screening is present in the epithelial isoform of DST suggesting this isoform is able to interact with STX19. DST is a spectraplakin protein which, in keratinocytes, localises to hemidesmosomes. Here, it mediates attachment of cells at the bottom layer of the epidermis to the basal lamina. These cells are undifferentiated and upon differentiation, they lose attachment to the basal lamina and migrate progressively up through the layers of the epidermis at different stages of differentiation (Walko, Castañón and Wiche, 2015). DST has also been shown to restrict keratinocyte migration as Epidermis Bullosa patients with mutations in DST have defects in cell spreading and migration (Michael *et al.*, 2014). Despite the predicted interaction, DST and STX19 are localised to different structures in keratinocytes. We predict the structures DST localises to are forms of hemidesmosomes mediating cell attachment. These data would suggest that STX19 is not in the same pathways or processes that mediate cell attachment as DST. However, we could speculate that DST has an unknown moonlighting function as cells detach from the basal lamina and migrate up the epidermis. In contrast to keratinocytes with patient mutations, DST knockout keratinocytes demonstrate a loss of front to rear polarity and impaired migration. This defect was found to be the result of impaired

Rac1 activation in DST knockout cells suggesting that DST is important for modulating Rac1 activity to maintain polarisation and induce migration (Hamill *et al.*, 2009). Therefore, we could speculate that STX19 does not interact with DST for roles in cell adhesion but may play a role in regulating cell polarity.

To truly understand the function of STX19 in keratinocytes, we will first need to be able to manipulate gene expression in these cells. Keratinocytes are not a cell line we have used previously in the lab and due to time constraints, we were unable to optimise transfection or transduction of these cells. In the future, it will be interesting to determine how STX19 overexpression or knockdown affects some of the membrane markers we have stained for. It will be particularly interesting to determine how STX19 overexpression affects VAMP8 localisation and LC3/P62 expression. Analysing how localisation of markers such as MICAL-L1, Rac1, CD59 and pAKT are affected in STX19-transfected or knockdown keratinocytes may provide insight into the specific pathways and processes it plays a role in.

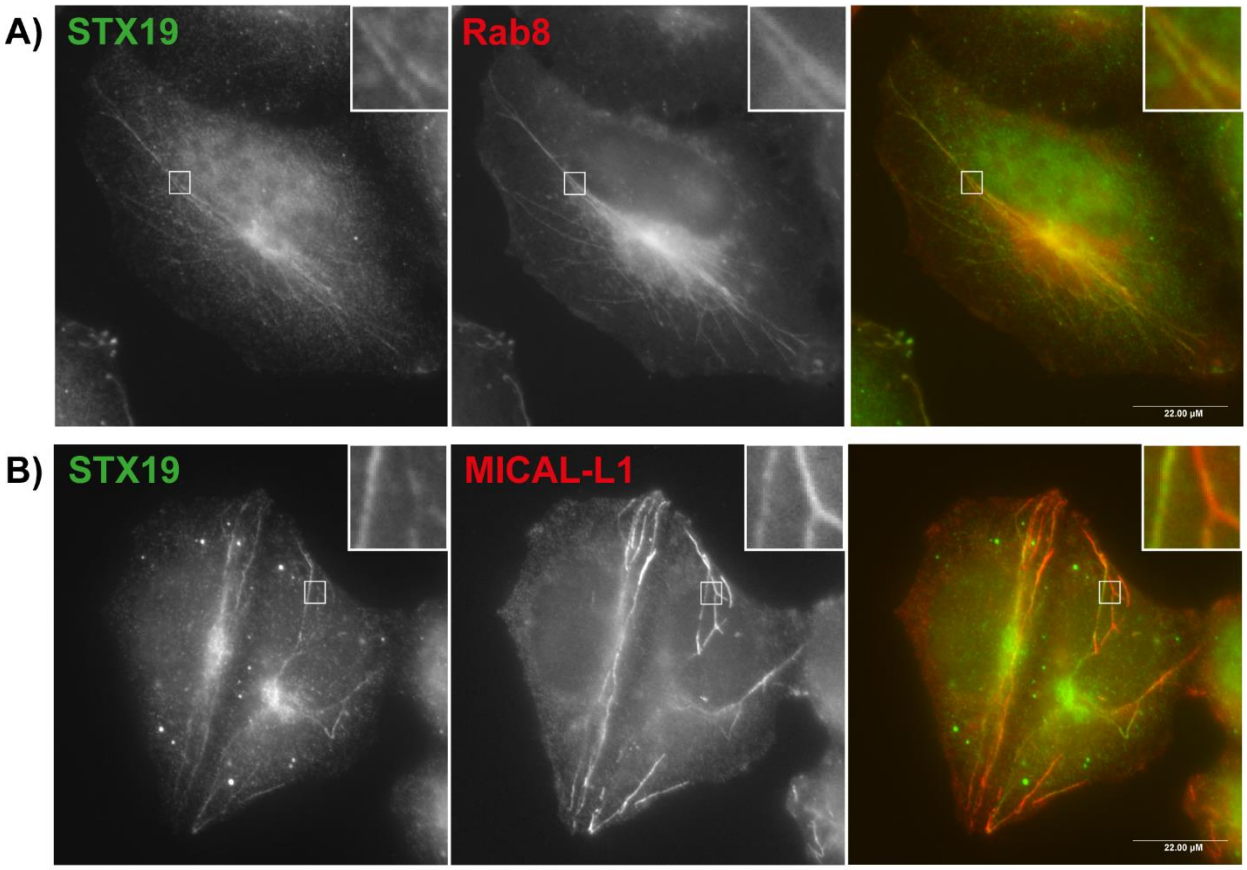

Figure 4-1: STX19 localises to tubular recycling endosomes in HeLaM cells. *Data produced by Khamal Ampah and published in Ampah et al., 2018. J Cell Sci.* **A)** HeLaM cells were transfected with Strawberry-Rab8. Cells were then fixed using 4 % PFA and stained using anti-STX19 antibodies. Rab8 localises to tubular recycling endosomes and the plasma membrane. STX19 localises to Rab8-positive tubular recycling endosomes. **B)** HeLaM cells were fixed using 4 % PFA and stained using anti-STX19 and anti-MICAL-L1 antibodies. MICAL-L1 localises to tubular recycling endosomes and the cytoplasm. STX19 localises to MICAL-L1-positive tubular recycling endosomes. Scale bar: 22.00 µM

A)

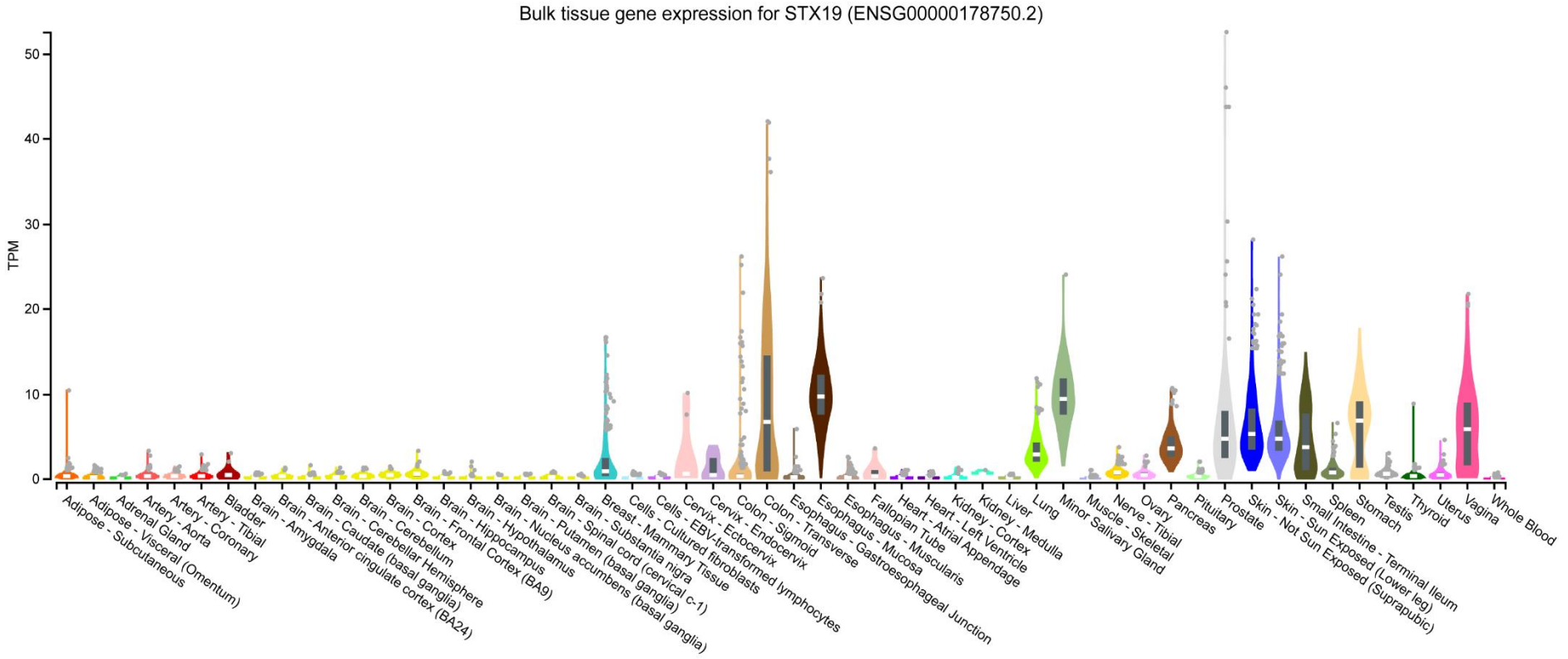
Bulk tissue gene expression for STX19 (ENSG00000178750.2)
TPM
50
40
30
20
10
0
Adipose - Subcutaneous
Adipose - Visceral (Omentum)
Adrenal Gland
Artery - Aorta
Artery - Coronary
Artery - Tibial
Bladder
Brain - Amygdala
Brain - Anterior cingulate cortex (BA24)
Brain - Caudate (basal ganglia)
Brain - Cerebellar Hemisphere
Brain - Cerebellum
Brain - Cortex
Brain - Frontal Cortex (BA9)
Brain - Hippocampus
Brain - Hypothalamus
Brain - Nucleus accumbens (basal ganglia)
Brain - Putamen (basal ganglia)
Brain - Spinal cord (cervical c-1)
Brain - Substantia nigra
Breast - Mammary Tissue
Cells - Cultured fibroblasts
Cells - EBV-transformed lymphocytes
Cervix - Ectocervix
Cervix - Endocervix
Colon - Sigmoid
Colon - Transverse
Esophagus - Gastroesophageal Junction
Esophagus - Mucosa
Esophagus - Muscularis
Fallopian Tube
Heart - Atrial Appendage
Heart - Left Ventricle
Kidney - Cortex
Kidney - Medulla
Liver
Lung
Minor Salivary Gland
Muscle - Skeletal
Nerve - Tibial
Ovary
Pancreas
Pituitary
Prostate
Skin - Not Sun Exposed (Suprapubic)
Skin - Sun Exposed (Lower leg)
Small Intestine - Terminal Ileum
Spleen
Stomach
Testis
Thyroid
Uterus
Vagina
Whole Blood

B)

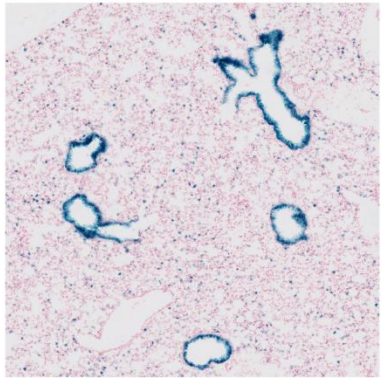

C)

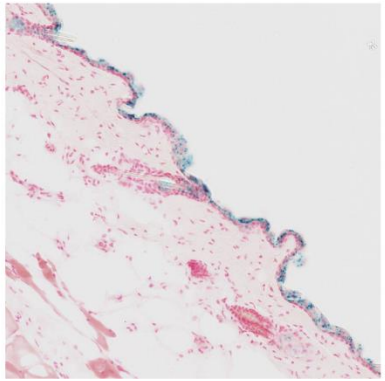

D)

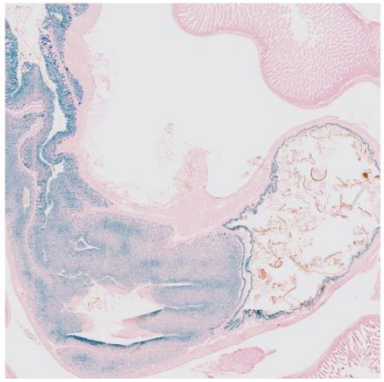

E)

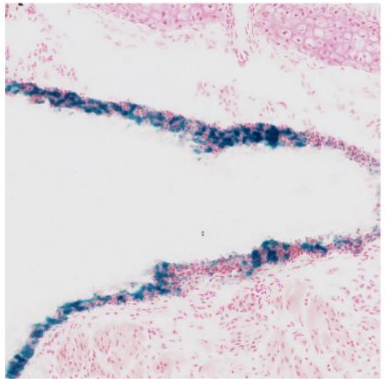

Figure 4-2: STX19 has a limited tissue distribution in epithelial tissues and the skin. **A)** Bulk tissue expression data from The GTEx project. Tissues from 948 donors were analysed using RNA-seq to determine transcripts per million (TPM) per tissue for any given gene. STX19 is relatively highly expressed in epithelial tissues such as stomach (TPM 6.846), lung (TPM 2.811), skin (TPM 5.263), and transverse colon (TPM 6.700). STX19 expression in non-epithelial is very low such as kidney (cortex; TPM 0.0979) and brain tissues (amygdala; TPM 0.08905). Box plots are shown as median, 25th, and 75th percentiles. This data was generated by The GTEx consortium *Lonsdal et al., 2013. Nature Genetics. doi.org/10.1038/ng.2653* from the current V8 release, and accessed through the GTEx Portal website, *https://gtexportal.org/home/gene/STX19%20* **B-E)** Tissue-specific expression of STX19 using a lacZ reporter from the International Mouse Phenotyping Consortium. Blue staining represents LacZ activity. Tissue samples were obtained from a female heterozygous knockout mouse. Images were obtained from the International Mouse Phenotyping Consortium website, *https://www.mousephenotype.org/data/genes/MGI:1915409#phenotypesTab.* **B)** STX19 expression in lung tissue. **C)** STX19 expression in the skin. **D)** STX19 expression in the stomach. **E)** STX19 expression in the trachea.

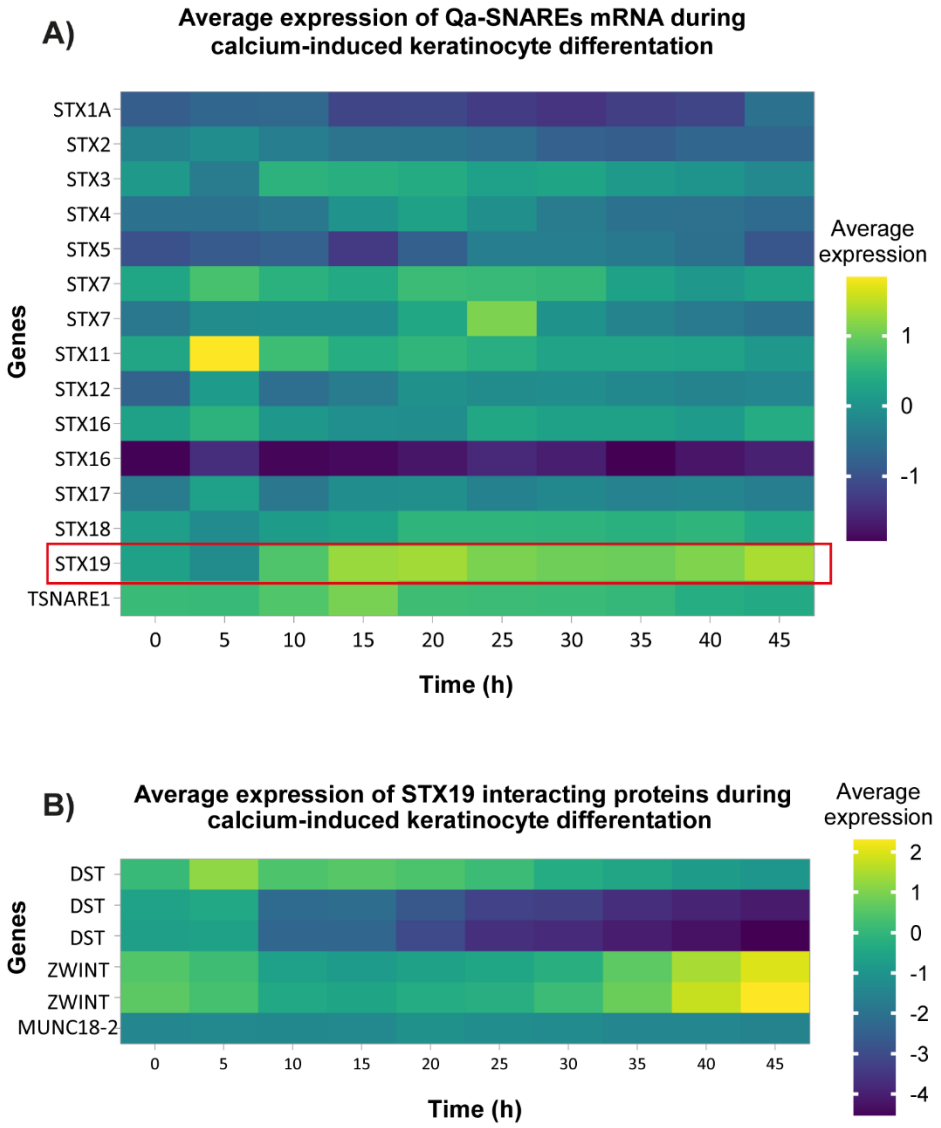

Figure 4-3: Heatmap depicting the fold change in mRNA expression of Qa-SNAREs during calcium-induced differentiation of keratinocytes.The average expression of mRNA for each given gene in calcium-induced differentiated keratinocytes (relative to undifferentiated cells) was measured every 5 hours, over a 45 hour differentiation period. mRNA expression was measured by microarray analysis and normalised between samples. Multiple copies of the same gene represent different probe IDs. **A)** Qa-SNAREs mRNA expression over a 45 hour differentiation period. For the majority of Qa-SNAREs there is little change in mRNA expression over 45 hours. STX11 mRNA expression increased after 5 hours but returns to normal after 45 hours. STX19 expression (highlighted by the red box) was upregulated by a 5.20 fold change over a 45 hour period. **B)** STX19 interacting proteins mRNA expression over the 45 hour differentation period. Two probes for DST show a decrease in mRNA expression over the 45 hours. ZWINT shows an increase in mRNA expression over the 45 hour period. Munc18-2 shows no change in mRNA expression over the 45 hour period. These heatmaps were generated by Shabeeha Wahid based on data generated in *Toufighi et al., 2015. PLoS Computation Biology. doi.org/10.1371/journal.pcbi.1004256*

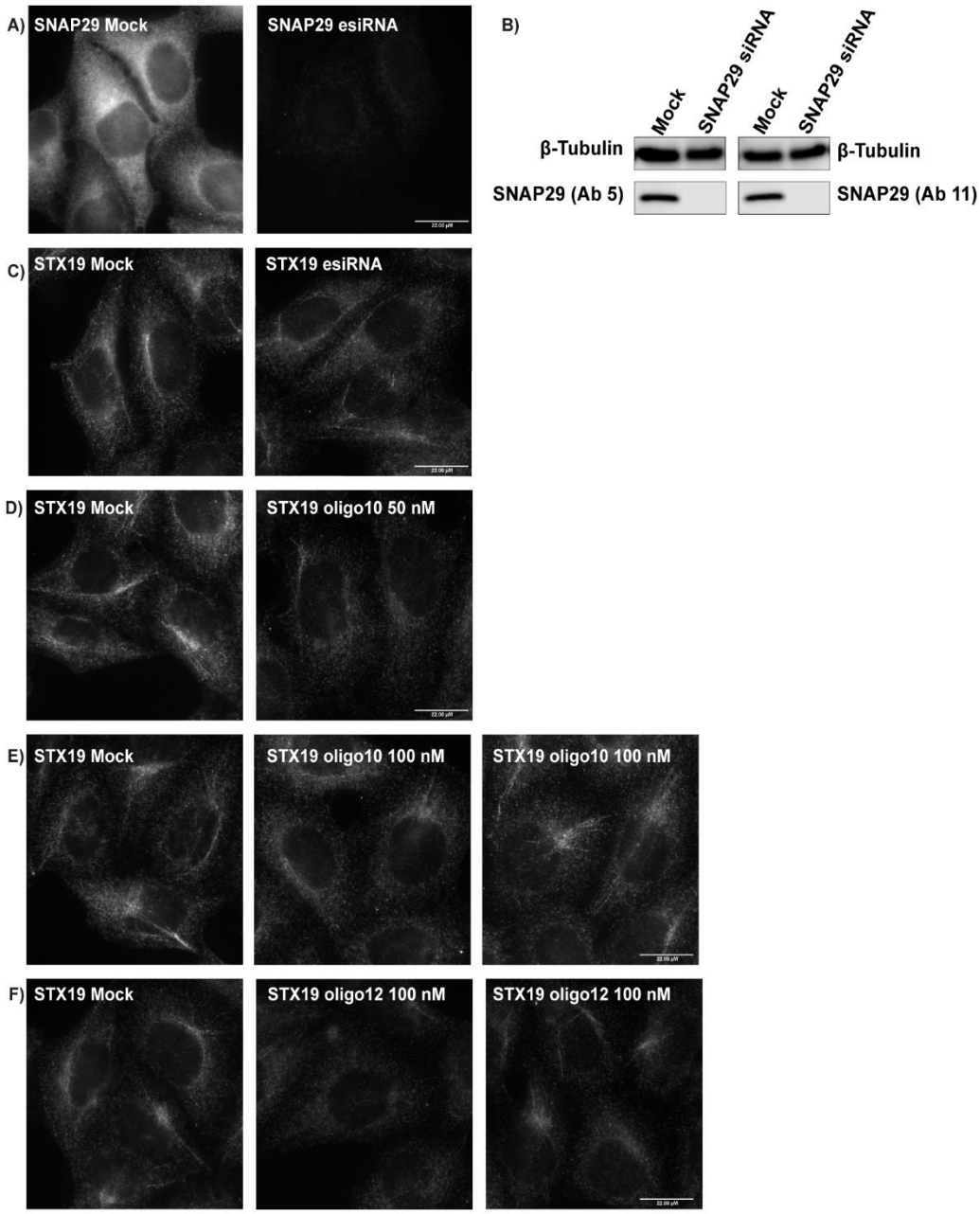

Figure 4-4: Optimisation of STX19 siRNA knockdown

HeLaM cells were transfected with either STX19 esiRNA, oligo10, or oligo12 at a concentration of either 50 nM or 100 nM siRNA 24 hours and 72 hours after seeding. Cells were fixed using 4 % PFA 96 hours post-transfection. Cells were stained with an anti-STX19 antibody to detect endogenous STX19. SNAP29 siRNA knockdown was used as a positive control. **A)** Mock transfected cells shows SNAP29 localises to the cytoplasm. Cells transfected with SNAP29 esiRNA showed reduced levels of SNAP29. **B)** Western blot showing SNAP29 knockdown. Cells were transfected with SNAP29 siRNA, lysed and blotted. The blot was probed using two different antibodies against SNAP29 (antibody 5 and antibody 11). β-Tubulin was used as a loading control. In mock transfected cell lysates, SNAP29 has a strong band at 29 kDa and β-Tubulin at 50 kDa. In SNAP29 siRNA transfected cells, the band for SNAP29 is lost whilst the β-Tubulin band remains. **C)** Mock transfected cells show STX19 localises to tubular recycling endosomes and the cytoplasm. Cells transfected with STX19 esiRNA also shows localisation to tubular recycling endomes and the cytoplasm. **D)** Mock transfected cells show STX19 localises to tubular recycling endosomes. Cells transfected with STX19 50 nM oligo10 siRNA also shows localisation to tubular recycling endomes and the cytoplasm. **E)** Mock transfected cells show STX19 localises to tubular recycling endosomes. Some cells transfected with STX19 100 nM oligo10 siRNA appeared to show reduced staining on tubular recycling endosomes however other cells showed both tubular recycling endosomal and cytoplasmic staining. **F)** Mock transfected cells show STX19 localises to tubular recycling endosomes. Some cells transfected with STX19 100 nM oligo12 siRNA appeared to show reduced staining on tubular recycling endosomes and in the cytoplasm, however other cells showed both tubular recycling endosomal and cytoplasmic staining. Scale bar: 22.00 μM.

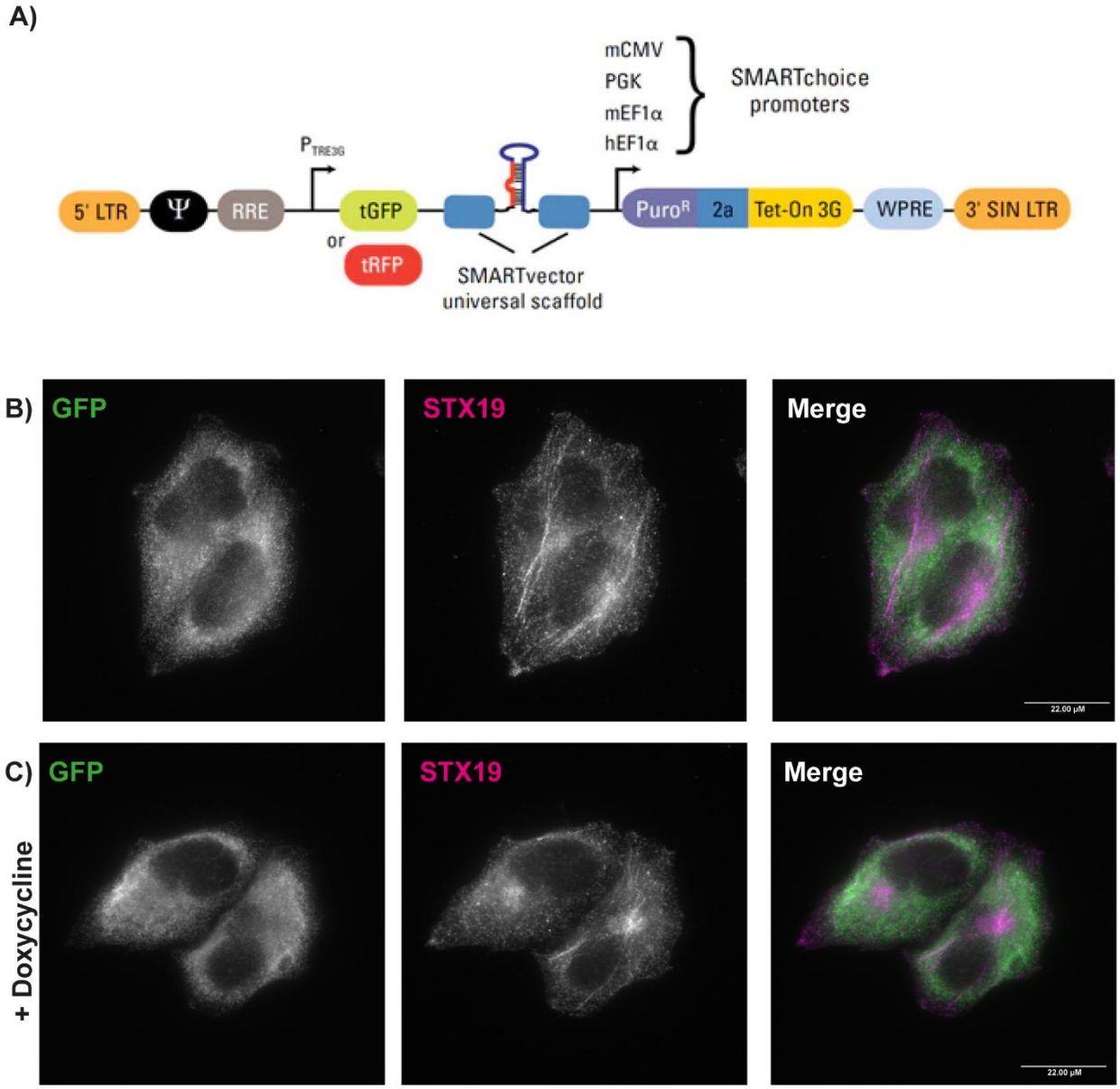

Figure 4-5: Tet-inducible shRNA does not knockdown STX19

A) Elements of the SMARTvector Inducible shRNA Lentiviral Backbone. The lentiviral backbone consists of a 5' Long Terminal Repeat (5'LTR), a Psi packcing sequence (Ψ), an inducible promoter with a Tetracycline Response Element activated by Tet-On 3G protein in the presence of doxycycline (P_{TRE3G}), turboGFP reporter (tGFP), SMARTvector universal scaffold which contains gene targeting sequence, puromycin resistance ($Puro^R$), a self cleaving peptide allowing $Puro^R$ and Tet-On 3G expression from a single RNA pol II promoter (2a), Tet-On 3G - doxycycline-regulated transactivator protein, Woodchuck Hepatitis Post-transcriptional Regulatory Element (WPRE), and a 3' self-inactivating Long Terminal Repeat. **B-C)** HeLaM cells were infected with a tet-inducible shRNA lentiviral viral plasmid against STX19 and treated with 1 µg/mL doxycycline. Non-treated cells were a negative control. Cells were fixed using 4 % PFA and stained for STX19 using an anti-STX19 antibody. **B)** In the absence of doxycyline, GFP expression can be seen in the cytoplasm whilst STX19 localises to tubular recycling endosomes, the cytoplasm, and puncta throughout the cell. **C)** In the presence of doxycyline, FGFP expression can be seen in the cytoplasm whilst STX19 localises to tubular recycling endosomes, the cytoplasm, and puncta throughout the cell. Scale bar: 22.00 µM.

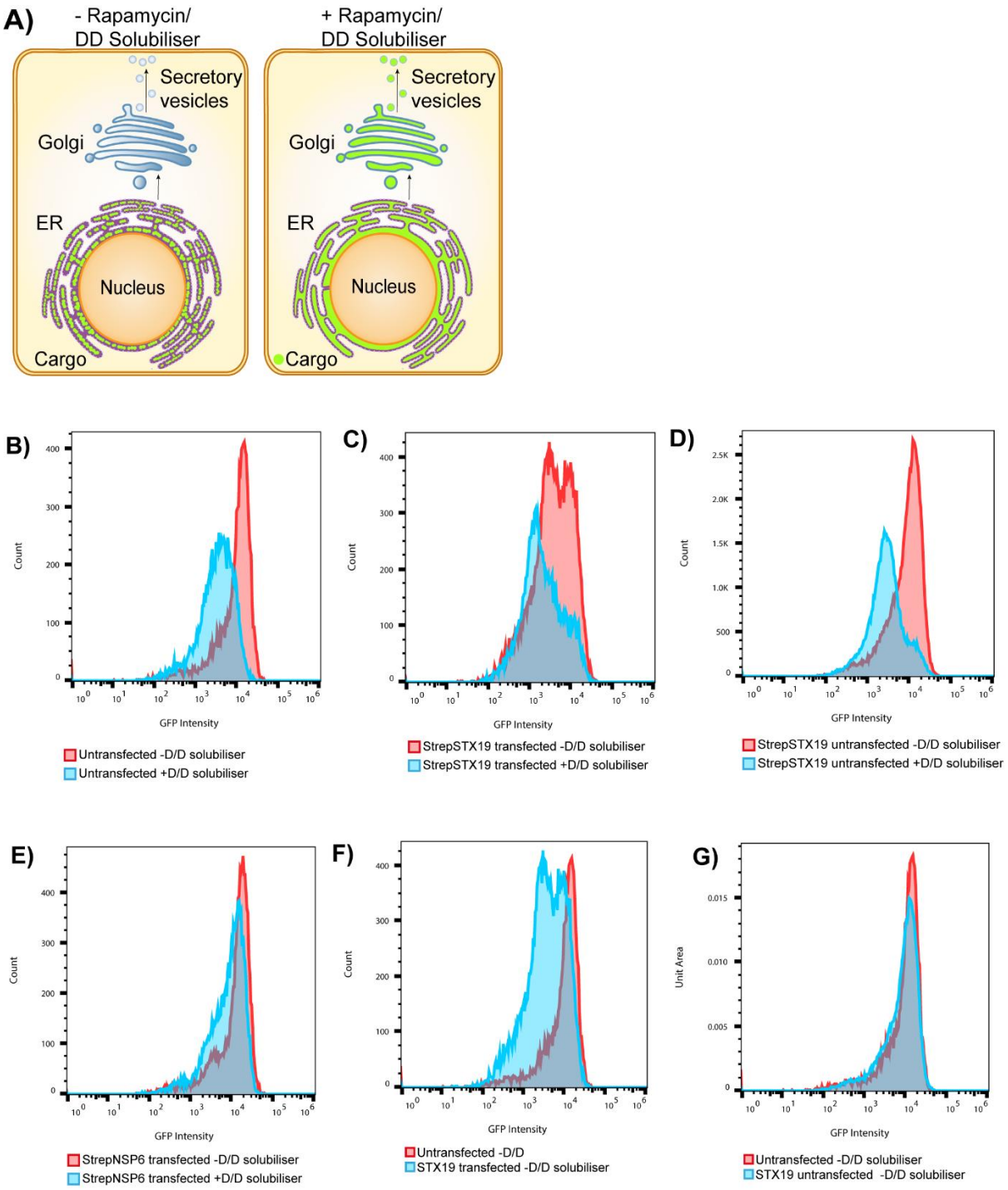
A)
- Rapamycin/
DD Solubiliser
+ Rapamycin/
DD Solubiliser
Secretory vesicles
Golgi
ER
Nucleus
Cargo
B)
Count
GFP Intensity
Untransfected -D/D solubiliser
Untransfected +D/D solubiliser
C)
StrepSTX19 transfected -D/D solubiliser
StrepSTX19 transfected +D/D solubiliser
D)
StrepSTX19 untransfected -D/D solubiliser
StrepSTX19 untransfected +D/D solubiliser
E)
StrepNSP6 transfected -D/D solubiliser
StrepNSP6 transfected +D/D solubiliser
F)
Untransfected -D/D
STX19 transfected -D/D solubiliser
G)
Unit Area
Untransfected -D/D solubiliser
STX19 untransfected -D/D solubiliser

Figure 4-6: Overexpression of STX19 in flow cytometry-based assay to measure constitutive secretion. A stable HeLaM cell line stably expressing pQCXIP-S1-eGFP-FM_4-FCS-hGH was used in this assay. This construct contains a signal sequence (S1), eGFP, four F_M aggregation domains, furin cleavage site (FCS) and human growth hormone (hGH). **A)** This construct is trapped in the ER until release by treatment with D/D solubiliser where it can traffic to the plasma membrane and be secreted by the cells, as described in *Gordon et al., 2010*. **B-G)** The stable cell line were either left untransfected, transfected with StrepSTX19, or transfected with StrepNSP6. Cells were incubated for 24 hours before treatment with 1 µg/mL D/D solubiliser for 120 minutes. Cells were then fixed using 4 % PFA and stained using anti-Strep antibodies and GFP fluorescent intensity was measure by flow cytometry. **B)** The intensity of GFP fluorescence in untransfected cells untreated (red) or treated with D/D solubiliser (blue). Untreated cells show a clear peak of intensity. After treatment, this peak is shifted to the right. **C)** The intensity of GFP fluorescence in StrepSTX19 transfected cells untreated (red) or treated with D/D solubiliser (blue). Untreated cells show a broad peak of intensity. After treatment, this peak is slightly shifted to the right but remains broad. **D)** The StrepSTX19 transfected cell sample was gated for those that were positive for StrepSTX19 expression and those that were negative for StrepSTX19 expression and thus untransfected. The cells that were negative for StrepSTX19 expression are termed StrepSTX19 untransfected. The intensity of GFP fluorescence in StrepSTX19 untransfected cells untreated (red) or treated with D/D solubiliser (blue). Untreated cells show a clear peak of intensity. After treatment, this peak is shifted to the right. **E)** The intensity of GFP fluorescence in StrepNSP6 transfected cells untreated (red) or treated with D/D solubiliser (blue). Untreated cells show a clear peak of intensity. After treatment, this peak shows a similar GFP fluorescent intensity as the untreated population. **F)** Comparison of Untransfected cells without D/D solubiliser treatment (red) and StrepSTX19 transfected cells without D/D solubiliser treatment (blue). The StrepSTX19 transfected population of cells shows a broader than the untransfected population suggesting a larger distribution of GFP fluorescence intensity in these cells. **G)** Comparison of Untransfected cells without D/D solubiliser treatment (red) and StrepSTX19 untransfected cells without D/D solubiliser (blue). Both untransfected cells and StrepSTX19 untransfected cells show a clear peak at similar GFP fluorescent intensities.

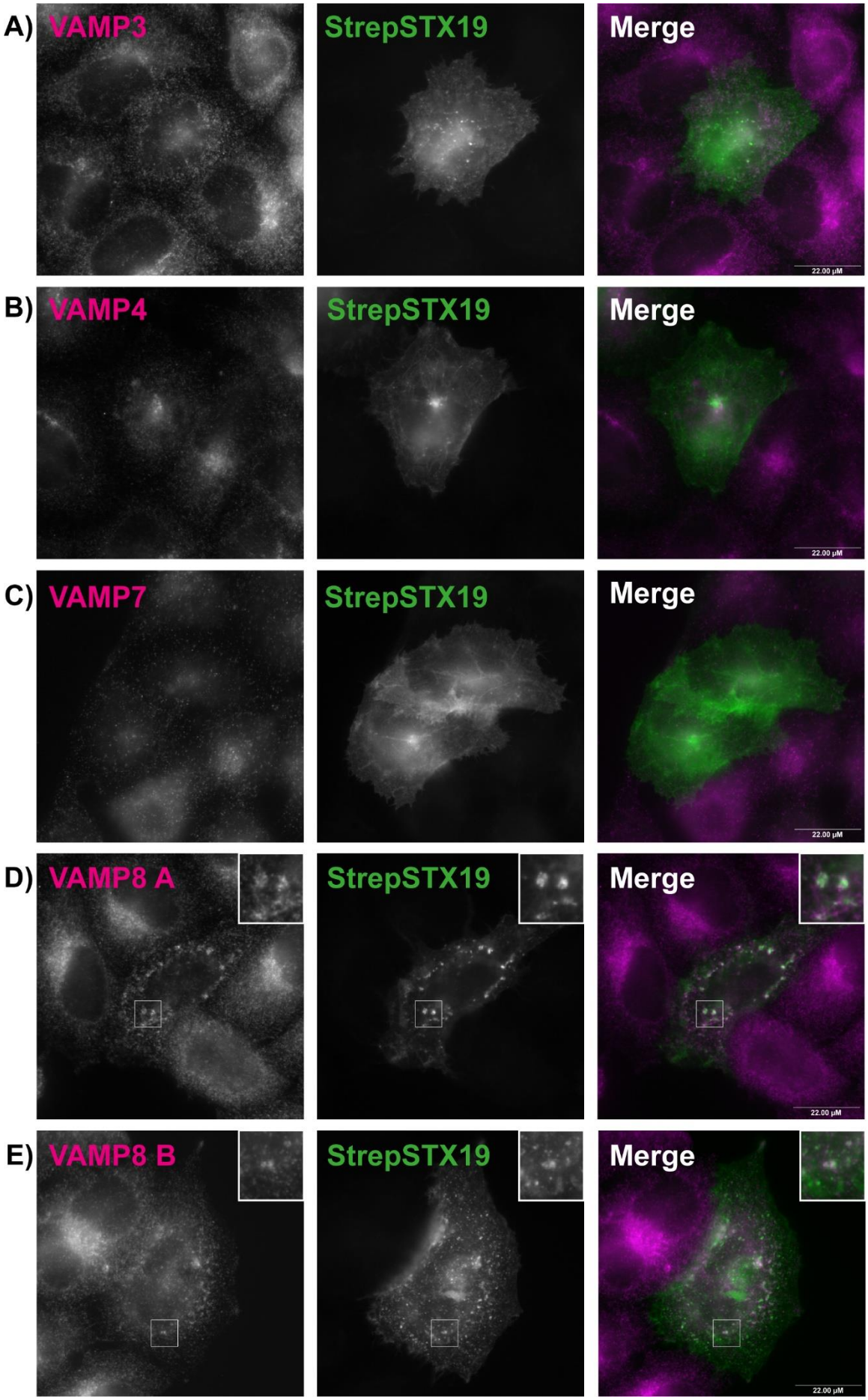
A)
VAMP3
StrepSTX19
Merge
22.00 µM
B)
VAMP4
StrepSTX19
Merge
22.00 µM
C)
VAMP7
StrepSTX19
Merge
22.00 µM
D)
VAMP8 A
StrepSTX19
Merge
22.00 µM
E)
VAMP8 B
StrepSTX19
Merge
22.00 µM

Figure 4-7: Overexpression of a STX19 results in the altered steady state distribution of VAMP8. HeLaM cells were transfected with StrepSTX19 and then fixed using 4 % PFA and stained with anti-Strep549 conjugate antibodies and anti-VAMPs 3, 4, 7, 8A, and 8B antibodies. **A-E)** StrepSTX19 localises to the plasma membrane and tubular recycling endosomes, and shows vesicular staining throughout the cytoplasm as well as puncta distributed throughout the cell. **A)** In untransfected and transfected cells, VAMP3 shows vesicular staining throughout the cytoplasm with an enrichment in the perinuclear area. **B)** In untransfected and transfected cells, VAMP4 shows vesicular staining throughout the cytoplasm with an enrichment in the perinuclear area. **C)** In untransfected and transfected cells, VAMP7 shows faint vesicular staining throughout the cytoplasm. **D)** In untransfected cells VAMP8 A shows vesicular staining throughout the cytoplasm which is enriched in the perinuclear region. In StrepSTX19 transfected cells, VAMP8 A shows vesicular staining throughout the cytoplasm as well as large puncta which are StrepSTX19-positive, highlighted by the insert. **E)** In untransfected cells VAMP8 B shows vesicular staining throughout the cytoplasm which is enriched in the perinuclear region. In StrepSTX19 transfected cells, VAMP8 B shows vesicular staining throughout the cytoplasm as well as larger puncta that are StrepSTX19-positive, highlighted by the insert. Scale bar: 22.00 μM.

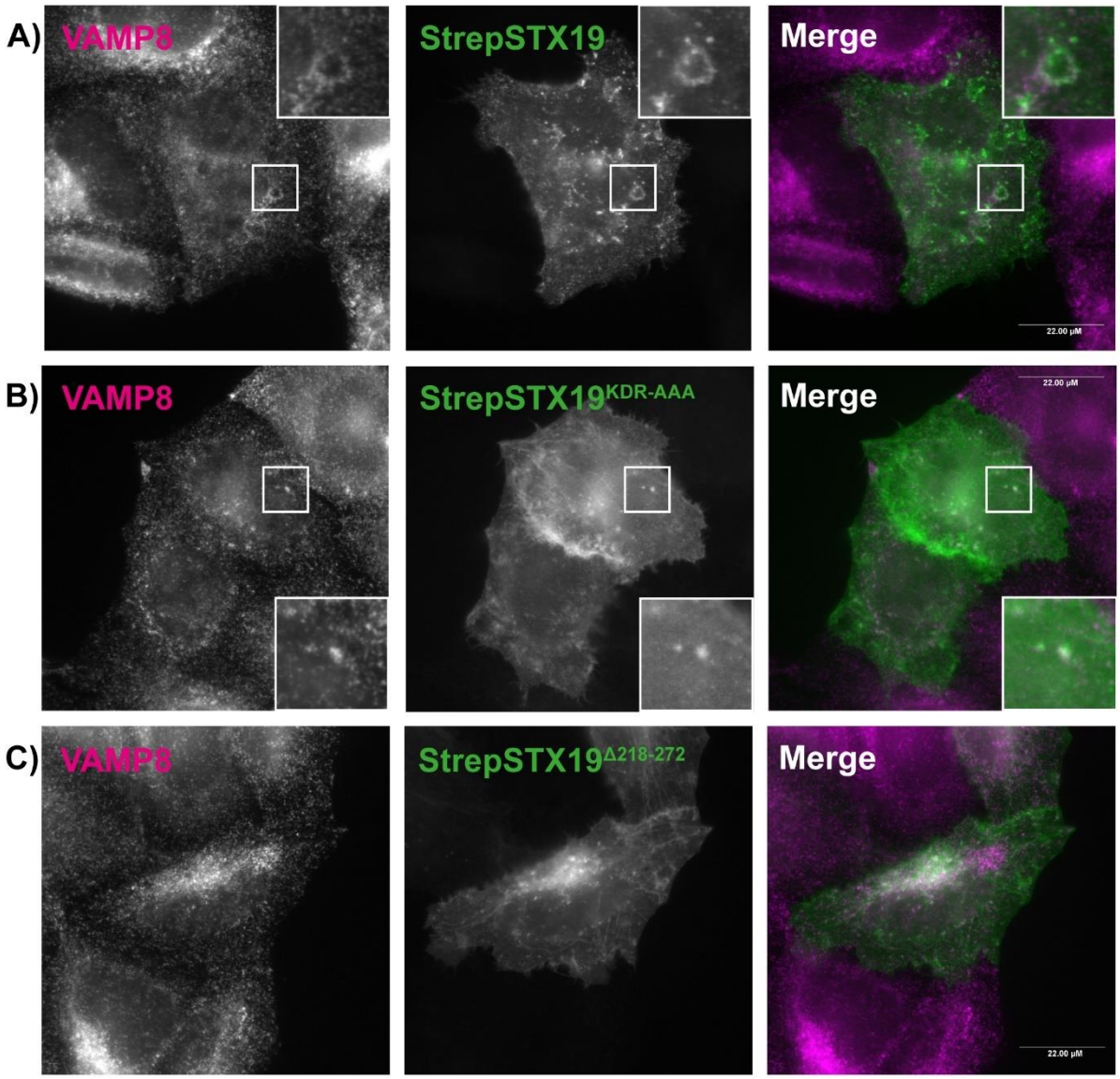

Figure 4-8: Overexpression of strep-tagged wildtype and KDR-AAA mutant STX19 constructs result in an altered distribution of VAMP8. HeLaM cells were transfected with strep-tagged wildtype and mutant STX19 constructs. Cells were fixed using 4 % PFA and stained with anti-VAMP8 to label the endogenous protein. **A-C)** StrepSTX19, StrepSTX-19$^{KDR-AAA}$, and StrepSTX19$^{\Delta 218-272}$ localise to the plasma membrane, tubular recycling endosomes, and puncta distributed throughout the cytoplasm**. A)** In untransfected cells, VAMP8 shows vesicular staining throughout the cytoplasm which is enriched in the perinuclear area. In transfected cells, VAMP8 shows vesicular staining throughout the cytoplasm and localises to larger circular structures. **B)** In transfected cells, VAMP8 shows vesicular staining throughout the cytoplasm and localises to larger puncta distributed throughout the cytoplasm. **C)** In transfected cells, VAMP8 shows vesicular staining throughout the cytoplasm with a pool enriched in the perinuclear area. Scale bar: 22.00 µM

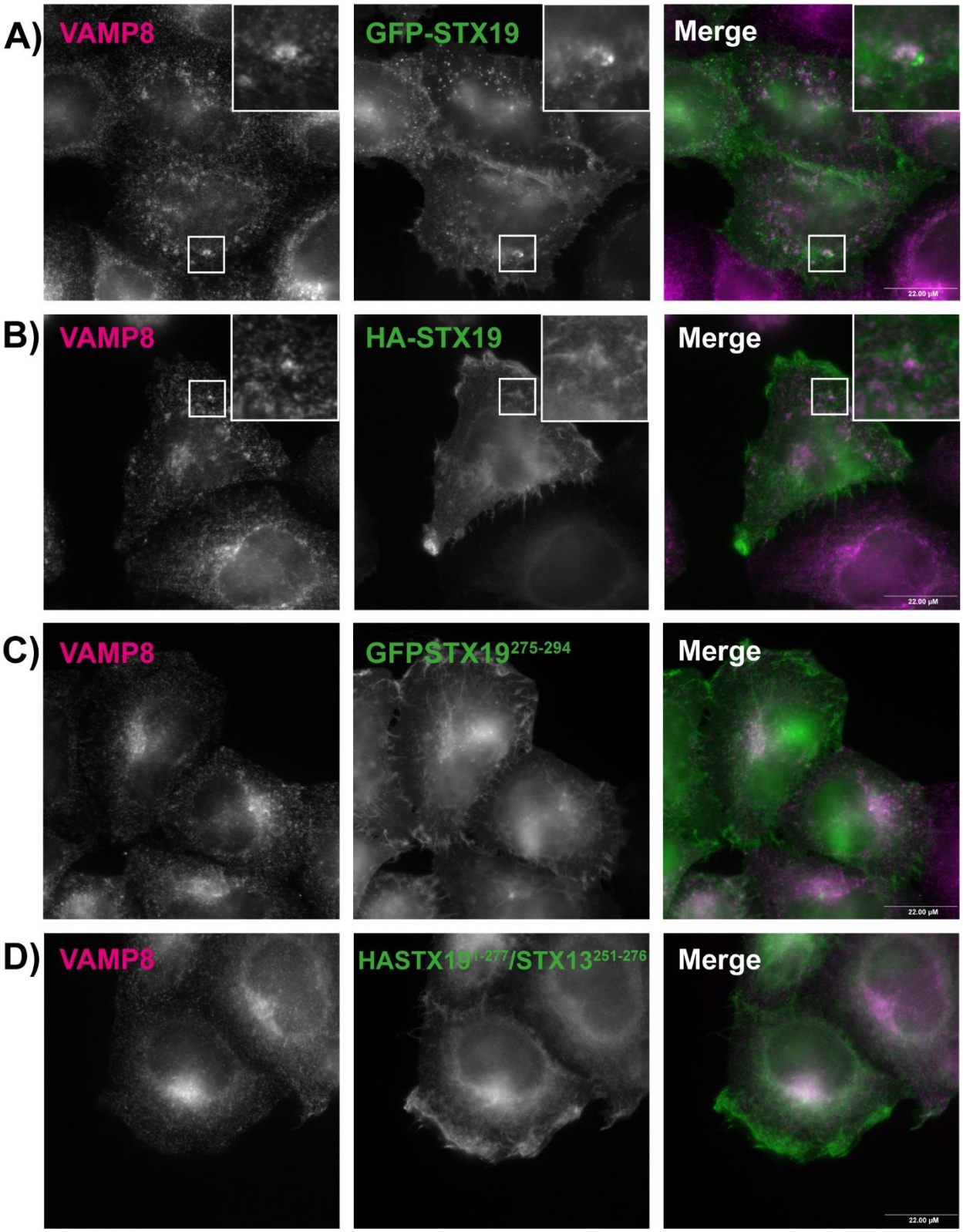
A)
VAMP8
GFP-STX19
Merge
22.00 µM
B)
VAMP8
HA-STX19
Merge
22.00 µM
C)
VAMP8
GFPSTX19275-294
Merge
22.00 µM
D)
VAMP8
HASTX191-277/STX13251-276
Merge
22.00 µM

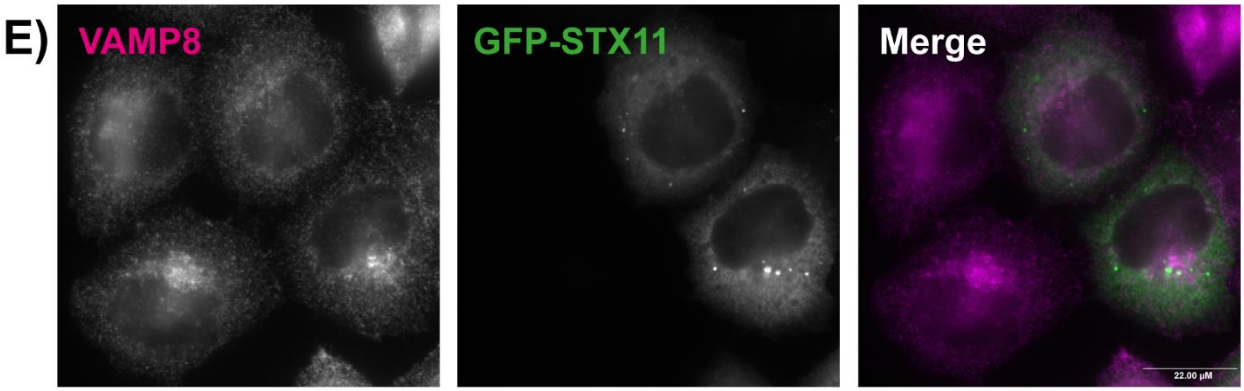

Figure 4-9: Overexpression of full length STX19 constructs result in an altered distribution of VAMP8. HeLaM cells were transfected with various STX19 constructs and GFP-STX11 as a negative control. Cells were fixed using 4 % PFA stained with anti-VAMP8 to label the endogenous protein. **A)** GFP-STX19 localises to the plasma membrane, tubular recycling endosomes, and puncta throughout the cell. In transfected cells, VAMP8 shows vesicular staining throughout the cytoplasm and localisation to larger puncta distributed throughout the cell. **B)** HA-STX19 localises to the plasma membrane and tubular recycling endosomes. In transfected cells, VAMP8 shows vesicular staining throughout the cytoplasm and localisation to larger puncta distributed throughout the cell. **C)** GFP-STX19$^{275-294}$ localises to the plasma membrane and tubular recycling endosomes. In transfected cells, VAMP8 shows a vesicular staining throughout the cytoplasm which is enriched in the perinuclear area. **D)** HASTX19$^{1-277}$/STX13$^{251-276}$ localises to the plasma membrane and shows vesicular staining throughout the cytoplasm. In transfected cells, VAMP8 shows vesicular staining throughout the cytoplasm which is enriched in the perinuclear area. **E)** GFP-STX11 shows vesicular staining and localisation to puncta throughout the cytoplasm. In transfected cells, VAMP8 shows vesicular staining throughout the cytoplasm which is concentrated in the perinuclear region. Scale bar: 22.00 µM

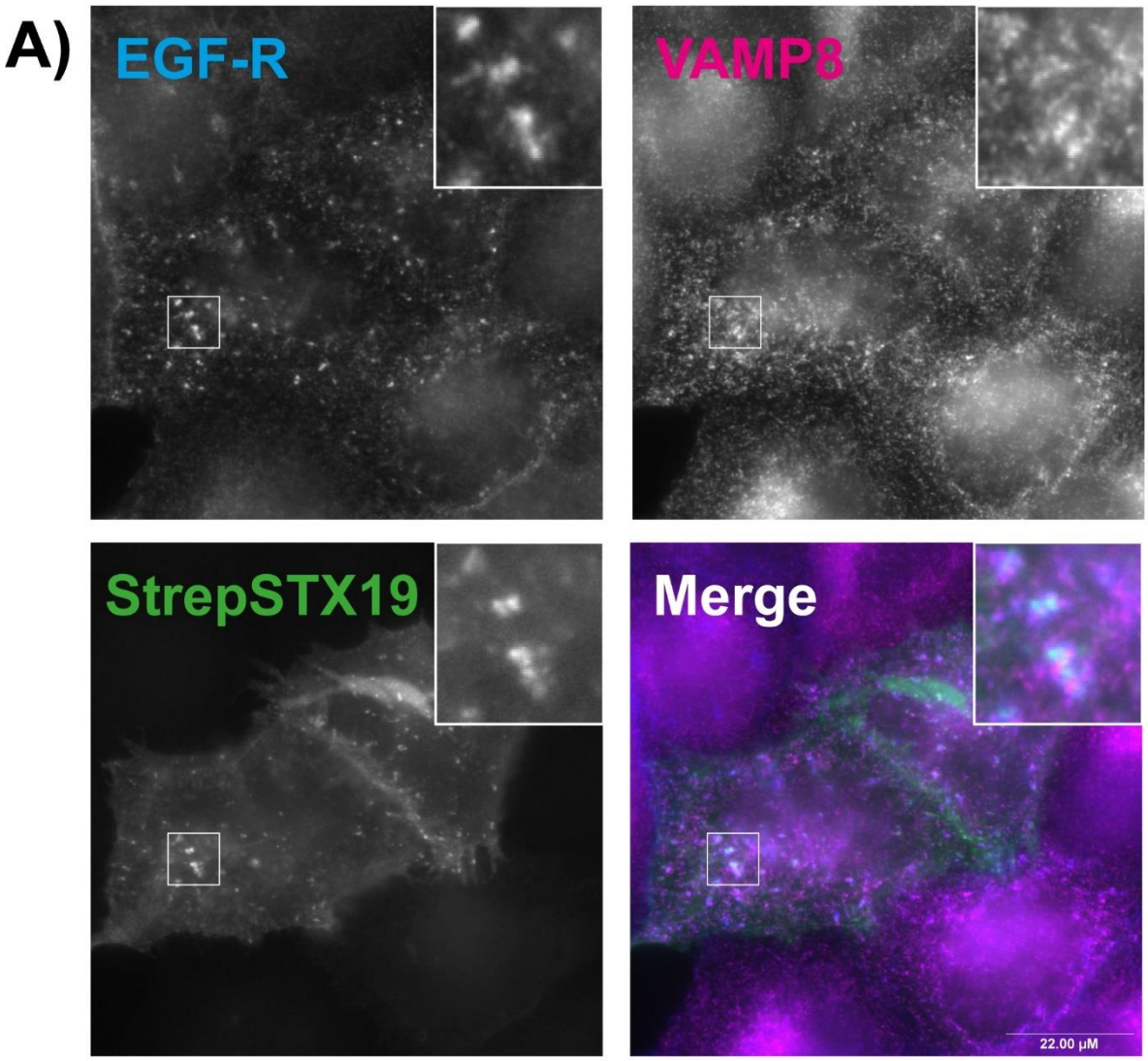

Figure 4-10: StrepSTX19 is enriched in similar areas to VAMP8 and EGF-R. HeLaM cells were transfected with StrepSTX19 then fixed using 4 % PFA and stained with anti-VAMP8 and anti-EGF-R antibodies. **A)** VAMP8 shows vesicular staining throughout the cytoplasm and localises to larger puncta distributed throughout the cell. EGF-R shows a punctate staining pattern throughout the cytoplasm and localises to larger puncta distributed throughout the cell. StrepSTX19 localises to the plasma membrane and puncta distributed throughout the cell. EGF-R and StrepSTX19 localise to similar puncta demonstrated by the insert. VAMP8 does not completely colocalise with the EGF-R/StrepSTX19 puncta but is enriched in similar areas. Scale bar: 22.00 µM.

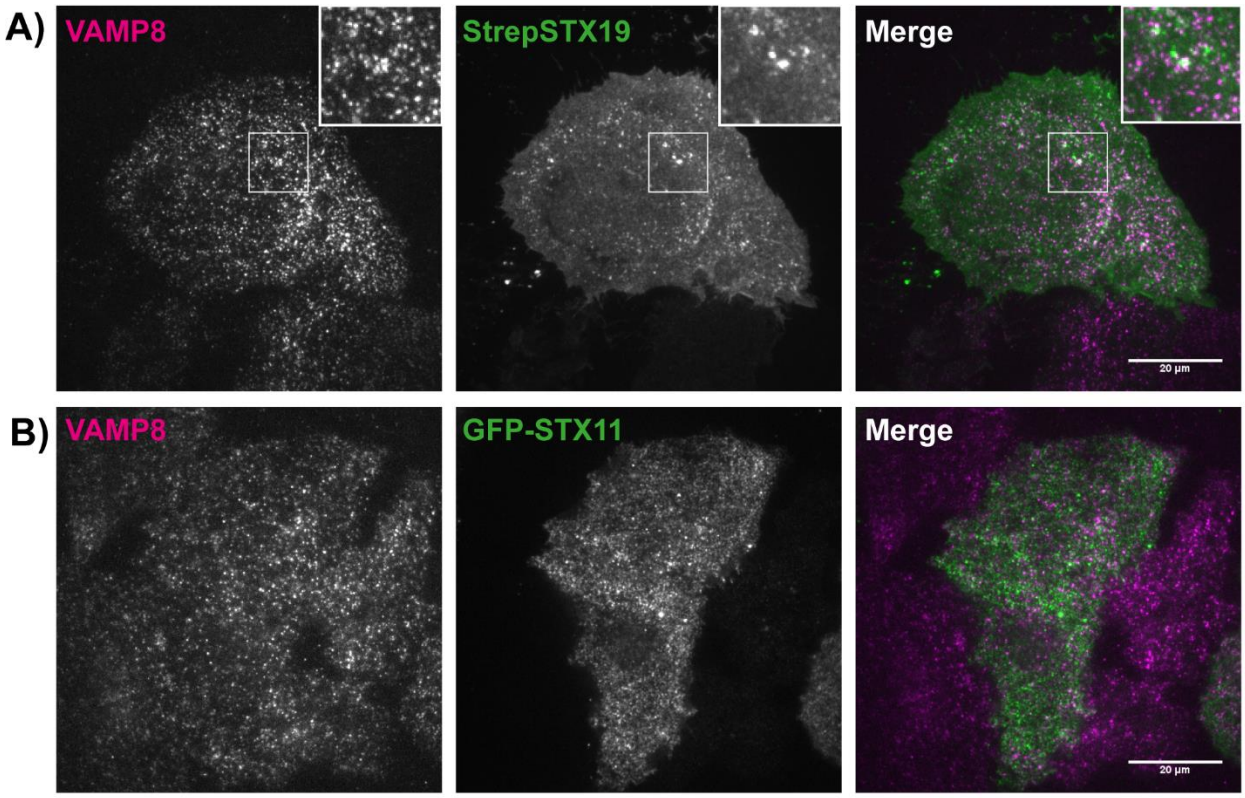

Figure 4-11: StrepSTX19 is enriched in similar puncta to VAMP8 at the cell surface. HeLaM cells were transfected with either StrepSTX19 or GFPSTX11, then fixed using 4 % PFA and stained with an anti-VAMP8 antibody. Cells were imaged using TIRF microscopy to visualise localisation at a 100 nM depth from the cell surface. **A)** STX19 and VAMP8 localises to puncta which are present in the TIRF field, thus either at the cell surface or just below. A small number of VAMP8 puncta are localised in similar areas to StrepSTX19 puncta, highlighted by the insert. **B)** GFP-STX11 and VAMP8 localise to puncta which are present in the TIRF field. There is limited cross over of VAMP8 and GFP-STX11 puncta. Scale bar: 20.00 µM.

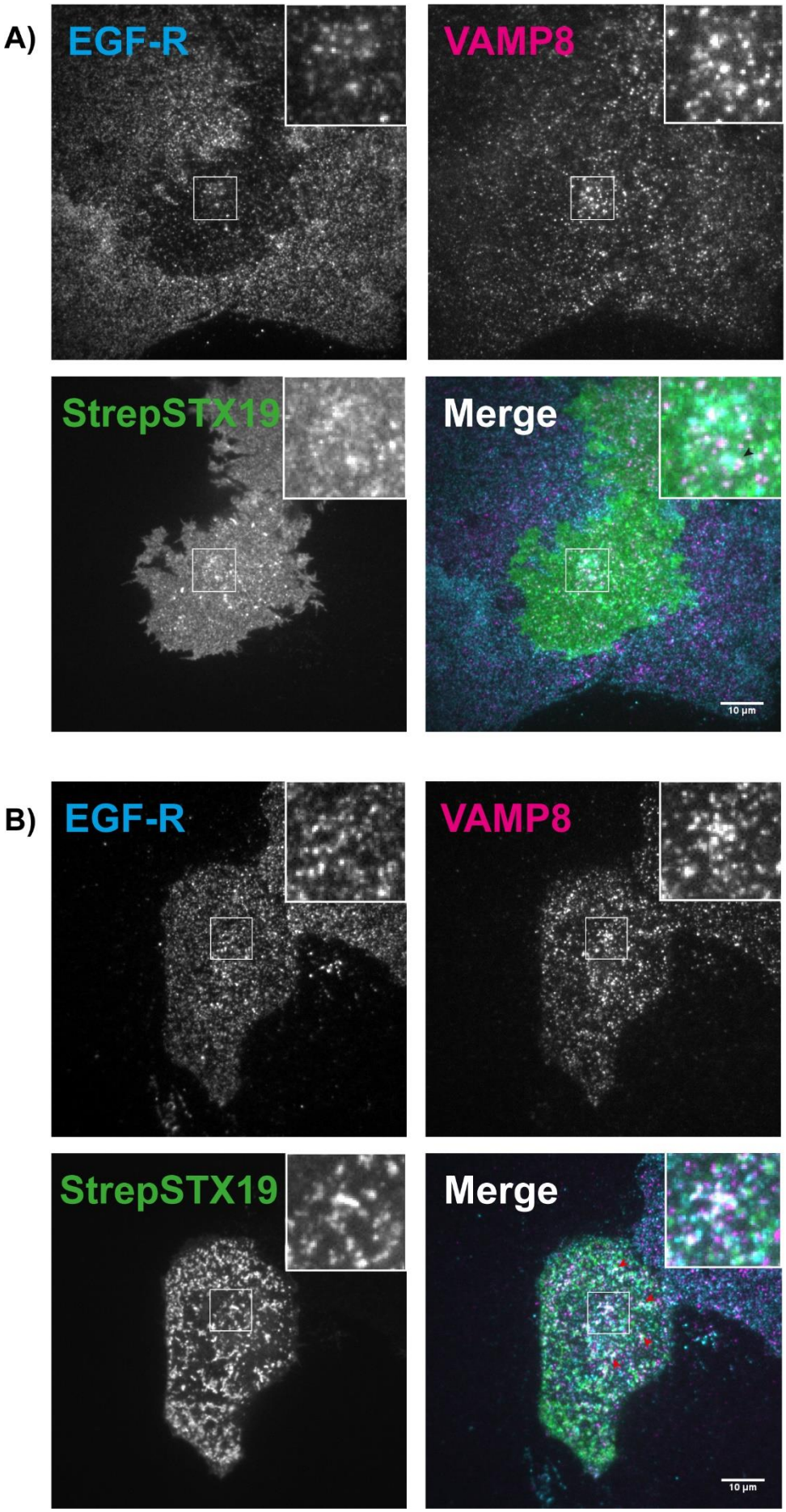
A)
EGF-R
VAMP8
StrepSTX19
Merge
10 µm
B)
EGF-R
VAMP8
StrepSTX19
Merge
10 µm

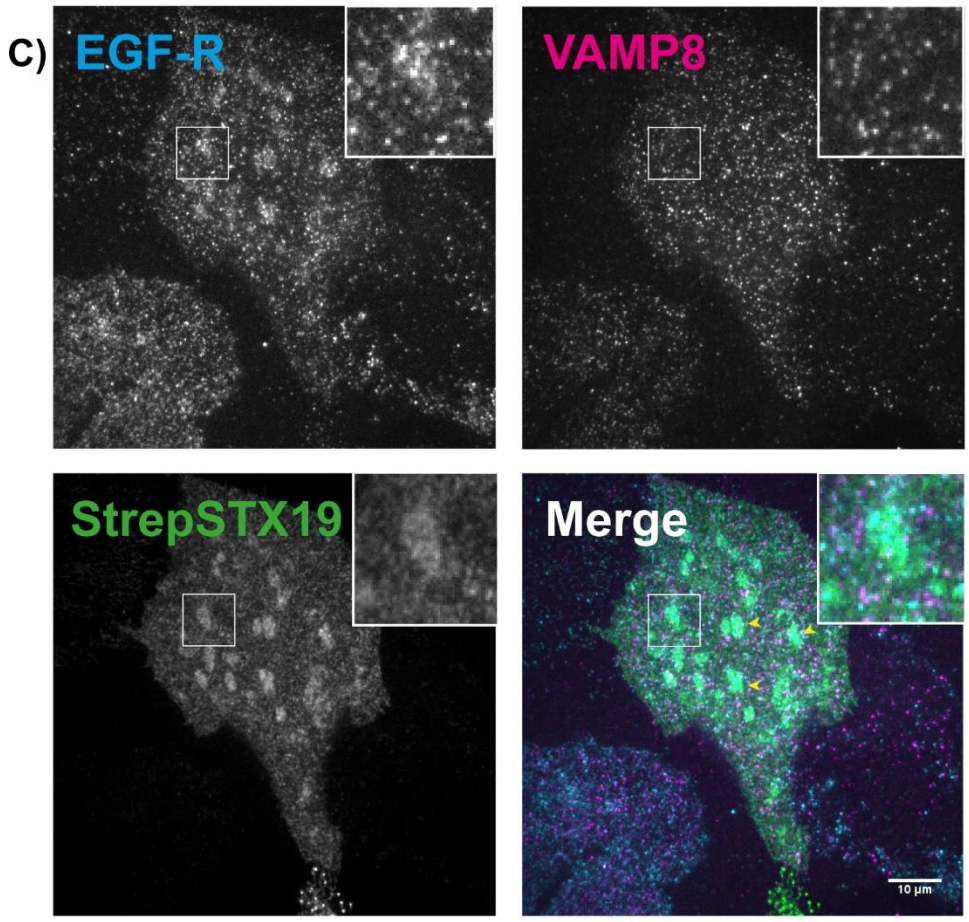
C)
EGF-R
VAMP8
StrepSTX19
Merge
10 µm

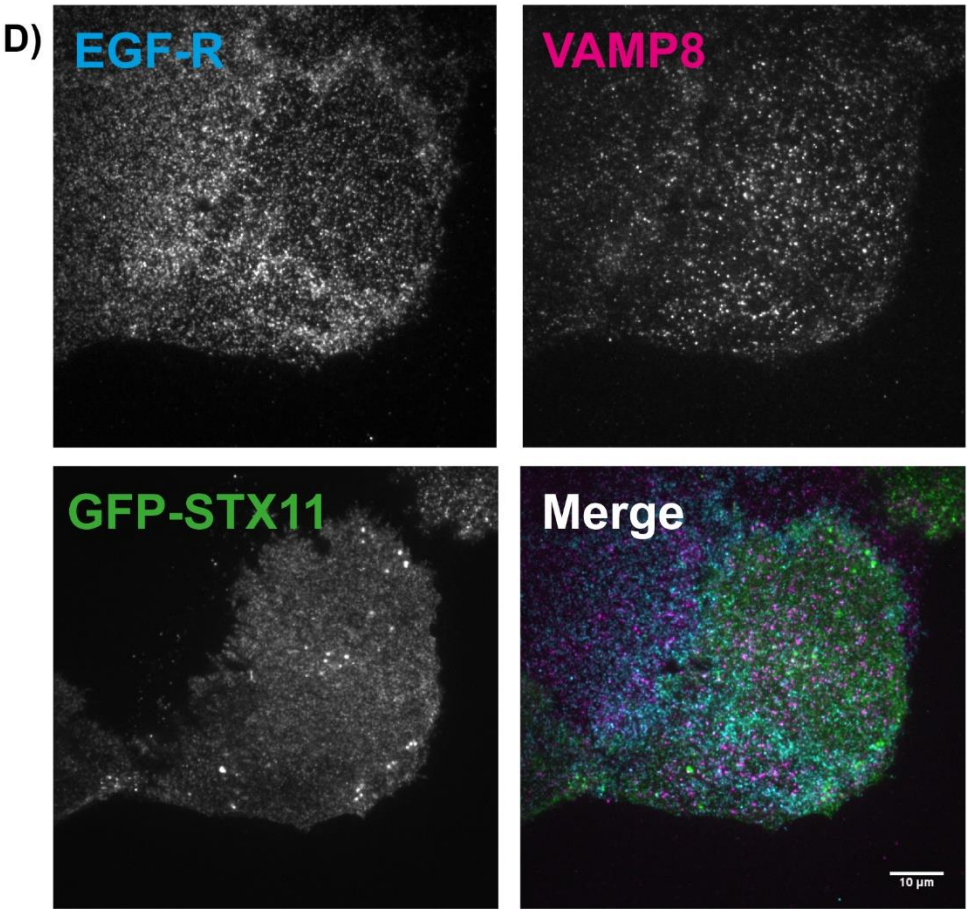
D)
EGF-R
VAMP8
GFP-STX11
Merge
10 µm

Figure 4-12: StrepSTX19 is enriched in subdomains of the plasma membrane with either EGF-R or VAMP8. HeLaM cells were transfected with either StrepSTX19 or GFP-STX11, then fixed using 4 % PFA and stained with anti-VAMP8 and anti-EGFR antibodies. Cells were imaged using TIRF microscopy to visualise localisation at a 100 nM depth from the cell surface. **A)** EGF-R, VAMP8, and STX19 are localised to puncta which are present in the TIRF field, thus either at or just below the cell surface. A pool of these markers appear to be enriched in similar domains of he plasma membrane but show limited co-localisation, as highlighted by the insert. **B)** EGF-R, VAMP8, and STX19 are localised to puncta which are present in the TIRF field. StrepSTX19 and VAMP8 are enriched in a number of the same puncta (red arrows; highlighted by the insert). EGF-R is not present in StrepSTX19/VAMP8 puncta. **C)** EGF-R and StrepSTX19 are enriched in similar uncharacterised patches at the cell surface (yellow arrows; highlighted by the insert). VAMP8 localises to puncta across the cell surface but is not present in the EGF-R/StrepSTX19 patches. **D)** EGF-R, VAMP8, and GFP-STX11 localise to puncta which are present in the TIRF field. The EGF-R, VAMP8, and GFP-STX11 puncta do not colocalise. Scale bar: 10.00 µM.

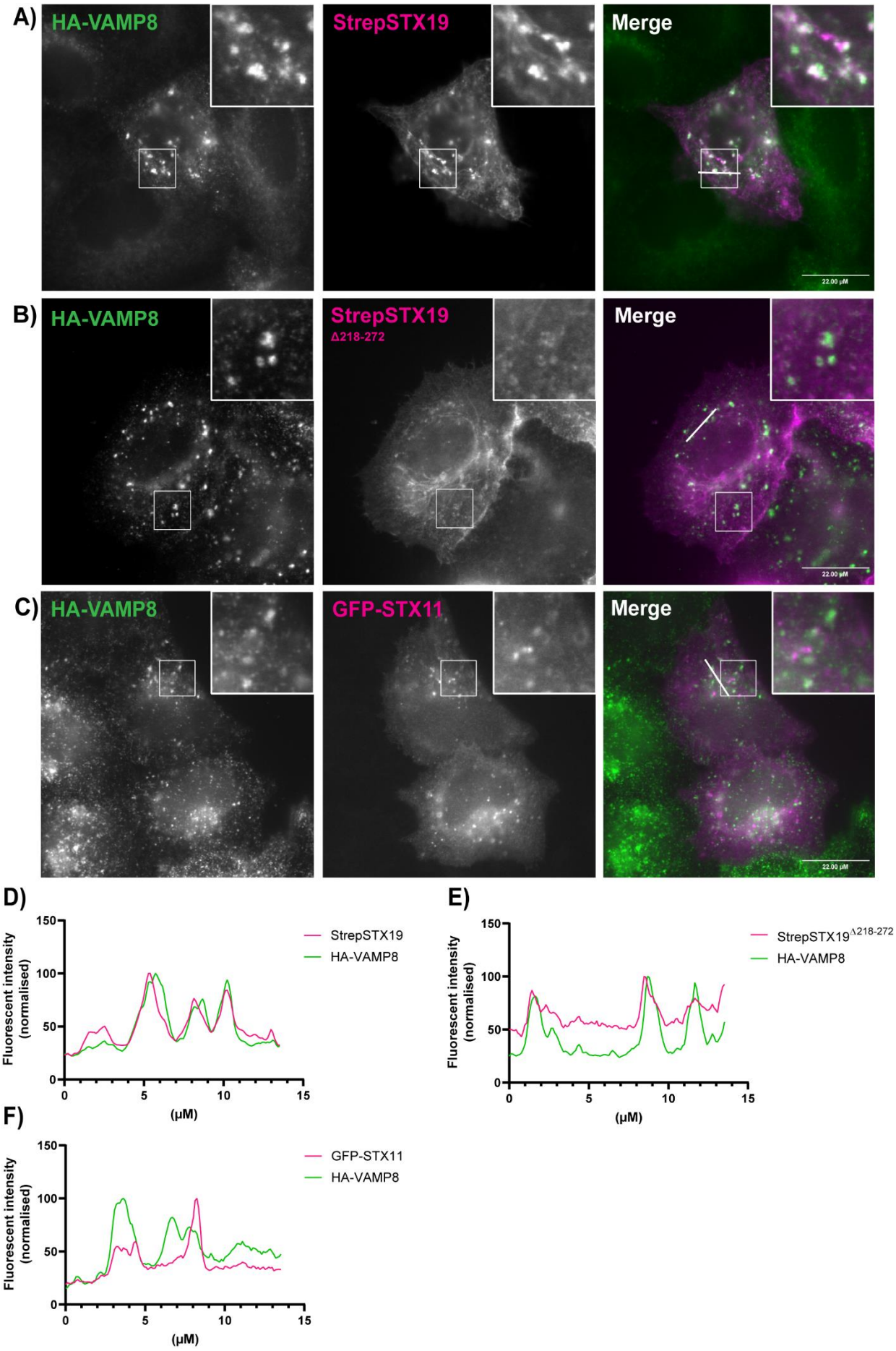
A)
HA-VAMP8
StrepSTX19
Merge
22.00 µM
B)
HA-VAMP8
StrepSTX19
Δ218-272
Merge
22.00 µM
C)
HA-VAMP8
GFP-STX11
Merge
22.00 µM
D)
Fluorescent intensity (normalised)
150
100
50
0
0
5
10
15
(µM)
StrepSTX19
HA-VAMP8
E)
Fluorescent intensity (normalised)
150
100
50
0
0
5
10
15
(µM)
StrepSTX19Δ218-272
HA-VAMP8
F)
Fluorescent intensity (normalised)
150
100
50
0
0
5
10
15
(µM)
GFP-STX11
HA-VAMP8

Figure 4-13: StrepSTX19 and VAMP8 co-localise in endocytic carriers. HeLaM cells stably expressing HA-VAMP8 were transfected with either StrepSTX19, StrepSTX19$^{\Delta 218\text{-}272}$ or GFP-STX11. Cells were treated with anti-HA antibodies in culture media and incubated for 30 minuts at 37 °C. Cells were then fixed using 4 % PFA and stained with anti-Strep594 conjugate antibodies and anti-VAMP8 antibodies. **A)** StrepSTX19 localises to the plasma membrane, tubular recycling endosomes and is enriched in puncta in the cytoplasm. VAMP8 shows enrichment in puncta in the cytoplasm and co-localises with StrepSTX19 at these puncta as demonstrated by the line scan analysis. STX19 and VAMP8 puncta are highlighted by the insert. **B)** StrepSTX19$^{\Delta 218\text{-}272}$ localises to the plasma membrane, tubular recycling endosomes and is enriched in puncta in the cytoplasm. VAMP8 shows enrichment in puncta in the cytoplasm and co-localises with StrepSTX19$^{\Delta 218\text{-}272}$ at these puncta as demonstrated by the line scan analysis. StrepSTX19$^{\Delta 218\text{-}272}$ and VAMP8 puncta are highlighted by the insert.**C)** GFP-STX11 localises to the cytoplasm and is enriched in puncta in the cytoplasm. VAMP8 shows enrichment in puncta in the cytoplasm but does not co-localises with GFP-STX11 at these puncta as demonstrated by the line scan analysis. The insert highlights that GFP-STX11 and VAMP8 puncta do not co-localise. Scale bar: 22.00 µM.

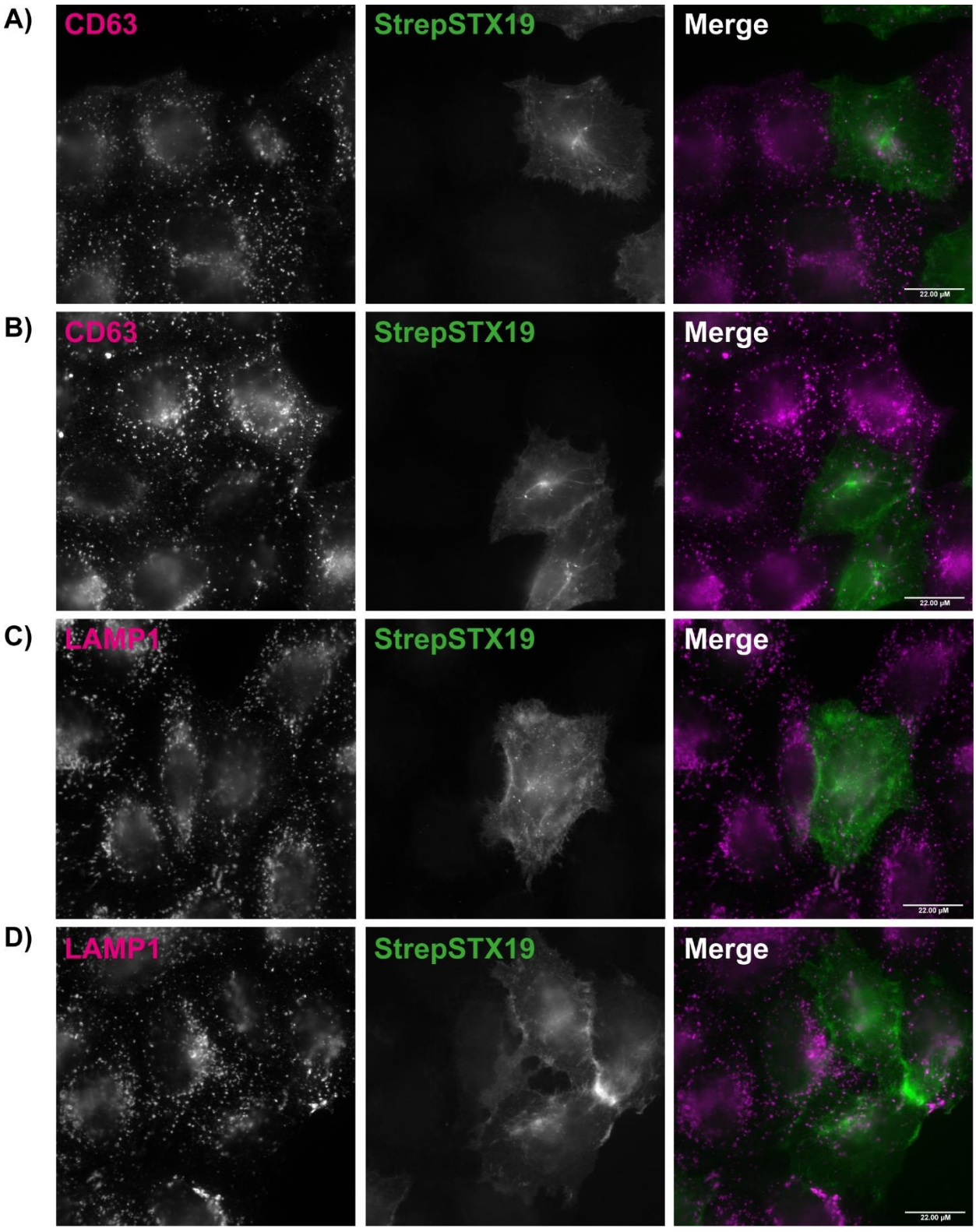
A)
CD63
StrepSTX19
Merge
22.00 µM
B)
CD63
StrepSTX19
Merge
22.00 µM
C)
LAMP1
StrepSTX19
Merge
22.00 µM
D)
LAMP1
StrepSTX19
Merge
22.00 µM

Figure 4-14: StrepSTX19 overexpression may alter the distribution of lysosomal markers. HeLaM cells were transfected with StrepSTX19. Cells were then fixed using 4 % PFA and stained for lysosomal makers using anti-CD63 and anti-LAMP1 antibodies. **A-B)** StrepSTX19 localises to the plasma membrane, tubular recycling endosomes, and unknown puncta. In untransfected cells, CD63 localises to puncta largely concentrated in the perinuclear region. In StrepSTX19 transfected cells, CD63 levels are reduced and there are fewer CD63-positive puncta. **C-D)** StrepSTX19 localises to the plasma membrane, tubular recycling endosomes, and unknown puncta. In untransfected cells, LAMP1 localises to puncta largely concentrated in the perinuclear region of the cell. In StrepSTX19 transfected cells, fewer LAMP1 puncta are concentrated in the perinuclear region and more LAMP1 puncta distributed towards the periphery of the cell. Scale bar: 22.00 μM.

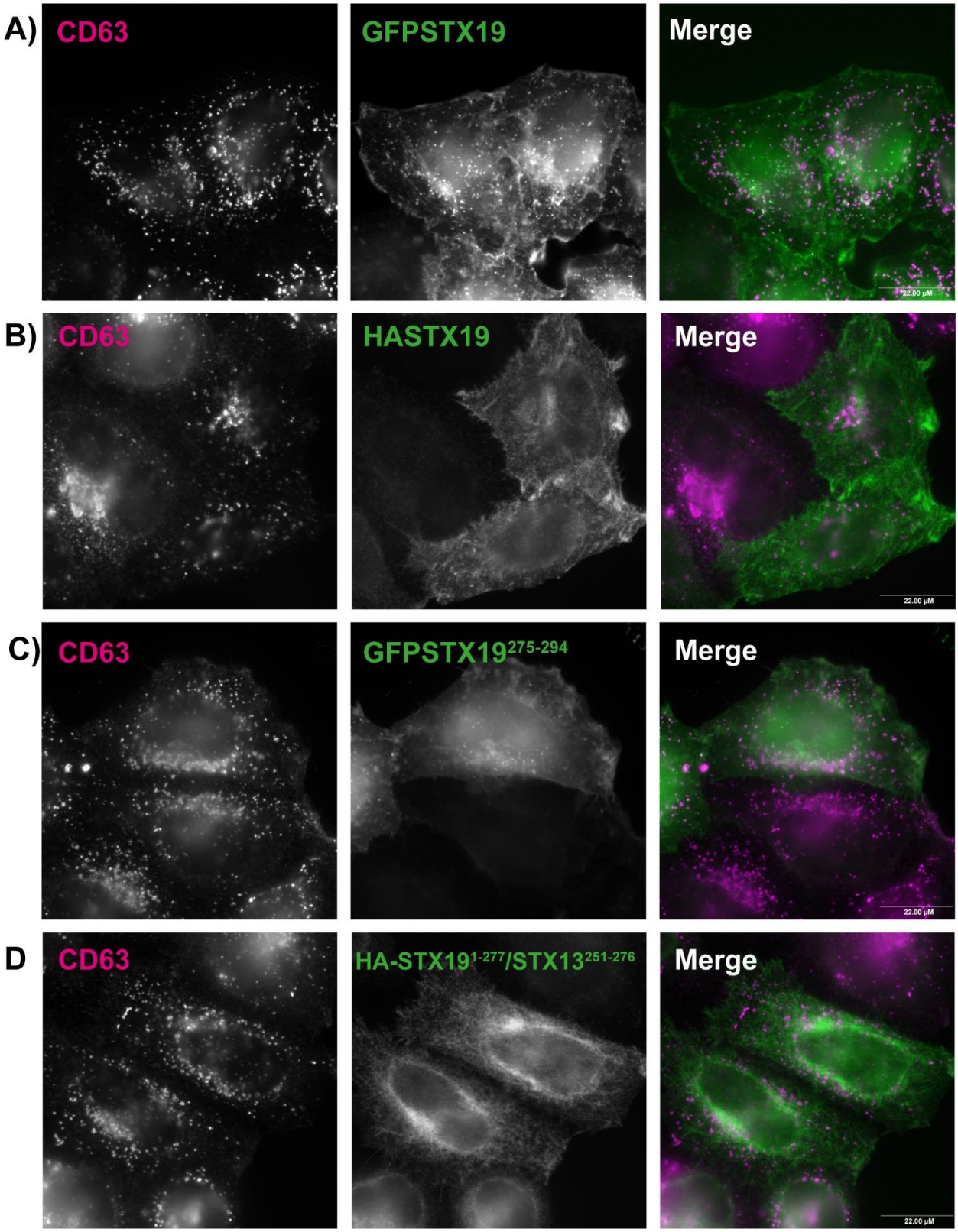
A)
CD63
GFPSTX19
Merge
22.00 µM
B)
CD63
HASTX19
Merge
22.00 µM
C)
CD63
GFPSTX19275-294
Merge
22.00 µM
D
CD63
HA-STX191-277/STX13251-276
Merge
22.00 µM

Figure 4-15: CD63 may change distribution upon overexpression of STX19 constructs
HeLaM cells were transfected with either GFP-STX19, HA-SXT19, GFP-STX19$^{275-294}$, HA-STX19$^{1-277}$/STX13$^{251-276}$, fixed using 4 % PFA and stained using anti-CD63 antibodies. **A)** GFP-STX19 localises to the plasma membrane, tubular recycling endosomes and puncta throughout the cytoplasm. In transfected cells, CD63 localises to puncta throughout the cytoplasm with a pool of puncta concentrated in the perinuclear area. There is some overlap between CD63 and GFP-STX19 puncta. **B)** HA-STX19 localises to the plasma membrane and tubular recycling endosomes. In untransfected cells, CD63 shows cytoplasmic staining and localises to puncta distributed throughout the cell with a pool of puncta concentrated in the perinuclear region. In transfected cells, CD63 localises to fewer puncta distributed throughout the cytoplasm compared with untransfected cells. **C)** GFP-STX19$^{275-294}$ localises to the plasma membrane, tubular recycling endosomes, and puncta in the cytoplasm. In transfected cells, CD63 localises to the cytoplasm and puncta in the cell which are largely concentrated in the perinuclear area. **D)** HA-STX19$^{1-277}$/STX13$^{251-276}$ localises to the plasma membrane and shows vesicular staining throughout the cytoplasm which is enriched in the perinuclear area. In transfected cells, CD63 localises to the cytoplasm and puncta in the cell which are largely concentrated in the perinuclear area.
Scale bar: 22.00 µM.

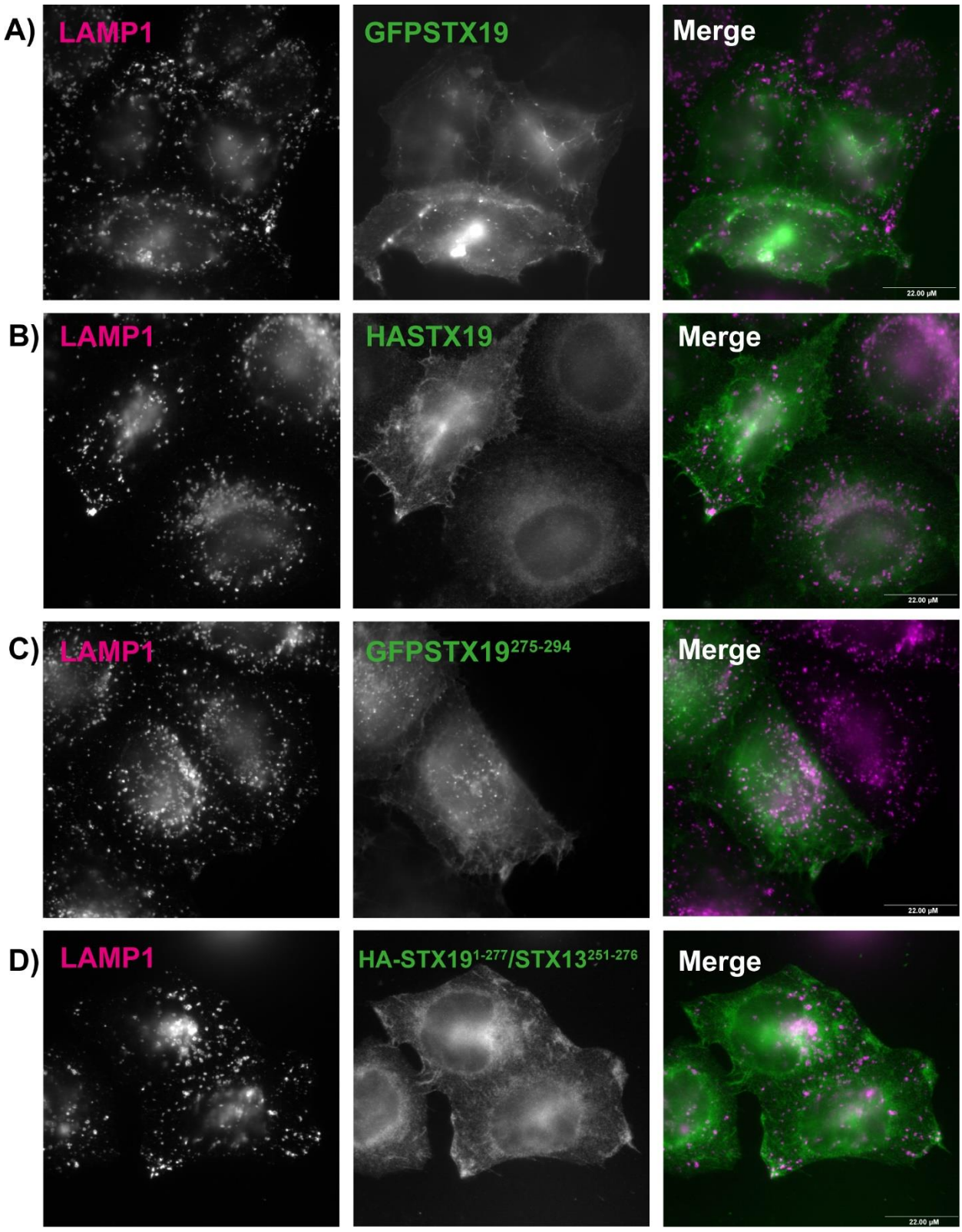
A)
LAMP1
GFPSTX19
Merge
22.00 µM
B)
LAMP1
HASTX19
Merge
22.00 µM
C)
LAMP1
GFPSTX19275-294
Merge
22.00 µM
D)
LAMP1
HA-STX191-277/STX13251-276
Merge
22.00 µM

Figure 4-16: LAMP1 may change distribution upon overexpression of STX19 constructs. HeLaM cells were transfected with either GFP-STX19, HA-SXT19, GFP-STX-$19^{275-294}$, HA-$STX19^{1-277}$/$STX13^{251-276}$, fixed using 4 % PFA and stained using anti-LAMP1 antibodies. **A)** GFP-STX19 localises to the plasma membrane, tubular recycling endosomes, and puncta in the cytoplasm. In transfected cells, LAMP1 localises to puncta that are distributed towards the cell periphery. **B)** HA-STX19 localises to the plasma membrane and tubular recycling endosomes. In untransfected cells, LAMP1 localises to puncta largely concentrated in the perinuclear region. In transfected cells, LAMP1 localises to puncta that appear to be distributed towards the cell periphery. **C)** GFP-$STX19^{275-294}$ localises to the plasma membrane, tubular recycling endosomes, and puncta in the cytoplasm. In transfected cells, LAMP1 localises to puncta in the cytoplasm which are largely concentrated in the perinuclear region. LAMP1 distrubition appears similar in transfected and untransfected cells. **D)** HA-$STX19^{1-277}$/$STX13^{251-276}$ localises to the plasma membrane and shows vesicular staining throughout the cytoplasm which is enriched in the perinuclear area. In transfected cells, LAMP1 localises to puncta that appear to be distributed towards the cell periphery though there are a number of puncta in the perinuclear region. Scale bar: 22.00 µM.

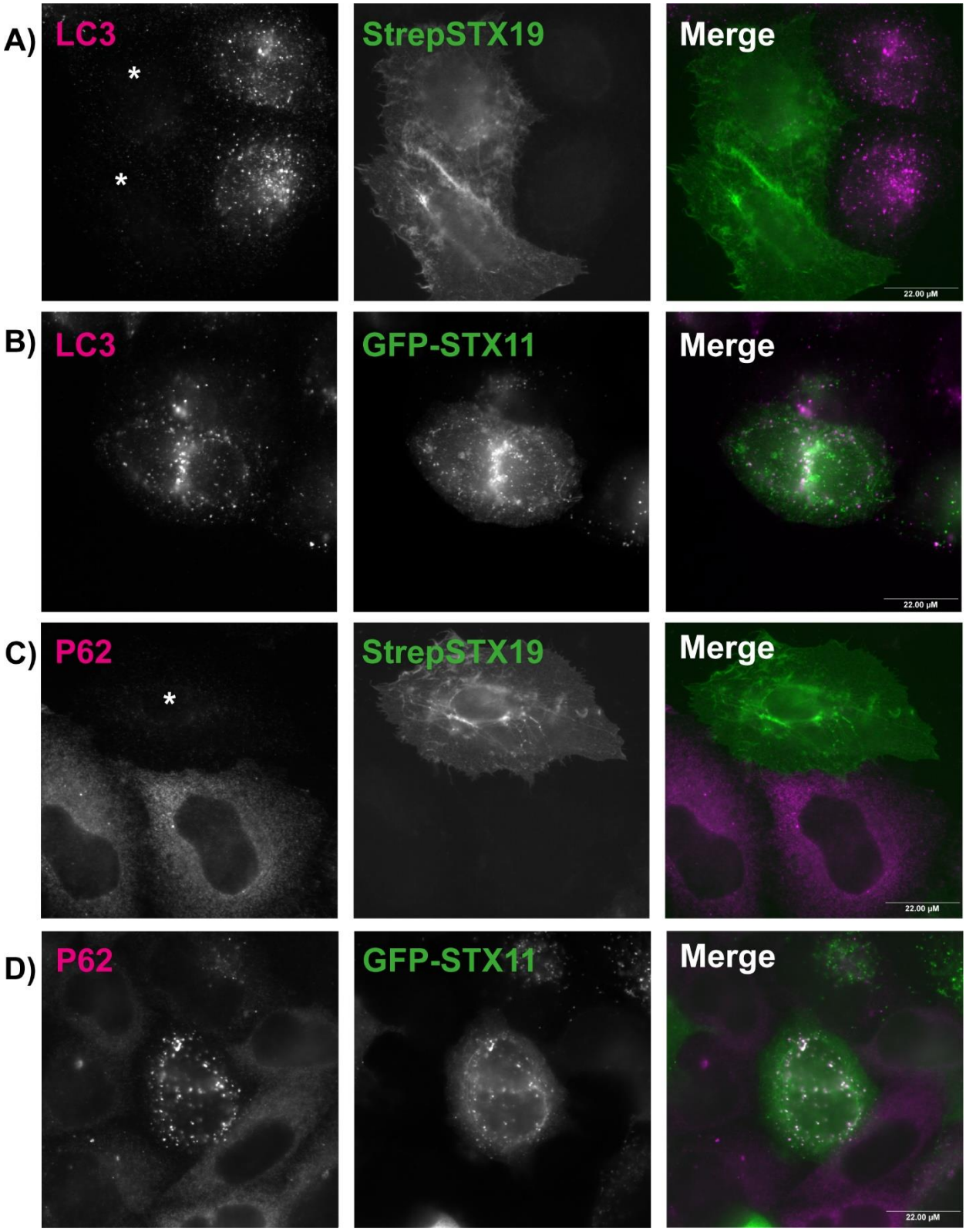
A)
LC3
StrepSTX19
Merge
22.00 µM
B)
LC3
GFP-STX11
Merge
22.00 µM
C)
P62
StrepSTX19
Merge
22.00 µM
D)
P62
GFP-STX11
Merge
22.00 µM

Figure 4-17: StrepSTX19 overexpression reduces endogenous LC3 and P62 levels.
HeLaM cells were transfected with either StrepSTX19 and GFP-STX11 and serum starved overnight to induce autophagy. Cells were then fixed using 4 % PFA and stained for autophagosomal makers using anti-LC3 and anti-P62 antibodies. White astrix denotes StrepSTX19 transfected cells in LC3 and P62 images. **A)** StrepSTX19 localises to the plasma membrane, tubular recycling endosomes, and puncta distributed in the cytoplasm. In untransfected cells, LC3 localises to puncta throughout the cell. In StrepSTX19 transfected cells, no LC3 puncta are visible. **B)** GFP-STX11 localises to the cytoplasm and puncta in the cytoplasm. In transfected cells, LC3 localises to puncta throughout the cell. There is some overlap between GFP-STX11 and LC3 in puncta within the cytoplasm. **C)** StrepSTX19 localises to the plasma membrane, tubular recycling endosomes, and puncta distributed throughout the cell. In untransfected cells, P62 shows a cytoplasmic localisation. In StrepSTX19 transfected cells, there is very little P62 staining. **D)** GFP-STX11 localises to the cytoplasm and puncta in the cytoplasm. In transfected cells, P62 localises to puncta throughout the cell. There is some co-localisation between GFP-STX11 and P62 in puncta within the cytoplasm. In untransfected cells, P62 localises to the cytoplasm. Scale bar: 22.00 μM.

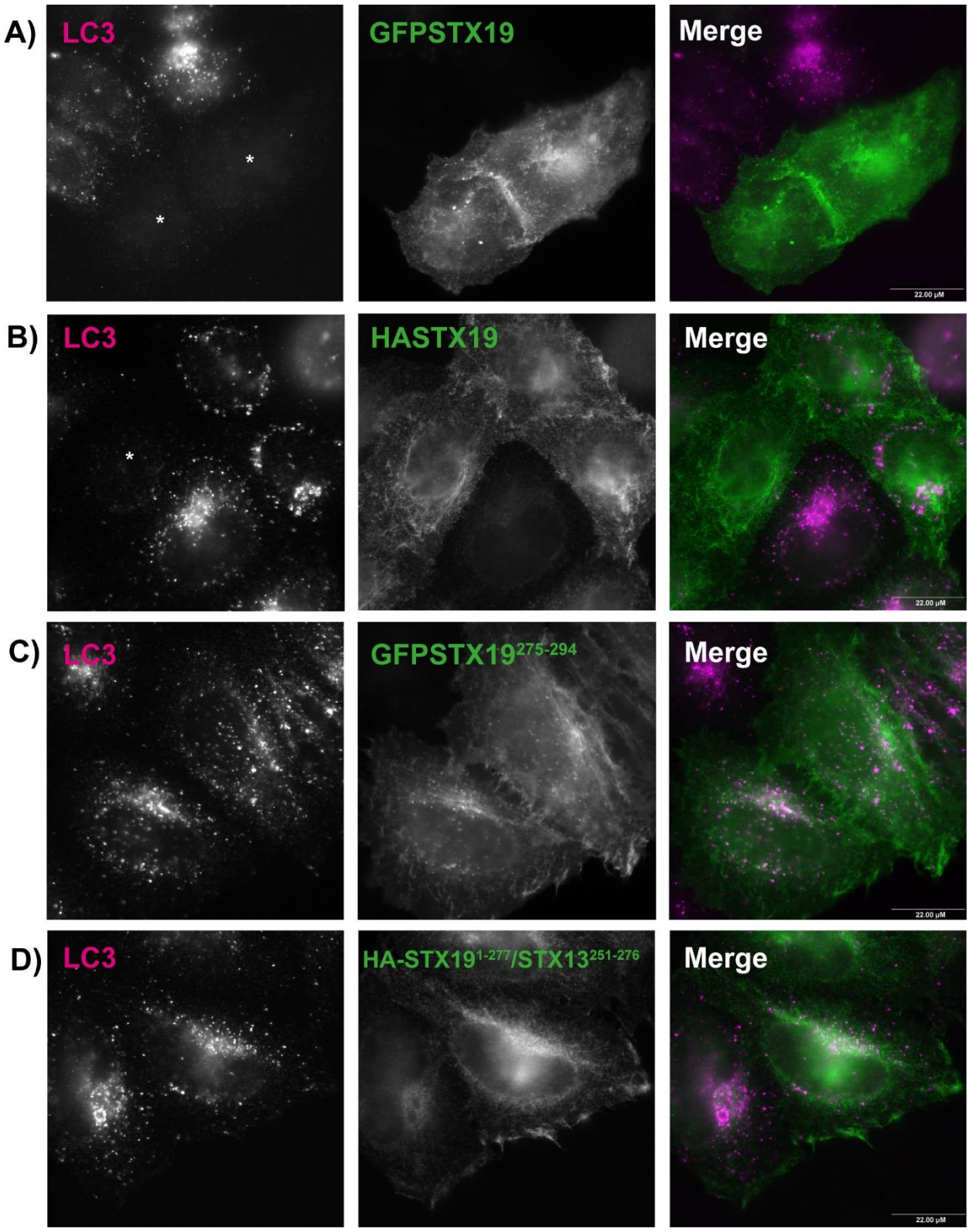
A)
LC3
GFPSTX19
Merge
22.00 µM
B)
LC3
HASTX19
Merge
22.00 µM
C)
LC3
GFPSTX19275-294
Merge
22.00 µM
D)
LC3
HA-STX191-277/STX13251-276
Merge
22.00 µM

Figure 4-18: GFP-STX19 expression reduces levels of endogenous LC3. HeLaM cells were transfected with either GFP-STX19, HA-SXT19, GFP-STX19$^{275-294}$, HA-STX-19$^{1-277}$/STX13$^{251-276}$. Cells were serum starved overnight to induce autopahgy and then fixed using 4 % PFA and stained using anti-LC3 antibodies. **A)** GFP-STX19 localises to the plasma membrane, tubular recycling endosomes and puncta throughout the cytoplasm. In untransfected cells, LC3 localises to puncta distributed throughout the cytoplasm. In transfected cells, there is very little LC3 staining in the cytoplasm. White asterixs denote GFP-STX19 transfected cells in the LC3 image. **B)** HA-STX19 localises to the plasma membrane and tubular recycling endosomes. In untransfected cells, LC3 localises to puncta distributed througout the cell. Some HA-STX19 transfected cells, LC3 shows bright punctate staining though there appear to be fewer puncta than untransfected cells. In others, very little LC3 staining can be seen. **C)** GFP-STX19$^{275-294}$ localises to the plasma membrane, tubular recycling endosomes, and puncta in the cytoplasm. In transfected cells, LC3 localisation to puncta distributed throughout the cell. **D)** HA-STX19$^{1-277}$/STX13$^{251-276}$ localises to the plasma membrane and shows a vesicular staining in the cytoplasm which is enriched in the perinuclear area. In transfected cells, LC3 localises to puncta distributed throughout the cytoplasm. Scale bar: 22.00 μM.

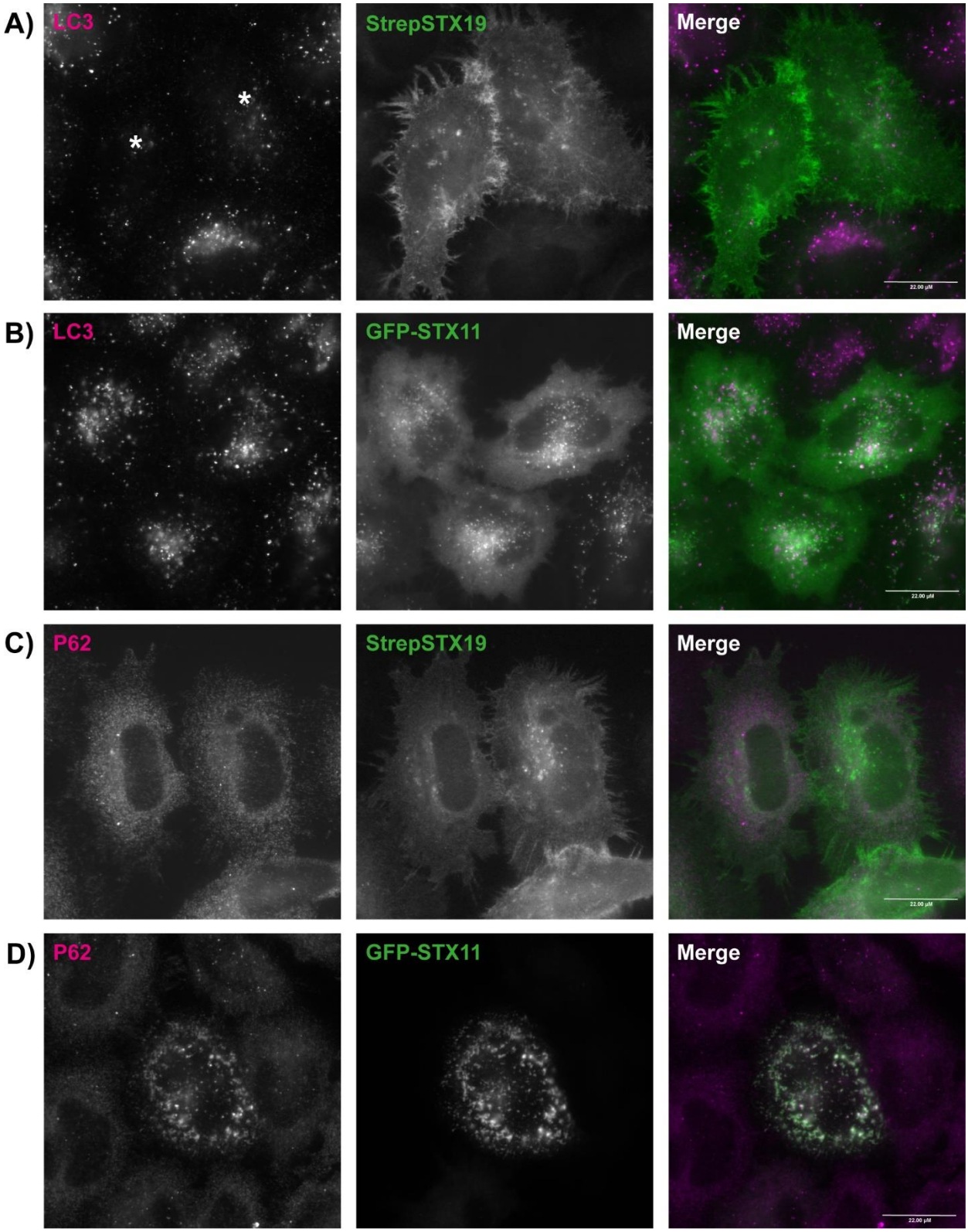
A)
LC3
StrepSTX19
Merge
B)
LC3
GFP-STX11
Merge
C)
P62
StrepSTX19
Merge
D)
P62
GFP-STX11
Merge

Figure 4-19: StrepSTX19 overexpression reduces endogenous levels of LC3, but not P62, after 12 hours transfection. HeLaM cells were transfected with either StrepSTX19 and GFP-STX11. After 6 hours, cells were serum starved to induce autophagy. After an additional 6 hours, cells were fixed using 4 % PFA and stained for autophagosomal makers using anti-LC3 and anti-P62 antibodies. White astrix denotes StrepSTX19 transfected cells in LC3 images. **A)** StrepSTX19 localises to the plasma membrane, tubular recycling endosomes, and puncta distributed throughout the cell. In untransfected cells, LC3 localises to puncta throughout the cell. In transfected cells, there is very little LC3 staining. **B)** GFP-STX11 localises to the cytoplasm and puncta in the cytoplasm. In transfected cells, LC3 localises to puncta throughout the cell. **C)** StrepSTX19 localises to the plasma membrane, tubular recycling endosomes, and puncta distributed throughout the cell. In transfected cells, P62 shows a cytoplasmic localisation and puncta in the cytoplasm. **D)** GFP-STX11 localises to the cytoplasm and puncta in the cytoplasm. In transfected cells, P62 localises to puncta throughout the cell. P62 and GFP-STX11 co-localise in the same puncta. In untransfected cells, P62 localises to the cytoplasm. Scale bar: 22.00 μM.

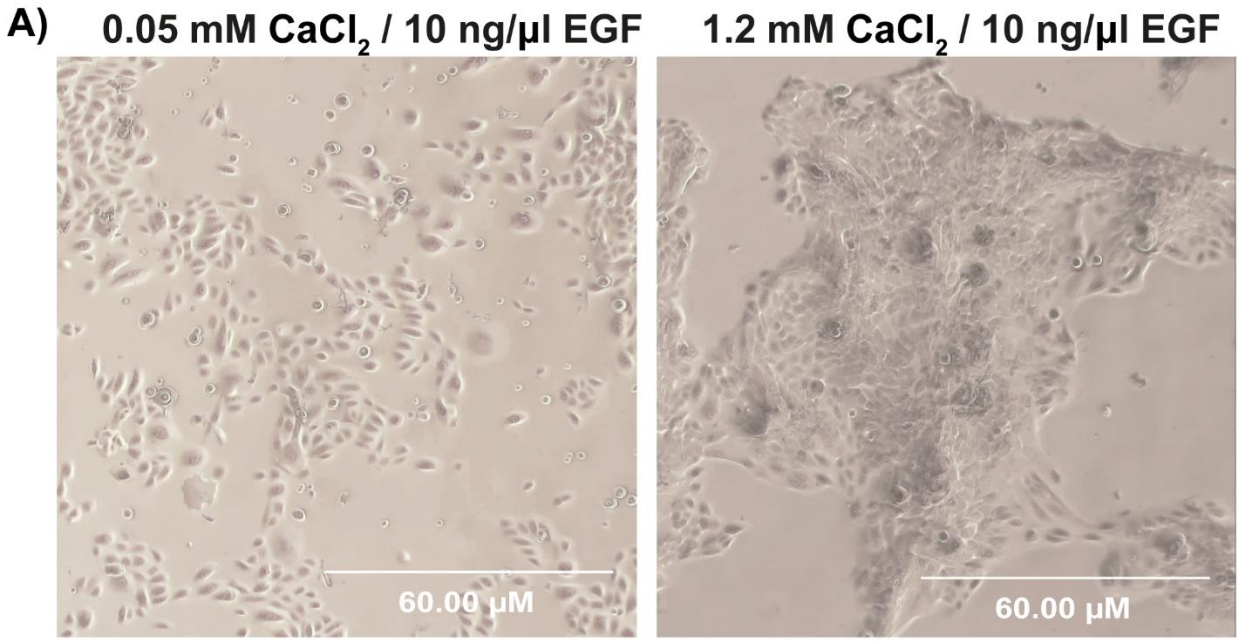

Figure 4-20: Keratinocyte morphology before and after differentation.
Human epidermal keratinocytes were cultured at <50 % confluency in 0.05 mM $CaCl_2$ and 10 ng/µL EGF to maintain an undifferentiated state. To induce differentation, keratinocytes were grown to 80 % confluency and treated with 1.2 mM $CaCl_2$ and 10 ng/µL EGF. **A)** Keratinocytes cultured in 0.05 mM $CaCl_2$ have a smaller, relatively flat morphology and are generally well distributed. Keratinocytes cultured in 1.2 mM $CaCl_2$ are clustered together, demonstrating a more epithelial-like morphology. Cells towards the periphery of the cluster are larger than cells in the centre. Scale bar: 60.00 µM.

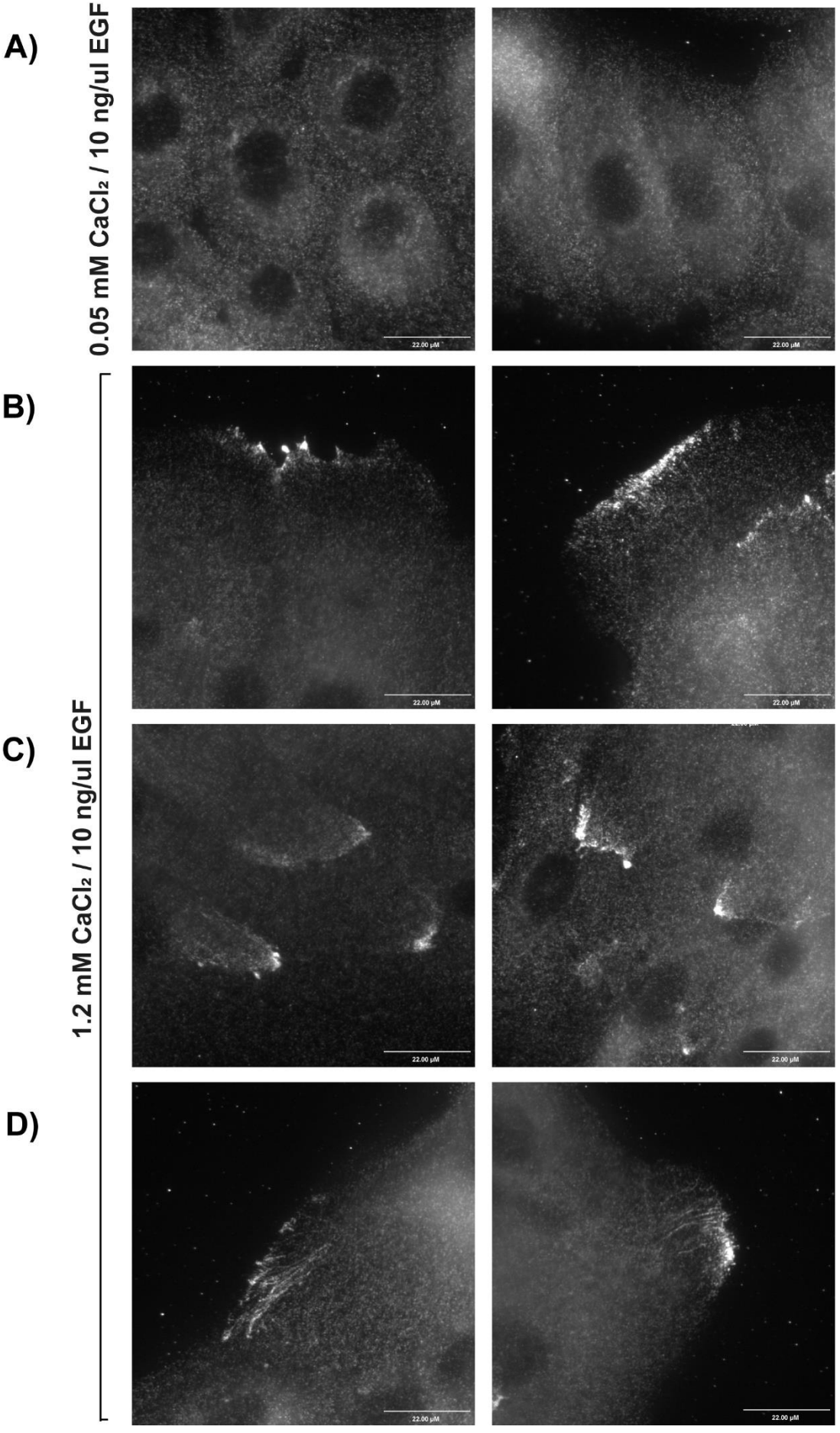
A)
B)
C)
D)
0.05 mM CaCl₂ / 10 ng/ul EGF
1.2 mM CaCl₂ / 10 ng/ul EGF
22.00 µM

Figure 4-21: STX19 localisation in Human Epidermal Keratinocytes. Human Epiderminal Keratinocytes were cultured in either 0.05 mM $CaCl_2$ to maintain undifferentiated state or 1.2 mM $CaCl_2$ and 10 ng/µL EGF to induce differentiation. Cells were then fixed using 4 % PFA and stained using an anti-STX19 antibody. **A)** Keratinocytes cultured in 0.05 mM $CaCl_2$ do not show any specific staining for STX19, cells have a non-distinct background staining pattern. **B-D)** Keratinocytes cultured in 1.2 mM $CaCl_2$ and 10 ng/µL EGF demonstrate staining for STX19 at the distinct domains of the plasma membrane. The plasma membrane domains STX19 localises to either face the extracellular environment (**B** and **D**) or are at the edges of keratinocytes growing over each other in a 'fish scale' pattern (**C**). STX19 also localises to tubular structures emanating from the plasma membrane domain (**D**) though the tubular structures are not apparent in every cell. Scale bar: 22.00 µM.

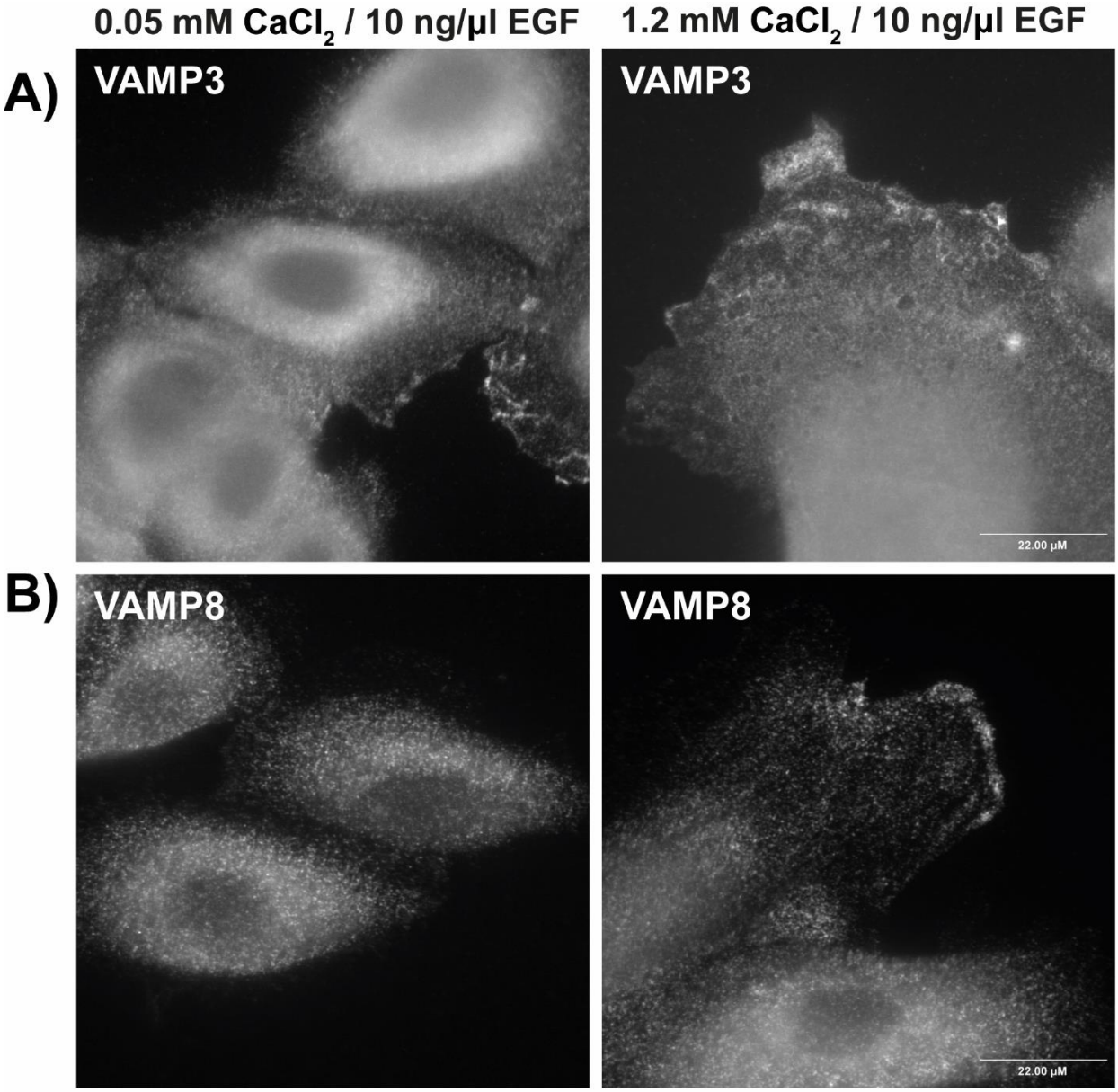

Figure 4-22: VAMP3 and VAMP8 are enriched in distinct regions of the plasma membrane in keratinocytes. Human epidermal keratinocytes were cultured at <50 % confluency in 0.05 mM $CaCl_2$ and 10 ng/µL EGF to maintain an undifferentiated state. To induce differentation, keratinocytes were grown to 80 % confluency and treated with 1.2 mM $CaCl_2$ and 10 ng/µL EGF. Keratinocytes were then fixed using 4 % PFA and stained using anti-VAMP3 and anti-VAMP8 antibodies. **A)** Keratinocytes cultured in 0.05 mM $CaCl_2$ show VAMP3 staining at the plasma membrane and the cytoplasm. Keratinocytes cultured in 1.2 mM $CaCl_2$ shows VAMP3 staining at the plasma membrane and in the cytoplasm as well as vesicular structures in the cytoplasm. **B)** Keratinocytes cultured in 0.05 mM $CaCl_2$ show VAMP8 staining in the cytoplasm. Keratinocytes cultured in 1.2 mM $CaCl_2$ shows VAMP8 staining at distinct regions of the plasma membrane facing the extracellular environment and cytoplasmic staining. Scale bar: 22.00 µM.

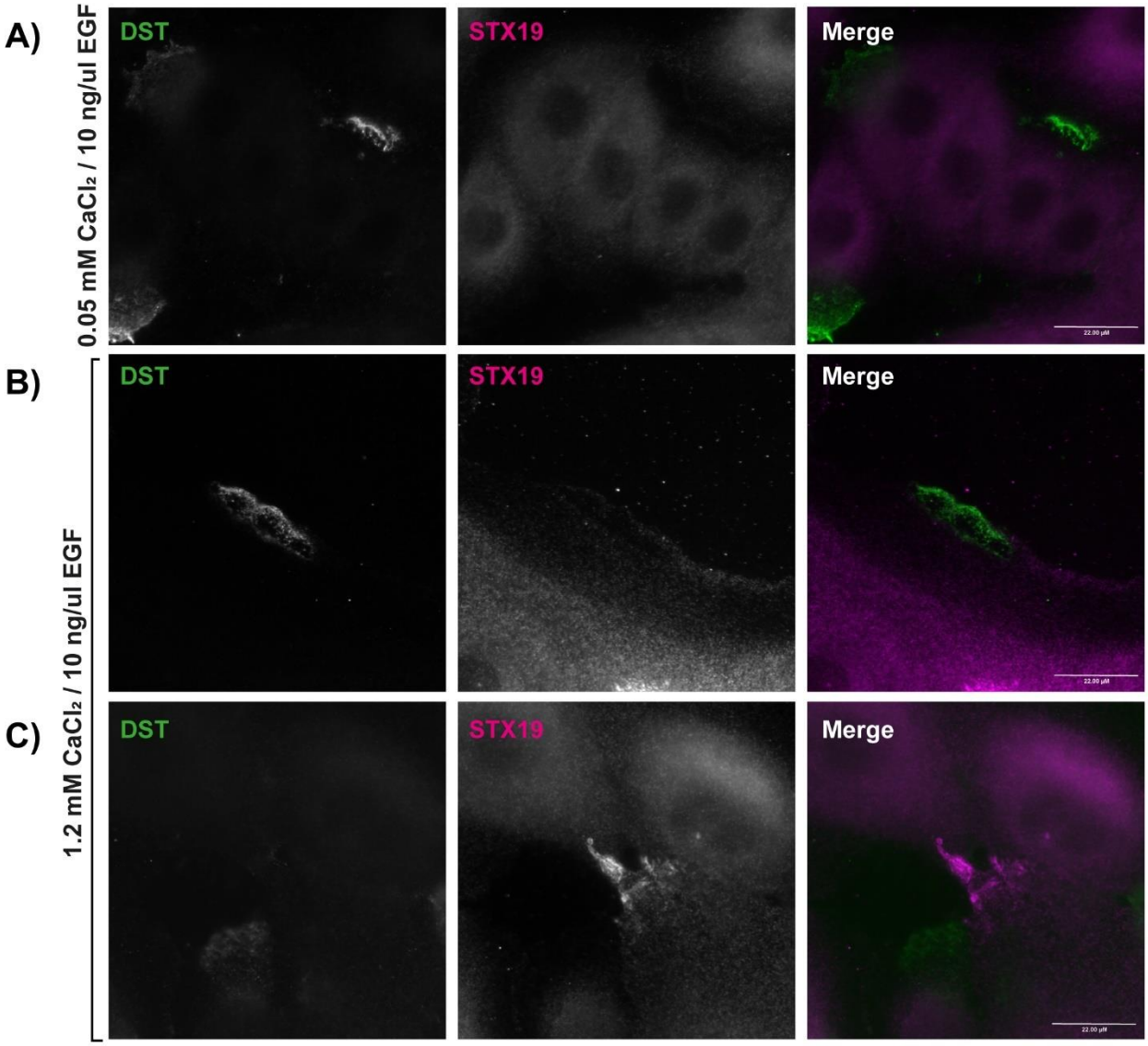

Figure 4-23: STX19 does not co-localise with DST in keratinocytes. Human Epidermal Keratinocytes were cultured in either 0.05 mM $CaCl_2$ and and 10 ng/µL EGF to maintain undifferentiated state or 1.2 mM $CaCl_2$ and 10 ng/µL EGF to induce differentiation. Cells were then fixed using 4 % PFA and stained using anti-DST and anti-STX19 antibodies. **A)** Cells cultured in 0.05 mM $CaCl_2$ demonstrate localisation of DST to specific structures consisting of a short section of plasma membrane staining with puncta directly below likely to be hemidesmosomes. STX19 does not have specific staining in undifferentiated cells. **B)** After differentiation with 1.2 mM $CaCl_2$, DST remains localised to the specific structures but there is no staining for STX19 in this structure. **C)** Also shows keratinocytes differentiated with 1.2 mM $CaCl_2$. STX19 localises to distinct membrane domains in the protrusions of the cells but there is no staining for DST in membrane protrusions. Scale bar: 22.00 µM.

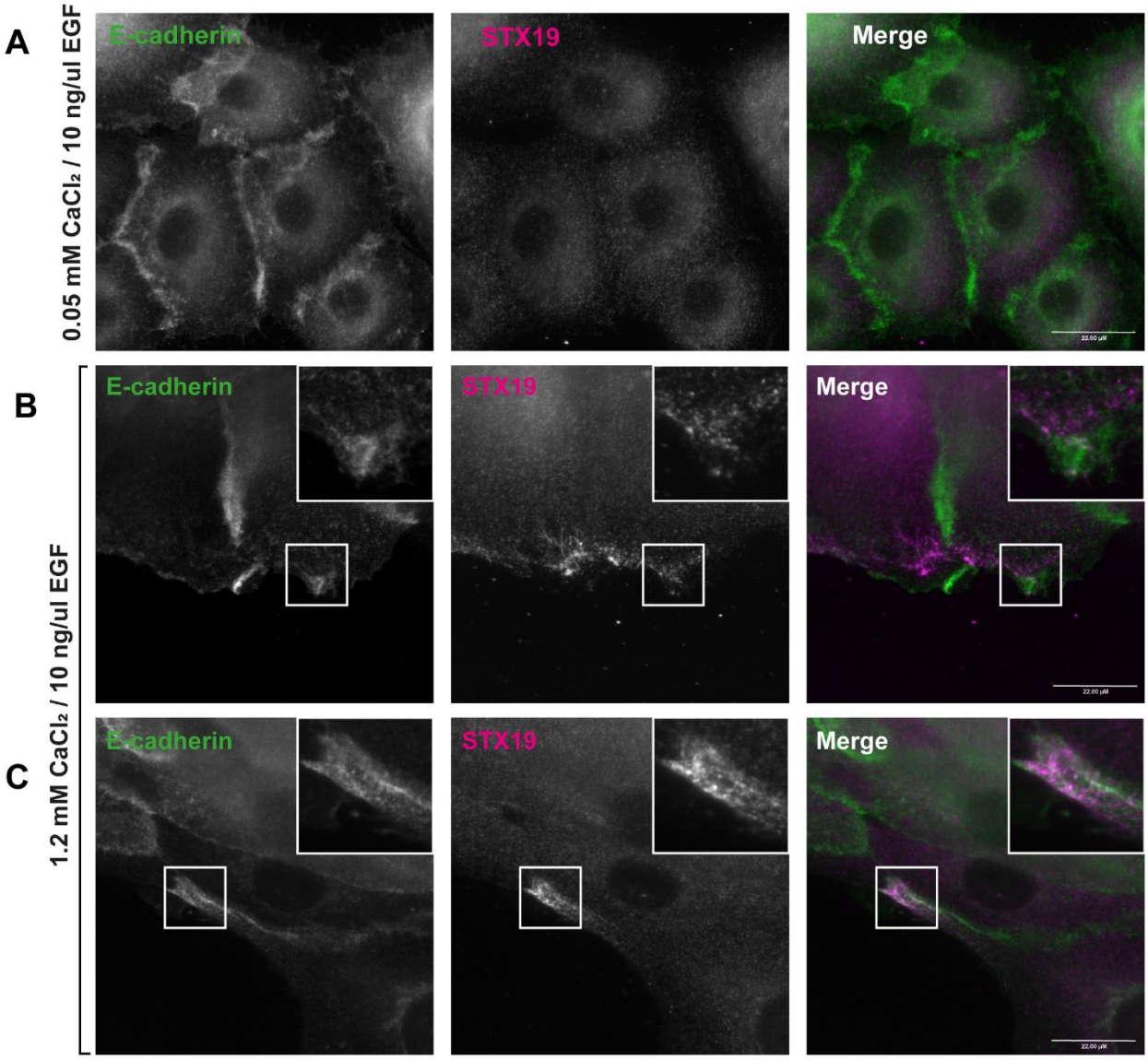

Figure 4-24: STX19 is not localised to adherens junctions with E-cadherin. Human Epiderminal Keratinocytes were cultured in either 0.05 mM $CaCl_2$ and and 10 ng/µL EGF to maintain undifferentiated state or 1.2 mM $CaCl_2$ and 10 ng/µL EGF to induce differentiation. Cells were then fixed using 4 % PFA and stained using anti-E-cadherin and anti-STX19 antibodies. E-cadherin is a marker of adherens junctions. **A)** Cells cultured in 0.05 mM $CaCl_2$ demonstrate localisation of E-cadherin to the plasma membrane at borders between cells indicating adherens junctions, as well as a pool of staining in the cytoplasm. STX19 does not have specific staining in undifferentiated cells. **B)** After differentiation with 1.2 mM $CaCl_2$, E-cadherin remains localised to adherens junctions and localises at regions of the plasma membrane that faces the extracellular space. STX19 localises to domains of the plasma membrane that faces the extracellular space but this staining does not overlap with that of E-cadherin. **C)** Also shows keratinocytes differentiated with 1.2 mM $CaCl_2$. E-cadherin is enriched in the periphery of a protrusion of a cell. STX19 also enriched in this protrusion but does not co-localise with E-cadherin. Scale bar: 22.00 µM.

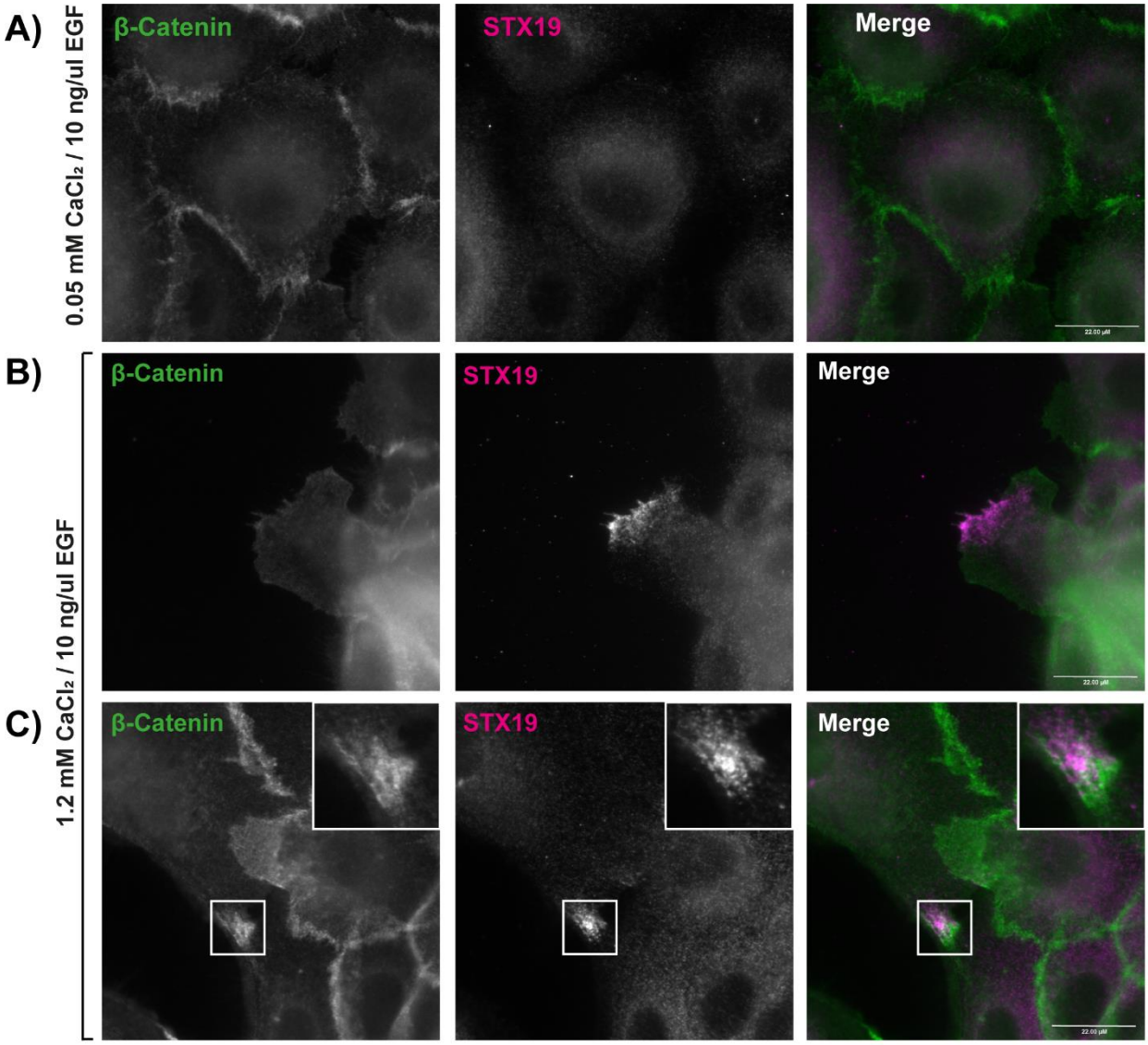

Figure 4-25: STX19 is not localised to adherens junctions with β-catenin. Human Epiderminal Keratinocytes were cultured in either 0.05 mM $CaCl_2$ and and 10 ng/µL EGF to maintain undifferentiated state or 1.2 mM $CaCl_2$ and 10 ng/µL EGF to induce differentiation. Cells were then fixed using 4 % PFA and stained using anti-β-catenin and anti-STX19 antibodies. β-catenin is a marker of adherens junctions in epithelial tissues. **A)** Cells cultured in 0.05 mM $CaCl_2$ demonstrate localisation of β-catenin to the plasma membrane borders between cells. STX19 does not have specific staining in undifferentiated cells. **B)** After differentiation with 1.2 mM $CaCl_2$, STX19 localises to a distinct subdomain of the plasma membrane that faces the extracellular space. This does not co-localise with β-catenin which has very low expression at this area of the plasma membrane. **C)** Also shows keratinocytes differentiated with 1.2 mM $CaCl_2$. β-catenin shows a strong staining pattern at the borders between cells indicating adherens junctions including staining at a protruding tip of a cell. STX19 is also enriched in this protrusion but behind β-catenin staining. Scale bar: 22.00 µM.

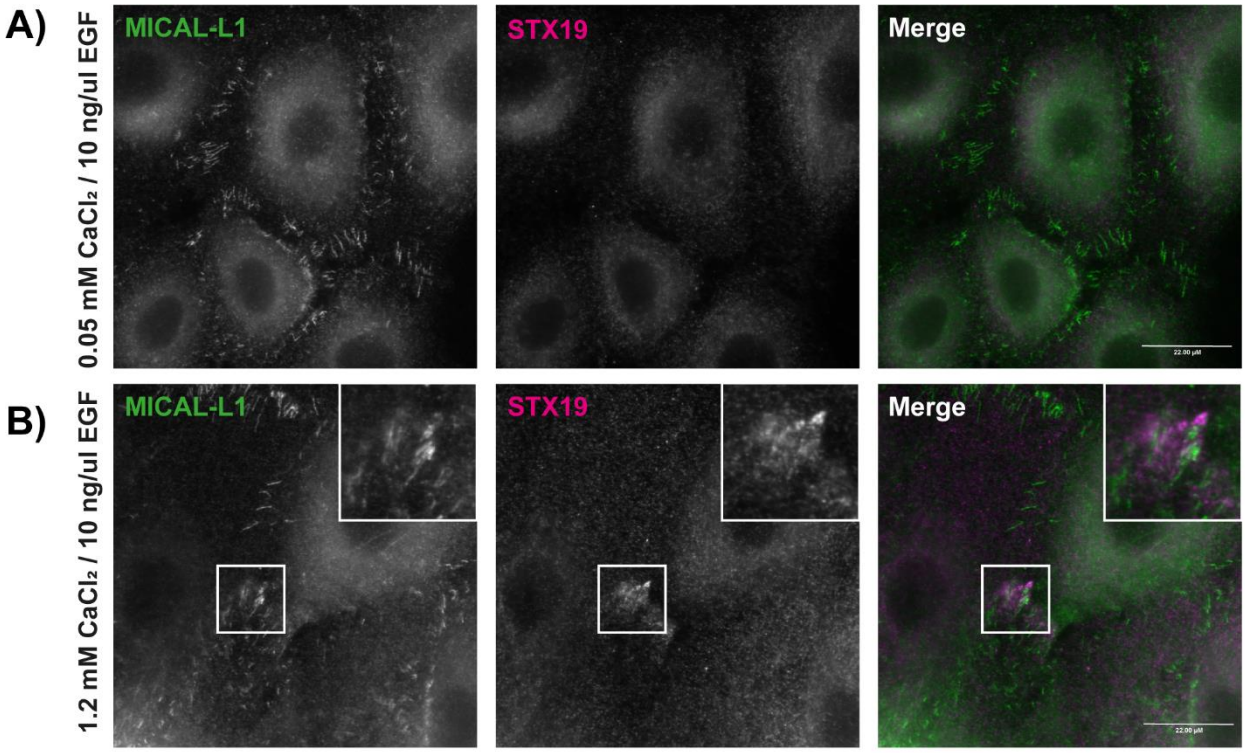

Figure 4-26: STX19 does not co-localise with MICAL-L1. Human Epiderminal Keratinocytes were cultured in either 0.05 mM $CaCl_2$ and and 10 ng/µL EGF to maintain undifferentiated state or 1.2 mM $CaCl_2$ and 10 ng/µL EGF to induce differentiation. Cells were then fixed using 4 % PFA and stained using anti-MICAL-L1 and anti-STX19 antibodies. MICAL-L1 is a marker of tubular recycling endosomes. **A)** Cells cultured in 0.05 mM $CaCl_2$ demonstrate localisation of MICAL-L1 short tubular structures. STX19 does not have specific staining in undifferentiated cells. **B)** After differentiation with 1.2 mM $CaCl_2$, STX19 localises to a distinct subdomain of the membrane in a membrane protrusion. This does not co-localise with MICAL-L1 which localises to short tubular structures throughout the cell. MICAL-L1 staining can be seen in the protruding structure adjacent to STX19 staining. Scale bar: 22.00 µM.

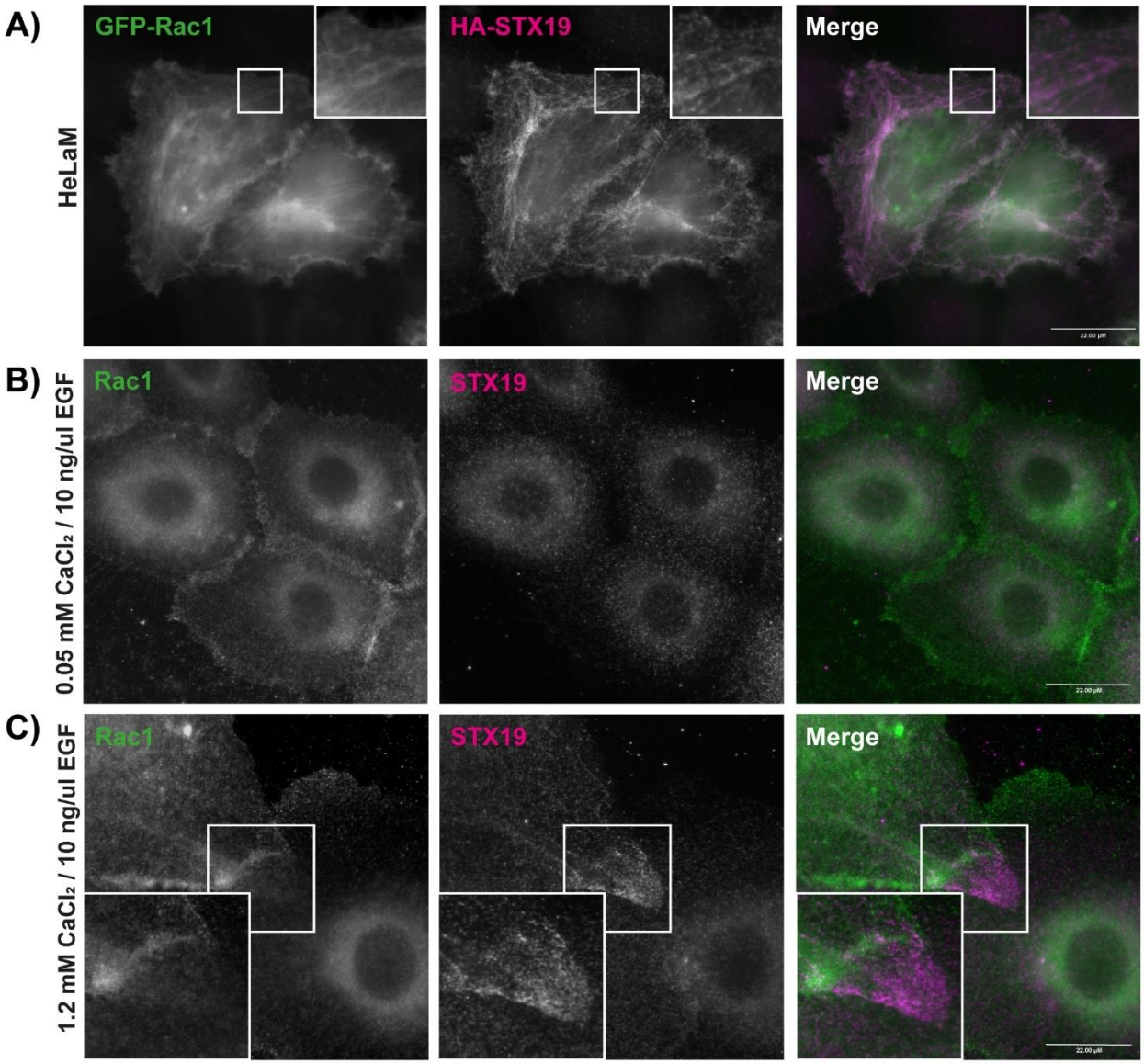

Figure 4-27: STX19 co-localises with Rac1 in HeLaM cells but not keratinocytes
A) HeLaM cells were transfected with GFP-Rac1 and HA-STX19 and fixed using 4 % PFA and stained using anti-HA antibodies. GFP-Rac1 localises to the plasma membrane and tubular recycling endosomes. HA-STX19 localises to the plasma membrane and tubular recycling endosomes. **B-C)** Human Epiderminal Keratinocytes were cultured in either 0.05 mM $CaCl_2$ and and 10 ng/µL EGF to maintain undifferentiated state or 1.2 mM $CaCl_2$ and 10 ng/µL EGF to induce differentiation. Cells were then fixed using 4 % PFA and stained using anti-Rac1 and anti-STX19 antibodies. **B)** Cells cultured in 0.05 mM $CaCl_2$ demonstrate localisation of Rac1 to the plasma membrane and the cytoplasm. STX19 does not have specific staining in undifferentiated cells. **C)** After differentiation with 1.2 mM $CaCl_2$, STX19 is enriched at the tip of a membrane protrusion with faint tubular structues emanating from the enriched region. Rac1 is localised to the plasma membrane and the cytoplasm. There is an enrichment of Rac1 staining in close proximity to the pool of STX19 staining in the membrane protrusion. Scale bar: 22.00 µM.

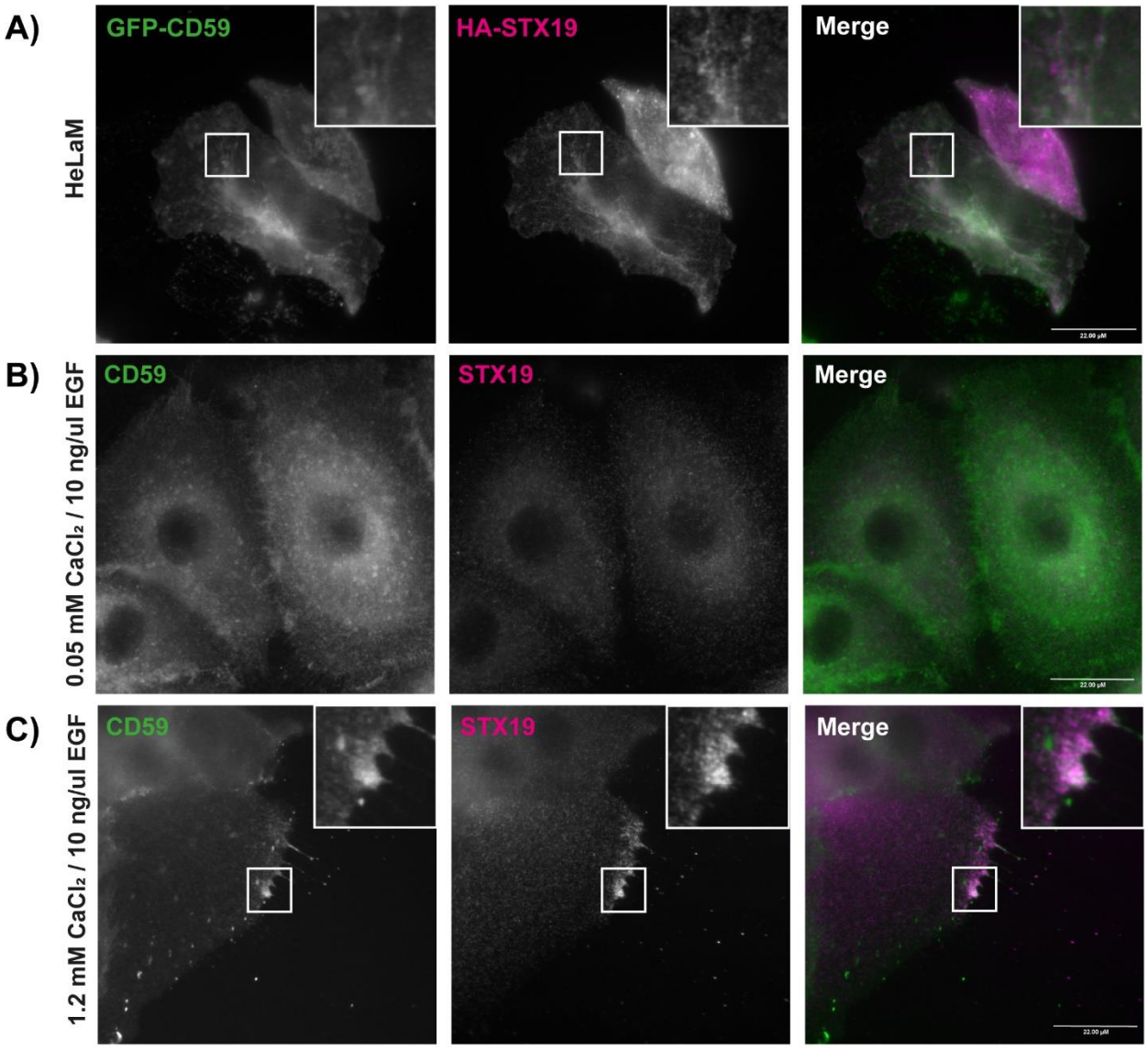

Figure 4-28: STX19 co-localises with CD59 in HeLaM cells and differentiated keratinocytes. A) HeLaM cells were transfected with HA-STX19 and GFP-CD59 and fixed using 4 % PFA and stained using anti-HA antibodies. GFP-CD59 localises to the plasma membrane, tubular recycling endosomes and faint punctate structures in the cytoplasm. HA-STX19 localises to the plasma membrane and tubular recycling endosomes. HA-STX19 co-localises with CD59 at tubular recycling endosomes and the plasma membrane. **B-C)** Human Epiderminal Keratinocytes were cultured in either 0.05 mM $CaCl_2$ and and 10 ng/µL EGF to maintain undifferentiated state or 1.2 mM $CaCl_2$ and 10 ng/µL EGF to induce differentiation. Cells were then fixed using 4 % PFA and stained using anti-CD59 and anti-STX19 antibodies. **B)** Cells cultured in 0.05 mM $CaCl_2$ demonstrate localisation of CD59 to the plasma membrane, the cytoplasm and punctate structures in the cytoplasm. STX19 does not have specific staining in undifferentiated cells. **C)** After differentiation with 1.2 mM $CaCl_2$, STX19 is enriched in a distinct region of the plasma membrane facing the extracellular environement. CD59 is also enriched in the same distinct region of the plasma membrane. Scale bar: 22.00 µM.

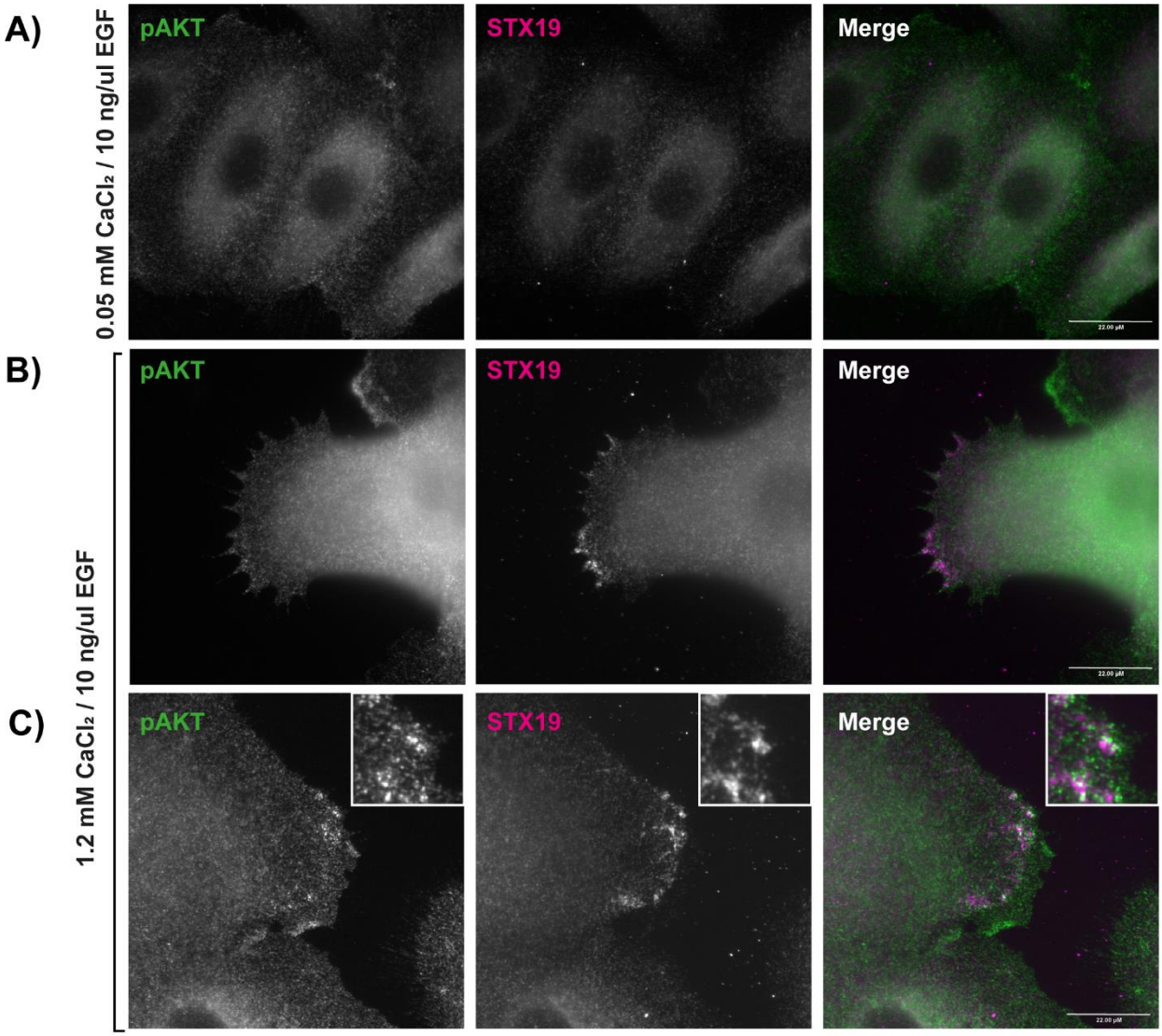

Figure 4-29: STX19 co-localises with pAKT in differentiated keratinocytes. Human Epiderminal Keratinocytes were cultured in either 0.05 mM $CaCl_2$ and and 10 ng/µL EGF to maintain undifferentiated state or 1.2 mM $CaCl_2$ and 10 ng/µL EGF to induce differentiation. Cells were then fixed using 4 % PFA and stained using anti-pAKT and anti-STX19 antibodies. **A)** Cells cultured in 0.05 mM $CaCl_2$ demonstrate faint cytoplasmic staining of pAKT. STX19 does not have specific staining in undifferentiated cells. **B)** After differentiation with 1.2 mM $CaCl_2$, STX19 is enriched in a distinct region of the plasma membrane facing the extracellular environement. pAKT shows cytoplasmic staining and is not enriched at the plasma membrane with STX19. **C)** After differentiation with 1.2 mM $CaCl_2$, STX19 is enriched in a distinct region of the plasma membrane facing the extracellular environment. pAKT shows cytoplasmic staining and puncta at the cell periphery. Scale bar: 22.00 µM.

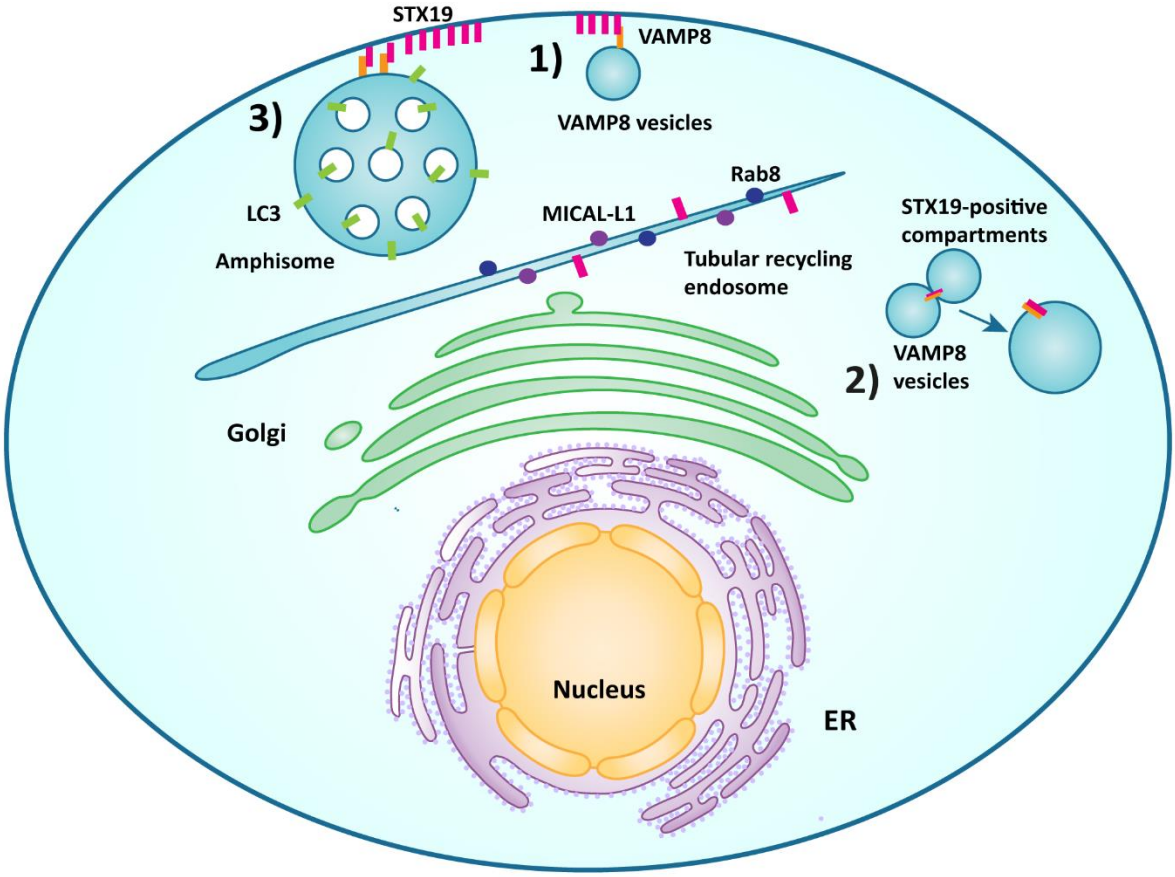

Figure 4-30: Schematic depicting a hypothesis that STX19 overexpression drives fusion of VAMP8-positive compartments internally and at the cell surface. Overexpression of STX19 alters the steady-state distribution of VAMP8 which we hypothesise may be due to a number of reasons. **1)** Overexpressed STX19 drives fusion of VAMP8-positive (orange rectangle) vesicles with the plasma membrane. **2)** Overexpresed STX19 drives the intracellular fusion of VAMP8-positive vesicles with STX19-positive compartments resulting in enlarged structures. **3)** Overexpressed STX19 drives the fusion of VAMP8-positive compartments such as amphisomes, with the plasma membrane. Amphisomal fusion with the plasma membrane subsequently results in the secretion of extracellular vesicles containing LC3 (green rectangle).

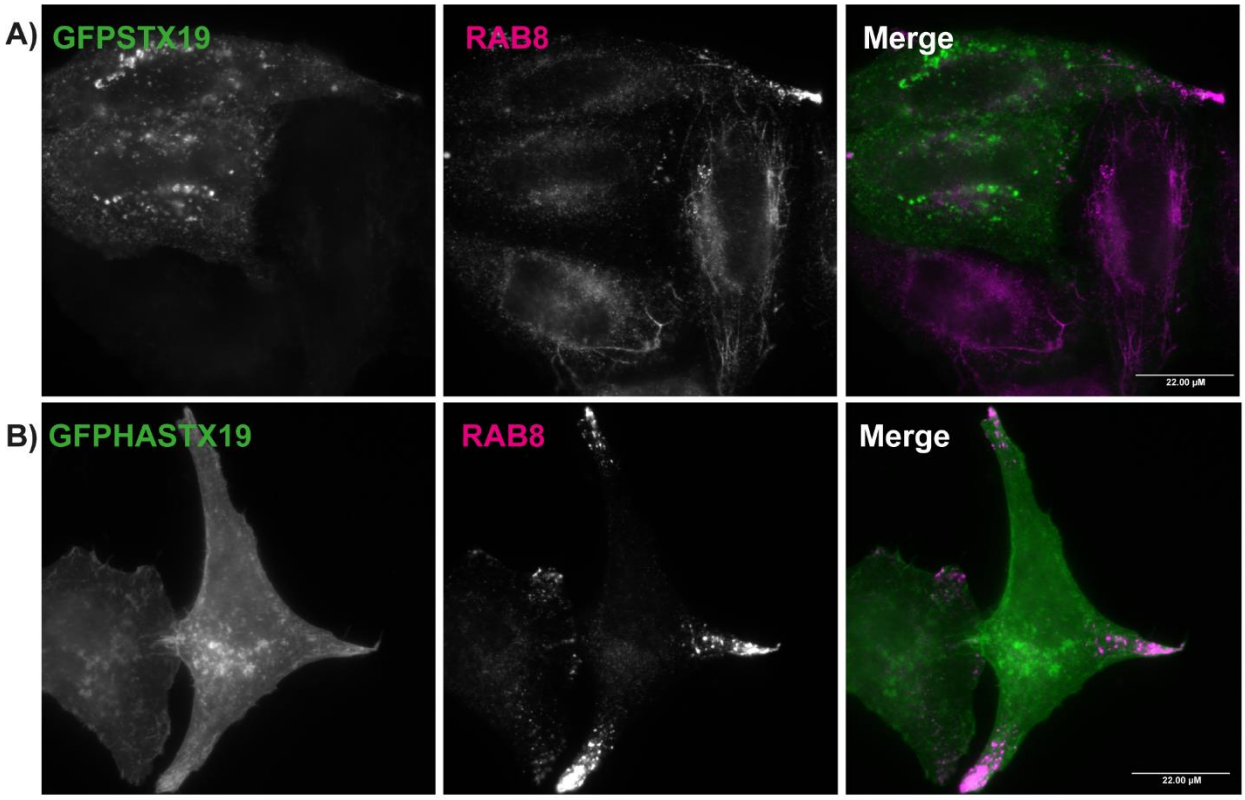

Supplementary Figure 4-1: Overexpression of STX19 traps Rab8 in cellular protrusions. HeLaM cells were transfected with either GFP-STX19 or GFP-HA-STX19. Cells were then fixed using 4 % PFA and stained using anti-Rab8 antibodies. **A)** GFP-STX19 localises to puncta throughout the cell. In untransfected cells, Rab8 localises to tubular recycling endosomes. In transfected cells, Rab8 is enriched in puncta at the tips of cellular protrusions. **B)** GFP-HA-STX19 localises to the plasma memrbane and puncta throughout the cell. Rab localises to puncta enriched in cellular protrusions. Scale bar: 22.00 µM.

Table 4-1: Description of STX19 constructs

STX19 construct	Description	Localisation
StrepSTX19	Strep-tagged full length STX19 wild type	Plasma membrane, tubular recycling endosomes, punctate and vesicular staining in the cytoplasm
StrepSTX19$^{\Delta 218\text{-}272}$	Strep-tagged STX19 with deletion of the SNARE domain, residues 218 – 272. Non-fusogenic SNARE but still able to bind Munc18-2	Plasma membrane, tubular recycling endosomes, punctate and vesicular staining in the cytoplasm
StrepSTX19$^{KDR\text{-}AAA}$	Strep-tagged STX19 with N-terminal mutation in the KDR motif, KDR-AAA, residues 2-4. Does not bind Munc18-2 but unclear if still functional	Plasma membrane, tubular recycling endosomes, punctate and vesicular staining in the cytoplasm
GFP-STX19	GFP-tagged full length STX19 wild type, proposed to act as a dominant active construct	Plasma membrane, tubular recycling endosomes, punctate and vesicular staining in the cytoplasm
HA-STX19	HA-tagged full length STX19 wild type	Plasma membrane, tubular recycling endosomes, punctate and vesicular staining in the cytoplasm
GFP-STX19$^{275\text{-}294}$	GFP-tagged STX19 C-terminal S-acylation domain, residues 275 – 294	Plasma membrane, tubular recycling endosomes, punctate and vesicular staining in the cytoplasm
HA-STX19$^{1\text{-}277}$ /STX13$^{251\text{-}276}$	HA-tagged STX19 truncated construct lacking the C-terminal S-acylation domain, residues 1 – 277, conjugated to the transmembrane domain of STX13, residues 251 – 276	Plasma membrane and vesicular staining in the cytoplasm enriched in the perinuclear region

Table 4-2: Distribution of different markers in cells transfected with various STX19 constructs.

	Marker			
STX19 construct	*VAMP8*	*CD63*	*LAMP1*	*LC3*
GFP-STX19	Loss of perinuclear vesicular staining, VAMP8 localises to enlarged endosomes distributed throughout the cell	CD63-positive puncta distributed throughout the cytoplasm with a pool concentrated in the perinuclear area, potential reduction of vesicular staining in the cytoplasm	LAMP1-positive puncta distributed throughout the cytoplasm and towards the periphery of the cell	Striking reduction in the number of LC3-positive puncta
HA-STX19	Loss of perinuclear vesicular staining, VAMP8 localises to enlarged endosomes distributed throughout the cell	Fewer CD63-postive puncta distributed towards the cell periphery, potential reductio of vesicular staining in the cytoplasm	LAMP1-positive puncta distributed throughout the cytoplasm and towards the periphery of the cell	Striking reduction in the number of LC3-positive puncta in some cells, other cells have LC3-positive puncta
GFP-STX19$^{275-294}$	Vesicular staining enriched in the perinuclear region	CD63-positive puncta distributed throughout the cytoplasm with a pool concentrated in the perinuclear area, vesicular staining in the cytoplasm	LAMP1-positive puncta distributed throughout the cytoplasm with a pool of puncta concentrated in the perinuclear region	LC3-positive puncta distributed throughout the cytoplasm
HA-STX19$^{1-277}$ /STX13$^{251-276}$	Vesicular staining enriched in the perinuclear region	CD63-positive puncta distributed throughout the cytoplasm with a pool concentrated in the perinuclear area, vesicular staining in the cytoplasm	LAMP1-positive puncta distributed throughout the cytoplasm and towards the periphery of the cell	LC3-positive puncta distributed throughout the cytoplasm

Chapter 5

Discussion and future studies

5.1 Introduction

STX19 is a poorly characterised post-Golgi Qa-SNARE. To date, the literature on STX19 describes its localisation in HeLaM cells, its membrane targeting (Ampah *et al.*, 2018), and possible roles for STX19 in secretion of soluble and membrane-anchored cargo (Gordon *et al.*, 2010; Simpson *et al.*, 2012). It remains unclear which pathways and processes STX19 functions in and how STX19 function is regulated. The aim of this study was to gain insight into the function and regulation of STX19. To do so, we have used mitochondrial re-routing assays to investigate potential STX19 interactors and used overexpression studies to analyse effects on STX19 SNARE binding partners and different compartmental markers. We have also established a physiologically relevant cell model in which STX19 function can be studied. Throughout this study we have gained insight into the interactions that may regulate STX19 function, STX19 overexpression phenotypes, and characterised STX19 localisation in a physiologically relevant cell model. A number of questions about STX19 function remain including if lipid-anchored STX19 is able to drive fusion, the molecular mechanisms that regulate it function, and the pathways which may require STX19-mediated fusion.

5.2 STX19 may drive vesicle fusion at the plasma membrane

STX19 is a post-Golgi SNARE that localises to tubular recycling endosomes (TREs) and the plasma membrane (Ampah *et al.*, 2018). Previous studies have demonstrated interaction of STX19 with SNARE binding partners, SNAPs 23, 25, and 29, and VAMPs 3 and 8, which are known to mediate fusion at the plasma membrane. Additionally, STX19 was identified to have a role in secretion and knockdown led to a decrease in the number of fusion events at the cell surface (Gordon *et al.*, 2010). Moreover, we have found that STX19 localises to distinct regions of the plasma membrane and membrane protrusions in physiologically relevant cell model – calcium-induced differentiated keratinocytes. Taken together, these data suggest that STX19 is acting as a Q-SNARE for the fusion of material with the plasma membrane.

5.2.1 Can STX19 drive fusion?

Whilst we predict STX19 to function at the plasma membrane, it remains unclear if STX19 is able to form fusion-competent SNARE complexes and drive membrane fusion. STX19 does not contain a transmembrane domain and is S-acylated at its C-terminus forming a lipid anchor that allows association with membranes (Ampah *et al.*, 2018). It is debated in the field as to whether lipid anchor SNAREs can drive fusion. Previous studies on yeast vacuole fusion have demonstrated that replacing the transmembrane domain (TMD) of either Q-SNARE Vam3p, or R-SNARE, Nyv1p with a prenyl lipid anchor abolished vacuolar fusion (Rohde *et al.*, 2003; Jun *et al.*, 2007). This suggests lipid anchored SNAREs are not able to drive fusion. This is supported by liposome assays with SNARE constructs generated from the soluble domains of STX1A and VAMP2 conjugated to a lipid anchor. Lipid-anchored STX1A and VAMP2

were able to form trans-SNARE complexes and dock vesicles but not drive hemifusion or complete fusion(J. A. McNew, Weber, *et al.*, 2000). Similarly, lipid-anchored VAMP2 constructs also failed to mediate Ca^{2+} dense core vesicle exocytosis, spontaneous synaptic vesicle exocytosis, and Ca^{2+}-synaptotagmin enhanced liposome fusion (Chang *et al.*, 2016b).

In contrast, there is emerging evidence that lipid-anchored SNAREs are able to drive fusion. Xu et al, also studied yeast vacuole SNAREs and found that whilst lipid-anchored constructs of R-SNARE Nyv1p alone was not able to drive fusion, addition of fusion accessory proteins (HOPS, Sec17p, and Sec18p) allowed complete fusion (Xu *et al.*, 2011). This suggests that lipid-anchored SNAREs are able to mediate fusion and previous *in vitro* studies did not account for additional proteins required for membrane fusion. Similarly, Zhou et al., have shown that lipid-anchors support membrane fusion by replacing the STX1 TMD with the S-acylation domain of STX19. Lipid-anchored STX1 was able to mediate synaptic vesicle fusion (Zhou, Bacaj T, *et al.*, 2013). Therefore, the lipid-anchor of STX19 does not affect fusion. This suggests that STX19 may be able to drive membrane fusion. Future studies using STX19 and its SNARE binding partners in liposome assays should be carried out to determine if STX19 can drive fusion. It would also be interesting to study single vesicle fusion events using TIRF microscopy where STX19 and secretory cargo are labelled.

5.2.2 How does endocytosis and recycling regulate the cellular localisation of STX19?

The difference in the endogenous staining of STX19 in HeLaM cells and keratinocytes might represent where its trafficking. In HeLaM cells, endogenous STX19 localises to TREs whilst in keratinocytes, endogenous STX19 localises to the plasma membrane. Since STX19 is expressed at relatively high levels in the skin compared with other tissues and is upregulated during keratinocyte differentiation, we predict that STX19 is functionally active in differentiated keratinocytes. Therefore, it is possible STX19 is functioning at the plasma membrane and its localisation to TREs in HeLaM cells represents the compartments through which it is recycling. Very little is known about Q-SNARE recycling kinetics however, most post-Golgi R-SNAREs recycle over the plasma membrane (Gordon *et al.*, 2009). The balance between rates of endocytosis and recycling control how much of the protein is at the cell surface. Fast recycling and slow endocytosis rates will result in more STX19 at the plasma membrane and vice versa would result in more internalised STX19. It remains unclear if and how STX19 is being endocytosed. It would be interesting to address what endocytic machinery is involved in STX19 endocytosis and if both HeLaM and keratinocytes used the same mechanisms for STX19 endocytosis and recycling.

Overexpressed STX19 also localises to the plasma membrane in HeLaM cells. This may suggest that the antibody epitope is masked when STX19 is associated with membranes or in complex at the plasma membrane and would explain why endogenous STX19 in not seen at the plasma membrane in HeLaM

cells. However, we would predict this not to be the cases since the anti-STX19 antibody is able to bind STX19 at the plasma membrane in keratinocytes. It may be that overexpression saturates the machinery required for the endocytosis of STX19 and thus more STX19 sequestered is at the plasma membrane.

It would be interesting to follow STX19 trafficking using photoactivable GFP-tagged constructs and determine if STX19 is recycling through a Rab8/ARF6-dependent pathway on TREs in HeLaM cells. Since we observed that TREs in keratinocytes are shorter than TREs in HeLaM cells, it would also be interesting to determine if differentiated keratinocytes have a Rab8/ARF6 recycling pathways or is STX19 recycling relies on different machinery in this cell type.

There may be alternative reasons for a difference in endogenous localisation. HeLaM cells are likely to express lower levels of STX19 than differentiated keratinocytes. Lower levels of STX19 at the plasma membrane may not be visible due its large surface area. However, the smaller surface area of TREs may concentrate STX19 such that it is visible. Additionally, there may be specific protein interactions in keratinocytes that target STX19 to the plasma membrane that do not occur in HeLaM cells.

5.2.3 Does STX19 regulate trafficking through TREs or delivery to the cell surface?

STX19 may localise to TREs to play a role in receptor recycling. Both Rab8 and MICAL-L1 have been implicated in recycling of β1-integrins, transferrin receptors, and GPI-anchored cargo through TREs (Hattula *et al.*, 2006; Sharma *et al.*, 2009a; Rahajeng *et al.*, 2012). However, MICAL-L1 and Rab8 have also been shown to regulate exocytosis at the plasma membrane. MICAL-L1 was shown to be required for TNFα delivery to the cell surface (Sikora *et al.*, 2021) and has also been implicated in the trafficking of Src from TREs to the plasma membrane(Reinecke *et al.*, 2014). Rab8 has also been shown to have roles in regulating vesicle docking and fusion at the cell surface (Grigoriev *et al.*, 2011). It would be interesting to follow cargo trafficking through this pathway upon STX19 knockdown to elucidate if STX19 has roles in delivery to the cell surface or recycling. However, an endosomal defect may eventually lead to a block in secretion which makes dissecting which parts of the pathway STX19 functions in challenging.

5.3 Munc18-2 is likely to regulate the function of STX19

To gain insight into the regulation of STX19, we investigated STX19 interaction with Munc18 proteins. Through our interaction studies using knocksideways and mitochondrial targeting assays, we have found that STX19 interacts with Munc18-2 via an N-terminal KDR peptide. Additionally, overexpression studies suggested that STX19 recruits Munc18-2 to TREs and the plasma membrane via this peptide. SM proteins are well-known to regulate SNARE function and as such, it is highly likely that Munc18-2 regulates the function of STX19. However, the molecular mechanisms by which Munc18-2 regulates STX19 function remain unclear. Previous studies have shown that N-terminal binding of Munc18 proteins can facilitate

SNARE complex formation. This is widely reported for Munc18-1 interaction with STX1 (Dulubova *et al.*, 2007; Khvotchev *et al.*, 2007; Burkhardt *et al.*, 2008; Deák *et al.*, 2009) and has been demonstrated for Munc18-3 interaction with STX4 (Aran *et al.*, 2009) and Vps45 interaction with STX16 (Eisemann *et al.*, 2020). STX11 also binds Munc18-2 at an N-terminal KDR peptide and requires Munc18-2 binding for complete fusion (Spessott *et al.*, 2017b). Based on our findings and the literature, we hypothesise that Munc18-2 binds to the STX19 N-terminal peptide to facilitate SNARE complex formation. To expand on this, it would be useful to determine if STX19 can interact with the endogenous Munc18-2 protein. The availability of good antibodies for Munc18-2 are limited and as such, identifying interaction with the endogenous proteins using the mitochondria re-routing assay may be challenging. An alternative solution may be to use proximity-dependent ligation assays. It would also be interesting to conduct these experiments in keratinocytes to understand if they endogenous proteins interaction in a physiologically relevant cell model.

To further explore the molecular mechanisms of Munc18-2 regulation, it will be necessary to conduct future studies to understand how Munc18-2 binding affects the ability of STX19 to form SNARE complexes and drive fusion. This may be achieved by co-expressing Munc18-2 and STX19 wildtype or KDR mutants in liposome assays or by determining how the presence of Munc18-2 affects STX19 co-immunoprecipitation with its SNARE binding partners.

Additionally, Munc18 proteins are suggested to have dual binding modes on syntaxins and how SNARE function is regulated depends on where the Munc18 is bound. For example, it has been shown that Munc18-1 binds STX1 at its Habc domain whilst it is trafficking from the ER to the plasma membrane. Binding of Munc18-1 at the Habc domain holds STX1 in a closed confirmation and therefore prevents the formation of SNARE complexes at inappropriate membranes. When STX1 reaches the cell surface, Munc18-1 binds at the N-terminal peptide to facilitate SNARE complex formation (Khvotchev *et al.*, 2007; Rickman *et al.*, 2007). It would therefore be interesting to determine if Munc18-2 also has a binding site at the Habc domain of STX19. Co-localisation studies with Munc18-2 and STX19 KDR mutants or open confirmation mutants would indicate if Munc18-2 binds at different sites on STX19 at different intracellular compartments. Additionally, Sec/Munc18 proteins have been shown to chaperone and regulate SNARE expression levels (Shanks *et al.*, 2012). To gain insight into how Munc18-2 regulates STX19, it would be interesting to determine how knockdown of Munc18-2 would affect the levels of STX19.

Finally, Munc18-2 has been shown to regulate apical trafficking in intestinal epithelial cells (Vogel *et al.*, 2015). Mutations in Munc18-2 result in Familial Hemophagocytic Lymphohistiocytosis 5 (FHL5) which is an autosomal recessive disease characterised by a severe hyperinflammatory phenotype and chronic

enteropathies (Vogel *et al.*, 2017) and Microvillus Inclusions Disease (MVID) which is a congenital enteropathy disorder (Schneeberger *et al.*, 2018). As STX19 is highly expressed in colon and small intestine tissues, it would be interesting to explore the physiological relevance of the STX19/Munc18-2 interaction in intestinal tissues and understand if STX19 interaction is affected in pathophysiological conditions.

5.4 STX19 may form a complex with ZWINT to mediate vesicle tethering

Previous interaction screens performed by my group have identified ZWINT as a potential interactor of STX19. Our mitochondrial re-routing data also suggests ZWINT interacts with STX19 at the plasma membrane. ZWINT is a kinetochore-localised protein that is required for microtubule attachment to kinetochores during mitosis (Woo Seo *et al.*, 2015). Given that STX19 is post-Golgi SNARE and has no known role in mitosis, it is unclear why STX19 would interact with ZWINT. ZWINT has been shown to recruit ZW10 to kinetochores to facilitate spindle assembly (H. Wang *et al.*, 2004). ZW10 has also been reported to have a moonlighting function in ER-Golgi trafficking where it forms a complex with Nag1 and RINT-1 (NRZ complex). This complex interacts with STX18 to mediate vesicle docking. Structural similarities between the NRZ complex and the exocyst complex have been reported (Tagaya *et al.*, 2014). Since ZWINT can recruit ZW10 to kinetochores, it may also be able to recruit other tethering complexes to the plasma membrane. ZWINT may then interact with STX19 to facilitate vesicle docking. To explore this hypothesis, it would be interesting to determine the effect of ZWINT overexpression or knockdown on STX19-positive vesicles at the cell surface using TIRF microscopy. It would also be useful to analyse STX19 recycling kinetics upon overexpression of ZWINT to understand if more STX19 is localised at the plasma membrane.

Alternatively, STX19 may have a moonlighting function in mitosis. SNAP29 has been identified as SNARE binding partner of STX19 and has been shown to localise to the outer kinetochore where it is implicated in promoting kinetochore assembly and preventing chromosome mis-segregation (Morelli *et al.*, 2016b). It may be that STX19 interacts with ZWINT at the kinetochore to regulate trafficking during mitosis. Future studies determining STX19 localisation in dividing cells may provide insight to this hypothesis.

Interestingly, similar to STX19, ZWINT mRNA expression levels have been reported to be upregulated in differentiated keratinocytes (figure 4-3B; Toufighi *et al.*, 2015). It is unclear why a protein involved in mitosis would be upregulated in differentiated cells which are typically non-mitotic. This could support a moonlighting role for ZWINT, aside from kinetochore assembly in non-dividing cells. As STX19 and ZWINT co-localise at the plasma membrane in HeLaM cells, it would be interesting to determine if STX19 and ZWINT localise to the same regions of the plasma membrane in differentiated keratinocytes.

Our knocksideways and mitochondrial targeting assays provided further insight into the interaction between STX19 and ZWINT. Our data suggested that ZWINT is only able to interact with full length STX19 associated with the plasma membrane. Truncated constructs of STX19 lacking the C-terminal S-acylation domain were unable to re-route ZWINT to the mitochondria. Additionally, overexpression studies suggested that ZWINT and STX19 localise to the same distinct regions of the plasma membrane. Plasma membrane localisation of ZWINT was only observed upon expression of a full length flag-tagged ZWINT construct (both N- and C-terminally tagged constructs) and was not seen using anti-ZWINT antibodies. It may be that the antibody epitope is masked when ZWINT is in complex with other proteins or associated with the plasma membrane. ZWINT does not have a transmembrane domain and therefore, it is likely its plasma membrane targeting is via an intermediate protein. ZWINT localises to the plasma membrane without STX19 co-expression suggesting STX19 is not responsible for its membrane targeting. However, ZWINT is also predicted to interact with STXs 3, 11, and 18, and SNAPs 25 and 29 (Huttlin *et al.*, 2015, 2017), all of which (except STX18) are known to mediate fusion with the plasma membrane. It is possible ZWINT membrane targeting occurs through one of these SNARE proteins. It would be interesting to determine if the interaction between STX19 and ZWINT relies on a lipid component using *in vitro* purified protein interaction studies. Previous co-immunoprecipitation experiments have shown that ZWINT is precipitated with STX19. Taken together with the mitochondrial re-routing data this suggests that the proteins can still interact in the absence of the membrane but the two proteins need to be in the correct place for them to interact physiologically. Alternatively, ZWINT may interact with the S-acylation domain of STX19. To determine if this is the site of interaction, it would be necessary to perform additional co-immunoprecipitation studies with truncated STX19 constructs.

5.5 STX19 interacts with DST but the physiological relevance of this interaction remains unclear

Dystonin (DST/BPAG1) was identified as a potential STX19 interactor in yeast-two hybrid screens and proximity-dependent biotinylation proteomics. To further validate this interaction, we co-expressed a GFP-tagged DST construct based on the yeast-two hybrid fragment and STX19 in our knocksideways and mitochondrial targeting assays. Interestingly, STX19 was able to re-route DST to the mitochondria and to STX19/mitochondrial clusters at the cell surface in the knocksideways assay but not in the mitochondrial targeting assay. The knocksideways assay allows proteins to interact prior to mitochondrial re-routing induced by rapamycin treatment. In contrast, the mitochondrial targeting assay directly targets STX19 to the mitochondria. One explanation for our results may be that DST and STX19 are able to interact in their endogenous locations initially and rapamycin treatment allows the STX19/DST complex to re-route to the mitochondria. However, the strength of the interaction may not be great enough to re-route DST alone when STX19 is directly targeted to the mitochondria. Additionally, four potential binding sites for STX19 on DST were identified in yeast-two hybrid screens. Our GFP-tagged DST construct contains only one of

the binding sites. It is possible that interaction with only one binding site weakens the strength of the interaction. It would be interesting to determine if STX19 is able to re-route DST constructs containing two or more potential binding sites to the mitochondria.

Our knocksideways assays have suggested interaction between DST and STX19 yet the physiological relevance of this interaction remains unclear. DST belongs to the spectraplakin family of proteins which have roles in cross linking actin filaments and microtubules to mediate the re-organisation of the cytoskeleton (Ali *et al.*, 2017). Previous studies have indicated a role for spectraplakin proteins in regulating focal adhesion dynamics through co-ordinated interactions with microtubules and actin filaments and directional migration in skin epidermis of mice (Wu, Kodama and Fuchs, 2008; Yue *et al.*, 2016). Additionally, spectraplakin proteins has been shown to positively regulate preosteoblast migration by mediating focal adhesion turnover (Su *et al.*, 2020). It has been shown that 'hotspots' of polarised exocytosis can occur juxtaposed to focal adhesions and microtubule organisation at focal adhesions is important in the delivery of vesicles to these hotspots (Fourriere *et al.*, 2019). It remains unclear however how vesicle fusion machinery is recruited to these 'hotspots'. One possible hypothesis is that that DST may cross link microtubules and actin filaments to allow vesicle delivery to focal adhesions and act as a scaffold to recruit SNARE proteins such as STX19 allowing fusion and exocytosis of cargo at focal adhesions. This hypothesis would require additional studies to determine if STX19 and DST are able to interact in the vicinity of focal adhesion and investigate if STX19 mediates vesicle fusion in close proximity to focal adhesions.

Despite predicted interaction between STX19 and DST in our knocksideways assays, DST and STX19 did not co-localise in differentiated keratinocytes. DST has four isoforms, one of which is epithelial specific (BPAG1e). BPAG1e is localised to hemidesmosomes in keratinocytes which mediates cell attachment to the basal lamina (Walko, Castañón and Wiche, 2015). From our immunofluorescence studies, it is unclear which isoform of DST we observed. It is likely we were observing the BPAG1e isoform as BPAG1e is highly expressed in keratinocytes and the structures in which we observed DST staining were representative of hemidesmosomes (Koster *et al.*, 2003). Additionally, other BPAG1 isoforms are neuronal and muscle tissue-specific (Poliakova *et al.*, 2014).

The cells attached to the basal lamina are undifferentiated and are in the bottom layer of the epidermis. As keratinocyte progressively differentiate, they migrate up the layers of the epidermis (Simpson, Patel and Green, 2011). Since STX19 is upregulated in differentiated keratinocytes and BPAG1e plays a key role in undifferentiated keratinocytes, it remains unclear why STX19 would interact with BPAG1e. This is supported by our immunofluorescence studies which suggested no co-localisation between DST and STX19. Our GFP-DST construct used for interaction studies contains a potential binding site that is found

in the BPAG1e isoform suggesting that STX19 could interact with BPAG1e but this interaction may not have a physiological relevance in keratinocytes. It may be that STX19 interacts with a different isoform of DST. For example, BPAG1a and b have been shown to have roles in mediating vesicle transport along microtubules during myoblast migration (Poliakova *et al.*, 2014). However, BPAG1a is neuronal tissue-specific and BPAG1b is muscle tissue-specific. Both tissues do not highly express STX19. Another possible hypothesis is that BPAG1e may have an unknown moonlighting function as keratinocytes differentiate. As discussed, BPAG1e is required for hemidesmosome assembly and cell attachment, however, as cells differentiate and migrate up the epidermis, they lose attachment to the basal lamina and thus BPAG1e is no longer required in hemidesmosomes (Michael *et al.*, 2014). It may be that BPAG1e is then utilised in a different role that may include regulating cytoskeletal organisation to mediate vesicle trafficking similar to the other isoforms. Further investigations are required to understand the interaction of STX19 and DST. It would be useful to repeat our interaction studies using full-length DST constructs. It will also be important to confirm which binding sites on DST are required for STX19 interaction and with which isoforms does STX19 interact with physiologically.

5.6 STX19 may function in an unconventional autophagy-dependant secretory pathway

Previous studies have suggested a role for STX19 in secretion (Gordon *et al.*, 2010; Simpson, Joggerst, Laketa, Verissimo, Cetin, Erfle, Bexiga, Singan, J. K. Hériché, *et al.*, 2012). However, STX19 has a limited tissue distribution and its levels are thought to be regulated by ubiquitinylation in HeLaM cells (Ampah *et al.*, 2018). This suggests that STX19 has a role in specialised secretory pathways rather than general bulk secretion. To gain further insight into the pathways in which STX19 may play a role, we conducted overexpression studies and analysed STX19 SNARE binding partners. We found that STX19 overexpression alters the steady-state distribution of VAMP8. We hypothesised that the overexpression of STX19 is driving fusion of VAMP8-positive compartments to form large puncta which are likely swollen endosomes and is recruiting VAMP8 to the cell surface where they form a complex to mediate fusion.

To further explore this phenotype, we overexpressed STX19 and analysed the localisation of markers for different compartments that VAMP8 is known to mediate fusion with. VAMP8 is known to localise to lysosomes and mediate their fusion with autophagosomes in the autophagy pathway (Itakura, Kishi-Itakura and Mizushima, 2012). As such, we analysed the expression of autophagosomal markers, LC3 and P62. We found a striking loss of LC3 staining upon overexpression of STX19 both 12 hours and 24 hours post-transfection. This suggests that overexpression of STX19 is affecting the autophagy pathway. Additionally, we found a loss of P62 at 24 hours post-transfection but not at 12 hours post-transfection suggesting that the loss of LC3 precedes loss of P62. We predicted that STX19 is not a major player in autophagosomal-lysosomal fusion as STX17 and SNAP29 are characterised in driving this fusion (Itakura,

Kishi-Itakura and Mizushima, 2012). We also predicted that loss of LC3 was not due to a block in autophagosomal formation as STX19 does not reside on the membranes (mitochondrial, ER, ERGIC, Golgi) which are thought to give rise to autophagosomal initiation membranes (Razi, Chan and Tooze, 2009; Van der Vaart and Reggiori, 2010; Cook *et al.*, 2014; Ge, Zhang and Schekman, 2014). As LC3 and P62 can be degraded by autophagy themselves (Pankiv *et al.*, 2007; Leidal *et al.*, 2020), it is useful to measure autophagic flux as opposed to LC3 and P62 expression levels to fully understand phenotypes in the autophagy pathway. As such, it will be important to investigate the effect of STX19 overexpression on autophagic flux using tandem GFP-mCherry-LC3 constructs. It will also be interesting to determine the effect of STX19 overexpression in the presence of bafilomycin which inhibits autophagosomal-lysosomal fusion.

One possible hypothesis is that STX19 is driving the fusion of VAMP8-positive compartments with the plasma membrane which may include LC3-positive compartments resulting in their secretion. What remains unclear is if this overexpression phenotype is representative of STX19 function or is an overexpression artefact. It would be interesting to determine the effect of STX19 knockdown on the steady state distribution or trafficking dynamics of VAMP8 and LC3.

If this phenotype is not an overexpression artefact, it may be possible that STX19 is working in concert with autophagic machinery to regulate secretion. An unconventional autophagy-dependant secretory pathway has previously been reported. In this pathway, autophagosomes can fuse with endosomes, as opposed to lysosomes, forming amiphsomes. Amphisomes subsequently fuse with the plasma membrane releasing their contents into the extracellular environment (Ponpuak *et al.*, 2015). Alternatively, autophagosomes can fuse directly with the plasma membrane (Kimura, Jia, Kumar, *et al.*, 2017). LC3 and P62 can both be secreted by amphisomal fusion at the plasma membrane (Leidal *et al.*, 2020). Interestingly, this pathway has been shown to be regulated by Rab8 (Dupont *et al.*, 2011). Since STX19 localises to Rab8-positive TREs, it may be likely that Rab8 is also regulating STX19 function and therefore possible that STX19 is functioning in an Rab8-dependent secretory pathway. Additionally, proximity-dependent biotinylation studies has identified TBK1 as a potential STX19 interactor. TBK1 is multimeric kinase that has roles in phosphorylating autophagy receptors that link cargo to autophagosomal membranes (Richter *et al.*, 2016). This could suggest that STX19 is able to interact with and be regulated by autophagy machinery. R-SNARE Sec22B and Q-SNAREs SNAP 23 and 29, and STXs 3 and 4 have been implicated in mediating the direct fusion of autophagosomes with the plasma membrane (Kimura, Jia, Kumar, *et al.*, 2017). This could suggest that STX19 is not directly mediating in the autophagy-dependent secretory pathway and the loss of LC3 staining upon STX19 expression represents is not physiologically relevant. However, it remains unclear which SNAREs regulate the fusion of amphisomes with the plasma

membrane. Future studies such as probing for secreted LC3 in the culture media of STX19-transfected cells would provide insight into if LC3 is secreted upon STX19 overexpression.

As STX19 is enriched in epithelial tissues (Wang *et al.*, 2006; Lonsdale *et al.*, 2013), it would be important to understand if STX19 is playing a role in an autophagy-dependent pathway in a physiologically relevant cell model. To gain insight into this, it would be interesting to determine if STX19 overexpression in keratinocytes effects LC3 and P62 levels. The autophagy-dependent secretory pathway has recently been reported in keratinocytes. It was shown that leaderless cytokine, High Mobility Group Box 1 (HMGB1) is secreted by the autophagy-dependant pathway resulting in increased severity of psoriasis inflammation (Wang *et al.*, 2020). This suggests that the autophagy-dependent secretory pathway is functional in keratinocytes and it would be interesting to determine how overexpression or knockdown of STX19 affects HMGB1 trafficking.

5.7 Characterisation of STX19 localisation in keratinocytes may provide clues into which pathways it functions on

STX19 is relatively highly expressed in epithelial cells and the skin (Wang *et al.*, 2006; Lonsdale *et al.*, 2013) and has been found to be upregulated during calcium-induced keratinocyte differentiation (Toufighi *et al.*, 2015). Therefore, to understand the function of STX19, it is important to use a physiologically relevant cell model. One of the aims of this study was to establish a physiologically relevant cell model for studying STX19 function. In line with previous microarray analyses (Toufighi *et al.*, 2015), we found STX19 was expressed in calcium-induced differentiated keratinocytes. In differentiated keratinocytes, we observed STX19 localisation to distinct regions of the plasma membrane, tubular structures emanating from the membrane, and membrane protrusions. Therefore, differentiated keratinocytes would be a useful model for studying STX19 function.

To characterise the localisation of STX19, we co-stained differentiated keratinocytes with various markers. Excitingly, we found that STX19 localises to the plasma membrane in close proximity to activated Akt. Akt is involved in a number of pathways with overlapping components to regulate various cellular processes such as survival, proliferation, differentiation, and migration (Calautti *et al.*, 2005; Chin and Toker, 2009; Revathidevi and Munirajan, 2019). Localisation of STX19 directly next to activated Akt puncta at the plasma membrane may suggest that STX19 is functioning in similar pathways to Akt. It may be that STX19 is involved in the delivery of cargo to the cell surface in Akt regulated pathways or that Akt is regulating the function of STX19. It would be interesting to determine if STX19 localises to similar regions of the plasma membrane to only activated forms of Akt or to total Akt.

Since Akt functions in complex signalling networks, it may be difficult to distinguish if and which Akt pathways STX19 may function in. However, proximity-dependent biotinylation assays have identified Akt-effector Girdin as a potential STX19 interactor. Girdin is an actin-binding protein that is important in the formation of lamellipodia in migrating cells. Akt phosphorylates Girdin which results in its accumulation at the leading edge of the migrating cells (Enomoto *et al.*, 2005; Weng *et al.*, 2006). Our localisation studies could suggest that STX19 localises to the tips of membrane protrusions at the leading edge of cells. We observed enrichment of STX19 in close proximity to E-cadherin and beta-catenin in the tips of membrane protrusions. E-cadherin and Beta-catenin are usually localised to membranes between neighbouring cells where the form adherens junctions (Niessen, 2007). However, it has been shown that E-cadherin and beta-catenin are internalised and recycling in membrane protrusions to aid migration (Odenwald, Prosperi and Goss, 2013; Brüser and Bogdan, 2017; Grimaldi *et al.*, 2020). Rac1 is downstream of Akt activation (Henderson *et al.*, 2015) and has been shown to regulate E-cadherin recycling in membrane protrusions (Akhtar and Hotchin, 2017). Rac1 also has crucial roles in the formation of lamellipodia and promoting migration (Kurokawa *et al.*, 2004). We also observed enrichment of STX19 in front of Rac1 localisation in the tips of membrane protrusions. Taken together, this data suggests that STX19 may localise to membrane protrusions at the leading edge of the cell. Since Girdin localises to the leading edge of the cell upon Akt activation, we hypothesise that STX19 may form a complex with Girdin to regulate trafficking at the leading edge of cells. To explore this hypothesis, it would be interesting to determine if Girdin and STX19 co-localise in the same regions of the plasma membrane as STX19 in differentiated keratinocytes.

Alternatively, Akt phosphorylation may regulate STX19 function. Downstream effectors of Akt have been shown to phosphorylate other syntaxins such as STX7 phosphorylation by colony-stimulating factor 1 (CSF-1; Achuthan *et al.*, 2008) and STX17 by TBK1 (Kumar *et al.*, 2019). TBK1 has also been identified as a potential STX19 interactor in proximity-dependent biotinylation screens. It would also be interesting to determine if STX19 is phosphorylated using mass-spectrometry studies and determine how TBK1 knockdown effects the phosphorylation status of STX19.

Akt also has roles in regulating autophagy. Akt inhibits autophagy and expression of a constitutively active mutant decreases LC3 levels but increases P62 levels (Wang *et al.*, 2012). It remains unclear if Akt has roles in regulating autophagy-dependent secretory pathways. However, inhibition of degradative autophagy has been shown to increase autophagy-dependent secretion. Interleukin 1β (IL-1β) has been shown to be secreted via autophagy-dependent secretion (Kimura, Jia, Kumar, *et al.*, 2017). Inhibition of autophagy using PI3K inhibitors increased serum levels of IL-1β whilst induction of autophagy using rapamycin reduced IL-1β secretion (Harris *et al.*, 2011). This could suggest that Akt positively regulates the autophagy-dependent secretory pathway. It would be interesting to determine how expression of a

constitutively active or dominant negative Akt mutants would affect the loss of LC3 upon STX19 overexpression.

Akt also plays a role in regulating insulin secretion in pancreatic β-cells. Reduction of Akt activity in transgenic mice results in defective insulin secretion and impaired glucose tolerance (Bernal-Mizrachi *et al.*, 2004). Additionally, adaptor protein APPL1 enhances activity of Akt. APPL1-deficient mice also exhibit impaired insulin secretion. Interestingly, APPL1-deficient mice also have reduced levels of SNARE proteins required for insulin secretion, STX1, SNAP25, and VAMP2. Insulin secretion and SNARE levels can be rescued by expression of constitutively active Akt (Cheng *et al.*, 2012). This suggests that Akt has roles in regulating SNARE expression levels. Since STX19 is enriched in pancreatic tissues and STX19 knockout mice have a decrease in the circulating levels of insulin, it would be interesting to explore the role of Akt in the regulation of STX19 in pancreatic tissues.

5.8 Concluding remarks

Throughout this study, we have characterised novel machinery which is likely to regulate STX19 function and potentially gained insight into some of the pathways and processes STX19 might function on. At this stage, the hypothesises discussed in this study are largely speculative and require additional investigation. However, there are a number of exciting questions which have arisen from these studies including: what are the molecular mechanisms by which Munc18-2 regulates STX19 function, does STX19 have a specific role in an autophagy-dependent secretory pathway, and do Akt signalling pathways regulate STX19 function? Future studies in physiologically relevant cell and animal models will be important to address these questions. There is currently a STX19 CRISPR knockout zebrafish in development which interestingly displays defects in otolith formation in the inner ear. This model could be useful in understanding true physiological function of STX19.

References

Abramov, D., Guiberson, N. G. L. and Burré, J. (2021) 'STXBP1 encephalopathies: Clinical spectrum, disease mechanisms, and therapeutic strategies.', *Journal of neurochemistry*, 157(2), pp. 165–178. doi: 10.1111/jnc.15120.

Achuthan, A. *et al.* (2008) 'Regulation of the Endosomal SNARE Protein Syntaxin 7 by Colony-Stimulating Factor 1 in Macrophages', *Molecular and Cellular Biology*, 28(20), pp. 6149–6159. doi: 10.1128/MCB.00220-08.

Aguilar, R. C. and Wendland, B. (2005) 'Endocytosis of membrane receptors: Two pathways are better than one', *Proceedings of the National Academy of Sciences*, 102(8), pp. 2679–2680. doi: 10.1073/PNAS.0500213102.

Akabane, S. *et al.* (2021) 'KIFC1 regulates ZWINT to promote tumor progression and spheroid formation in colorectal cancer.', *Pathology international*, 71(7), pp. 441–452. doi: 10.1111/pin.13098.

Akhtar, N. and Hotchin, N. A. (2017) 'RAC1 Regulates Adherens Junctions through Endocytosis of E-Cadherin', *https://doi.org/10.1091/mbc.12.4.847*, 12(4), pp. 847–862. doi: 10.1091/MBC.12.4.847.

Ali, A. *et al.* (2017) 'BPAG1, a distinctive role in skin and neurological diseases.', *Seminars in cell & developmental biology*, 69, pp. 34–39. doi: 10.1016/j.semcdb.2017.06.005.

Allen, A. S. *et al.* (2013) 'De novo mutations in epileptic encephalopathies', *Nature 2013 501:7466*, 501(7466), pp. 217–221. doi: 10.1038/nature12439.

Ampah, K. K. *et al.* (2018) 'S-acylation regulates the trafficking and stability of the unconventional Q-SNARE STX19', *Journal of Cell Science*, 131(20). doi: 10.1242/jcs.212498.

Aran, V. *et al.* (2009) 'Characterization of two distinct binding modes between syntaxin 4 and Munc18c', *Biochemical Journal*, 419(3), pp. 655–660. doi: 10.1042/BJ20082293.

Baker, R. W. *et al.* (2015) 'A direct role for the Sec1/Munc18-family protein Vps33 as a template for SNARE assembly', *Science*, 349(6252), pp. 1111–1114. doi: 10.1126/SCIENCE.AAC7906.

Balch, W. E. *et al.* (1984) *Reconstitution of the Transport of Protein between Successive Compartments of the Golgi Measured by the Coupled Incorporation of N-Acetylglucosamine*, *Cell*.

Balch, W. E., Glick, B. S. and Rothman, J. E. (1984) 'Sequential intermediates in the pathway of intercompartmental transport in a cell-free system', *Cell*, 39(3 PART 2), pp. 525–536. doi: 10.1016/0092-8674(84)90459-8.

Barlan, K. and Gelfand, V. I. (2017) 'Microtubule-based transport and the distribution, tethering, and organization of organelles', *Cold Spring Harbor Perspectives in Biology*, 9(5), p. a025817. doi: 10.1101/cshperspect.a025817.

Barlowe, C. *et al.* (1994) 'COPII: A membrane coat formed by Sec proteins that drive vesicle budding from the endoplasmic reticulum', *Cell*, 77(6), pp. 895–907. doi: 10.1016/0092-8674(94)90138-4.

Barlowe, C. and Helenius, A. (2016) 'Cargo Capture and Bulk Flow in the Early Secretory Pathway', *Annual Review of Cell and Developmental Biology*, 32(1), pp. 197–222. doi: 10.1146/annurev-cellbio-111315-125016.

Barlowe, C. K. and Miller, E. A. (2013) 'Secretory protein biogenesis and traffic in the early secretory pathway', *Genetics*, 193(2), pp. 383–410. doi: 10.1534/genetics.112.142810.

Beckers, C. J. M. *et al.* (1989) 'Vesicular transport between the endoplasmic reticulum and the Golgi stack requires the NEM-sensitive fusion protein', *Nature*, 339(6223), pp. 397–398. doi: 10.1038/339397a0.

Bennett, M. K. *et al.* (1993) 'The syntaxin family of vesicular transport receptors', *Cell*, 74(5), pp. 863–873. doi: 10.1016/0092-8674(93)90466-4.

Bennett, M. K., Calakos, N. and Scheller, R. H. (1992) 'Syntaxin: A synaptic protein implicated in docking of synaptic vesicles at presynaptic active zones', *Science*, 257(5067), pp. 255–259. doi: 10.1126/science.1321498.

Bernal-Mizrachi, E. *et al.* (2004) 'Defective insulin secretion and increased susceptibility to experimental diabetes are induced by reduced Akt activity in pancreatic islet β cells', *The Journal of Clinical Investigation*, 114(7), pp. 928–936. doi: 10.1172/JCI20016.

Bi, Y. and Williams, J. A. (2005) 'A role for Rho and Rac in secretagogue-induced amylase release by pancreatic acini', *https://doi.org/10.1152/ajpcell.00395.2004*, 289(1 58-1), pp. 22–32. doi: 10.1152/AJPCELL.00395.2004.

Blasi, J. *et al.* (1993) 'Botulinum neurotoxin A selectively cleaves the synaptic protein SNAP-25', *Nature 1993 365:6442*, 365(6442), pp. 160–163. doi: 10.1038/365160a0.

Block, M. R. *et al.* (1988) 'Purification of an N-ethylmaleimide-sensitive protein catalyzing vesicular transport', *Proceedings of the National Academy of Sciences*, 85(21), pp. 7852–7856. doi: 10.1073/PNAS.85.21.7852.

Borradori, L. and Sonnenberg, A. (1999) 'Structure and function of hemidesmosomes: more than simple

adhesion complexes', *The Journal of investigative dermatology*, 112(4), pp. 411–418. doi: 10.1046/J.1523-1747.1999.00546.X.

Botros, L. *et al.* (2020) 'Bosutinib prevents vascular leakage by reducing focal adhesion turnover and reinforcing junctional integrity', *Journal of Cell Science*, 133(9). doi: 10.1242/JCS.240077.

Braell, W. A. *et al.* (1984) 'The glycoprotein that is transported between successive compartments of the golgi in a cell-free system resides in stacks of cisternae', *Cell*, 39(3 PART 2), pp. 511–524. doi: 10.1016/0092-8674(84)90458-6.

Brasher, M. I. *et al.* (2017) 'Interaction of Munc18c and syntaxin4 facilitates invadopodium formation and extracellular matrix invasion of tumor cells', *Journal of Biological Chemistry*, 292(39), pp. 16199–16210. doi: 10.1074/JBC.M117.807438.

Bravo-Cordero *et al.* (2016) 'A novel high-content analysis tool reveals Rab8-driven cytoskeletal reorganization through Rho GTPases, calpain and MT1-MMP', *Journal of cell science*, 129(8), pp. 1734–1749. doi: 10.1242/JCS.174920.

Bravo-Cordero, J. J. *et al.* (2007) 'MT1-MMP proinvasive activity is regulated by a novel Rab8-dependent exocytic pathway', *The EMBO Journal*, 26(6), pp. 1499–1510. doi: 10.1038/SJ.EMBOJ.7601606.

Brochetta, C. *et al.* (2008) 'Involvement of Munc18 isoforms in the regulation of granule exocytosis in neutrophils', *Biochimica et biophysica acta*, 1783(10), pp. 1781–1791. doi: 10.1016/J.BBAMCR.2008.05.023.

Brochetta, C. *et al.* (2014) 'Munc18-2 and Syntaxin 3 Control Distinct Essential Steps in Mast Cell Degranulation', *The Journal of Immunology*, 192(1), pp. 41–51. doi: 10.4049/JIMMUNOL.1301277.

Brüser, L. and Bogdan, S. (2017) 'Adherens Junctions on the Move—Membrane Trafficking of E-Cadherin', *Cold Spring Harbor Perspectives in Biology*, 9(3). doi: 10.1101/CSHPERSPECT.A029140.

Bryant, N. J. and James, D. E. (2001) 'Vps45p stabilizes the syntaxin homologue Tlg2p and positively regulates SNARE complex formation', *The EMBO Journal*, 20(13), p. 3380. doi: 10.1093/EMBOJ/20.13.3380.

Bryceson, Y. T. *et al.* (2007) 'Defective cytotoxic lymphocyte degranulation in syntaxin-11–deficient familial hemophagocytic lymphohistiocytosis 4 (FHL4) patients', *Blood*, 110(6), pp. 1906–1915. doi: 10.1182/BLOOD-2007-02-074468.

Burgess, T. L. and Kelly, R. B. (1987) 'Constitutive and regulated secretion of proteins.', *Annual review of cell biology*. Annu Rev Cell Biol, pp. 243–293. doi: 10.1146/annurev.cb.03.110187.001331.

Burkhardt, P. *et al.* (2008) 'Munc18a controls SNARE assembly through its interaction with the syntaxin N-peptide', *The EMBO Journal*, 27(7), pp. 923–933. doi: 10.1038/EMBOJ.2008.37.

Cai, B. *et al.* (2011) 'Pre-Sorting Endosomal Transport of the GPI-Anchored Protein, CD59, is Regulated by EHD1', *Traffic*, 12(1), pp. 102–120. doi: 10.1111/j.1600-0854.2010.01135.x.

Cai, B. *et al.* (2014) 'GRAF1 forms a complex with MICAL-L1 and EHD1 to cooperate in tubular recycling endosome vesiculation', *Frontiers in Cell and Developmental Biology*, 0(MAY), p. 22. doi: 10.3389/FCELL.2014.00022.

Calautti, E. *et al.* (2005) 'Phosphoinositide 3-Kinase Signaling to Akt Promotes Keratinocyte Differentiation Versus Death *', *Journal of Biological Chemistry*, 280(38), pp. 32856–32865. doi: 10.1074/JBC.M506119200.

Campa, C. C. *et al.* (2018) 'Rab11 activity and PtdIns(3)P turnover removes recycling cargo from endosomes', *Nature Chemical Biology*, 14(8), pp. 801–810. doi: 10.1038/s41589-018-0086-4.

Caparrós-Pérez, E. *et al.* (2017) 'Down Regulation of the Munc18b-syntaxin-11 Complex and β1-tubulin Impairs Secretion and Spreading in Neonatal Platelets', *Thrombosis and Haemostasis*, 117(11), pp. 2079–2091. doi: 10.1160/TH17-04-0241.

Cardenas, E. I. *et al.* (2019) 'Munc18-2, but not Munc18-1 or Munc18-3, regulates platelet exocytosis, hemostasis, and thrombosis', *Journal of Biological Chemistry*, 294(13), pp. 4784–4792. doi: 10.1074/JBC.RA118.006922.

Caro, L. G. and Palade, G. E. (1964) 'Protein synthesis, storage, and discharge in the pancreatic exocrine cell. An autoradiographic study.', *The Journal of cell biology*, 20, pp. 473–95. doi: 10.1083/jcb.20.3.473.

Carvill, G. L. *et al.* (2014) 'GABRA1 and STXBP1: Novel genetic causes of Dravet syndrome', *Neurology*, 82(14), pp. 1245–1253. doi: 10.1212/WNL.0000000000000291.

Cetica, V. *et al.* (2010) 'STXBP2 mutations in children with familial haemophagocytic lymphohistiocytosis type 5', *Journal of Medical Genetics*, 47(9), pp. 595–600. doi: 10.1136/JMG.2009.075341.

Chai, Y. J. *et al.* (2016) 'Munc18-1 is a molecular chaperone for α-synuclein, controlling its self-replicating aggregation', *Journal of Cell Biology*, 214(6), pp. 705–718. doi: 10.1083/JCB.201512016.

Chang, C.-W. *et al.* (2016a) 'Lipid-anchored Synaptobrevin Provides Little or No Support for Exocytosis or Liposome Fusion *', *Journal of Biological Chemistry*, 291(6), pp. 2848–2857. doi: 10.1074/JBC.M115.701169.

Chang, C.-W. *et al.* (2016b) 'Lipid-anchored Synaptobrevin Provides Little or No Support for Exocytosis

or Liposome Fusion *', *Journal of Biological Chemistry*, 291(6), pp. 2848–2857. doi: 10.1074/JBC.M115.701169.

Chen, G. *et al.* (2003) 'Glucosamine-induced insulin resistance is coupled to O-linked glycosylation of Munc18c', *FEBS Letters*, 534(1–3), pp. 54–60. doi: 10.1016/S0014-5793(02)03774-2.

Chen, W. *et al.* (2020) 'Stxbp1/Munc18-1 haploinsufficiency impairs inhibition and mediates key neurological features of STXBP1 encephalopathy', *eLife*, 9. doi: 10.7554/ELIFE.48705.

Chen, Y. A. *et al.* (1999) 'SNARE Complex Formation Is Triggered by Ca2+ and Drives Membrane Fusion', *Cell*, 97(2), pp. 165–174. doi: 10.1016/S0092-8674(00)80727-8.

Chen, Y. A. and Scheller, R. H. (2001) 'Snare-mediated membrane fusion', *Nature Reviews Molecular Cell Biology*. Nature Publishing Group, pp. 98–106. doi: 10.1038/35052017.

Cheng, K. K. Y. *et al.* (2012) 'APPL1 potentiates insulin secretion in pancreatic β cells by enhancing protein kinase Akt-dependent expression of SNARE proteins in mice', *Proceedings of the National Academy of Sciences*, 109(23), pp. 8919–8924. doi: 10.1073/PNAS.1202435109.

Chin, Y. R. and Toker, A. (2009) 'Function of Akt/PKB Signaling to Cell Motility, Invasion and the Tumor Stroma in Cancer', *Cellular signalling*, 21(4), p. 470. doi: 10.1016/J.CELLSIG.2008.11.015.

Clary, D. O., Griff, I. C. and Rothman, J. E. (1990) 'SNAPs, a family of NSF attachment proteins involved in intracellular membrane fusion in animals and yeast', *Cell*, 61(4), pp. 709–721. doi: 10.1016/0092-8674(90)90482-T.

Cogliati, F. *et al.* (2019) 'Pathogenic Variants in STXBP1 and in Genes for GABAa Receptor Subunities Cause Atypical Rett/Rett-like Phenotypes', *International Journal of Molecular Sciences 2019, Vol. 20, Page 3621*, 20(15), p. 3621. doi: 10.3390/IJMS20153621.

Comegna, M. *et al.* (2018) 'Two cases of microvillous inclusion disease caused by novel mutations in MYO5B gene', *Clinical Case Reports*, 6(12), p. 2451. doi: 10.1002/CCR3.1879.

Cook, K. *et al.* (2014) 'Mitochondria directly donate their membrane to form autophagosomes during a novel mechanism of parkin-associated mitophagy', *Cell & bioscience*, 4(1). doi: 10.1186/2045-3701-4-16.

Cornick, S. *et al.* (2019) 'VAMP8-mediated MUC2 mucin exocytosis from colonic goblet cells maintains innate intestinal homeostasis', *Nature Communications 2019 10:1*, 10(1), pp. 1–14. doi: 10.1038/s41467-019-11811-8.

Côte, M. *et al.* (2009) 'Munc18-2 deficiency causes familial hemophagocytic lymphohistiocytosis type 5 and impairs cytotoxic granule exocytosis in patient NK cells', *The Journal of Clinical Investigation*,

119(12), pp. 3765–3773. doi: 10.1172/JCI40732.

Cullen, P. J. and Steinberg, F. (2018) 'To degrade or not to degrade: mechanisms and significance of endocytic recycling', *Nature Reviews Molecular Cell Biology*. Nature Publishing Group, pp. 679–696. doi: 10.1038/s41580-018-0053-7.

D'Agostino, M. *et al.* (2017) 'A tethering complex drives the terminal stage of SNARE-dependent membrane fusion', *Nature 2017 551:7682*, 551(7682), pp. 634–638. doi: 10.1038/nature24469.

D'Andrea-Merrins, M. *et al.* (2007) 'Munc18c Interaction with Syntaxin 4 Monomers and SNARE Complex Intermediates in GLUT4 Vesicle Trafficking *', *Journal of Biological Chemistry*, 282(22), pp. 16553–16566. doi: 10.1074/JBC.M610818200.

Daste, F., Galli, T. and Tareste, D. (2015) 'Structure and function of longin SNAREs', *Journal of Cell Science*, 128(23), pp. 4263–4272. doi: 10.1242/JCS.178574.

Davis, L. J. *et al.* (2021) 'Organelle tethering, pore formation and SNARE compensation in the late endocytic pathway', *Journal of Cell Science*, 134(10). doi: 10.1242/JCS.255463.

Deák, F. *et al.* (2009) 'Munc18-1 binding to the neuronal SNARE complex controls synaptic vesicle priming.', *The Journal of cell biology*, 184(5), pp. 751–764. doi: 10.1083/jcb.200812026.

Deneka, M. *et al.* (2003) 'Rabaptin-5a/rabaptin-4 serves as a linker between rab4 and γ1-adaptin in membrane recycling from endosomes', *The EMBO Journal*, 22(11), pp. 2645–2657.

Deshaies, R. J. and Schekman, R. (1987) 'A yeast mutant defective at an early stage in import of secretory protein precursors into the endoplasmic reticulum', *Journal of Cell Biology*, 105(2), pp. 633–645. doi: 10.1083/jcb.105.2.633.

Dhara, M. *et al.* (2016) 'v-SNARE transmembrane domains function as catalysts for vesicle fusion', *eLife*, 5. doi: 10.7554/ELIFE.17571.

Dickinson, M. E. *et al.* (2016) 'High-throughput discovery of novel developmental phenotypes', *Nature*, 537(7621), pp. 508–514. doi: 10.1038/nature19356.

Dieckmann, N. M. G. *et al.* (2015) 'Munc18-2 is required for Syntaxin 11 Localization on the Plasma Membrane in Cytotoxic T-Lymphocytes', *Traffic*, 16(12), pp. 1330–1341. doi: 10.1111/TRA.12337.

Dolai, S., Liang, T., Orabi, A. I., Xie, L., *et al.* (2018) 'Depletion of the membrane-fusion regulator Munc18c attenuates caerulein hyperstimulation–induced pancreatitis', *Journal of Biological Chemistry*, 293(7), pp. 2510–2522. doi: 10.1074/JBC.RA117.000792.

Dolai, S., Liang, T., Orabi, A. I., Holmyard, D., *et al.* (2018) 'Pancreatitis-Induced Depletion of Syntaxin 2 Promotes Autophagy and Increases Basolateral Exocytosis', *Gastroenterology*, 154(6), pp. 1805-1821.e5. doi: 10.1053/J.GASTRO.2018.01.025.

Doussau, F. *et al.* (2000) 'A Rho-related GTPase is involved in Ca(2+)-dependent neurotransmitter exocytosis', *The Journal of biological chemistry*, 275(11), pp. 7764–7770. doi: 10.1074/JBC.275.11.7764.

Dulubova, I. *et al.* (1999) 'A conformational switch in syntaxin during exocytosis: role of munc18', *The EMBO Journal*, 18, pp. 4372–4382. doi: 10.1093/emboj.

Dulubova, I. *et al.* (2007) 'Munc18-1 binds directly to the neuronal SNARE complex', *Proceedings of the National Academy of Sciences*, 104(8), pp. 2697–2702. doi: 10.1073/PNAS.0611318104.

Dupont, N. *et al.* (2011) 'Autophagy-based unconventional secretory pathway for extracellular delivery of IL-1β', *The EMBO Journal*, 30(23), pp. 4701–4711. doi: 10.1038/EMBOJ.2011.398.

Eisemann, T. J. *et al.* (2020) 'The sec1/munc18 protein vps45 holds the qa-snare tlg2 in an open conformation', *eLife*, 9, pp. 1–18. doi: 10.7554/ELIFE.60724.

Elsholz, F. *et al.* (2014) 'Calcium - a central regulator of keratinocyte differentiation in health and disease', *European Journal of Dermatology*, 24(6), pp. 650–661. doi: 10.1684/EJD.2014.2452.

Enomoto, A. *et al.* (2005) 'Akt/PKB Regulates Actin Organization and Cell Motility via Girdin/APE', *Developmental Cell*, 9(3), pp. 389–402. doi: 10.1016/J.DEVCEL.2005.08.001.

Eskelinen, E. L. (2006) 'Roles of LAMP-1 and LAMP-2 in lysosome biogenesis and autophagy', *Molecular Aspects of Medicine*, 27(5–6), pp. 495–502. doi: 10.1016/J.MAM.2006.08.005.

Eyster, C. A. *et al.* (2009) 'Discovery of New Cargo Proteins that Enter Cells through Clathrin-Independent Endocytosis', *Traffic*, 10(5), pp. 590–599. doi: 10.1111/J.1600-0854.2009.00894.X.

Fasshauer, D. *et al.* (1998) 'Conserved structural features of the synaptic fusion complex: SNARE proteins reclassified as Q- and R-SNAREs', *Proceedings of the National Academy of Sciences of the United States of America*, 95(26), pp. 15781–15786. doi: 10.1073/pnas.95.26.15781.

Fdez, E. *et al.* (2010) 'Transmembrane-domain determinants for SNARE-mediated membrane fusion', *Journal of Cell Science*, 123(14), pp. 2473–2480. doi: 10.1242/JCS.061325.

Fourriere, L. *et al.* (2019) 'RAB6 and microtubules restrict protein secretion to focal adhesions', *Journal of Cell Biology*, 218(7), pp. 2215–2231. doi: 10.1083/jcb.201805002.

Frémont, S. *et al.* (2017) 'Emerging roles of MICAL family proteins - from actin oxidation to membrane

trafficking during cytokinesis', *Journal of Cell Science*. Company of Biologists Ltd, pp. 1509–1517. doi: 10.1242/jcs.202028.

Fukasawa, M. *et al.* (2004) 'Localization and activity of the SNARE Ykt6 determined by its regulatory domain and palmitoylation', *Proceedings of the National Academy of Sciences*, 101(14), pp. 4815–4820. doi: 10.1073/PNAS.0401183101.

Fukuda, M. *et al.* (2008) 'Large scale screening for novel rab effectors reveals unexpected broad rab binding specificity', *Molecular and Cellular Proteomics*, 7(6), pp. 1031–1042. doi: 10.1074/mcp.M700569-MCP200.

Gaisano, H. Y. and Gorelick, F. S. (2009) 'New Insights Into the Mechanisms of Pancreatitis', *Gastroenterology*, 136(7), pp. 2040–2044. doi: 10.1053/J.GASTRO.2009.04.023.

Gaisano, H. Y., Sheu, L. and Whitcomb, D. (2004) 'Alcoholic chronic pancreatitis involves displacement of Munc18c from the pancreatic acinar basal membrane surface.', *Pancreas*, 28(4), pp. 395–400. doi: 10.1097/00006676-200405000-00008.

Ge, L., Zhang, M. and Schekman, R. (2014) 'Phosphatidylinositol 3-kinase and COPII generate LC3 lipidation vesicles from the ER-Golgi intermediate compartment', *eLife*, 3(November), pp. 1–13. doi: 10.7554/ELIFE.04135.

Ghosh, P. *et al.* (2010) 'A Gαi–GIV Molecular Complex Binds Epidermal Growth Factor Receptor and Determines Whether Cells Migrate or Proliferate', *https://doi.org/10.1091/mbc.e10-01-0028*, 21(13), pp. 2338–2354. doi: 10.1091/MBC.E10-01-0028.

Ghosh, P., Garcia-Marcos, M. and Farquhar, M. G. (2011) 'GIV/Girdin is a rheostat that fine-tunes growth factor signals during tumor progression', *http://dx.doi.org/10.4161/cam.5.3.15909*, 5(3). doi: 10.4161/CAM.5.3.15909.

Gillingham, A. K. *et al.* (2019) 'In vivo identification of GTPase interactors by mitochondrial relocalization and proximity biotinylation.', *eLife*, 8. doi: 10.7554/eLife.45916.

Giridharan, S. S. P. *et al.* (2013) 'Cooperation of MICAL-L1, syndapin2, and phosphatidic acid in tubular recycling endosome biogenesis', *Molecular Biology of the Cell*, 24(11), pp. 1776–1790. doi: 10.1091/mbc.E13-01-0026.

Giridharan, S. S. P. and Caplan, S. (2014) 'MICAL-family proteins: Complex regulators of the actin cytoskeleton', *Antioxidants and Redox Signaling*. Mary Ann Liebert Inc., pp. 2059–2073. doi: 10.1089/ars.2013.5487.

Gordon, D. E. *et al.* (2009) 'Coiled-coil interactions are required for post-Golgi R-SNARE trafficking', *EMBO reports*, 10(8), pp. 851–856. doi: 10.1038/EMBOR.2009.96.

Gordon, D. E. *et al.* (2010) 'A targeted siRNA screen to identify SNAREs required for constitutive secretion in mammalian cells', *Traffic*, 11(9), pp. 1191–1204. doi: 10.1111/j.1600-0854.2010.01087.x.

Gordon, D. E. *et al.* (2017) 'VAMP3/Syb and YKT6 are required for the fusion of constitutive secretory carriers with the plasma membrane', *PLOS Genetics*, 13(4), p. e1006698. doi: 10.1371/JOURNAL.PGEN.1006698.

Gordon, D. E. *et al.* (2021) 'Quantitative Flow Cytometry-Based Assays for Measuring Constitutive Secretion', *Methods in Molecular Biology*, 2233, pp. 115–129. doi: 10.1007/978-1-0716-1044-2_8.

Graham, M. *et al.* (2008) 'A gain-of-function mutant of Munc18-1 stimulates secretory granule recruitment and exocytosis and reveals a direct interaction of Munc18-1 with Rab3', *The Biochemical journal*, 409(2), pp. 407–416. doi: 10.1042/BJ20071094.

Grant, B. D. and Donaldson, J. G. (2009) 'Pathways and mechanisms of endocytic recycling'. doi: 10.1038/nrm2755.

Greaves, J. *et al.* (2010) 'Palmitoylation of the SNAP25 Protein Family: SPECIFICITY AND REGULATION BY DHHC PALMITOYL TRANSFERASES *', *Journal of Biological Chemistry*, 285(32), pp. 24629–24638. doi: 10.1074/JBC.M110.119289.

Greaves, J. and Chamberlain, L. H. (2011) 'Differential palmitoylation regulates intracellular patterning of SNAP25', *Journal of Cell Science*, 124(8), pp. 1351–1360. doi: 10.1242/JCS.079095.

Grigoriev, I. *et al.* (2007) 'Rab6 regulates transport and targeting of exocytotic carriers.', *Developmental cell*, 13(2), pp. 305–14. doi: 10.1016/j.devcel.2007.06.010.

Grigoriev, I. *et al.* (2011) 'Rab6, Rab8, and MICAL3 cooperate in controlling docking and fusion of exocytotic carriers', *Current Biology*, 21(11), pp. 967–974. doi: 10.1016/j.cub.2011.04.030.

Grimaldi, C. *et al.* (2020) 'E-cadherin focuses protrusion formation at the front of migrating cells by impeding actin flow', *Nature Communications 2020 11:1*, 11(1), pp. 1–15. doi: 10.1038/s41467-020-19114-z.

Gu, Y. *et al.* (2019) 'Mammalian Atg8 proteins regulate lysosome and autolysosome biogenesis through SNAREs', *The EMBO Journal*, 38(22), p. e101994. doi: 10.15252/EMBJ.2019101994.

Guo, W. *et al.* (1999) 'The exocyst is an effector for Sec4p, targeting secretory vesicles to sites of exocytosis.', *The EMBO journal*, 18(4), pp. 1071–80. doi: 10.1093/emboj/18.4.1071.

Guo, Y., Sirkis, D. W. and Schekman, R. (2014) ' Protein Sorting at the trans -Golgi Network ', *Annual Review of Cell and Developmental Biology*, 30(1), pp. 169–206. doi: 10.1146/annurev-cellbio-100913-013012.

Gutierrez, B. A. *et al.* (2018) 'Munc18-2, but not Munc18-1 or Munc18-3, controls compound and single-vesicle-regulated exocytosis in mast cells', *Journal of Biological Chemistry*, 293(19), pp. 7148–7159. doi: 10.1074/JBC.RA118.002455.

Hackmann, Y. *et al.* (2013) 'Syntaxin binding mechanism and disease-causing mutations in Munc18-2.', *Proceedings of the National Academy of Sciences of the United States of America*, 110(47), pp. E4482-91. doi: 10.1073/pnas.1313474110.

Halimani, M. *et al.* (2014) 'Syntaxin11 serves as a t-SNARE for the fusion of lytic granules in human cytotoxic T lymphocytes', *European Journal of Immunology*, 44(2), pp. 573–584. doi: 10.1002/EJI.201344011.

Hamdan, F. F. *et al.* (2009) 'De novo STXBP1 mutations in mental retardation and nonsyndromic epilepsy', *Annals of Neurology*, 65(6), pp. 748–753. doi: 10.1002/ANA.21625.

Hamdan, F. F. *et al.* (2011) 'Intellectual disability without epilepsy associated with STXBP1 disruption', *European Journal of Human Genetics 2011 19:5*, 19(5), pp. 607–609. doi: 10.1038/ejhg.2010.183.

Hamill, K. J. *et al.* (2009) 'BPAG1e maintains keratinocyte polarity through beta4 integrin-mediated modulation of Rac1 and cofilin activities.', *Molecular biology of the cell*, 20(12), pp. 2954–2962. doi: 10.1091/mbc.e09-01-0051.

Harris, J. *et al.* (2011) 'Autophagy Controls IL-1β Secretion by Targeting Pro-IL-1β for Degradation', *Journal of Biological Chemistry*, 286(11), pp. 9587–9597. doi: 10.1074/JBC.M110.202911.

Harter, C. and Reinhard, C. (2002) 'Fusion of Biological Membranes and Related Problems', *Sub-cellular biochemistry*. Edited by H. Hilderson and S. Fuller, 34, pp. 1–38. doi: 10.1007/b114370.

Hartsock, A. and Nelson, W. J. (2008) 'Adherens and tight junctions: Structure, function and connections to the actin cytoskeleton', *Biochimica et Biophysica Acta (BBA) - Biomembranes*, 1778(3), pp. 660–669. doi: 10.1016/J.BBAMEM.2007.07.012.

Hattula, K. *et al.* (2006) 'Characterization of the Rab8-specific membrane traffic route linked to protrusion formation', *Journal of Cell Science*, 119(23), pp. 4866–4877. doi: 10.1242/jcs.03275.

Al Hawas, R. *et al.* (2012) 'Munc18b/STXBP2 is required for platelet secretion', *Blood*, 120(12), pp. 2493–2500. doi: 10.1182/BLOOD-2012-05-430629.

Hein, M. Y. *et al.* (2015) 'A Human Interactome in Three Quantitative Dimensions Organized by Stoichiometries and Abundances', *Cell*, 163(3), pp. 712–723. doi: 10.1016/J.CELL.2015.09.053.

Hellewell, A. L. *et al.* (2014) 'Analysis of Familial Hemophagocytic Lymphohistiocytosis Type 4 (FHL-4) Mutant Proteins Reveals that S-Acylation Is Required for the Function of Syntaxin 11 in Natural Killer Cells', *PLOS ONE*, 9(6), p. e98900. doi: 10.1371/JOURNAL.PONE.0098900.

Henderson, V. *et al.* (2015) 'Snail promotes cell migration through PI3K/AKT-dependent Rac1 activation as well as PI3K/AKT-independent pathways during prostate cancer progression', *Cell adhesion & migration*, 9(4), pp. 255–264. doi: 10.1080/19336918.2015.1013383.

Hirst, J. *et al.* (2018) 'Role of the AP-5 adaptor protein complex in late endosome-to-Golgi retrieval.', *PLoS biology*, 16(1), p. e2004411. doi: 10.1371/journal.pbio.2004411.

Hirst, J. and Robinson, M. S. (1998) 'Clathrin and adaptors', *Biochimica et Biophysica Acta - Molecular Cell Research*, 1404(1–2), pp. 173–193. doi: 10.1016/S0167-4889(98)00056-1.

Hou, J. C. and Pessin, J. E. (2007) 'Ins (endocytosis) and outs (exocytosis) of GLUT4 trafficking', *Current Opinion in Cell Biology*, 19(4), pp. 466–473. doi: 10.1016/J.CEB.2007.04.018.

Hutchins, J. R. A. *et al.* (2010) 'Systematic Analysis of Human Protein Complexes Identifies Chromosome Segregation Proteins', *Science*, 328(5978), pp. 593–599. doi: 10.1126/SCIENCE.1181348.

Huttlin, E. L. *et al.* (2015) 'The BioPlex Network: A Systematic Exploration of the Human Interactome', *Cell*, 162(2), pp. 425–440. doi: 10.1016/J.CELL.2015.06.043.

Huttlin, E. L. *et al.* (2017) 'Architecture of the human interactome defines protein communities and disease networks', *Nature 2016 545:7655*, 545(7655), pp. 505–509. doi: 10.1038/nature22366.

Imai, A., Nashida, T. and Shimomura, H. (2004) 'Roles of Munc18-3 in amylase release from rat parotid acinar cells', *Archives of Biochemistry and Biophysics*, 422(2), pp. 175–182. doi: 10.1016/J.ABB.2003.12.021.

Itakura, E., Kishi-Itakura, C. and Mizushima, N. (2012) 'The Hairpin-type Tail-Anchored SNARE Syntaxin 17 Targets to Autophagosomes for Fusion with Endosomes/Lysosomes', *Cell*, 151(6), pp. 1256–1269. doi: 10.1016/J.CELL.2012.11.001.

Jahn, R. and Scheller, R. H. (2006) 'SNAREs - Engines for membrane fusion', *Nature Reviews Molecular Cell Biology*, pp. 631–643. doi: 10.1038/nrm2002.

Jain, S. S. *et al.* (2012) 'Munc18c provides stimulus-selective regulation of GLUT4 but not fatty acid transporter trafficking in skeletal muscle', *FEBS Letters*, 586(16), pp. 2428–2435. doi:

10.1016/J.FEBSLET.2012.05.061.

Jakhanwal, S. *et al.* (2017) 'An activated Q-SNARE/SM protein complex as a possible intermediate in SNARE assembly', *The EMBO Journal*, 36(12), pp. 1788–1802. doi: 10.15252/EMBJ.201696270.

Jamieson, J. D. and Palade, G. E. (1967) 'Intracellular transport of secretory proteins in the pancreatic exocrine cell. I. Role of the peripheral elements of the Golgi complex.', *The Journal of cell biology*, 34(2), pp. 577–596. doi: 10.1083/jcb.34.2.577.

Jean, S. *et al.* (2015) 'Starvation-induced MTMR13 and RAB21 activity regulates VAMP8 to promote autophagosome–lysosome fusion', *EMBO reports*, 16(3), pp. 297–311. doi: 10.15252/EMBR.201439464.

Jewell, J. L. *et al.* (2011) 'Munc18c phosphorylation by the insulin receptor links cell signaling directly to SNARE exocytosis', *Journal of Cell Biology*, 193(1), pp. 185–199. doi: 10.1083/JCB.201007176.

Jiang, P. *et al.* (2008) 'An actin-binding protein Girdin regulates the motility of breast cancer cells', *Cancer research*, 68(5), pp. 1310–1318. doi: 10.1158/0008-5472.CAN-07-5111.

Jiang, X. *et al.* (2020) 'CD9 regulates keratinocyte differentiation and motility by recruiting E-cadherin to the plasma membrane and activating the PI3K/Akt pathway', *Biochimica et Biophysica Acta (BBA) - Molecular Cell Research*, 1867(2), p. 118574. doi: 10.1016/J.BBAMCR.2019.118574.

Jiao, J. *et al.* (2018) 'Munc18-1 catalyzes neuronal SNARE assembly by templating SNARE association', *eLife*, 7. doi: 10.7554/eLife.41771.

Jun, Y. *et al.* (2007) 'Sec18p and Vam7p remodel trans-SNARE complexes to permit a lipid-anchored R-SNARE to support yeast vacuole fusion', *The EMBO Journal*, 26(24), p. 4935. doi: 10.1038/SJ.EMBOJ.7601915.

Kabeya *et al.* (2000) 'LC3, a mammalian homologue of yeast Apg8p, is localized in autophagosome membranes after processing', *The EMBO journal*, 19(21), pp. 5720–5728. doi: 10.1093/EMBOJ/19.21.5720.

Kanno, E. *et al.* (2010) 'Comprehensive Screening for Novel Rab-Binding Proteins by GST Pull-Down Assay Using 60 Different Mammalian Rabs‡', *Traffic*, 11(4), pp. 491–507. doi: 10.1111/j.1600-0854.2010.01038.x.

Kelly, R. B. (1985) 'Pathways of protein secretion in eukaryotes', *Science*, 230(4721), pp. 25–32. doi: 10.1126/science.2994224.

Khan, A. H. *et al.* (2001) 'Munc18c Regulates Insulin-stimulated GLUT4 Translocation to the Transverse Tubules in Skeletal Muscle *', *Journal of Biological Chemistry*, 276(6), pp. 4063–4069. doi:

10.1074/JBC.M007419200.

Khvotchev, M. *et al.* (2007) 'Cellular/Molecular Dual Modes of Munc18-1/SNARE Interactions Are Coupled by Functionally Critical Binding to Syntaxin-1 N Terminus'. doi: 10.1523/JNEUROSCI.3655-07.2007.

Kimura, S., Noda, T. and Yoshimura, T. (2007) 'Dissection of the autophagosome maturation process by a novel reporter protein, tandem fluorescent-tagged LC3', *Autophagy*, 3(5), pp. 452–460. doi: 10.4161/AUTO.4451.

Kimura, T., Jia, J., Claude-Taupin, A., *et al.* (2017) 'Cellular and molecular mechanism for secretory autophagy', *AUTOPHAGY*, 13(6), pp. 1084–1085. doi: 10.15252/embj.201695081.

Kimura, T., Jia, J., Kumar, S., *et al.* (2017) 'Dedicated SNAREs and specialized TRIM cargo receptors mediate secretory autophagy', *The EMBO Journal*, 36(1), pp. 42–60. doi: 10.15252/EMBJ.201695081.

Kobayashi, H. *et al.* (2014) 'Rab35 promotes the recruitment of Rab8, Rab13 and Rab36 to recycling endosomes through MICAL-L1 during neurite outgrowth', *Biology Open*, 3(9), pp. 803–814. doi: 10.1242/BIO.20148771.

Kops, G. J. P. L. *et al.* (2005) 'ZW10 links mitotic checkpoint signaling to the structural kinetochore.', *The Journal of cell biology*, 169(1), pp. 49–60. doi: 10.1083/jcb.200411118.

Koster, J. *et al.* (2003) 'Analysis of the interactions between BP180, BP230, plectin and the integrin α6β4 important for hemidesmosome assembly', *Journal of Cell Science*, 116(2), pp. 387–399. doi: 10.1242/JCS.00241.

Koubek, E. J. and Santy, L. C. (2018) 'ARF1 and ARF6 regulate recycling of GRASP/Tamalin and the Rac1-GEF Dock180 during HGF-induced Rac1 activation', *Small GTPases*, 9(3), p. 242. doi: 10.1080/21541248.2016.1219186.

Kouranti, I. *et al.* (2006) 'Rab35 Regulates an Endocytic Recycling Pathway Essential for the Terminal Steps of Cytokinesis', *Current Biology*, 16(17), pp. 1719–1725. doi: 10.1016/j.cub.2006.07.020.

Kruse, K. *et al.* (2019) 'N-cadherin signaling via Trio assembles adherens junctions to restrict endothelial permeability', *Journal of Cell Biology*, 218(1), pp. 299–316. doi: 10.1083/JCB.201802076.

Kubo, K. *et al.* (2015) 'SNAP23/25 and VAMP2 mediate exocytic event of transferrin receptor-containing recycling vesicles', *Biology Open*, 4(7), pp. 910–920. doi: 10.1242/BIO.012146.

Kumar, S. *et al.* (2019) 'Phosphorylation of Syntaxin 17 by TBK1 Controls Autophagy Initiation', *Developmental Cell*, 49(1), pp. 130-144.e6. doi: 10.1016/J.DEVCEL.2019.01.027.

Kurokawa, K. *et al.* (2004) 'Coactivation of Rac1 and Cdc42 at Lamellipodia and Membrane Ruffles Induced by Epidermal Growth Factor', *Molecular Biology of the Cell*, 15(3), p. 1003. doi: 10.1091/MBC.E03-08-0609.

Kuster, A. *et al.* (2015) 'The Q-soluble N-Ethylmaleimide-sensitive Factor Attachment Protein Receptor (Q-SNARE) SNAP-47 Regulates Trafficking of Selected Vesicle-associated Membrane Proteins (VAMPs) *', *Journal of Biological Chemistry*, 290(47), pp. 28056–28069. doi: 10.1074/JBC.M115.666362.

Larocque, G. *et al.* (2020) 'Tumor protein D54 defines a new class of intracellular transport vesicles', *Journal of Cell Biology*, 219(1). doi: 10.1083/JCB.201812044.

Lee, H.-K. *et al.* (2002) 'Identification of a novel SNAP25 interacting protein (SIP30)', *Journal of Neurochemistry*, 81(6), pp. 1338–1347. doi: 10.1046/J.1471-4159.2002.00937.X.

Leidal, A. M. *et al.* (2020) 'The LC3-conjugation machinery specifies the loading of RNA-binding proteins into extracellular vesicles', *Nature Cell Biology 2020 22:2*, 22(2), pp. 187–199. doi: 10.1038/s41556-019-0450-y.

Leung, C. *et al.* (2001) 'The BPAG1 locus: Alternative splicing produces multiple isoforms with distinct cytoskeletal linker domains, including predominant isoforms in neurons and muscles', *The Journal of cell biology*, 154(4), pp. 691–697. doi: 10.1083/JCB.200012098.

Liang, T. *et al.* (2017) 'New Roles of Syntaxin-1A in Insulin Granule Exocytosis and Replenishment', *The Journal of biological chemistry*, 292(6), pp. 2203–2216. doi: 10.1074/JBC.M116.769885.

Lindsay, A. J. *et al.* (2002) 'Rab coupling protein (RCP), a novel Rab4 and Rab11 effector protein', *Journal of Biological Chemistry*, 277(14), pp. 12190–12199. doi: 10.1074/jbc.M108665200.

Lindsay, A. J. and McCaffrey, M. W. (2004) 'The C2 domains of the class I Rab11 family of interacting proteins target recycling vesicles to the plasma membrane', *Journal of Cell Science*, 117(19), pp. 4365–4375. doi: 10.1242/jcs.01280.

Link, E. *et al.* (1992) 'Tetanus toxin action: Inhibition of neurotransmitter release linked to synaptobrevin proteolysis', *Biochemical and Biophysical Research Communications*, 189(2), pp. 1017–1023. doi: 10.1016/0006-291X(92)92305-H.

Litjens, S., JM, de P. and A, S. (2006) 'Current insights into the formation and breakdown of hemidesmosomes', *Trends in cell biology*, 16(7), pp. 376–383. doi: 10.1016/J.TCB.2006.05.004.

Liu, J. *et al.* (2007) 'Phosphatidylinositol 4,5-bisphosphate mediates the targeting of the exocyst to the plasma membrane for exocytosis in mammalian cells', *Molecular Biology of the Cell*, 18(11), pp. 4483–

4492. doi: 10.1091/mbc.E07-05-0461.

Lonsdale, J. *et al.* (2013) *The Genotype-Tissue Expression (GTEx) project*. doi: 10.1038/ng.2653.

Low, S. H. *et al.* (1996) 'Differential localization of syntaxin isoforms in polarized Madin-Darby canine kidney cells', *Molecular Biology of the Cell*, 7(12), pp. 2007–2018. doi: 10.1091/mbc.7.12.2007.

Lu, Q. *et al.* (2015) 'Early steps in primary cilium assembly require EHD1/EHD3-dependent ciliary vesicle formation', *Nature cell biology*, 17(3), pp. 228–240. doi: 10.1038/NCB3109.

Ma, C. *et al.* (2013) 'Reconstitution of the Vital Functions of Munc18 and Munc13 in Neurotransmitter Release', *Science*, 339(6118), pp. 421–425. doi: 10.1126/SCIENCE.1230473.

Ma, L. *et al.* (2015) 'Munc18-1-regulated stage-wise SNARE assembly underlying synaptic exocytosis', *eLife*, 4. doi: 10.7554/ELIFE.09580.

Macaulay, S. L. *et al.* (2002) 'Cellular munc18c levels can modulate glucose transport rate and GLUT4 translocation in 3T3L1 cells', *FEBS Letters*, 528(1–3), pp. 154–160. doi: 10.1016/S0014-5793(02)03279-9.

Malhotra, V. *et al.* (1988) 'Role of an N-ethylmaleimide-sensitive transport component in promoting fusion of transport vesicles with cisternae of the Golgi stack', *Cell*, 54(2), pp. 221–227. doi: 10.1016/0092-8674(88)90554-5.

Marsh, R. A. *et al.* (2010) 'STX11 mutations and clinical phenotypes of familial hemophagocytic lymphohistiocytosis in North America', *Pediatric Blood & Cancer*, 55(1), pp. 134–140. doi: 10.1002/PBC.22499.

Marshall, M. R. *et al.* (2015a) 'VAMP8-dependent fusion of recycling endosomes with the plasma membrane facilitates T lymphocyte cytotoxicity', *Journal of Cell Biology*, 210(1), pp. 135–151. doi: 10.1083/JCB.201411093.

Marshall, M. R. *et al.* (2015b) 'VAMP8-dependent fusion of recycling endosomes with the plasma membrane facilitates T lymphocyte cytotoxicity', *Journal of Cell Biology*, 210(1), pp. 135–151. doi: 10.1083/JCB.201411093.

Martin-Verdeaux, S. *et al.* (2003) 'Evidence of a role for Munc18-2 and microtubules in mast cell granule exocytosis', *Journal of Cell Science*, 116(2), pp. 325–334. doi: 10.1242/JCS.00216.

Martinez-Arca, S. *et al.* (2003) 'A dual mechanism controlling the localization and function of exocytic v-SNAREs', *Proceedings of the National Academy of Sciences*, 100(15), pp. 9011–9016. doi: 10.1073/PNAS.1431910100.

Maxfield, F. R. and McGraw, T. E. (2004) 'Endocytic recycling', *Nature Reviews Molecular Cell Biology*. Nat Rev Mol Cell Biol, pp. 121–132. doi: 10.1038/nrm1315.

McCaffrey, M. W. *et al.* (2001) 'Rab4 affects both recycling and degradative endosomal trafficking', *FEBS Letters*, 495(1–2), pp. 21–30. doi: 10.1016/S0014-5793(01)02359-6.

McNew, J. *et al.* (2000) 'Close is not enough: SNARE-dependent membrane fusion requires an active mechanism that transduces force to membrane anchors', *The Journal of cell biology*, 150(1), pp. 105–117. doi: 10.1083/JCB.150.1.105.

McNew, J. A., Weber, T., *et al.* (2000) 'Close Is Not EnoughSnare-Dependent Membrane Fusion Requires an Active Mechanism That Transduces Force to Membrane Anchors', *Journal of Cell Biology*, 150(1), pp. 105–118. doi: 10.1083/JCB.150.1.105.

McNew, J. A., Parlati, F., *et al.* (2000) 'Compartmental specificity of cellular membrane fusion encoded in SNARE proteins', *Nature 2000 407:6801*, 407(6801), pp. 153–159. doi: 10.1038/35025000.

Medine, C. N. *et al.* (2007) 'Munc18-1 prevents the formation of ectopic SNARE complexes in living cells', *Journal of Cell Science*, 120(24), pp. 4407–4415. doi: 10.1242/JCS.020230.

Mehlmann, Uliasz and Lowther (2019) 'SNAP23 is required for constitutive and regulated exocytosis in mouse oocytes†', *Biology of reproduction*, 101(2), pp. 338–346. doi: 10.1093/BIOLRE/IOZ106.

Melia, T. J., Lystad, A. H. and Simonsen, A. (2020) 'Autophagosome biogenesis: From membrane growth to closure', *Journal of Cell Biology*, 219(6). doi: 10.1083/JCB.202002085.

Messenger, S. W. *et al.* (2014) 'Vesicle Associated Membrane Protein 8 (VAMP8)-mediated Zymogen Granule Exocytosis Is Dependent on Endosomal Trafficking via the Constitutive-Like Secretory Pathway *'. doi: 10.1074/jbc.M114.593913.

Michael, M. *et al.* (2014) 'BPAG1-e restricts keratinocyte migration through control of adhesion stability.', *The Journal of investigative dermatology*, 134(3), pp. 773–782. doi: 10.1038/jid.2013.382.

Michail, S. *et al.* (1998) 'Abnormal expression of brush-border membrane transporters in the duodenal mucosa of two patients with microvillus inclusion disease', *Journal of pediatric gastroenterology and nutrition*, 27(5), pp. 536–542. doi: 10.1097/00005176-199811000-00008.

Misura, K. M. S., Scheller, R. H. and Weis, W. I. (2000) 'Three-dimensional structure of the neuronal-Sec1–syntaxin 1a complex', *Nature 2000 404:6776*, 404(6776), pp. 355–362. doi: 10.1038/35006120.

ML, C. *et al.* (2001) 'Phox domain interaction with PtdIns(3)P targets the Vam7 t-SNARE to vacuole membranes', *Nature cell biology*, 3(7), pp. 613–618. doi: 10.1038/35083000.

Morelli, E. *et al.* (2014) 'Multiple functions of the SNARE protein Snap29 in autophagy, endocytic, and exocytic trafficking during epithelial formation in Drosophila', *Autophagy*, 10(12), p. 2251. doi: 10.4161/15548627.2014.981913.

Morelli, E. *et al.* (2016a) 'An essential step of kinetochore formation controlled by the SNARE protein Snap29', *The EMBO Journal*, 35(20), pp. 2223–2237. doi: 10.15252/EMBJ.201693991.

Morelli, E. *et al.* (2016b) 'An essential step of kinetochore formation controlled by the SNARE protein Snap29', *The EMBO Journal*, 35(20), p. 2223. doi: 10.15252/EMBJ.201693991.

Moritz, O. L. *et al.* (2001) 'Mutant rab8 Impairs Docking and Fusion of Rhodopsin-bearing Post-Golgi Membranes and Causes Cell Death of Transgenic Xenopus Rods', *Molecular Biology of the Cell*, 12(8), p. 2341. doi: 10.1091/MBC.12.8.2341.

Mosa, M. H. *et al.* (2018) 'Dynamic Formation of Microvillus Inclusions During Enterocyte Differentiation in Munc18-2–Deficient Intestinal Organoids', *CMGH*, 6(4), pp. 477-493.e1. doi: 10.1016/j.jcmgh.2018.08.001.

Muller, M.-L. *et al.* (2014) 'An N-Terminal Missense Mutation in STX11 Causative of FHL4 Abrogates Syntaxin-11 Binding to Munc18-2', *Frontiers in Immunology*, 0(JAN), p. 515. doi: 10.3389/FIMMU.2013.00515.

Müller, M. L. *et al.* (2014) 'An N-terminal missense mutation in STX11 causative of FHL4 abrogates syntaxin-11 binding to Munc18-2', *Frontiers in Immunology*, 4(JAN). doi: 10.3389/fimmu.2013.00515.

Nachury, M. V. *et al.* (2007) 'A Core Complex of BBS Proteins Cooperates with the GTPase Rab8 to Promote Ciliary Membrane Biogenesis', *Cell*, 129(6), pp. 1201–1213. doi: 10.1016/J.CELL.2007.03.053.

Naslavsky, N., Weigert, R. and Donaldson, J. G. (2004) 'Characterization of a Nonclathrin Endocytic Pathway: Membrane Cargo and Lipid Requirements', *https://doi.org/10.1091/mbc.e04-02-0151*, 15(8), pp. 3542–3552. doi: 10.1091/MBC.E04-02-0151.

Nelson, B. A., Robinson, K. A. and Buse, M. G. (2002) 'Insulin Acutely Regulates Munc18-c Subcellular Trafficking: ALTERED RESPONSE IN INSULIN-RESISTANT 3T3-L1 ADIPOCYTES *', *Journal of Biological Chemistry*, 277(6), pp. 3809–3812. doi: 10.1074/JBC.C100645200.

Niessen, C. M. (2007) 'Tight Junctions/Adherens Junctions: Basic Structure and Function', *Journal of Investigative Dermatology*, 127(11), pp. 2525–2532. doi: 10.1038/SJ.JID.5700865.

Ninomiya, Y. *et al.* (1997) 'Kinetic diversity in the fusion of exocytotic vesicles', *The EMBO journal*, 16(5), pp. 929–934. doi: 10.1093/EMBOJ/16.5.929.

Nishimura, Y. *et al.* (2015) 'EGF-stimulated AKT activation is mediated by EGFR recycling via an early endocytic pathway in a gefitinib-resistant human lung cancer cell line', *International Journal of Oncology*, 46(4), pp. 1721–1729. doi: 10.3892/IJO.2015.2871.

Nobes, C. and Hall, A. (1995) 'Rho, rac, and cdc42 GTPases regulate the assembly of multimolecular focal complexes associated with actin stress fibers, lamellipodia, and filopodia', *Cell*, 81(1), pp. 53–62. doi: 10.1016/0092-8674(95)90370-4.

Novick, P., Field, C. and Schekman, R. (1980) 'Identification of 23 complementation groups required for post-translational events in the yeast secretory pathway', *Cell*, 21(1), pp. 205–215. doi: 10.1016/0092-8674(80)90128-2.

Novick, P. and Schekman, R. (1979) 'Secretion and cell-surface growth are blocked in a temperature-sensitive mutant of Saccharomyces cerevisiae', *Proceedings of the National Academy of Sciences of the United States of America*, 76(4), pp. 1858–1862. doi: 10.1073/pnas.76.4.1858.

Nüchel, J. *et al.* (2018) 'TGFB1 is secreted through an unconventional pathway dependent on the autophagic machinery and cytoskeletal regulators', *https://doi.org/10.1080/15548627.2017.1422850*, 14(3), pp. 465–486. doi: 10.1080/15548627.2017.1422850.

Odenwald, M. A., Prosperi, J. R. and Goss, K. H. (2013) 'APC/β-catenin-rich complexes at membrane protrusions regulate mammary tumor cell migration and mesenchymal morphology', *BMC Cancer 2013 13:1*, 13(1), pp. 1–12. doi: 10.1186/1471-2407-13-12.

Oh, E. *et al.* (2005) 'Munc18c Heterozygous Knockout Mice Display Increased Susceptibility for Severe Glucose Intolerance', *Diabetes*, 54(3), pp. 638–647. doi: 10.2337/DIABETES.54.3.638.

Oh, E. *et al.* (2012) 'Munc18-1 regulates first-phase insulin release by promoting granule docking to multiple syntaxin isoforms.', *The Journal of biological chemistry*, 287(31), pp. 25821–25833. doi: 10.1074/jbc.M112.361501.

Otsuka, M. *et al.* (2010) 'STXBP1 mutations cause not only Ohtahara syndrome but also West syndrome—Result of Japanese cohort study', *Epilepsia*, 51(12), pp. 2449–2452. doi: 10.1111/J.1528-1167.2010.02767.X.

Ouahed, J. *et al.* (2021) 'Variants in STXBP3 Are Associated With Very Early Onset Inflammatory Bowel Disease, Bilateral Sensorineural Hearing Loss and Immune Dysregulation', *Journal of Crohn's and Colitis*, 17, p. 20. doi: 10.1093/ECCO-JCC/JJAB077.

Oyler, G. A. *et al.* (1989) 'The identification of a novel synaptosomal-associated protein, SNAP-25, differentially expressed by neuronal subpopulations', *Journal of Cell Biology*, 109(6 I), pp. 3039–3052.

doi: 10.1083/jcb.109.6.3039.

Palade, G. (1975) 'Intracellular aspects of the process of protein synthesis', *Science*, 189(4200), pp. 347–358. doi: 10.1126/science.1096303.

Pallet, N. *et al.* (2013) 'A comprehensive characterization of membrane vesicles released by autophagic human endothelial cells', *PROTEOMICS*, 13(7), pp. 1108–1120. doi: 10.1002/PMIC.201200531.

Pankiv, S. *et al.* (2007) 'p62/SQSTM1 binds directly to Atg8/LC3 to facilitate degradation of ubiquitinated protein aggregates by autophagy', *The Journal of biological chemistry*, 282(33), pp. 24131–24145. doi: 10.1074/JBC.M702824200.

Parisotto, D. *et al.* (2014) 'An Extended Helical Conformation in Domain 3a of Munc18-1 Provides a Template for SNARE (Soluble N-Ethylmaleimide-sensitive Factor Attachment Protein Receptor) Complex Assembly *', *Journal of Biological Chemistry*, 289(14), pp. 9639–9650. doi: 10.1074/JBC.M113.514273.

Parri, M. and Chiarugi, P. (2010) 'Rac and Rho GTPases in cancer cell motility control', *Cell Communication and Signaling 2010 8:1*, 8(1), pp. 1–14. doi: 10.1186/1478-811X-8-23.

Peden, A. A. *et al.* (2002) 'Assembly and function of AP-3 complexes in cells expressing mutant subunits', *Journal of Cell Biology*, 156(2), pp. 327–336. doi: 10.1083/JCB.200107140.

Peden, A. A. *et al.* (2004) 'The RCP-Rab11 complex regulates endocytic protein sorting', *Molecular Biology of the Cell*, 15(8), pp. 3530–3541. doi: 10.1091/mbc.E03-12-0918.

Peng, F. *et al.* (2019) 'ZWINT is the next potential target for lung cancer therapy.', *Journal of cancer research and clinical oncology*, 145(3), pp. 661–673. doi: 10.1007/s00432-018-2823-1.

Peränen, J. (2011) 'Rab8 GTPase as a regulator of cell shape', *Cytoskeleton*, 68(10), pp. 527–539. doi: 10.1002/CM.20529.

Pertsinidis, A. *et al.* (2013) 'Ultrahigh-resolution imaging reveals formation of neuronal SNARE/Munc18 complexes in situ', *Proceedings of the National Academy of Sciences*, 110(30), pp. E2812–E2820. doi: 10.1073/PNAS.1310654110.

Pevsner, J. *et al.* (1994) 'Specificity and regulation of a synaptic vesicle docking complex', *Neuron*, 13(2), pp. 353–361. doi: 10.1016/0896-6273(94)90352-2.

Poliakova, K. *et al.* (2014) 'BPAG1a and b Associate with EB1 and EB3 and Modulate Vesicular Transport, Golgi Apparatus Structure, and Cell Migration in C2.7 Myoblasts', *PLOS ONE*, 9(9), p. e107535. doi: 10.1371/JOURNAL.PONE.0107535.

Pols, M. S. and Klumperman, J. (2009) 'Trafficking and function of the tetraspanin CD63', *Experimental Cell Research*, 315(9), pp. 1584–1592. doi: 10.1016/J.YEXCR.2008.09.020.

Ponpuak, M. *et al.* (2015) 'Secretory autophagy', *Current Opinion in Cell Biology*, 35, pp. 106–116. doi: 10.1016/J.CEB.2015.04.016.

Porter, K. R., Claude, A. and Fullam, E. F. (1945) 'A study of tissue culture cells by electron microscopy: Methods and preliminary observations', *Journal of Experimental Medicine*, 81(3), pp. 233–246. doi: 10.1084/jem.81.3.233.

Pradhipa Karuna, M. *et al.* (2020) 'Phosphorylation of Ykt6 SNARE Domain Regulates Its Membrane Recruitment and Activity', *Biomolecules 2020, Vol. 10, Page 1560*, 10(11), p. 1560. doi: 10.3390/BIOM10111560.

Price, L. S. *et al.* (1995) 'The small GTPases Rac and Rho as regulators of secretion in mast cells', *Current Biology*, 5(1), pp. 68–73. doi: 10.1016/S0960-9822(95)00018-2.

Price, L. S. *et al.* (1998) 'Activation of Rac and Cdc42 by Integrins Mediates Cell Spreading', *Molecular Biology of the Cell*, 9(7), p. 1863. doi: 10.1091/MBC.9.7.1863.

Pryor, P. R. *et al.* (2004) 'Combinatorial SNARE complexes with VAMP7 or VAMP8 define different late endocytic fusion events', *EMBO reports*, 5(6), pp. 590–595. doi: 10.1038/SJ.EMBOR.7400150.

Pulkkinen, L. and Uitto, J. (1998) 'Hemidesmosomal variants of epidermolysis bullosa. Mutations in the alpha6beta4 integrin and the 180-kD bullous pemphigoid antigen/type XVII collagen genes.', *Experimental dermatology*, 7(2–3), pp. 46–64. doi: 10.1111/j.1600-0625.1998.tb00304.x.

Puntman, D. C. *et al.* (2021) 'Munc18-1 is essential for neuropeptide secretion in neurons.', *The Journal of neuroscience : the official journal of the Society for Neuroscience*, 41(28), pp. 5980–5993. doi: 10.1523/JNEUROSCI.3150-20.2021.

Rahajeng, J. *et al.* (2012) 'MICAL-L1 is a Tubular Endosomal Membrane Hub that Connects Rab35 and Arf6 With Rab8a', *Traffic*, 13(1), pp. 82–93. doi: 10.1111/j.1600-0854.2011.01294.x.

Rathore, S. S. *et al.* (2010) 'Syntaxin N-terminal peptide motif is an initiation factor for the assembly of the SNARE–Sec1/Munc18 membrane fusion complex', *Proceedings of the National Academy of Sciences*, 107(52), pp. 22399–22406. doi: 10.1073/PNAS.1012997108.

Razi, M., Chan, E. Y. W. and Tooze, S. A. (2009) 'Early endosomes and endosomal coatomer are required for autophagy', *Journal of Cell Biology*, 185(2), pp. 305–321. doi: 10.1083/JCB.200810098.

Reales, E. *et al.* (2011) 'Basolateral Sorting of Syntaxin 4 Is Dependent on Its N-terminal Domain and the

AP1B Clathrin Adaptor, and Required for the Epithelial Cell Polarity', *PLOS ONE*, 6(6), p. e21181. doi: 10.1371/JOURNAL.PONE.0021181.

Reinecke, J. B. *et al.* (2014) 'Regulation of Src trafficking and activation by the endocytic regulatory proteins MICAL-L1 and EHD1', *Journal of Cell Science*, 127(8), pp. 1684–1698. doi: 10.1242/JCS.133892.

Ren, M. *et al.* (1998) 'Hydrolysis of GTP on rab11 is required for the direct delivery of transferrin from the pericentriolar recycling compartment to the cell surface but not from sorting endosomes', *Proceedings of the National Academy of Sciences of the United States of America*, 95(11), pp. 6187–6192. doi: 10.1073/pnas.95.11.6187.

Revathidevi, S. and Munirajan, A. K. (2019) 'Akt in cancer: Mediator and more', *Seminars in Cancer Biology*, 59, pp. 80–91. doi: 10.1016/J.SEMCANCER.2019.06.002.

Richter, B. *et al.* (2016) 'Phosphorylation of OPTN by TBK1 enhances its binding to Ub chains and promotes selective autophagy of damaged mitochondria', *Proceedings of the National Academy of Sciences*, 113(15), pp. 4039–4044. doi: 10.1073/PNAS.1523926113.

Rickman, C. *et al.* (2007) 'Functionally and Spatially Distinct Modes of munc18-Syntaxin 1 Interaction *', *Journal of Biological Chemistry*, 282(16), pp. 12097–12103. doi: 10.1074/JBC.M700227200.

Riento, K. *et al.* (2000) 'Munc18-2, a functional partner of syntaxin 3, controls apical membrane trafficking in epithelial cells', *Journal of Biological Chemistry*, 275(18), pp. 13476–13483. doi: 10.1074/jbc.275.18.13476.

Ritto, D. *et al.* (2017) 'Astaxanthin induces migration in human skin keratinocytes via Rac1 activation and RhoA inhibition', *Nutrition Research and Practice*, 11(4), p. 275. doi: 10.4162/NRP.2017.11.4.275.

Robinson, M. S. (2004) 'Adaptable adaptors for coated vesicles', *Trends in Cell Biology*. Elsevier, pp. 167–174. doi: 10.1016/j.tcb.2004.02.002.

Robinson, M. S., Sahlender, D. A. and Foster, S. D. (2010) 'Rapid Inactivation of Proteins by Rapamycin-Induced Rerouting to Mitochondria', *Developmental Cell*, 18(2), pp. 324–331. doi: 10.1016/j.devcel.2009.12.015.

Rohde, J. *et al.* (2003) 'The Transmembrane Domain of Vam3 Affects the Composition ofcis- and trans-SNARE Complexes to Promote Homotypic Vacuole Fusion *', *Journal of Biological Chemistry*, 278(3), pp. 1656–1662. doi: 10.1074/JBC.M209522200.

Roland, J. T. *et al.* (2007) 'Myosin Vb interacts with Rab8a on a tubular network containing EHD1 and EHD3', *Molecular Biology of the Cell*, 18(8), pp. 2828–2837. doi: 10.1091/mbc.E07-02-0169.

Rothman, J. E. and Warren, G. (1994) 'Implications of the SNARE hypothesis for intracellular membrane topology and dynamics.', *Current biology : CB*, 4(3), pp. 220–233. doi: 10.1016/s0960-9822(00)00051-8.

Saitsu, H. *et al.* (2008) 'De novo mutations in the gene encoding STXBP1 (MUNC18-1) cause early infantile epileptic encephalopathy', *Nature Genetics 2008 40:6*, 40(6), pp. 782–788. doi: 10.1038/ng.150.

Sato *et al.* (2007) 'The Rab8 GTPase regulates apical protein localization in intestinal cells', *Nature*, 448(7151), pp. 366–369. doi: 10.1038/NATURE05929.

Sato, M. *et al.* (2008) 'Regulation of endocytic recycling by C. elegans Rab35 and its regulator RME-4, a coated-pit protein', *EMBO Journal*, 27(8), pp. 1183–1196. doi: 10.1038/emboj.2008.54.

Schaaf, M. B. E. *et al.* (2016) 'LC3/GABARAP family proteins: autophagy-(un)related functions', *The FASEB Journal*, 30(12), pp. 3961–3978. doi: 10.1096/FJ.201600698R.

Schiavo, G. *et al.* (1992) 'Tetanus toxin is a zinc protein and its inhibition of neurotransmitter release and protease activity depend on zinc.', *The EMBO Journal*, 11(10), pp. 3577–3583. doi: 10.1002/J.1460-2075.1992.TB05441.X.

Schiavo, G. *et al.* (1995) 'Botulinum Neurotoxin Type C Cleaves a Single Lys-Ala Bond within the Carboxyl-terminal Region of Syntaxins', *Journal of Biological Chemistry*, 270(18), pp. 10566–10570. doi: 10.1074/JBC.270.18.10566.

Schillemans, M. *et al.* (2018) 'Weibel-Palade Body Localized Syntaxin-3 Modulates Von Willebrand Factor Secretion From Endothelial Cells', *Arteriosclerosis, Thrombosis, and Vascular Biology*, 38(7), pp. 1549–1561. doi: 10.1161/ATVBAHA.117.310701.

Schneeberger, K. *et al.* (2018) 'Intestinal epithelial cell polarity defects in disease: lessons from microvillus inclusion disease', *Disease Models & Mechanisms*, 11(2). doi: 10.1242/DMM.031088.

Schollmeier, Y. *et al.* (2011) 'Resolving the Function of Distinct Munc18-1/SNARE Protein Interaction Modes in a Reconstituted Membrane Fusion Assay', *Journal of Biological Chemistry*, 286(35), pp. 30582–30590. doi: 10.1074/JBC.M111.269886.

Shanks, S. G. *et al.* (2012) 'The Sec1/Munc18 Protein Vps45 Regulates Cellular Levels of Its SNARE Binding Partners Tlg2 and Snc2 in Saccharomyces cerevisiae', *PLOS ONE*, 7(11), p. e49628. doi: 10.1371/JOURNAL.PONE.0049628.

Sharma, M. *et al.* (2009a) 'MICAL-L1 links EHD1 to tubular recycling endosomes and regulates receptor recycling', *Molecular Biology of the Cell*, 20(24), pp. 5181–5194. doi: 10.1091/mbc.E09-06-0535.

Sharma, M. *et al.* (2009b) 'MICAL-L1 Links EHD1 to Tubular Recycling Endosomes and Regulates Receptor Recycling', *https://doi.org/10.1091/mbc.e09-06-0535*, 20(24), pp. 5181–5194. doi: 10.1091/MBC.E09-06-0535.

Sharma, N. *et al.* (2006) 'Apical targeting of syntaxin 3 is essential for epithelial cell polarity', *Journal of Cell Biology*, 173(6), pp. 937–948. doi: 10.1083/JCB.200603132.

Shen, C. *et al.* (2018) 'The N-peptide– binding mode is critical to Munc18-1 function in synaptic exocytosis', *Journal of Biological Chemistry*, 293(47), pp. 18309–18317. doi: 10.1074/jbc.RA118.005254.

Siekevitz, P. and Palade, G. E. (1958a) 'A cyto-chemical study on the pancreas of the guinea pig. III. In vivo incorporation of leucine-1-C14 into the proteins of cell fractions.', *The Journal of biophysical and biochemical cytology*, 4(5), pp. 557–66. doi: 10.1083/jcb.4.5.557.

Siekevitz, P. and Palade, G. E. (1958b) 'A cytochemical study on the pancreas of the guinea pig. I. Isolation and enzymatic activities of cell fractions.', *The Journal of biophysical and biochemical cytology*, 4(2), pp. 203–218. doi: 10.1083/jcb.4.2.203.

Siekevitz, P. and Palade, G. E. (1958c) 'A cytochemical study on the pancreas of the guinea pig. II. Functional variations in the enzymatic activity of microsomes.', *The Journal of biophysical and biochemical cytology*, 4(3), pp. 309–18. doi: 10.1083/jcb.4.3.309.

Sikora, R. *et al.* (2021) 'MICAL-L1 is required for cargo protein delivery to the cell surface', *Biology Open*, 10(6). doi: 10.1242/BIO.058008.

Simpson, C. L., Patel, D. M. and Green, K. J. (2011) 'Deconstructing the skin: cytoarchitectural determinants of epidermal morphogenesis', *Nature Reviews Molecular Cell Biology 2011 12:9*, 12(9), pp. 565–580. doi: 10.1038/nrm3175.

Simpson, J. C., Joggerst, B., Laketa, V., Verissimo, F., Cetin, C., Erfle, H., Bexiga, M. G., Singan, V. R., Hériché, J.-K., *et al.* (2012) 'Genome-wide RNAi screening identifies human proteins with a regulatory function in the early secretory pathway', *Nature Cell Biology 2012 14:7*, 14(7), pp. 764–774. doi: 10.1038/ncb2510.

Simpson, J. C., Joggerst, B., Laketa, V., Verissimo, F., Cetin, C., Erfle, H., Bexiga, M. G., Singan, V. R., Hériché, J. K., *et al.* (2012) 'Genome-wide RNAi screening identifies human proteins with a regulatory function in the early secretory pathway', *Nature Cell Biology*, 14(7), pp. 764–774. doi: 10.1038/ncb2510.

Sirois, I. *et al.* (2012) 'Caspase activation regulates the extracellular export of autophagic vacuoles'. doi: 10.4161/auto.19768.

van der Sluijs, P. *et al.* (1992) 'The small GTP-binding protein rab4 controls an early sorting event on the endocytic pathway', *Cell*, 70(5), pp. 729–740. doi: 10.1016/0092-8674(92)90307-X.

Smithers, N. P. *et al.* (2008) 'Insulin-triggered repositioning of munc18c on syntaxin-4 in GLUT4 signalling', *Biochemical Journal*, 410(2), pp. 255–260. doi: 10.1042/BJ20070802.

Söllner, T *et al.* (1993) 'A protein assembly-disassembly pathway in vitro that may correspond to sequential steps of synaptic vesicle docking, activation, and fusion', *Cell*, 75(3), pp. 409–418. doi: 10.1016/0092-8674(93)90376-2.

Söllner, Thomas *et al.* (1993) 'SNAP receptors implicated in vesicle targeting and fusion', *Nature*, 362(6418), pp. 318–324. doi: 10.1038/362318a0.

Sönnichsen, B. *et al.* (2000) 'Distinct membrane domains on endosomes in the recycling pathway visualized by multicolor imaging of Rab4, Rab5, and Rab11', *Journal of Cell Biology*, 149(4), pp. 901–913. doi: 10.1083/jcb.149.4.901.

Soo Hoo, L. *et al.* (2016) 'The SNARE Protein Syntaxin 3 Confers Specificity for Polarized Axonal Trafficking in Neurons', *PLOS ONE*. Edited by J. G. Donaldson, 11(9), p. e0163671. doi: 10.1371/journal.pone.0163671.

Sørensen, J. B. *et al.* (2003) 'Differential Control of the Releasable Vesicle Pools by SNAP-25 Splice Variants and SNAP-23', *Cell*, 114(1), pp. 75–86. doi: 10.1016/S0092-8674(03)00477-X.

Spessott, W. A. *et al.* (2015) 'Hemophagocytic lymphohistiocytosis caused by dominant-negative mutations in STXBP2 that inhibit SNARE-mediated membrane fusion', *Blood*, 125(10), pp. 1566–1577. doi: 10.1182/blood-2014-11-610816.

Spessott, W. A. *et al.* (2017a) 'SM protein Munc18-2 facilitates transition of Syntaxin 11-mediated lipid mixing to complete fusion for T-lymphocyte cytotoxicity', *Proceedings of the National Academy of Sciences of the United States of America*, 114(11), pp. E2176–E2185. doi: 10.1073/pnas.1617981114.

Spessott, W. A. *et al.* (2017b) 'SM protein Munc18-2 facilitates transition of Syntaxin 11-mediated lipid mixing to complete fusion for T-lymphocyte cytotoxicity', *Proceedings of the National Academy of Sciences*, 114(11), pp. E2176–E2185. doi: 10.1073/PNAS.1617981114.

zur Stadt, U. *et al.* (2009) 'Familial Hemophagocytic Lymphohistiocytosis Type 5 (FHL-5) Is Caused by Mutations in Munc18-2 and Impaired Binding to Syntaxin 11', *The American Journal of Human Genetics*, 85(4), pp. 482–492. doi: 10.1016/J.AJHG.2009.09.005.

Stamberger, H., Weckhuysen, S. and Jonghe, P. De (2017) 'STXBP1 as a therapeutic target for epileptic

encephalopathy', *https://doi.org/10.1080/14728222.2017.1386175*, 21(11), pp. 1027–1036. doi: 10.1080/14728222.2017.1386175.

Stanley, A. C. *et al.* (2014) 'The Rho GTPase Rac1 is required for recycling endosome-mediated secretion of TNF in macrophages', *Immunology and Cell Biology*, 92(3), pp. 275–286. doi: 10.1038/ICB.2013.90.

Struthers, M. S. *et al.* (2009) 'Functional homology of mammalian syntaxin 16 and yeast Tlg2p reveals a conserved regulatory mechanism', *Journal of Cell Science*, 122(13), pp. 2292–2299. doi: 10.1242/JCS.046441.

Su, P. *et al.* (2020) 'MACF1 promotes preosteoblast migration by mediating focal adhesion turnover through EB1', *Biology Open*, 9(3). doi: 10.1242/BIO.048173.

Südhof, T. C. *et al.* (1989) 'A synaptic vesicle membrane protein is conserved from mammals to Drosophila', *Neuron*, 2(5), pp. 1475–1481. doi: 10.1016/0896-6273(89)90193-1.

Südhof, T. C. and Rothman, J. E. (2009) 'Membrane fusion: Grappling with SNARE and SM proteins', *Science*. Science, pp. 474–477. doi: 10.1126/science.1161748.

Sutton, R. B. *et al.* (1998) 'Crystal structure of a SNARE complex involved in synaptic exocytosis at 2.4 Å resolution', *Nature*. Nature Publishing Group, pp. 347–353. doi: 10.1038/26412.

Tagaya, M. *et al.* (2014) 'Moonlighting functions of the NRZ (mammalian Dsl1) complex', *Frontiers in Cell and Developmental Biology*, 0(JUN), p. 25. doi: 10.3389/FCELL.2014.00025.

Tellam, J. T., McIntosh, S. and James, D. E. (1995) 'Molecular Identification of Two Novel Munc-18 Isoforms Expressed in Non-neuronal Tissues (∗)', *Journal of Biological Chemistry*, 270(11), pp. 5857–5863. doi: 10.1074/JBC.270.11.5857.

Teo, Q. W., Leur, S. W. van and Sanyal, S. (2021) 'Escaping the Lion's Den: redirecting autophagy for unconventional release and spread of viruses', *The FEBS Journal*, 288(13), pp. 3913–3927. doi: 10.1111/FEBS.15590.

Thurmond, D. C. *et al.* (1998) 'Regulation of Insulin-stimulated GLUT4 Translocation by Munc18c in 3T3L1 Adipocytes *', *Journal of Biological Chemistry*, 273(50), pp. 33876–33883. doi: 10.1074/JBC.273.50.33876.

Thurmond, D. C. *et al.* (2000) 'Munc18c Function Is Required for Insulin-Stimulated Plasma Membrane Fusion of GLUT4 and Insulin-Responsive Amino Peptidase Storage Vesicles', *Molecular and Cellular Biology*, 20(1), pp. 379–388. doi: 10.1128/MCB.20.1.379-388.2000.

Tomas, A., Futter, C. E. and Eden, E. R. (2014) 'EGF receptor trafficking: consequences for signaling and

cancer', *Trends in Cell Biology*, 24(1), p. 26. doi: 10.1016/J.TCB.2013.11.002.

Toonen, R. F. G. *et al.* (2006) 'Munc18-1 expression levels control synapse recovery by regulating readily releasable pool size', *Proceedings of the National Academy of Sciences*, 103(48), pp. 18332–18337. doi: 10.1073/PNAS.0608507103.

Tooze, S. A. (1998) 'Biogenesis of secretory granules in the trans-Golgi network of neuroendocrine and endocrine cells', *Biochimica et Biophysica Acta - Molecular Cell Research*, 1404(1–2), pp. 231–244. doi: 10.1016/S0167-4889(98)00059-7.

Torres, J. *et al.* (2011) 'The Syntaxin 4 N Terminus Regulates Its Basolateral Targeting by Munc18c-dependent and -independent Mechanisms *', *Journal of Biological Chemistry*, 286(12), pp. 10834–10846. doi: 10.1074/JBC.M110.186668.

Toufighi, K. *et al.* (2015) 'Dissecting the Calcium-Induced Differentiation of Human Primary Keratinocytes Stem Cells by Integrative and Structural Network Analyses', *PLOS Computational Biology*, 11(5), p. e1004256. doi: 10.1371/JOURNAL.PCBI.1004256.

Trimble, W. S., Cowan, D. M. and Scheller, R. H. (1988) 'VAMP-1: A synaptic vesicle-associated integral membrane protein', *Proceedings of the National Academy of Sciences of the United States of America*, 85(12), pp. 4538–4542. doi: 10.1073/pnas.85.12.4538.

Ueyama, T. *et al.* (2020) 'Rac-Dependent Signaling from Keratinocytes Promotes Differentiation of Intradermal White Adipocytes', *Journal of Investigative Dermatology*, 140(1), pp. 75-84.e6. doi: 10.1016/J.JID.2019.06.140.

Ullrich, O. *et al.* (1996) 'Rab11 regulates recycling through the pericentriolar recycling endosome', *Journal of Cell Biology*, 135(4), pp. 913–924. doi: 10.1083/jcb.135.4.913.

Van der Vaart, A. and Reggiori, F. (2010) 'The Golgi complex as a source for yeast autophagosomal membranes', *Autophagy*, 6(6), pp. 2270–2284. doi: 10.1091/MBC.E09-04-0345.

Verhage, M. *et al.* (1997) 'DOC2 Proteins in Rat Brain: Complementary Distribution and Proposed Function as Vesicular Adapter Proteins in Early Stages of Secretion', *Neuron*, 18(3), pp. 453–461. doi: 10.1016/S0896-6273(00)81245-3.

Verhage, M. *et al.* (2000) 'Synaptic Assembly of the Brain in the Absence of Neurotransmitter Secretion', *Science*, 287(5454), pp. 864–869. doi: 10.1126/SCIENCE.287.5454.864.

Vidal-Quadras, M. *et al.* (2017) 'Endocytic turnover of Rab8 controls cell polarization', *Journal of Cell Science*, 130(6), pp. 1147–1157. doi: 10.1242/JCS.195420.

Voets, T. *et al.* (2001) 'Munc18-1 Promotes Large Dense-Core Vesicle Docking', *Neuron*, 31(4), pp. 581–592. doi: 10.1016/S0896-6273(01)00391-9.

Vogel, G. F. *et al.* (2015) 'Cargo-selective apical exocytosis in epithelial cells is conducted by Myo5B, Slp4a, Vamp7, and Syntaxin 3.', *The Journal of cell biology*, 211(3), pp. 587–604. doi: 10.1083/jcb.201506112.

Vogel, G. F. *et al.* (2017) 'Disrupted apical exocytosis of cargo vesicles causes enteropathy in FHL5 patients with Munc18-2 mutations', *JCI insight*, 2(14). doi: 10.1172/jci.insight.94564.

Walko, G., Castañón, M. J. and Wiche, G. (2015) 'Molecular architecture and function of the hemidesmosome', *Cell and Tissue Research*, 360, pp. 529–544. doi: 10.1007/s00441-015-2216-6.

Wang, C. *et al.* (2004) 'A role of VAMP8/endobrevin in regulated exocytosis of pancreatic acinar cells', *Developmental cell*, 7(3), pp. 359–371. doi: 10.1016/J.DEVCEL.2004.08.002.

Wang, H. *et al.* (2004) 'Human Zwint-1 specifies localization of Zeste White 10 to kinetochores and is essential for mitotic checkpoint signaling.', *The Journal of biological chemistry*, 279(52), pp. 54590–54598. doi: 10.1074/jbc.M407588200.

Wang, R. C. *et al.* (2012) 'Akt-mediated regulation of autophagy and tumorigenesis through Beclin 1 phosphorylation', *Science*, 338(6109), pp. 956–959. doi: 10.1126/SCIENCE.1225967.

Wang, Y. *et al.* (2006) 'Syntaxin 9 is Enriched in Skin Hair Follicle Epithelium and Interacts With the Epidermal Growth Factor Receptor', *Traffic*, 7(2), pp. 216–226. doi: 10.1111/J.1600-0854.2005.00378.X.

Wang, Y. *et al.* (2021) 'Syntaxin 2 promotes colorectal cancer growth by increasing the secretion of exosomes', *Journal of Cancer*, 12(7), pp. 2050–2058. doi: 10.7150/JCA.51494.

Wang, Z. *et al.* (2020) 'Autophagy-based unconventional secretion of HMGB1 by keratinocytes plays a pivotal role in psoriatic skin inflammation', *https://doi.org/10.1080/15548627.2020.1725381*, 17(2), pp. 529–552. doi: 10.1080/15548627.2020.1725381.

Weber, T. *et al.* (1998) 'SNAREpins: Minimal machinery for membrane fusion', *Cell*, 92, pp. 759–772.

Weidman, P. J. *et al.* (1989) 'Binding of an N-ethylmaleimide-sensitive fusion protein to Golgi membranes requires both a soluble protein(s) and an integral membrane receptor', *The Journal of Cell Biology*, 108(5), p. 1589. doi: 10.1083/JCB.108.5.1589.

Wen, W. *et al.* (2010) 'Lipid-Induced Conformational Switch Controls Fusion Activity of Longin Domain SNARE Ykt6', *Molecular Cell*, 37(3), pp. 383–395. doi: 10.1016/J.MOLCEL.2010.01.024.

Weng, L. *et al.* (2006) 'Girdin, a Novel Actin-Binding Protein, and Its Family of Proteins Possess Versatile Functions in the Akt and Wnt Signaling Pathways', *Annals of the New York Academy of Sciences*, 1086(1), pp. 169–184. doi: 10.1196/ANNALS.1377.016.

Weng, L. *et al.* (2010) 'Girding for migratory cues: roles of the Akt substrate Girdin in cancer progression and angiogenesis', *Cancer Science*, 101(4), pp. 836–842. doi: 10.1111/J.1349-7006.2009.01487.X.

Weninger, K. *et al.* (2008) 'Accessory Proteins Stabilize the Acceptor Complex for Synaptobrevin, the 1:1 Syntaxin/SNAP-25 Complex', *Structure*, 16(2), pp. 308–320. doi: 10.1016/J.STR.2007.12.010.

Westlake, C. J. *et al.* (2011) 'Primary cilia membrane assembly is initiated by Rab11 and transport protein particle II (TRAPPII) complex-dependent trafficking of Rabin8 to the centrosome', *Proceedings of the National Academy of Sciences of the United States of America*, 108(7), pp. 2759–2764. doi: 10.1073/pnas.1018823108.

Whiteheart, S. W. *et al.* (1992) 'Soluble N-ethylmaleimide-sensitive fusion attachment proteins (SNAPs) bind to a multi-SNAP receptor complex in Golgi membranes.', *Journal of Biological Chemistry*, 267(17), pp. 12239–12243. doi: 10.1016/S0021-9258(19)49830-X.

Whyte, J. R. C. and Munro, S. (2002) 'Vesicle tethering complexes in membrane traffic', *Journal of Cell Science*, 115(13), pp. 2627–2637.

Wilson, D. W. *et al.* (1992) 'A multisubunit particle implicated in membrane fusion.', *Journal of Cell Biology*, 117(3), pp. 531–538. doi: 10.1083/JCB.117.3.531.

Wit, H. de *et al.* (2006) 'Docking of Secretory Vesicles Is Syntaxin Dependent', *PLOS ONE*, 1(1), p. e126. doi: 10.1371/JOURNAL.PONE.0000126.

de Wit, H. *et al.* (2009) 'Synaptotagmin-1 Docks Secretory Vesicles to Syntaxin-1/SNAP-25 Acceptor Complexes', *Cell*, 138(5), pp. 935–946. doi: 10.1016/J.CELL.2009.07.027.

Woo Seo, D. *et al.* (2015) 'Zwint-1 is required for spindle assembly checkpoint function and kinetochore-microtubule attachment during oocyte meiosis', *Scientific Reports 2015 5:1*, 5(1), pp. 1–11. doi: 10.1038/srep15431.

Wu, X., Kodama, A. and Fuchs, E. (2008) 'ACF7 Regulates Cytoskeletal-Focal Adhesion Dynamics and Migration and Has ATPase Activity', *Cell*, 135(1), pp. 137–148. doi: 10.1016/j.cell.2008.07.045.

Xie, S. *et al.* (2016) 'The endocytic recycling compartment maintains cargo segregation acquired upon exit from the sorting endosome', *Molecular Biology of the Cell*, 27(1), pp. 108–126. doi: 10.1091/mbc.E15-07-0514.

Xie, Z., Nair, U. and Klionsky, D. (2008) 'Atg8 controls phagophore expansion during autophagosome formation', *Molecular biology of the cell*, 19(8), pp. 3290–3298. doi: 10.1091/MBC.E07-12-1292.

Xu, H. *et al.* (2011) 'A lipid-anchored SNARE supports membrane fusion', *Proceedings of the National Academy of Sciences*, 108(42), pp. 17325–17330. doi: 10.1073/PNAS.1113888108.

Xu, H. and Wickner, W. (2012) 'N-terminal domain of vacuolar SNARE Vam7p promotes trans-SNARE complex assembly', *Proceedings of the National Academy of Sciences of the United States of America*, 109(44), pp. 17936–17941. doi: 10.1073/PNAS.1216201109.

Yang, B. *et al.* (2000) 'Nsec1 Binds a Closed Conformation of Syntaxin1a', *Journal of Cell Biology*, 148(2), pp. 247–252. doi: 10.1083/JCB.148.2.247.

Yang, Y. *et al.* (2011) 'Activation of Rac1-PI3K/Akt is required for epidermal growth factor-induced PAK1 activation and cell migration in MDA-MB-231 breast cancer cells', *Journal of Biomedical Research*, 25(4), p. 237. doi: 10.1016/S1674-8301(11)60032-8.

Ye, S. *et al.* (2012) 'Syntaxin-11, but not syntaxin-2 or syntaxin-4, is required for platelet secretion', *Blood*, 120(12), pp. 2484–2492. doi: 10.1182/BLOOD-2012-05-430603.

Yi, M. *et al.* (2020) 'Identifying Tumorigenesis and Prognosis-Related Genes of Lung Adenocarcinoma: Based on Weighted Gene Coexpression Network Analysis.', *BioMed research international*, 2020, p. 4169691. doi: 10.1155/2020/4169691.

Ying, H. *et al.* (2018) 'Overexpression of Zwint predicts poor prognosis and promotes the proliferation of hepatocellular carcinoma by regulating cell-cycle-related proteins.', *OncoTargets and therapy*, 11, pp. 689–702. doi: 10.2147/OTT.S152138.

Yoshii, S. R. and Mizushima, N. (2017) 'Monitoring and Measuring Autophagy', *International Journal of Molecular Sciences*, 18(9). doi: 10.3390/IJMS18091865.

Yoshimura, S. *et al.* (2007) 'Functional dissection of Rab GTPases involved in primary cilium formation', *The Journal of Cell Biology*, 178(3), p. 363. doi: 10.1083/JCB.200703047.

Yudowski, G. A. *et al.* (2009) 'Cargo-mediated regulation of a rapid Rab4-dependent recycling pathway', *Molecular Biology of the Cell*, 20(11), pp. 2774–2784. doi: 10.1091/mbc.E08-08-0892.

Yue, J. *et al.* (2016) 'In vivo epidermal migration requires focal adhesion targeting of ACF7', *Nature Communications 2016 7:1*, 7(1), pp. 1–15. doi: 10.1038/ncomms11692.

Zaessinger, S. *et al.* (2015) 'Drosophila MAGI interacts with RASSF8 to regulate E-Cadherin-based adherens junctions in the developing eye', *Development*, 142(6), pp. 1102–1112. doi:

10.1242/DEV.116277.

Zerial, M. and McBride, H. (2001) 'Rab proteins as membrane organizers', *Nature Reviews Molecular Cell Biology 2001 2:2*, 2(2), pp. 107–117. doi: 10.1038/35052055.

Zhang, J. *et al.* (2018) 'Dynamic cycling of t-SNARE acylation regulates platelet exocytosis', *Journal of Biological Chemistry*, 293(10), pp. 3593–3606. doi: 10.1074/JBC.RA117.000140.

Zhang, J., Yue, J. and Wu, X. (2017) 'Spectraplakin family proteins - cytoskeletal crosslinkers with versatile roles.', *Journal of cell science*, 130(15), pp. 2447–2457. doi: 10.1242/jcs.196154.

Zhang, Z. *et al.* (2020) 'CASK modulates the assembly and function of the Mint1/Munc18-1 complex to regulate insulin secretion.', *Cell discovery*, 6(1), p. 92. doi: 10.1038/s41421-020-00216-3.

Zhou, G., Shen, M. and Zhang, Z. (2020) 'ZW10 Binding Factor (ZWINT), a Direct Target of Mir-204, Predicts Poor Survival and Promotes Proliferation in Breast Cancer.', *Medical science monitor : international medical journal of experimental and clinical research*, 26, p. e921659. doi: 10.12659/MSM.921659.

Zhou, P., Pang, Zhiping P., *et al.* (2013) 'Syntaxin-1 N-peptide and H abc -domain perform distinct essential functions in synaptic vesicle fusion', *EMBO Journal*, 32(1), pp. 159–171. doi: 10.1038/emboj.2012.307.

Zhou, P., Pang, Zhiping P, *et al.* (2013) 'Syntaxin-1 N-peptide and Habc-domain perform distinct essential functions in synaptic vesicle fusion', *The EMBO Journal*, 32(1), pp. 159–171. doi: 10.1038/EMBOJ.2012.307.

Zhou, Z., T, Bacaj, *et al.* (2013) 'Lipid-anchored SNAREs lacking transmembrane regions fully support membrane fusion during neurotransmitter release', *Neuron*, 80(2), pp. 470–483. doi: 10.1016/J.NEURON.2013.09.010.

Zhu, D. *et al.* (2017) 'Syntaxin 2 Acts as Inhibitory SNARE for Insulin Granule Exocytosis', *Diabetes*, 66(4), pp. 948–959. doi: 10.2337/DB16-0636.

Ziegler, S. F. *et al.* (1996) 'Molecular Characterization of a Nonneuronal Human UNC18 Homolog', *Genomics*, 37(1), pp. 19–23. doi: 10.1006/GENO.1996.0515.

Zurzolo, C. and Simons, K. (2016) 'Glycosylphosphatidylinositol-anchored proteins: Membrane organization and transport', *Biochimica et Biophysica Acta (BBA) - Biomembranes*, 1858(4), pp. 632–639. doi: 10.1016/J.BBAMEM.2015.12.018.